

~~1065-10488~~

N65-16498

(ACCESSION NUMBER)

(THRU)

290

(PAGES)

CR 53674

(NASA CR OR TMX OR AD NUMBER)

(CODE)

30

(CATEGORY)

# MARS-VENUS CAPSULE PARAMETER STUDY

for the Jet Propulsion Laboratory  
under Contract No. JPL-950626

GPO PRICE \$ \_\_\_\_\_

OTS PRICE(S) \$ \_\_\_\_\_

Hard copy (HC) 6.00Microfiche (MF) 1.50

## VOLUME I

## introduction and analysis

**Arco**  
CORPORATION

research and advanced development division  
Wilmington, Massachusetts

t: MARS-VENUS CAPSULE  
PARAMETER STUDY.

→ Volume I:  
Introduction and Analysis

Prepared by

(2)  
RESEARCH AND ADVANCED DEVELOPMENT DIVISION

AVCO CORPORATION  
Wilmington, Massachusetts

Revision 1

(NASA CR-53674 Technical Report Vol. I,  
(JPL RAD-TR-64-1 Rev. 1)  
Contract 950626)

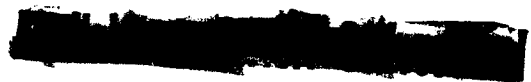
auth.

21 March 1964 290 p refs

Prepared for

JET PROPULSION LABORATORY  
CALIFORNIA INSTITUTE OF TECHNOLOGY  
Pasadena, California

Unc



## CONTENTS

I.	Introduction .....	1
	A. Objectives .....	1
	B. Scope of Study .....	5
	C. Approach .....	29
II.	Analytical Methods .....	33
	A. Coefficients Block .....	33
	B. Heating Block .....	42
	C. Trajectory Block .....	136
	D. Structures Block .....	170
	E. Heat Shield Block .....	237
	References .....	276

## ILLUSTRATIONS

Figure I-1	Geometry of Mars Vehicles .....	6
I-2	Case Generation Methodology for Mars Entry .....	11
I-3	Geometry of Venus Vehicles .....	17
I-4	Afterbody Surface Area .....	18
I-5	Case Generation Methodology for Venus Entry .....	24
I-6	Mars-Venus Capsule Shape Parameters .....	34
I-7	Convective Heating at a Stagnation Point (100-Percent CO <sub>2</sub> ) .....	84
I-8	Convective Heating at a Stagnation Point (90-Percent CO <sub>2</sub> and 10-Percent N <sub>2</sub> ) .....	85
I-9	Convective Heating at a Stagnation Point (50-Percent CO <sub>2</sub> and 50-Percent N <sub>2</sub> ) .....	86
I-10	Convective Heating at a Stagnation Point (10-Percent CO <sub>2</sub> and 90-Percent N <sub>2</sub> ) .....	87
I-11	Effect of Dynamics on Convective Heating .....	88
I-12	Radiative Heat Pulse Model .....	105
I-13	Comparison of Radiation Predictions With Experiment ....	121
I-14	Calculated Results for 9-Percent CO <sub>2</sub> and 91-Percent CO <sub>2</sub> .....	122
I-15	Results for 9-Percent CO <sub>2</sub> and 91-Percent N <sub>2</sub> from Venus-Mars Capsule Study, Volume II .....	123
I-16	Pressure Distribution of a Blunted Cylinder, $M_{\infty} = \infty$ .....	125
I-17	Pressure Distribution on a Blunted 5-Degree Cone, $M_{\infty} = \infty$ .....	126

## ILLUSTRATIONS (Cont'd)

Figure I-18	Pressure Distribution on a Blunted 10-Degree Cone, $M_\infty = \infty$ .....	127
I-19	Pressure Distribution on a Blunted 20-Degree Cone, $M_\infty = \infty$ .....	128
I-20	Pressure Distribution on a Blunted 30-Degree Cone, $M_\infty = \infty$ .....	129
I-21	Comparison with Cheng, $\gamma = 1.4$ .....	130
I-22	Comparison of Analytical and Experimental Results for Stagnation Point Heating in $\text{CO}_2$ - $\text{N}_2$ Mixtures .....	132
I-23	Stagnation Point Heating (M1 Configuration) .....	134
I-24	Comparison of Theoretical and Actual Shock Shapes (M1 Configuration) .....	135
I-25	Inertial Coordinate System for Planetary Entry .....	138
I-26	Coordinate System for Dynamics Analysis .....	156
I-27	Shape Parameters .....	171
I-28	Spherical Cap Geometry .....	176
I-29	Experimental Buckling of Spherical Shells .....	179
I-30	$\ln P_1$ versus $\ln S$ .....	188
I-31	Conical Sandwich Shell Geometry .....	192
I-32	Cone Geometry .....	209
I-33	Idealized Conical and Cylindrical Section .....	219
I-34	Impact Attenuation System--Idealized Model .....	229
I-35	Crushing Strength of Impact Material .....	231
I-36	Crushing Thickness Model .....	233
I-37	Radiation Shield Plus Structure .....	239

## ILLUSTRATIONS (Concl'd)

Figure 1-38	Typical Venus Heating Environment .....	241
1-39	Typical Maritian Heating Environment .....	242
1-40	Rear and Mean Temperature Rise in a Finite Medium with Constant Surface Temperature and Insulated Rear Boundary .....	247
1-41	Composite Slab with Constant Surface Temperature where Second Layer Acts as a Capacitance .....	249
1-42	Simple Ablation Shield .....	255
1-43	Enthalpy versus Temperature for Mars Kaplan Atmospheres .....	260
1-44	Enthalpy versus Temperature for Venus Kaplan Atmospherers .....	261
1-45	Ablation Performance of Mars Avcoat Material .....	264
1-46	Temperature Gradient Comparison .....	265
1-47	Effect of Radiant Heating on the Ablation Performance of a Graphite-Epoxy Composite .....	266
1-48	Heat Shield Thickness versus Time of Heat Shield Jettison .....	270
1-49	Heat Absorbed by Thermal Protection System versus Time of Heat Shield Jettison .....	272
1-50	Comparison of Ablation Weights Calculated by Approximate and Numerical Solutions .....	274
1-51	Comparison of Charring and Noncharring Theories .....	275

## TABLES

Table I-1	Mars Shape Parameters .....	7
I-2	Mars Entry Parameters .....	7
I-3	Mars Atmospheres .....	12
I-4	Nominal Values for Mars Study .....	13
I-5	Case Generation for Mars Study .....	14
I-6	Mars Entries--Case Identification .....	15
I-7	Venus Shape Parameters .....	20
I-8	Venus Entry Parameters .....	21
I-9	Venus Atmospheres .....	23
I-10	Nominal Values for Venus Study.....	26
I-11	Case Generation for Venus Study .....	27
I-12	Venus Entries--Case Identification .....	28
I-13	Reaction Matrix .....	46
I-14	Heats of Formation at 0°K .....	47
I-15	Equilibrium Constants .....	48
I-16	Molecular Constants .....	51
I-17	Atomic Constants .....	52
I-18	Partition Functions .....	54
I-19	Zone Tables .....	59
I-20	Table of Constants for the Emissivity Expressions .....	102

## TABLES (Concl'd)

Table I-21	Comparison of Improved and Approximate Radiation Theories .....	114
I-22	Constants for Equation (89) and Comparison with Equation (90) for the CO Molecule .....	116
I-23	A Comparison with the Kramer's Radiation from Argon ..	118
I-24	Conditions at Peak Dynamic Pressure .....	166
I-25	Trajectory Comparisons .....	167
I-26	Linear Solution Comparisons .....	167
I-27	Values for Plot of $\ln P_1$ versus $\ln S$ .....	200
I-28	Evaluation of Curve Fit for $P_1$ .....	201
I-29	Material Properties .....	268



## I. INTRODUCTION

### A. OBJECTIVES

This report presents the results of a 6-month parametric study conducted by the Avco Research and Advanced Development Division for the Jet Propulsion Laboratory. The objectives of this study were to obtain sufficiently comprehensive results which could be used to generate detailed preliminary design tradeoffs and other comparisons among the governing parameters associated with Mars and Venus entry capsule design, performance, and environment. Development of simplified methods was a keynote throughout the study due to the large number of parameters involved. By means of approximate methods, computer routines were compacted, computer calculation time reduced, and the capability of dealing with the broad scope of parameters was enhanced.

#### 1. Shape Study

The desirability of exploring the effects of vehicle shape on the weight and performance of an entry capsule led to the selection of characteristic parameters. The parameters chosen were such that every type of ballistic entry vehicle designed to date could be considered. For example, the simplest geometry could be a cone with a spherical nose, while complex geometries of elliptical nose shape and flared base could also be handled.

The choice of shapes for Mars and Venus was done with due consideration of preliminary investigations already performed. As a result of these preliminary studies, it was possible to narrow down the choice of shapes for Mars to blunt, high-drag designs with small surface area. This concept stemmed from the recently revised estimates of the surface pressure provided by the Jet Propulsion Laboratory, wherein vehicles of very low  $M/C_D A$  would be required to achieve suitable deceleration prior to impact. In the case of Venus, the large amount of radiative heating leads to the possibility of utilizing moderately slender bodies to alleviate the radiation heating problem. On the other hand, blunt, low-performance vehicles are more efficient in handling convective heating. Consequently, the choice of shapes for study for Venus covered a broad range to encompass both blunt and moderately slender design.

#### a. Aerodynamic Parameters

The trajectory, and hence the heating and loads, are closely connected to the estimated aerodynamic coefficients. Both angle of attack and Mach number effects can be important in establishing the trajectory of the vehicle and in determining the motions of the vehicle about its center of mass. Hence, in view of the significance of the dual variability of the coefficients, special effort was devoted to developing simplified

methods of analysis which would account for the predominant effects. The study was restricted to axisymmetric shapes with the center of mass on the longitudinal axis.

#### b. Kinematic Parameters

The flight path angle and velocity of the capsule at entry is related to the uncertainties in spacecraft guidance and launch data. Understanding the interrelationship of these two trajectory variables with capsule design was an aim of this study. The additional kinematic parameters of spin and angular motions of the capsule at entry were also deemed important variables.

#### c. Dynamics

The angle-of-attack history during entry was established as a prerequisite for determining the aerodynamic heating and loads and thereby deducing the elemental weights. Therefore, a measure of a capsule's performance is the ability of a particular shape to damp out motions at entry and achieve a small angle of attack at peak heating and peak dynamic pressure.

The low-altitude angle-of-attack history can be as important, or even more so, as the high altitude phase. For it is at low altitude that the blunt capsule, having exited from the gas dynamic region where hot plasma surrounds it, is to perform its mission. Consequently, sufficient static and dynamic stability of the capsule are needed to prevent the angular motions from increasing violently in the region of decreasing dynamic pressure. As a result of this problem, the ability of a capsule design to decelerate and maintain moderate angles of attack down to low supersonic Mach number, where a drogue might be deployed, or until impact, was considered as an important measure of its performance.

#### d. Radiation Heating

The increased severity of the radiation heating due to the compositions of the atmospheres specified gave rise to emphasis on these calculations. In the case of Mars entries, atmospheres of argon, carbon dioxide, and nitrogen were selected, whereas mixtures of carbon dioxide and nitrogen were selected for the Venus atmospheres. The emissivities of the prominent radiators were adjusted to bring the calculation model into agreement with available data. As a result of the importance of the radiative heating, the variation about the capsule, and hence the effects of angle of attack motions of the capsule on the radiative heating on sections of the capsule, were incorporated into the study.

#### e. Convective Heating

Preliminary studies indicated that the effects of atmospheric composition could change the convective heating significantly. Therefore, the correlation of numerical solutions of the boundary layer equations for several mixture of gases were incorporated into this study. The angle of attack effects, changing the trajectory, and changing the heating distribution about the capsule were also included as major factors in this study.

#### f. Loads

Analysis of the nature of the flow field about the capsule giving rise to the detailed pressure distributions and the aerodynamic loads presented a major problem. The range in shapes, gas mixtures, flight conditions, and angle of attack required the use of approximate methods. Mainly, it was important to establish consistent methods to deal with the wide variety of flow field problems, and to assess under what circumstances these methods could be subject to gross error.

### 2. Elemental Weights

The final measure of comparison between shapes and of the effects of the numerous parameters lies in the calculation of the elemental and residual weights of the capsule.

#### a. External Structure

The external structure supports the heat shield or, in some cases, was considered to act also as the heat shield. The weight of each structural section of the vehicle was assumed to be a function of the structural approach, i. e., honeycomb or stiffened sheet, the size of the vehicle and the maximum entry loads. A major problem area was determining the manner in which the inertia loads would be distributed, and accounting for the flanges, brackets, and miscellaneous hardware which affects the weight significantly. To arrive at weights which reflected an actual design, rather than simply a calculation of the external shell weight, a weight factor to be placed on the shell calculations had to be evolved by weight analysts engaged in entry vehicle design.

#### b. Heat Shield

The heat shield was assumed to provide thermal protection from the radiative and convective heating experienced during entry. The calculation of the heat shield weight was assumed to be a function of the structural temperature limitations, and the type of material employed. The development of simplified techniques, which compared well with more detailed calculations, was also a goal in the study.

c. Parachute

Parachute system weights for Mars capsules can be a significant fraction of the weight, depending on the descent time and/or impact velocity requirements. Provision was made for the calculation of a two-parachute descent system, using available performance data.

d. Internal Structure

The internal structure which supports the payload and the crushable energy-absorbing material, and which must also withstand the parachute loads, can be an important weight factor. A method for estimating the weight of the internal structure based on the payload (residual) weight, and the various loading conditions was evolved.

e. Residual Weight

The calculation of the residual (net payload) weight of the capsule was a prime objective of the study. The residual weight is found by subtracting the elemental weights noted above from the total weight, and therefore is an extremely complex function of all the parameters used in the study.

## B. SCOPE OF STUDY

### 1. Mars

#### a. Shapes

The original scope of the study provided for eight shapes to be evaluated for entry using the Schilling model atmospheres. However, revisions to the model atmosphere by JPL to include the low pressure (11 mb) and high-argon content cases required reevaluation of the suitability of the selected shapes.

To realign the Mars portion of the study to include the revised atmosphere models, the number of shapes was reduced to four and restricted to high drag, very blunt designs. Two forebody designs were considered; the bluff body, consisting of a large spherical nose cap, and the blunted cone, with a large cone angle. Two afterbody shapes were designed, one yielding low surface area while providing a low aerodynamic righting moment at high angles of attack; the other afterbody was identical with the first, but with the addition of a short cylindrical section to provide a larger aerodynamic righting moment at high angles of attack.

The selected shapes are shown in figure I-1. The M1 and M2 shapes are identical except for the addition of the short cylindrical section in M2. Similarly, the M3 and M4 are the same, except the M4 has a short cylindrical section. A summary of the Mars shape parameters is given in table I-1.

#### b. Governing Parameters

For each vehicle shape, a range of variation of key parameters was selected. A summary of the governing parameters is given in table I-2.

##### 1) Shape

The determination of the effect of shape on the elemental and residual weight of a Mars entry capsule was a prime objective of the study. High-drag bodies were used for the Mars study due to the small ballistic coefficient values needed to decelerate in the low-pressure atmosphere model.

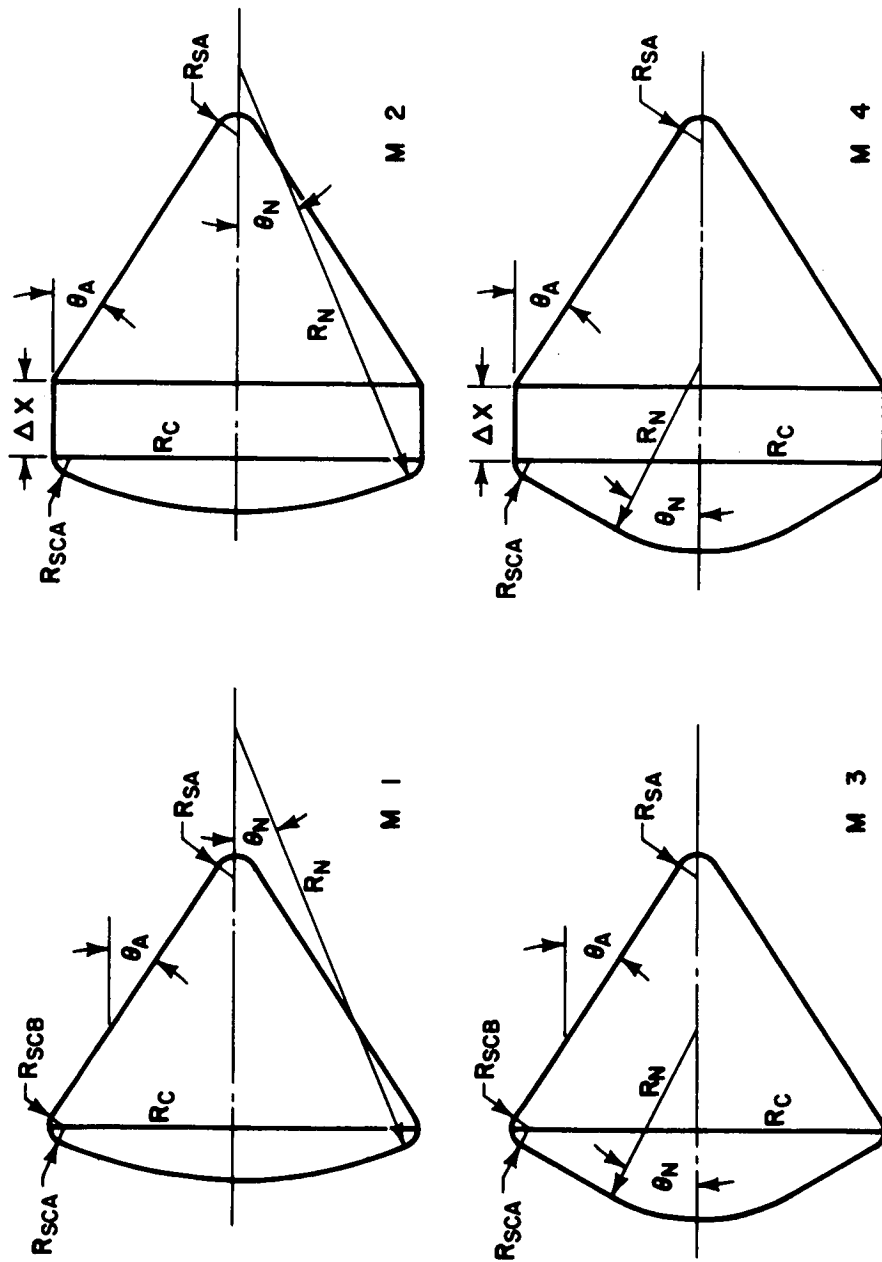


Figure I-1 GEOMETRY OF MARS VEHICLES

63-13175

TABLE I-1

## MARS SHAPE PARAMETERS

Shape	$R_N/R_C$	$\theta_N$ (degrees)	$R_{SCA}/R_C$	$\theta_C$ (degrees)	$\Delta X/2R_C$	$R_{SCB}/R_C$	$\theta_A$ (degrees)	$R_{SA}/R_C$
M1	2.4	23.08	0.1	0.0	0.0	0.1	33.0	0.119
M2	2.4	23.08	0.1	0.0	0.2	0.0	33.0	0.119
M3	1.0	30.0	0.1	60.0	0.0	0.1	33.0	0.119
M4	1.0	30.0	0.1	60.0	0.2	0.0	33.0	0.119

TABLE I-2

## MARS ENTRY PARAMETERS

Governing Parameter	Number
1. Shape	4
2. $M/C_D A$ , ballistic coefficient	2
3. $W_G$ , gross weight	2
4. $V_e$ , entry velocity	2
5. $\gamma_e$ , entry angle	2
6. Atmospheric model	4
7. $P$ , spin rate	2
8. $C_{m_\alpha}/I_y$ , stability factor	2
9. HUF, heating uncertainty factor	2
10. MUF, materials uncertainty factor	2
11. Structure	2
12. $\alpha_e$ , $Q_e$ , angle of attack and pitch rate at entry	<u>1</u>
Total Cases	160

2)  $M/C_D A$ , Ballistic Coefficient

The vehicle ballistic coefficient,  $M/C_D A$ , is a key trajectory, heating, and structural parameter. Values of 0.2 and 0.1 slug/ft<sup>2</sup> were selected for the Mars study. These values are based on the zero angle-of-attack hypersonic-drag coefficient.

3)  $W_G$ , Gross Weight

The gross weight affects the size of the vehicle and its inertial character, and hence is important from the standpoint of heating, structure, and dynamic performance. Maximum vehicle diameter was restricted to less than 12 feet for this study. Weights of 400 and 2000 pounds were selected as representative of the range of entry weights being considered for Mars.

4)  $v_e$ , Entry Velocity

The entry velocity governs the magnitude of the heating and loads. The hyperbolic excess velocity for this study was specified to lie between 9840 and 21,320 ft/sec. Entry velocities of 27,000 and 24,000 ft/sec were selected.

5)  $\gamma_e$ , Entry Angle

The flight path angle governs the capture and the heating and loads incurred during entry. A minimum capture angle of  $\gamma_e = -20$  degrees was used for Mars. The capture angle is most critical in the case of the high-velocity entry and low-density atmosphere. Two angles were selected for study,  $\gamma_e = -20$  degrees and  $\gamma_e = -90$  degrees, bracketing the expected range of entry conditions.

6) Atmospheric Model

The revised models specified by JPL were used in the study. These atmospheres are summarized in table I-3.

7)  $P$ , Spin Rate

The spin rate of the capsule can seriously influence the angle-of-attack convergence during entry, and hence influence the trajectory and the heat shield and structural weights significantly. Two values of spin rate, 1 and 4 rad/sec were selected, representing the estimated range of likely conditions.



8)  $C_{m\alpha}/I_y$  , , Stability Factor

This parameter is the ratio of the slope of the aerodynamic moment curve at zero angle of attack to the moment of inertia in pitch. Two values were selected for each vehicle. The stability factor provides for the evaluation of the effects of static stability and the moment of inertia in pitch on the angle of attack convergence and hence on the elemental weights.

9) HUF, Heating Uncertainty Factor

The heating uncertainty factor provides for the evaluation of the effects of uncertainty in heating estimates on the heat shield weight calculations. A factor of 30-percent increase in the radiative and convective heating was selected.

10) MUF, Materials Uncertainty Factor

The materials uncertainty factor provides for the evaluation of the effects of uncertainty in material properties on the heat shield weight calculations. The material factor selected to be perturbed is  $K\rho/C_p$  . This factor had been observed, from earlier studies, to play a key role in determining the heat shield weight for Mars entries.

11) Structure

Two structural concepts were selected and their relative merits sought; a cold honeycomb substructure supporting a heat shield, and a hot stiffened structure alone.

12)  $\alpha_e, Q_e$  , Entry Angle of Attack and Pitch Rate

The initial angle of attack and pitch rate at entry are of great importance in determining the angle of attack motion and resultant heating, loads, and elemental weights. A single set of conditions was selected for the study;  $\alpha_e$  -179 degrees, and  $Q_e$  0.1 rad/sec.

In addition to the governing parameters, heat shield material parameters were selected for Mars and Venus. The heat shield material selected for the Mars study is a low-density, low-conductivity, high-temperature charring ablator. The reasons for this selection are several:

- 1) Preliminary studies indicated that this material compared well, weightwise, with low-density cold-wall ablators.
- 2) The material, being a high temperature ablator, responds effectively to radiative heating, where the pulse is sharp and the surface temperature rises quickly causing significant reradiation.
- 3) The material selected can be sterilized and exhibits a high resistance to cold soak, as its thermal expansion coefficient very closely matches that for aluminum.

The heat shield materials selected for the Venus study were a reinforced-graphite material for the high-heat input, forebody, surfaces, and the low-conductivity material used in the Mars study for the afterbody low-heat input surfaces. The choice of the forebody material was aimed at utilizing the high heat of vaporization of graphite to overcome the severe radiation environment.

#### c. Case Generation

A general flow chart for the scope of analysis per shape is shown in figure I-2. The basic scheme utilizes a set of nominal conditions for each atmosphere, perturbing the governing parameters, one at a time, about the nominal. In this manner, the scope of the study was broadened without requiring an excessive number of cases.

The nominal values for the Mars study are given in table I-4. The range of parameters is given in table I-5. A case identification code was evolved and is summarized in table I-6. Each atmosphere, vehicle, and case combination are now identified.

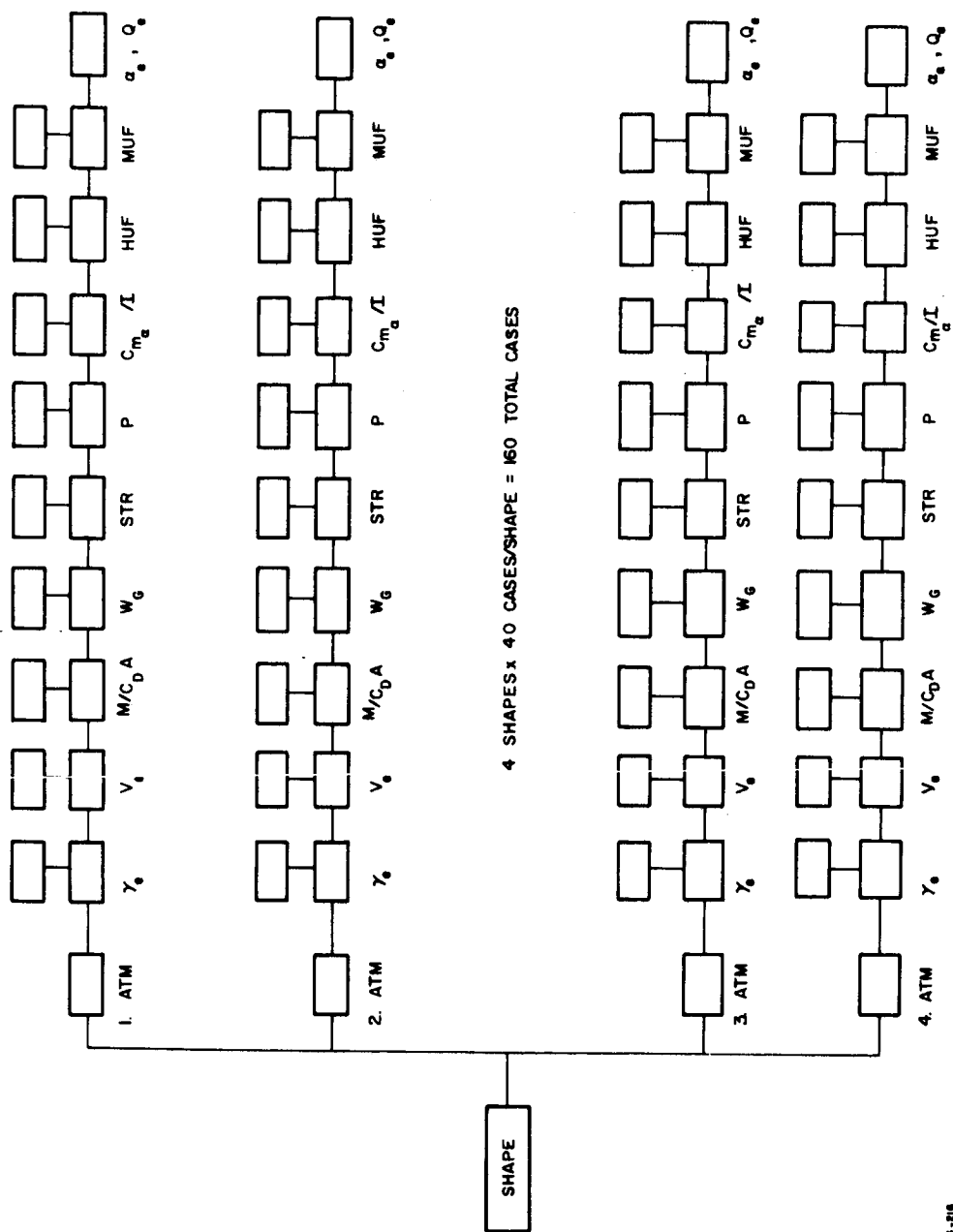


Figure 1-2 CASE GENERATION METHODOLOGY FOR MARS ENTRY

TABLE I-3

## MARS ATMOSPHERES

Listed below are the four atmospheres utilized in the Mars portion of this project.  
JPL revised the original atmospheres and specified these in TWX 213-449-2655  
(2 August 1963) MSG No. 032

Atmosphere	A1 Worst	A2 Worst	A3 Nominal	A4 Best
Molecular Weight	42.7	42.7	38.7	31.2
Sea Level Temperature (°K)	260.0	260.0	230.0	210.0
Sea Level Density (slug/ft <sup>3</sup> )	$4.21 \times 10^{-5}$	$4.21 \times 10^{-5}$	$5.89 \times 10^{-5}$	$1.04 \times 10^{-4}$
Sea Level Pressure (mb)	11.0	11.0	15.0	30.0
Sea Level Gravity (ft/sec <sup>2</sup> )	12.3	12.3	12.3	12.3
Temperature Gradient in the Troposphere--Fraction of Adiabatic Lapse Rate	1.0	1.0	1.0	1.0
Planet Sea Level Radius (feet)	$11.0 \times 10^6$	$11.0 \times 10^6$	$11.0 \times 10^6$	$11.0 \times 10^6$
Mole fraction of Nitrogen Content	0.00	0.00	0.25	0.76
Mole fraction of Carbon Dioxide Content	0.65	0.65	0.43	0.11
Mole fraction of Oxygen Content	0.00	0.00	0.00	0.00
Mole fraction of Argon Content	0.35	0.35	0.32	0.13
Stratosphere Temperature (°K)	130.0	230.0	180.0	130.0

TABLE I-4

NOMINAL VALUES FOR MARS STUDY

Shape	$W_G$ (pounds)	Structure	M/CDA (slug/ft <sup>2</sup> )	$C_{m_a}$ (1/rad)	$I_y/M R_c^2$	$R_c$ (feet)
M1	400	Aluminum Honeycomb	0.2	-0.181	$25.23 \times 10^{-2}$	3.69
M2	400	Aluminum Honeycomb	0.2	-0.156	$33.90 \times 10^{-2}$	3.69
M3	400	Aluminum Honeycomb	0.2	-0.250	$21.86 \times 10^{-2}$	4.05
M4	400	Aluminum Honeycomb	0.2	-0.174	$33.82 \times 10^{-2}$	4.05
<p><u>Materials</u></p> <p>Plastic Heat Shield, <math>(K\rho/C_p) = 6.8 \text{ lb}^2/\text{ft}^4 - \text{hr.}</math></p> <p>Structure: Aluminum Honeycomb</p>						
<p><math>\alpha_e = 179 \text{ degrees}</math>    <math>HUF = 1.0</math>    <math>V_e = 27,000 \text{ ft/sec}</math>    <math>P = 1 \text{ rad/sec}</math></p> <p><math>Q_e = 0.1 \text{ rad/sec}</math>    <math>MUF = 1.0</math>    <math>\gamma_e = -20 \text{ degrees}</math></p>						

TABLE I-5

CASE GENERATION FOR MARS ENTRY

SHAPES	Atmospheres	$\gamma_e$ (degrees)	$W_G$ (pounds)	$V_e$ ft/sec	P rad/sec	HUF	MUF	$a_e$ , $Q_e$	$C_{m_a}/I$	$M/C_{D^A}$
M-1	Kaplan's Re- vised Mars Atmospheres (4 atm.)	-20	400	27,000	1	$\left\{ \begin{array}{l} 1.3 \text{ rad}^1 \\ 1.3 \text{ conv}^1 \\ 1.0 \text{ rad}^1 \\ 1.0 \text{ conv}^1 \end{array} \right\}$ $\left\{ \begin{array}{l} (K \rho / C_p)^1 \\ (K \rho / C_p)^1 \\ (K \rho / C_p)^1 \\ (K \rho / C_p)^1 \end{array} \right\}$	$\left\{ \begin{array}{l} 1.0 \\ 1.3 \\ 1.3 \\ 1.3 \end{array} \right\}$ $\left\{ \begin{array}{l} (K \rho / C_p)^1 \\ (K \rho / C_p)^1 \\ (K \rho / C_p)^1 \\ (K \rho / C_p)^1 \end{array} \right\}$	$\left\{ \begin{array}{l} 179 \text{ deg} \\ \text{and} \\ 0.1 \\ \text{rad/sec} \end{array} \right\}$	$\left\{ \begin{array}{l} 1.0 \\ (C_{m_a}/I) \\ 2.0 \\ (C_{m_a}/I) \end{array} \right\}$	$\left\{ \begin{array}{l} 0.2 \\ 0.1 \end{array} \right\}$
M-2		-90	2000	21,000	4					
M-3										
M-4										

STRUCTURES

Composite Heat Shield and Structure--  
 Plastic Heat Shield and Aluminum Honeycomb  
 Hot Structure--All Beryllium

1 Nominal Values

TABLE I-6

## MARS ENTRIES--CASE IDENTIFICATION

A1 - JPL Worst Atmosphere  $T_{ST} = 130^{\circ}\text{K}$ A2 - JPL Worst Atmosphere  $T_{ST} = 230^{\circ}\text{K}$ 

A3 - JPL Nominal Atmosphere

A4 - JPL Best Atmosphere

CASE	$\gamma_e$ (degrees)	$V_e$ (ft/sec)	$M/C_{DA}$ slug/ft <sup>2</sup>	$W_T$ (pounds)	P (rad/sec)	$(C_{m_a}/I)^{1/2}$
1	-20	27000	0.2	400	1	1.0
2	<u>-90</u>	27000	0.2	400	1	1.0
3	-20	<u>24000</u>	0.2	400	1	1.0
4	-20	27000	<u>0.1</u>	400	1	1.0
5	-20	27000	0.2	<u>2000</u>	1	1.0
6	-20	27000	0.2	400	<u>4</u>	1.0
7	-20	27000	0.2	400	1	<u>2.0</u>
8	Change in structure material to all Beryllium, hence different structure weights					
9	Heating uncertainty factor, heat pulses increased by 30 percent					
10	Material uncertainty factor, $K\rho/C_p$ increased by 30 percent.					

NOTE: Underscore indicates change from nominal case (Case 1).

<sup>1</sup> Nominal Value

## 2. Venus

### a. Shapes

Seven configurations were selected for evaluation of their relative merits for Venus entry. The range of shapes cover the blunt, high drag, and slender blunt families. The selected shapes are shown in figure I-3, with their corresponding numerical designation.

The V1 shape has the same forebody as the NERV capsule, and the afterbody angle,  $\theta_A$ , was selected based on the availability of test data. The V2 and V6 shapes were selected on the basis of conducting a parametric study of spherically blunted cones. The V2 and V3 designs both have bluntness ratios ( $R_N/R_C$ ) of 0.8, but forecone angles of 30 and 60 degrees, respectively. The V1 shape essentially completes this family as it is an equivalent bluntness very close to 0.8 and a forecone angle of 10 degrees. Hence, we have three shapes with very nearly the same bluntness but widely differing forecone angles. Similarly, V4, V5, and V6 have bluntness ratios of 0.4 and cone angles covering 10, 30 and 60 degrees. In summary, the blunted cone parameter study involves two bluntness ratios, 0.4 and 0.8, and three forecone angles, 10, 30, and 60 degrees.

The afterbody shapes were chosen with the object of ensuring that the vehicles would all have a single nose-first trim attitude during the hypersonic flight regime, while keeping the surface area to a minimum to save weight.

The afterbodies of shapes V2, V3, V4 and V5 were varied in shape from a pure cone to a series of truncated cones, in a manner such that the same tail-first c.p. and static margin were chosen to give approximately the same degree of instability tail first as stability when nose first, using Newtonian theory.

A series of curves were then drawn showing the variation of nondimensional afterbody surface area  $S/d^2$  as a function of the truncation ratio  $\frac{d_B}{d}$ , and taking account of the contribution of the closed end. The curves shown in figure I-4 indicate little difference in surface area for small values of truncation and 25 percent truncation was selected for all the vehicles.

A blunt flared body was selected for study as a great deal of technology has been developed on this type of vehicle in the ICBM programs. Therefore, it was considered desirable to evaluate the applicability of this type of design for Venus entry.



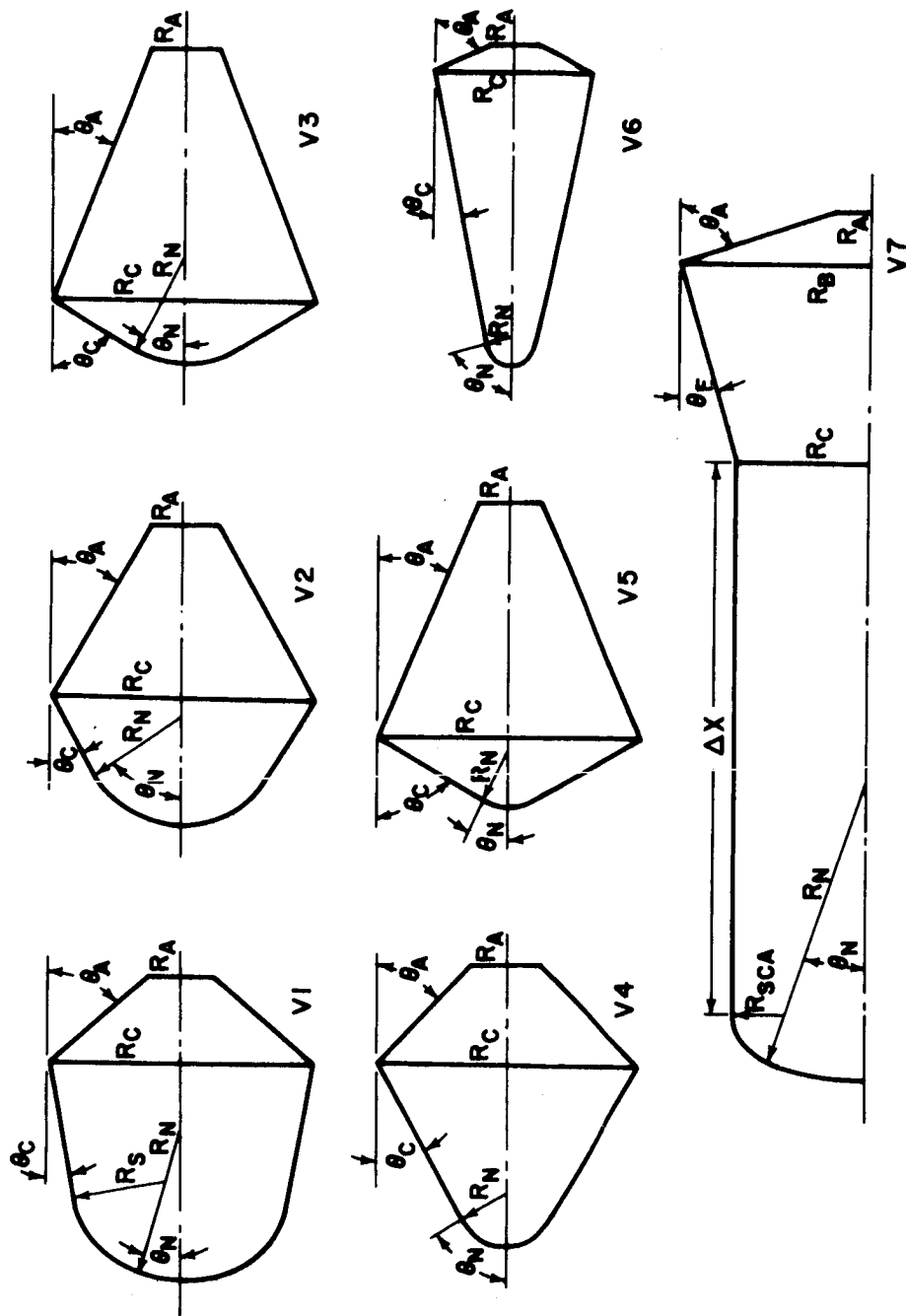
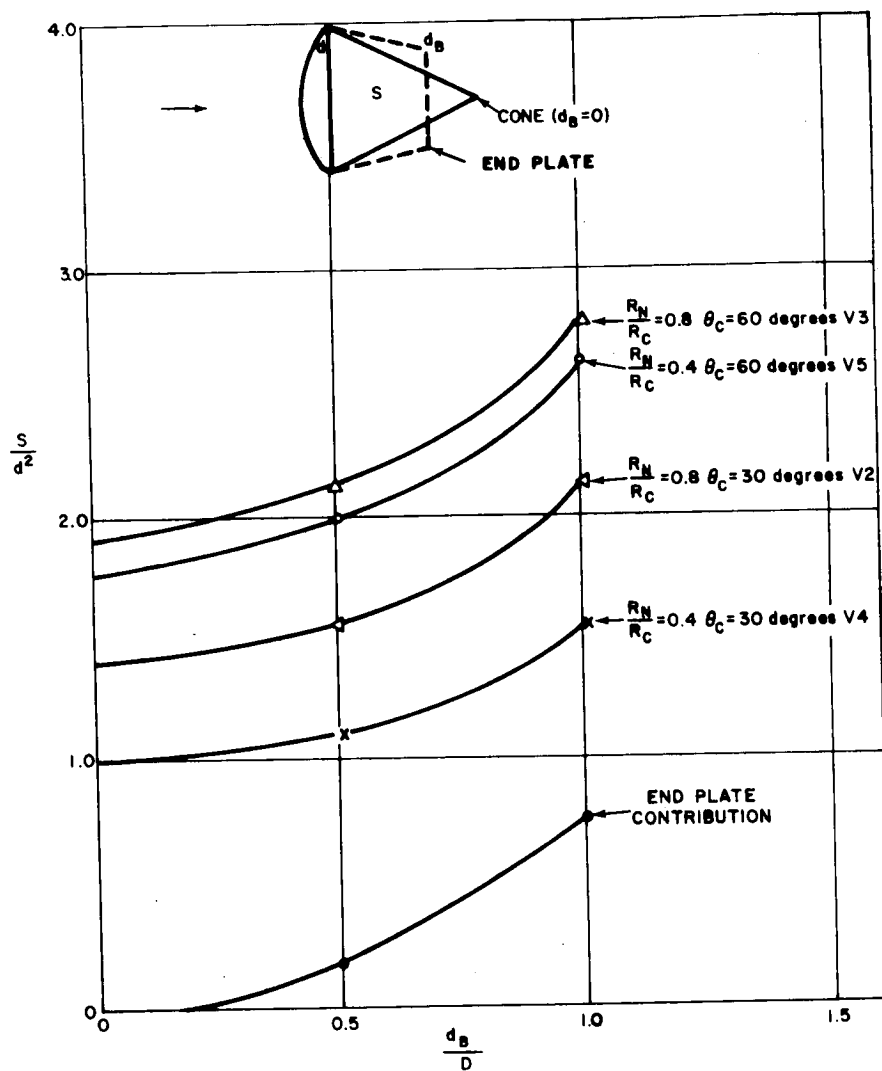


Figure 1-3 GEOMETRY OF VENUS VEHICLES

63-13174



64-218

Figure 1-4 AFTERBODY SURFACE AREA

A summary of the Venus shape parameters is given in table I-7.

b. Governing Parameters

For each shape considered, a range of variation of key parameters was selected. A summary of the governing parameters is given in table I-8.

1) Shape

The determination of the effect of shape on the elemental and residual weights of a Venus entry capsule was a prime objective of the study. The interplay of radiation and convective heating being complex, a series of shapes was selected covering a broad range of parameters, with the aim being to isolate the most favorable shape features.

2)  $M/C_D A$  , Ballistic Coefficient

The vehicle ballistic coefficient,  $M/C_D A$ , is a key trajectory, heating, and loads parameter. Since the pressure at the surface of Venus is estimated to be quite high, values of  $M/C_D A$  much higher than considered for Mars could be selected. Preliminary studies indicated that the most favorable  $M/C_D A$  for each vehicle, whereby the residual weight is maximized, is different for each vehicle. Consequently, an estimated range of  $M/C_D A$ , in which the case yielding the maximum residual weight would fall, was selected for each vehicle. Four values of  $M/C_D A$  were selected for each vehicle. The overall range of  $M/C_D A$ 's is 0.48 to 5.0 slug/ft<sup>2</sup>.

3)  $W_G$  , Gross Weight

Three gross weights were considered, 500, 1000, and 2000 pounds. This range of weight covers the anticipated weight of Venus entry capsules which enter directly.

4)  $v_e$  , Entry Velocity

The entry velocities chosen are 36,000, 38,000 and 40,000 ft/sec, covering the range of likely situations for direct entry.

5)  $\gamma_e$  , Entry Angle

The entry flight path angles selected are -15, -30, -45, and -90 degrees. The choice of four angles was deemed necessary due to the complex behaviour of the combined radiative and convective heating with entry angle.

TABLE I-7

## VENUS SHAPE PARAMETERS

SHAPE	$R_N/R_C$	$\theta_N$ (degrees)	$R_S/R_C$	$\theta_C$ (degrees)	$\Delta X/2R_C$	$\theta_F$ (degrees)	$R_B/R_C$	$\theta_A$ (degrees)	$R_A/R_C$
V1	1.088	16.55	0.728	10.0	0.0	0.0	0.00	50.0	0.25
V2	0.8	60.0	0.0	30.0	0.0	0.0	0.0	30.0	0.25
V3	0.8	30.0	0.0	60.0	0.0	0.0	0.0	21.5	0.25
V4	0.4	60.0	0.0	30.0	0.0	0.0	0.0	45.0	0.25
V5	0.4	30.0	0.0	60.0	0.0	0.0	0.0	23.0	0.25
V6	0.4	80.0	0.0	10.0	0.0	0.0	0.0	65.0	0.25
V7	2.22	19.17	0.4	0.0	2.091	16.5	1.455	71.88	0.25

TABLE I-8

## VENUS ENTRY PARAMETERS

Governing Parameter	Number of Cases
1 Shape	7
2 $M/C_D A$ , ballistic coefficient	4
3 $W_G$ , gross weight	3
4 $V_e$ , entry velocity	3
5 $\gamma_e$ , entry angle	4
6 $C_{m_\alpha}/I$ , stability factor	3
7 $P$ , spin rate	3
8 (HUF) Heating Uncertainty Factor	3
9 (MUF) Materials Uncertainty Factor	3
10 Atmospheric Model	2
11 $\alpha_e, Q_e$ angle of attack and pitch rate at entry.	1
Total Cases	266

6) Atmospheric Model

The model atmospheres for Venus were specified as the Kaplan models. The pertinent atmospheric parameters are summarized in table I-9.

7) P, Spin Rate

Capsule spin rates of 0, 2, and 4 rad/sec were selected as representative of the range of likely entry conditions.

8)  $C_{m_a}/I_y$ , Stability Factor

This stability factor, representing the ratio of the slope of the moment curve at zero angle of attack to the moment of inertia in pitch, was perturbed twice from the nominal value; the determination of this effect on the angle of attack envelope of this factor was sought.

9) HUF, Heating Uncertainty Factor

To ascertain the importance of accurate heating prediction in the delimitation of residual weight, two perturbations on the radiative and convective heating rates were selected.

10) MUF, Materials Uncertainty Factor

The influence of the uncertainties in the knowledge of heat shield material performance on the heat shield and residual weights can be found by perturbing the material properties and assessing their effects. In the case of Venus, considerable ablation can be expected, so the variables selected for study are the blowing factor ( $\eta$ ) and the heat of vaporation ( $H_v$ ) of the material.

11)  $\alpha_e, Q_e$ , Entry Angle of Attack and Pitch Rate

The entry angle of attack and pitch rate were selected as 179 degrees and 0.1 rad/sec, respectively. The selection of these values was aimed at uncovering problem areas associated with angle-of-attack entry.

c. Case Generation

A general flow chart for the scope of the study is shown in figure I-5. The parameter study was centered about a nominal set of conditions for each shape. The parameters were then changed, one at a time, in both directions from the nominal. In this way, a large area of

TABLE I-9

## VENUS ATMOSPHERES

Listed below are the two atmospheres utilized in the Venus portion of this project.

(Reference L.D. Kaplan, A Preliminary Model of the Venus Atmosphere, JPL Report No. 32-379 12 December 1962.)

Atmosphere	K1 Minimum Temperature	K2 Maximum Temperature
Molecular Weight	29.62	29.62
Sea Level Temperature (°K)	560.00	700.00
Sea Level Density (slug/ft <sup>3</sup> )	$15.43 \times 10^{-3}$	$6.17 \times 10^{-3}$
Sea Level Gravity (ft/sec <sup>2</sup> )	29.53	29.53
Temperature Gradient in the Troposphere -- Fraction of Adiabatic Lapse Rate	0.708	0.523
Temperature Gradient in the Thermosphere (°K/ft)	$5.32 \times 10^{-4}$	$5.32 \times 10^{-4}$
Planet Sea Level Radius	$1.99 \times 10^7$	$1.99 \times 10^7$
Mole Fraction Nitrogen Content	0.90	0.90
Mole Fraction Carbon Dioxide Content	0.10	0.10
Stratosphere Temperature (°K)	160.0	245.0





parameters could be covered without considering all permutations which would have resulted in an excessive number of cases.

The nominal values for the parameters used in the Venus study are given in table I-10. The range of parameters is given in table I-11. A case identification code was evolved and is summarized in table I-12. Each atmosphere, vehicle, and case combination are now identified.

### 3. Nomenclature

A	Reference area (ft <sup>2</sup> )
C <sub>D</sub>	Drag coefficient
d <sub>B</sub>	Base diameter of body (feet)
d	Body diameter (feet)
C <sub>m<sub>a</sub></sub>	Pitching moment derivative (per radian)
H <sub>v</sub>	Heat of vaporization (Btu/lb)
I <sub>x</sub> , I <sub>y</sub>	Moments of inertia about x and y axes.
P	Spin rate (rad/sec)
Q	Pitch rate (rad/sec)
W <sub>G</sub>	Gross Weight (pounds)
M	Mass (slugs)
T <sub>ST</sub>	Temperature in stratosphere (degrees Kelvin)
S	Surface area
V <sub>e</sub>	Entry Velocity (ft/sec)
X <sub>CG</sub>	Center of gravity location measured from nose (feet)
η <sub>L</sub>	Laminar blowing factor
η <sub>T</sub>	Turbulent blowing factor
R <sub>N</sub> , θ <sub>N</sub> , R <sub>S</sub> , θ <sub>C</sub> ,	Shape parameters defined in figures I-1 and I-3
ΔX, R <sub>C</sub> , θ <sub>F</sub> , R <sub>B</sub> ,	
θ <sub>A</sub> , R <sub>A</sub>	

### Subscript

(e) Conditions at entry

TABLE I-10

NOMINAL VALUES FOR VENUS STUDY

Shape	$W_G$ (pounds)	$M/C_D A$ (slug/ft <sup>2</sup> )	$C_{m_a}$ 1/rad	$l_y/MR_c^2$	$R_c$ (feet)
V1	1000	1.50	0.150	0.41	3.11
V2	1000	1.20	0.148	0.36	3.26
V3	1000	0.80	0.166	0.31	3.06
V4	1000	1.20	0.301	0.41	3.92
V5	1000	0.80	0.173	0.35	3.12
V6	1000	4.00	0.347	0.95	3.65
V7	1000	3.00	0.467	3.66	1.59
Materials		$H_v$ Btu/lb)	$\eta_L$	$\eta_T$	
Reinforced Graphite		11,000.0	0.56	0.36	
Low - Density Plastic		85.0	0.57	0.38	
$\alpha_e = 179 \text{ degrees}, \quad Q_e = 0.1 \text{ rad/sec}, \quad P = 2.0 \text{ rad/sec}$ $v_e = 38,000 \text{ ft/sec.}, \quad \gamma_e = -45 \text{ degrees}$ $HUF = 1.0, \quad MUF = 1.0$					

TABLE I-11

## CASE GENERATION FOR VENUS STUDY

Shapes	Atmospheres	$\gamma_e$ (deg.)	WG (lbs.)	$V_e$ (ft/sec)	$\dot{\phi}$ (rad/sec)	HUF	MUF	$\alpha_e, Q_e$	$C_{m_a}/I$	M/CDA Slug/ft <sup>2</sup>
V1	Kaplan Min Temp.	-90	500	36,000	0.0	$\left\{ \begin{array}{l} 1.3 \text{ rad}^1 \\ 1.0 \text{ conv}^1 \end{array} \right\}$	$0.7 H_v$ $1.0 \eta$	179 deg. and 0.1 rad/sec	$2.0(C_{m_a}/I)^1$ $1.0(C_{m_a}/I)^1$	$1.25(M/CDA)^1$ $1.0(M/CDA)^1$
V2		-45	1000	38,000	2	$\left\{ \begin{array}{l} 1.0 \text{ rad}^1 \\ 1.0 \text{ conv}^1 \end{array} \right\}$	$1.0 H_v$ $1.0 \eta$			
V3	Kaplan Max. Temp	-30	2000	40,000	4	$\left\{ \begin{array}{l} 1.0 \text{ rad}^1 \\ 1.3 \text{ conv}^1 \end{array} \right\}$	$1.0 H_v$ $0.7 \eta$		$0.5(C_{m_a}/I)^1$	$0.8(M/CDA)^1$ $0.6(M/CDA)^1$
V4		-15								
V5										
V6										
V7										

<sup>1</sup>Nominal Values

TABLE I-12

## VENUS ENTRIES -- CASE IDENTIFICATION

K1 - Kaplan's Minimum Temperature Atmosphere  $T_{ST} = 160^\circ K$ K2 - Kaplan's Maximum Temperature Atmosphere  $T_{ST} = 245^\circ K$ 

CASE	$\gamma_e$ (degrees)	$V_e$ (ft/sec)	$W_G$ (pounds)	P (rad/sec)	$C_{m_a} / I$	$M/C_D A$ (slug/ft <sup>2</sup> )	HUF	MUF
1	-45	38000	1000	2.0	*1.0	*1.0	1.0	1.0
2	<u>-15</u>	38000	1000	2.0	*1.0	*1.0	1.0	1.0
3	<u>-30</u>	38000	1000	2.0	*1.0	*1.0	1.0	1.0
4	<u>-90</u>	38000	1000	2.0	*1.0	*1.0	1.0	1.0
5	-45	<u>36000</u>	1000	2.0	*1.0	*1.0	1.0	1.0
6	-45	<u>40000</u>	1000	2.0	*1.0	*1.0	1.0	1.0
7	-45	38000	<u>500</u>	2.0	*1.0	*1.0	1.0	1.0
8	-45	38000	<u>2000</u>	2.0	*1.0	*1.0	1.0	1.0
9	-45	38000	1000	<u>0.0</u>	*1.0	*1.0	1.0	1.0
10	-45	38000	1000	<u>4.0</u>	*1.0	*1.0	1.0	1.0
11	-45	38000	1000	2.0	<u>*2.0</u>	*1.0	1.0	1.0
12	-45	38000	1000	2.0	<u>*0.5</u>	*1.0	1.0	1.0
13	-45	38000	1000	2.0	*1.0	<u>*1.25</u>	1.0	1.0
14	-45	38000	1000	2.0	*1.0	<u>*0.8</u>	1.0	1.0
15	-45	38000	1000	2.0	*1.0	<u>*0.6</u>	1.0	1.0
16	-45	38000	1000	2.0	*1.0	*1.0	<u>1.3q<sub>r</sub></u> <u>1.0q<sub>s</sub></u>	1.0
17	-45	38000	1000	2.0	*1.0	*1.0	<u>1.0q<sub>r</sub></u> <u>1.3q<sub>s</sub></u>	1.0
18	-45	38000	1000	2.0	*1.0	*1.0	1.0	<u>0.7H<sub>v</sub></u> <u>1.0<math>\eta</math></u>
19	-45	38000	1000	2.0	*1.0	*1.0	1.0	<u>1.0H<sub>v</sub></u> <u>0.7<math>\eta</math></u>

NOTE: Underscore indicates change from nominal (Case 1)

\*Reflects the number times the nominal  $C_{m_a} / I$  and  $M/C_D A$  for each vehicle.

## C. APPROACH

The technical approach to this study was based on the Avco Research and Development Division's unsolicited proposal, serial RAD-MS-62-80(L), Parametric Study of the Entry of Ballistic Capsules into the Atmosphere of Mars and Venus, the JPL Statement of Work SW-3117, and has as its primary objective the satisfaction of JPL Description of Work A209627 dated 25 February 1963.

The philosophy of this study was to include all the significant parameters that have been found from experience to influence the design of an atmospheric entry vehicle. The design parameters for all aspects of capsule design, such as aerodynamic, thermodynamic, and structural, were introduced into all calculations with accuracy sufficient that the importance of any resulting design uncertainties could be clearly established and evaluated.

The aim of the study was to obtain parametric weight calculations for vehicles of very different shapes and sizes entering a range of simulated atmospheres for Venus and Mars, and covering a wide range of entry conditions. Due to the large number of vehicle and trajectory design parameters involved in the study, an efficient computer program was necessary.

### 1. Computer Program

The computer program was divided into a number of blocks, as follows:

- a. Coefficients Block
- b. Heating Block
- c. Trajectory Block
- d. Structure Block
- e. Heat Shield Block

Sizing of the programs early in the study indicated a serious problem of core size limitations of the IBM 7094 computer, and at best two complete core loads would be required to put the whole program on at once. Hence, considerable effort was spent in programing to reduce the size of each block.

A brief summary of the calculations performed in each block follows:

a. Coefficient Block

This block calculates the Newtonian coefficients for vehicles specified by the shape parameters discussed earlier. Provision is made for center of gravity location to ensure a single stable trim point, and to calculate the moments of inertia about the pitch and roll axes.

When empirical data are available, this block can be bypassed or the results of the block modified for use in the trajectory block.

b. Heating Block

The radiative and convective heating are computed by this block. The approximation of using constant heating distributions throughout a trajectory was used which made the link between this block and the remainder of the program relatively weak. This block was divided into two problems; (1) computation of reference heat pulses, and (2) computation of the heating distributions.

The computation of the reference pulses was linked directly to the trajectory block. This required the combination of the trajectory, gasdynamics, and radiative heat transfer formulations. The reference radiative pulse is for the stagnation point. Two radiative heat pulses are evaluated, one based on equilibrium flow, and the other on the nonequilibrium contribution.

The reference laminar pulse is for the stagnation point and uses simplified correlations of numerical solutions for the computation. The reference turbulent pulse is for a sonic point on the body and again uses simplified correlations of detailed solutions.

The computation of the heating distribution is done separately, and factors obtained by which the reference pulses are to be multiplied to obtain the heating locally. All of the aspects of computing the heating distributions could not be programed due to the unusual flow fields occurring at large angles of attack. The block can, in general, be used to obtain convective heating distributions at small angles of attack.

#### c. Trajectory Block

The initial approach of using a particle trajectory computation and superimposing the dynamics on it frequently led to serious discrepancies with more exact solutions. Consequently, a more exact formulation was used, accounting for the effects of drag variation with angle of attack and the aerodynamic damping due to the plunging motion of the vehicle.

The resultant program has two options; (1) the approximate coupled four-degree-of-freedom solution, with coefficients which vary with angle of attack, and (2) the approximate linearized solution with coefficients varying with Mach number. The latter option can only be switched in below-peak dynamic pressure, and is done automatically.

This program computes the angle-of-attack envelope, and the altitude-velocity history. Additional information for the heating, loads, and parachute calculations are also provided.

#### d. Structures Block

This block computes a wide variety of structural weights for conical frustra and spherical caps. The honeycomb analysis was optimized and can handle various material properties.

Other aspects of this block are 1) the design of the internal package and evaluation of its weight, and 2) design of a crushable energy-absorbing structure and calculation of its weight. The parachute design and weight computation (when used) is also included in this block.

#### e. Heat Shield Block

The heat shield block computes the ablation and insulation material requirements for protecting the substructure from exceeding a specified temperature at a particular time. The designs in this study considered the structural temperature rise to impact.

The effects of radiative and convective heating are separated. Reinforced plastics can be handled by the program. The program accounts for the structural heat capacitance, which is very important for very low  $M/C_D A$  vehicles.

The program is an attempt to compromise the accuracy of calculation with simplicity, speed, and size of the program. In this light, considerable preparatory work was required to establish the merits of the approach.

## 2. Empirical Data

### a. Aerodynamic Coefficients

The literature was searched for data on shapes similar to the selected Mars and Venus configurations. The results of this survey are summarized in volume IV.

### b. Heating

Radiative heating data were gathered from the literature. In addition, considerable unpublished work has been done at Avco RAD which was also utilized. Discussions with Avco Everett personnel were also valuable in updating the estimated radiative heating estimates.

The nonequilibrium radiative estimates were based on the work done at the Avco Everett Laboratories on the nonequilibrium effects in air.

The convective heating estimates were correlated from independent research done at Avco RAD on heating in gas mixtures.

### c. Structures

The literature was surveyed for data on buckling of monocoque and honeycomb shells. The formulas used in the development of the program were empericized to agree with the data.

A considerable amount of consultation and support was given by the theoretical applied mechanics group at Avco RAD.

### d. Materials

The literature was surveyed for data on materials performance in gases similar to the Mars and Venus atmospheres. Also, data on the behavior of materials under combined radiative and convective heating was sought. The theoretical thermodynamics analysis group at Avco RAD participated in estimating the material performance in the Mars and Venus atmospheres.



## II. ANALYTICAL METHODS

### A. COEFFICIENTS BLOCK

#### 1. Introduction

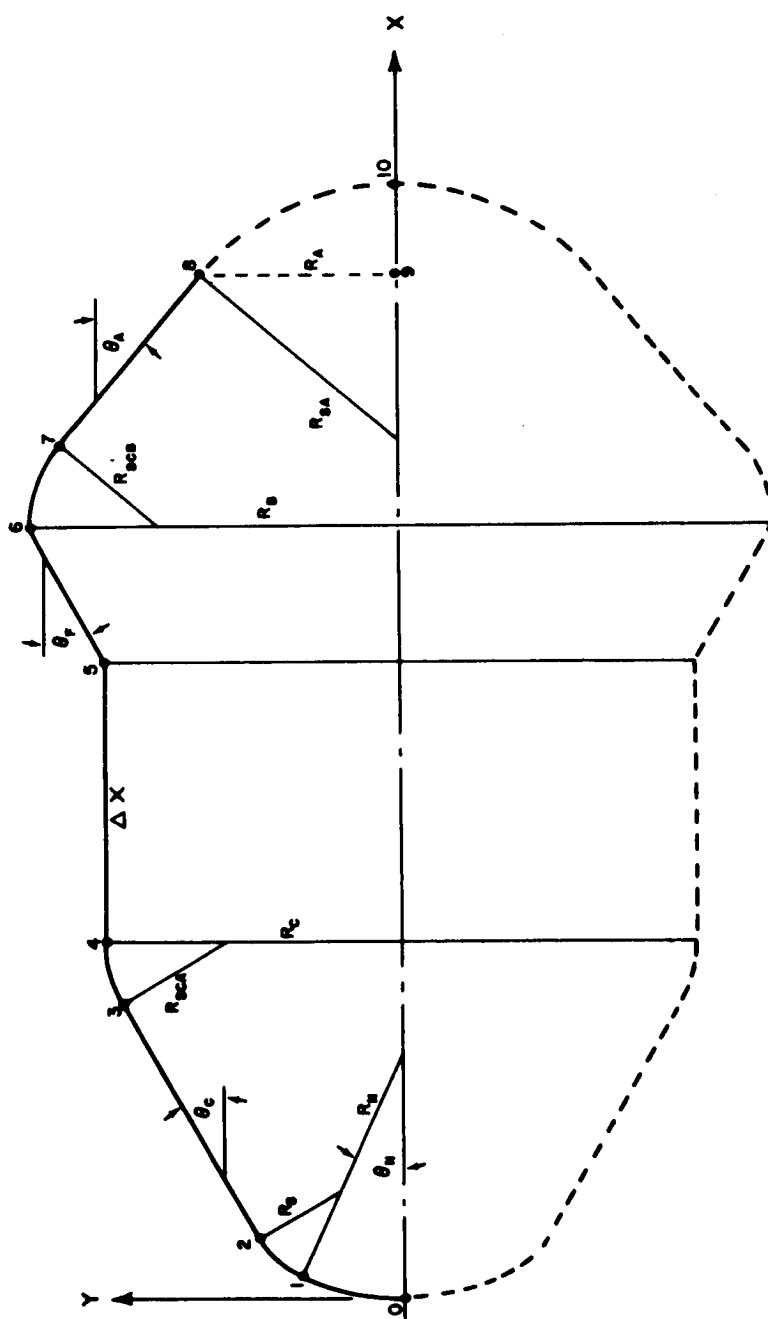
This program computes  $C_N$ ,  $C_X$ ,  $C_{L_a}$ ,  $C_{m_q}$ , and  $X_{CP}/d$  for arbitrary values of the angle of attack  $\alpha$  and pitching speed parameter  $Q = qd/2V$  (in radians). Moments of inertia  $I_x$  and  $I_y$  are also computed about the center of gravity. The vehicle is assumed uniformly dense fore and aft of the center of gravity. A center of gravity location can be optionally specified or is calculated from a specified  $C_{m_a}$  at angles of attack of zero and 180 degrees. The most forward (smallest as measured from nose) c. g. position is used.

The results are based on Newtonian theory, with the assumption that separate sections of the body possess shadows but do not cast shadows on other sections. The sections are limited to those shown in figure I-6. Cones, cone frustums, cylinders, and curved body sections may be handled by the program.

#### 2. Newtonian Calculations

##### a. Symbols

$A(x)$	Function defined by equation (7)
$B(x)$	Function defined by equation (8)
$C_D$	Drag coefficient
$C_L$	Lift coefficient
$C_m$	Moment coefficient (based on characteristic radius, $R$ , and characteristic length, $d$ )
$C_{M_a}$	$\partial C_m / \partial \alpha$
$C_{m_q}$	$(\partial C_m / \partial Q)$
$C_N$	Coefficient of force normal to body
$C_x$	Coefficient of force along body axis



04 - 220

Figure 1-6 MARS-VENUS CAPSULE SHAPE PARAMETERS

$d$	Characteristic length, diameter (feet)
$dQ$	Increment in $Q$ used to compute derivatives (radians)
$d\alpha$	Increment in $\alpha$ used to compute derivatives (radians)
$G(X)$	Function defined by equation (9)
$M$	Vehicle mass (slugs)
$M/C_D A$	Ballistic coefficient
$q$	Angular pitching speed (rad/sec)
$Q$	Pitching speed parameter: $Q = qd/2V$ (radians)
$R_A$	Radius of truncated afterbody
$R_B$	Radius of flare section
$R_C$	Characteristic radius (cylinder radius, usually) (feet)
$R_N$	Radius of spherical nose cap (feet)
$R_S$	Radius of section between nose cap and fore conical section
$R_{SA}$	Radius at afterbody
$R_{SCA}$	Radius at toroidal section
$R_{SCB}$	Radius at corner of flare section
$V$	Volume ( $\text{ft}^3$ )
$x$	Axial coordinate (feet); nose is located at $x = 0$
$X_B$	Length of body (feet)
$X_{CG}$	Distance of center of gravity from nose (feet)
$X_{CP}$	Distance of center of pressure from nose (feet)
$y$	Radial coordinate (feet)
$\alpha$	Angle of attack (radians or degrees)

$\Delta Q$	Interval between specified values of $Q$ (radians)
$\Delta X$	Length of cylindrical section
$\Delta a$	Interval between specified values of $a$ (radians)
$\theta_A$	Slope of Afterbody
$\theta_C$	Slope of fore conical section
$\theta_F$	Slope of flared section
$\theta_N$	Nose cap angle
$\omega^*$	Function defined by equation (10) (radians)

### Subscripts

A	Portion of vehicle aft of center of gravity
f	Length of body
i	i = 0 denotes moments taken about the nose; i = g denotes moments and motions taken about the center of gravity.
j	(j = 1, 2, ... ) numbering the sections of the body which are cone frustums or cylinders; See figure I-2.
N	Portion of vehicle forward of center of gravity

### b. Derivation of Equations

The force and moment coefficients are given by:

$$C_{N_i} = - \frac{2}{\pi R_c^2} \int_0^{x_f} \left[ -A(x) \cos \omega_i^* + B_i(x) \left( \frac{\omega_i^*}{2} - \frac{1}{4} \sin 2\omega_i^* + \frac{\pi}{4} \right) \right. \\ \left. - \frac{2}{3} G_i(x) \cos \omega_i^* (\sin^2 \omega_i^* + 2) \right] y(x) dx ,$$

$$C_{x_i} = \frac{2}{\pi R_c^2} \int_0^{x_f} \left[ A(x) \left( \omega_i^* + \frac{\pi}{2} \right) - B_i(x) \cos \omega_i^* \right. \\ \left. + 2 G_i(x) \left( \frac{\omega_i^*}{2} - \frac{1}{4} \sin 2 \omega_i^* + \frac{\pi}{4} \right) \right] y(x) \tan \theta \, dx, \quad (2)$$

$$C_{m_i} = \frac{2}{\pi R_c^2 d} \int_0^{x_f} \left[ -A(x) \cos \omega_i^* + B_i(x) \left( \frac{\omega_i^*}{2} - \frac{1}{4} \sin 2 \omega_i^* + \frac{\pi}{4} \right) \right. \\ \left. - \frac{2}{3} G_i(x) \cos \omega_i^* (\sin^2 \omega_i^* + 2) \right] [(x - x_i) y(x) + y^2(x) \tan \theta] \, dx, \quad (3)$$

$$C_{L_i} = -C_{x_i} \sin \alpha + C_{N_i} \cos \alpha, \quad (4)$$

$$C_{D_i} = C_{x_i} \cos \alpha + C_{N_i} \sin \alpha. \quad (5)$$

Also compute  $X_{CP}/d$

$$\frac{X_{CP}}{d} = -C_{m_o}/C_{N_o}. \quad (6)$$

Here the functions  $A$ ,  $B_i$ ,  $G_i$ , and  $\omega_i^*$  are given by

$$A(x) = 2 \sin^2 \theta \cos^2 \alpha \quad (7)$$

$$B_i(x) = -8Q \sin \theta \cos \alpha \left[ \left( \frac{x - x_i}{d} \right) \cos \theta + \frac{y(x)}{d} \sin \theta \right] - \sin 2\theta \sin 2\alpha, \quad (8)$$

$$G_i(x) = \left\{ 2Q \left[ \left( \frac{x - x_i}{d} \right) \cos \theta + \frac{y(x)}{d} \sin \theta \right] + \cos \theta \sin \alpha \right\}^2, \quad (9)$$

$$\omega_i^* = \begin{cases} \arcsin \left\{ \frac{\sin \theta \cos a}{\cos \theta \sin a} \right\} \equiv \arcsin k \text{ if } |k| \leq 1 \\ \pi/2 \text{ if } k > 1 \\ -\pi/2 \text{ if } k < -1 \end{cases} \quad (10)$$

with

$$\theta = \arcsin \frac{dy}{dx} \quad (11)$$

The subscript  $i$  takes on the values 0 and  $g$ .

The following derivatives are also computed:

$$C_{m_{a_i}} = \frac{\partial C_{m_i}}{\partial a} = \frac{C_{m_i}(a + da, Q) - C_{m_i}(a, Q)}{da} \quad (12)$$

$$C_{L_{a_i}} = \frac{\partial C_{L_i}}{\partial a} = \frac{C_{L_i}(a + da, Q) - C_{L_i}(a, Q)}{da} \quad (13)$$

$$C_{m_{q_i}} = \frac{\partial C_{m_i}}{\partial Q} = \frac{C_{m_i}(a, Q + dQ) - C_{m_i}(a, Q)}{dQ} \quad (14)$$

The values of  $a$  specified can be equally spaced in three separate ranges, the interval between two adjacent values being  $\Delta a$  in any one range;  $Q$  is spaced in only one range. The increment  $da$  in the above formulas is 0.01 radian, and similarly  $dQ$  is 0.01 radian.

### 3. Center-of-Gravity Location

The center of gravity can be optionally specified, if a suitable position is known in advance. On the other hand, the limitations on the center-of-gravity position, which meet the requirements of a single stable trim point, may be unknown. Therefore, an option is provided by which the minimum stability requirements are specified and from which the center of gravity is located.

If the center of gravity position is to be located based on either  $C_{m_\alpha}$  at  $\alpha = 0$  degrees and  $\alpha = 180$  degrees, then the following are necessary:

a. Evaluate  $C_{m_\alpha}$  at  $\alpha = 0$  and  $\alpha = 180$  for  $i = 0$  (equation (12)).

b. Solve for  $X_{CG}$ ,

$$(X_{CG})_{\alpha=0} = \frac{d}{C_{N_\alpha}} \left[ (C_{m_\alpha})_{\text{spec.}} - (C_{m_\alpha})_{i=0} \right]_{\alpha=0} \quad (15)$$

$$(X_{CG})_{\alpha=180} = \frac{d}{C_{N_\alpha}} \left[ (C_{m_\alpha})_{\text{spec.}} - (C_{m_\alpha})_{i=0} \right]_{\alpha=180} \quad (16)$$

c. A minimum static margin (SM) is also specified at zero angle of attack, which must be satisfied, so that, at  $\alpha = 0$

$$X_{CG} = X_{CP} - SM \quad (17)$$

d. The  $X_{CG}$  position must be tested at all angles of attack to ensure:

$$X_{CG} \leq X_{CP} \quad (18)$$

The smallest value of  $X_{CG}$  from equations 15, 16, 17, 18 is then used. Note that the specified  $(C_{m_\alpha})_{\text{spec}}$  at  $\alpha = 180$  degrees is positive if the body is to have an unstable trim at this point.

#### 4. Moments of Inertia

Under the assumption of uniform density fore and aft of the CG, the ratio of densities  $\rho_A / \rho_N$  must be found such that,

$$x_{CG} = \frac{\left[ \int_0^{x_{CG}} xy^2 dx + \frac{\rho_A}{\rho_N} \int_{x_{CG}}^{x_f} xy^2 dx \right]}{\left[ \int_0^{x_{CG}} y^2 dx + \frac{\rho_A}{\rho_N} \int_{x_{CG}}^{x_f} y^2 dx \right]} \quad (19)$$

From equation (19) the vehicle density ratio  $\rho_A/\rho_N$  can be calculated.

An expression for the total vehicle mass can be written such that the density forward of the  $X_{CG}$  position ( $\rho_N$ ) can be calculated.

$$M = \rho_N \left[ V_N + \frac{\rho_A}{\rho_N} V_A \right] \quad (20)$$

where

$$V_N = \pi \int_0^{x_{CG}} y^2 dx \quad \text{and} \quad V_A = \pi \int_{x_{CG}}^{x_f} y^2 dx$$

The moment of inertia about the pitch axis is given by

$$I_y = \pi \rho_N \left[ \int_0^{x_{CG}} x^2 y^2 dx + \frac{\rho_A}{\rho_N} \int_{x_{CG}}^{x_f} x^2 y^2 dx + \frac{1}{2} \int_0^{x_{CG}} y^4 dx + \frac{\rho_A}{2 \rho_N} \int_{x_{CG}}^{x_f} y^4 dx \right] - M x_{CG}^2 \quad (21)$$

Similarly, the moment of inertia in roll about the x axis is given by

$$I_{x_{CG}} = \frac{\pi \rho_N}{2} \left[ \int_0^{x_{CG}} y^4 dx + \frac{\rho_A}{\rho_N} \int_{x_{CG}}^{x_f} y^4 dx \right] \quad (22)$$

## 5. Evaluation of Coefficients Block

### a. Moments of Inertia and Center of Gravity

The moments of inertia in pitch and roll are based on a center of gravity location which is placed so as to obtain suitable stability ( $C_{m_\alpha}$ ) for all angles of attack. The center-of-gravity location is achieved by using constant vehicle densities for that portion of the vehicle forward and aft of the center of gravity position (densities are different from each other).



A comparison of the predicted moments of inertia was made with more exact methods using the elemental weights obtained from the heat shield and structure and residual weight calculations and the results are tabulated below:

Case M1-A1-1			
	$I_y$	$I_x$	C. G.
Constant Density Method	42.7	65.4	0.15d
Each Elemental Piece (heat shield, structure etc)	37.3	34.1	0.177d

The moment of inertia in pitch compares fairly close; however there is a notable discrepancy for the value about the roll axis. This is caused by the fact that the residual weight and the internal structure are concentrated more closely to the axis as compared with the uniformly distributed density method. This result brings out the need for iterative type center-of-gravity location and moments of inertia calculations based on actual heat shield, structural, and parachute weights.

#### b. Aerodynamic Coefficients

The aerodynamic coefficients, both as a function of angle of attack and Mach number, are tabulated in volume IV for each vehicle. A discussion of the reliability and methods of obtaining these coefficients is also found in volume IV. The coefficients tabulated are  $C_D$ ,  $C_{N_\alpha}$ ,  $X_{CP}/d$ ,  $C_{m_\alpha}$ ,  $C_{m_q}$ , and  $C_X$ .

## B. HEATING BLOCK

### 1. Introduction

The heating block is divided in two parts, consisting of the pressure and convective heating distributions and the radiation heating calculation. The radiation heating calculation was connected directly to the trajectory block, together with approximate expressions for the stagnation point convective heating and for the turbulent sonic point heating.

The heating analysis was aimed at accounting for the effects of angle of attack on both the convective and radiative heating distributions. In order to do this, estimated shock shapes at angle of attack were necessary.

The effects of gas composition on the convective and radiative heating are accounted for. In addition, the effects of nonequilibrium flow on the radiation heating is accounted for.

In order to handle the three dimensional flow aspects at angle of attack, approximate methods were evolved suitable for parametric studies.

### 2. Gas Properties

#### a. Symbols

$h, H$	Static and total enthalpy (Btu)
$M$	Molecular weight
$P$	Pressure (lb/ft <sup>2</sup> )
$Q_v, Q_r, Q_t, Q_e$	Vibrational, rotational, translational, and electronic partition functions, respectively
$T$	Temperature (°K)
$V$	Velocity (ft/sec)
$X_N, X_O, X_C, X_A$	Mole fractions of nitrogen, oxygen, carbon dioxide, and argon in the atmosphere, respectively
$\rho$	Density (slugs/ft <sup>3</sup> )

#### Subscripts

2	Conditions behind a normal shock
---	----------------------------------

i	Refers to ith specie
o	Reference condition
S	Stagnation point conditions
$\infty$	Free stream conditions

#### b. Flight Conditions

For the computation of the radiative heating over a wide range of flight conditions, it was decided to solve for the state of the gas at points along the trajectory. The trajectory variables are flight velocity and altitude. The altitude, of course, defines the ambient density and temperature. Rather than solve the normal shock solution precisely, a strong shock approximation was used.

The strong shock approximation is derived as follows. Applying the continuity and momentum equations across a normal shock, denoting conditions behind the bow shock with subscript (2) yields:

Continuity:

$$\rho_2 V_2 = \rho_\infty V_\infty$$

Momentum:

$$P_2 + \rho_2 V_2^2 = P_\infty + \rho_\infty V_\infty^2 \quad (2)$$

Eliminating the velocity  $V_2$  from the above relationships yields the static pressure behind the shock as

$$P_2 = P_\infty + \rho_\infty V_\infty^2 \left( 1 - \frac{\rho_\infty}{\rho_2} \right) \quad (3)$$

An expression for the stagnation pressure can be found by utilizing the adiabatic relationship

$$\frac{1}{\rho} dP = dh \quad (4)$$

Assuming  $h = \gamma P / (\gamma - 1) \rho$  where  $\gamma = \text{const.}$ , equation (4) integrates to

$$\frac{P_S}{P_2} = \left( \frac{h_S}{h_2} \right)^{\gamma/(\gamma-1)} \quad (5)$$

Since the fraction of kinetic energy in the flow behind a strong normal shock is small, equation (5) can be expanded as

$$P_S = P_2 + \frac{\rho_2 V_2^2}{2} = P_2 + \frac{1}{2} \frac{\rho_\infty}{\rho_2} \rho_\infty V_\infty^2 \quad (6)$$

Substituting the previous result for  $P_2$ , equation (3) into (6) yields

$$P_S = P_\infty + \rho_\infty V_\infty^2 \left( 1 - \frac{1}{2} \frac{\rho_\infty}{\rho_2} \right) \quad (7)$$

The ambient pressure ( $P$ ) is negligible, and the density ratio is usually greater than 10, so that the approximation

$$P_S \approx \rho_\infty V_\infty^2 \quad (8)$$

estimates the stagnation pressure to within 5 percent, and is on the high side. This will have an effect on the composition and radiation. Correlations of radiation heating indicate  $q_R \sim P_S^{1.5}$ , in which case the stagnation pressure estimate would result in less than 7.5 percent error in the heating, and is on the conservative side.

Utilizing the stagnation pressure approximation of twice the dynamic pressure and the stagnation enthalpy

$$H_S = \frac{V_\infty^2}{2} + h_\infty \quad (9)$$

the state of the gas is now identified at the stagnation point by  $P_S$ ,  $H_S$ . The flight velocity, ambient density, ambient temperature, and mole fractions of the atmospheric constituents are required to define each state point.

### c. Equilibrium Reactions Considered

To define the equilibrium composition, it is necessary to calculate the equilibrium constants for the chemical reactions which occur. These reactions can be expressed in the form



where  $A_i$  are the reactants and  $B_i$  the products, and  $a_i$  and  $b_i$  their respective stoichiometric coefficients. The pressure equilibrium constant for this reaction as defined in terms of the concentrations is

$$K_P = \frac{\prod X_i^{b_i} (B_i)}{[\prod X_i^{a_i} (A_i)] Z^{(b_i - a_i)}} \quad (11)$$

where:

$X (B_i)$  is the number of moles of each product per initial mole of gas

$X (A_i)$  is the number of moles of each reactant per initial mole of cold gas

$Z$  is the total number of moles per initial mole of cold gas and is sometimes called the compressibility factor.

For each reaction considered, an equation results. Besides this, a conservation relationship exists for each element in the initial mixture. Finally, charge conservation must be observed.

The equilibrium constant is related to the partition function  $Q_P$  by

$$\ln K_P = - \frac{\Delta E_o}{RT} + \sum b_i \ln Q_P (B_i) - \sum a_i \ln Q_P (A_i) \quad (12)$$

where

$$\Delta E_o \equiv \sum b_i E_o (B_i) - \sum a_i E_o (A_i) \quad (13)$$

is the zero point energy of the products less the zero point energy of the reactants. The reference state chosen is 0°K.

A matrix of all the reactions considered is given in table I-13. Fourteen reaction equations are used, with 19 species. Four elements, specified as molecular quantities, CO<sub>2</sub>, N<sub>2</sub>, O<sub>2</sub>, and A are considered. The charge (e<sup>-</sup>) conservation yields the final relationship.

The necessary heats of formation, at 0°K, are given in table I-14. The final form of the equilibrium constants is given in table I-15. It was initially planned to account for A<sup>++</sup>, but since so little ionization of argon was found to occur (as argon was specified for the Mars atmosphere only), it was dropped.

The choice of the reactions included those which formed the major radiating contributors and those which controlled the thermodynamics.

TABLE I-13

REACTION MATRIX\*

Reaction	A <sub>1</sub>	a <sub>1</sub>	B <sub>1</sub>	b <sub>1</sub>	B <sub>2</sub>	b <sub>2</sub>
1	CO <sub>2</sub>	1	CO	1	O <sub>2</sub>	1/2
2	O <sub>2</sub>	1	O	2	--	--
3	N <sub>2</sub>	1	N	2	--	--
4	CO	1	C	1	O	1
5	CN	1	C	1	N	1
6	NO	1	N	1	O	1
7	O	1	O <sup>+</sup>	1	e <sup>-</sup>	1
8	N	1	N <sup>+</sup>	1	e <sup>-</sup>	1
9	C	1	C <sup>+</sup>	1	e <sup>-</sup>	1
10	C <sup>+</sup>	1	C <sup>++</sup>	1	e <sup>-</sup>	1
11	N <sup>+</sup>	1	N <sup>++</sup>	1	e <sup>-</sup>	1
12	O <sup>+</sup>	1	O <sup>++</sup>	1	e <sup>-</sup>	1
13	N <sub>2</sub> <sup>+</sup>	1	N <sup>+</sup>	1	N	1
14	A	1	A <sup>+</sup>	1	e <sup>-</sup>	1

\*19 species

4 elements

TABLE I-14

## HEATS OF FORMATION AT 0°K

Specie	$E_0$ (°K)	$E_0/RT_0$	Reference
CN	101414	371.3	I-1
O	29684	108.7	I-1
O <sup>+</sup>	187722	687.2	I-1
O <sup>++</sup>	595705	2180.8	I-2
O <sub>2</sub>	0	0	
N <sub>2</sub>	0	0	
N	56631	207.3	I-1
N <sup>+</sup>	225283	824.7	I-1
N <sup>++</sup>	568944	2082.8	
NO	10811	39.6	I-1
C	132870	486.4	I-1
C <sup>+</sup>	263536	964.8	I-1
C <sup>++</sup>	546497	2000.6	I-2
CO	33641	123.2	I-1
CO <sub>2</sub>	0	0	
A	0	0	
A <sup>+</sup>	182891	669.5	I-1
A <sup>++</sup>	503491	1843.2	I-2
e <sup>-</sup>	0	0	

 $T_0 = 273.16^\circ\text{K}$

TABLE I-15

## EQUILIBRIUM CONSTANTS

The equilibrium constants in the program are given by:

$$\ln K_{P1} (\text{CO}_2 \rightarrow \text{CO} + \frac{1}{2} \text{O}_2) = - \frac{33500}{T} + \ln Q_P (\text{CO}) + \frac{1}{2} \ln Q_P (\text{O}_2) - \ln Q (\text{CO}_2)$$

$$\ln K_{P2} (\text{O}_2 \rightarrow 2\text{O}) = - \frac{59000}{T} + 2 \ln Q_P (\text{O}) - \ln Q_P (\text{O}_2)$$

$$\ln K_{P3} (\text{N}_2 \rightarrow 2\text{N}) = - \frac{113200}{T} + 2 \ln Q_P (\text{N}) - \ln Q_P (\text{N}_2)$$

$$\ln K_{P4} (\text{CO} \rightarrow \text{C} + \text{O}) = - \frac{128911}{T} - \ln Q_P (\text{CO}) + \ln Q_P (\text{C}) + \ln Q_P (\text{O})$$

$$\ln K_{P5} (\text{C} + \text{N} \rightarrow \text{CN}) = \frac{88087}{T} + \ln Q_P (\text{CN}) - \ln Q_P (\text{C}) - \ln Q_P (\text{N})$$

$$\ln K_{P6} (\text{N} + \text{O} \rightarrow \text{NO}) = \frac{75506}{T} + \ln Q_P (\text{NO}) - \ln Q_P (\text{N}) - \ln Q_P (\text{O})$$

$$\ln K_{P7} (\text{O} \rightarrow \text{O}^+ + \text{e}^-) = - \frac{158000}{T} + \ln Q_P (\text{O}^+) + \ln Q_P (\text{e}^-) - \ln Q_P (\text{O})$$

$$\ln K_{P8} (\text{N} \rightarrow \text{N}^+ + \text{e}^-) = - \frac{168800}{T} + \ln Q_P (\text{N}^+) + \ln Q_P (\text{e}^-) - \ln Q_P (\text{N})$$

$$\ln K_{P9} (\text{C} \rightarrow \text{C}^+ + \text{e}^-) = - \frac{131000}{T} + \ln Q_P (\text{C}^+) + \ln Q_P (\text{e}^-) - \ln Q_P (\text{C})$$

$$\ln K_{P10} (\text{C}^+ \rightarrow \text{C}^{++} + \text{e}^-) = - \frac{282000}{T} + \ln Q_P (\text{C}^{++}) + \ln Q_P (\text{e}^-) - \ln Q_P (\text{C}^+)$$

$$\ln K_{P11} (\text{N}^+ \rightarrow \text{N}^{++} + \text{e}^-) = - \frac{343000}{T} + \ln Q_P (\text{N}^{++}) + \ln Q_P (\text{e}^-) - \ln Q_P (\text{N}^+)$$

$$\ln K_{P12} (\text{O}^+ \rightarrow \text{O}^{++} + \text{e}^-) = - \frac{406000}{T} + \ln Q_P (\text{O}^{++}) + \ln Q_P (\text{e}^-) - \ln Q_P (\text{O}^+)$$

$$\ln K_{P13} (\text{N}_2^+ \rightarrow \text{N}^+ + \text{N}) = - \frac{100640}{T} + \ln Q_P (\text{N}^+) + \ln Q_P (\text{N}) - \ln Q_P (\text{N}_2^+)$$

$$\ln K_{P14} (\text{A} \rightarrow \text{A}^+ + \text{e}^-) = - \frac{182000}{T} + \ln Q_P (\text{A}^+) + \ln Q_P (\text{e}^-) - \ln Q_P (\text{A})$$

$$\ln K_{P15} (\text{A}^+ \rightarrow \text{A}^{++} + \text{e}^-) = - \frac{318000}{T} + \ln Q_P (\text{A}^{++}) + \ln Q_P (\text{e}^-) - \ln Q_P (\text{A}^+)$$



#### d. Partition Functions

All the thermodynamic properties of a gas can be calculated from their partition functions, e.g., Penner (ref. I-3), and Mayer and Mayer (ref. I-4). The partition function may be expressed as

$$Q = Q_t Q_r Q_v Q_e \quad (14)$$

The factors on the right of the equation are, respectively, the partition functions associated with the translational, rotational, vibrational and electronic energy levels of the gas particle.

The molecular model used in the computations considers the molecule as a rigid rotator and a harmonic oscillator. It is further assumed that the rotational and vibrational constants for all excited electronic states are the same as for the ground state. The limitations of these assumptions are discussed by Hertzberg (ref. I-5), from the microscopic viewpoint. The assumption of a rigid rotator, harmonic oscillator negates the effects of

- 1) Rotational correction factors for stretching
- 2) Vibrational corrections for anharmonicity
- 3) Vibration-rotation interaction
- 4) Azimuthal quantum effects.

The overall effects of these simplifying assumptions on the composition of the gas have been briefly examined by Rudin and Regent (ref. I-6) for air, where a maximum of 6 percent difference in the thermodynamic properties was observed for air up to 15,000°K. Comparisons of the calculated results with the results of other methods are given in a later section. By the methods of statistical mechanics for diatomic molecules, these factors are:

$$Q_t = \left( \frac{2 \pi m K T}{h^2} \right)^{3/2} \frac{RT}{P} \quad (15)$$

$$Q_r = \sum_{J=0}^{\infty} (2J+1) e^{\frac{-h^2 J(J+1)}{8\pi^2 I K T}} \approx \frac{8\pi^2 I K T}{\alpha h^2} \quad (16)$$

$$Q_v = \sum_{n=0}^{\infty} e^{\frac{-n h \nu}{KT}} = \left( 1 - e^{\frac{-h \nu}{KT}} \right)^{-1} \quad (17)$$

$$Q_e = \sum_{n=0}^{\infty} g_n e^{\frac{-\epsilon_n}{KT}} \quad (18)$$

The rotation and description above are common and are the same as given by Hansen (ref. I-10). For monatomic particles, the rotational and vibrational partition functions are taken as unity, and the remaining functions are given by equations (15) and (18).

The CO<sub>2</sub> molecule is a linear symmetric polyatomic molecule, for which Penner (ref. I-3) gives the form of the rotational and vibrational partition functions. The form of the rotational partition functions is the same as given by equation (16), with the symmetry number ( $\sigma$ ) equal to 2. The vibrational partition function for the CO<sub>2</sub> molecule has the form

$$Q_v = \prod_{i=1}^{i=4} \left( 1 - e^{\frac{-h \nu_i}{KT}} \right)^{-1} \quad (19)$$

A summary of the molecular constants used is given in table I-16 and the atomic constants are given in table I-17.

The atomic energy levels were taken from Moore (ref. I-7). The molecular constants were in the main, taken from Hertzberg (ref. I-5). The 9.76 electron-volt value for nitrogen dissociation is used. The spectra data for carbon dioxide was taken from McBride and Gordon (ref. I-8). Carbon dioxide has two identical vibrational frequencies, causing a resonance phenomenon, which is connected with the relatively long vibrational relaxation times observed for this molecule, e. g., Schwartz, Slawsky and Herzfeld (ref. I-9).

Finally, the form of the partition functions is given in table I-18.

TABLE I-16  
MOLECULAR CONSTANTS

DIATOMIC MOLECULE CONSTANTS						
Particle	Molecular Weight	Rotational Constant (°K)	Vibrational Constant (°K)	Dissociation Energy (°K)	Electronic Degeneracy ( $g_n$ )	Electronic Energy (°K)
N <sub>2</sub>	28	5.78	3390	113,200	1	0
O <sub>2</sub>	32	4.16	2270	59,000	3	0
					2	11,390
					1	18,990
CO	28	2.78	3130	128,911	1	0
CN	26	2.74	2980	88,087	2	0
					4	13,300
					2	37,000
NO	30	2.46	2740	75,506	2	0
					2	175
					2	63,400

POLYATOMIC MOLECULE CONSTANTS						
CO <sub>2</sub>	44	1.12	1940	33,500	1	0
			962			
			962			
			3380			

TABLE I-17  
ATOMIC CONSTANTS

Particle	Molecular Weight	Electronic Degeneracy ( $g_n$ )	Electronic Energy ( $^{\circ}\text{K}$ )	Ionization Energy ( $^{\circ}\text{K}$ )
O	16	5	0	158,000
		3	228	
		1	326	
		5	22,800	
		1	48,600	
N	14	4	0	168,000
		10	27,700	
		6	41,500	
O <sup>+</sup>	16	4	0	406,000
		10	38,600	
		6	58,200	
N <sup>+</sup>	14	1	0	343,000
		3	70	
		5	188	
		5	22,000	
		1	47,000	
		5	67,900	
e <sup>-</sup>	$\frac{1}{1820}$	2	0	
O <sup>++</sup>	16	1	0	
		3	163	
		5	442	
		5	29,200	
		1	62,100	
N <sup>++</sup>	14	2	0	
		4	252	

TABLE I-17 (Cont'd)

Particle	Molecular Weight	Electronic Degeneracy ( $g_n$ )	Electronic Energy ( $^{\circ}\text{K}$ )	Ionization Energy ( $^{\circ}\text{K}$ )
C	12	1	0	131,000
		3	23	
		5	62	
		5	14,700	
		1	31,200	
$\text{C}^+$	12	2	0	282,000
		4	92	
$\text{C}^{++}$	12	1	0	
A	40	1	0	182,000
$\text{A}^+$	40	4	0	318,000
		3	2060	
$\text{A}^{++}$	40	5	0	
		3	1600	
		1	2260	
		5	20,000	
		1	47,600	

TABLE I-18

## PARTITION FUNCTIONS

The logarithms of the partition functions are:

$$\ln Q (\text{CO}_2) = \frac{7}{2} \ln T + 1.90 - \ln (1 - e^{-1940/T}) - 2 \ln (1 - e^{-962/T}) - \ln (1 - e^{-33801/T}) - \ln p$$

$$\ln Q (\text{N}_2) = \frac{7}{2} \ln T - 0.42 - \ln (1 - e^{-3390/T}) - \ln p$$

$$\ln Q (\text{O}_2) = \frac{7}{2} \ln T + 0.11 - \ln (1 - e^{-2270/T}) + \ln (3 + 2e^{-11390/T} + e^{-18990/T}) - \ln p$$

$$\ln Q (\text{CO}) = \frac{7}{2} \ln T + 0.32 - \ln (1 - e^{-3130/T}) - \ln p$$

$$\ln Q (\text{NO}) = \frac{7}{2} \ln T + 0.54 - \ln (1 - e^{-2740/T}) + \ln (2 + 2e^{-175/T} + 2e^{-63400/T}) - \ln p$$

$$\ln Q (\text{CN}) = \frac{7}{2} \ln T + 0.22 - \ln (1 - e^{-2980/T}) + \ln (2 + 4e^{-13300/T} + 2e^{-37000/T}) - \ln p$$

$$\ln Q (\text{O}) = \frac{5}{2} \ln T + 0.50 + \ln (5 + 3e^{-228/T} + e^{-326/T} + 5e^{-22800/T} + e^{-48600/T}) - \ln p$$

$$\ln Q (\text{N}) = \frac{5}{2} \ln T + 0.30 + \ln (4 + 10e^{-27700/T} + 6e^{-41500/T}) - \ln p$$

$$\ln Q (\text{C}) = \frac{5}{2} \ln T + 0.07 + \ln (9 + 5e^{-14700/T} + e^{-31200/T}) - \ln p$$

$$\ln Q (\text{O}^+) = \frac{5}{2} \ln T + 0.50 + \ln (4 + 10e^{-38600/T} + 6e^{-58200/T}) - \ln p$$

$$\ln Q (\text{N}^+) = \frac{5}{2} \ln T + 0.30 + \ln (1 + 3e^{-71/T} + 5e^{-189/T} + 5e^{-22000/T} + e^{-47000/T} + 5e^{-67900/T}) - \ln p$$

$$\ln Q (\text{C}^+) = \frac{5}{2} \ln T + 0.07 + \ln (2 + 4e^{-92/T}) - \ln p$$

$$\ln Q (\text{O}^{++}) = \frac{5}{2} \ln T + 0.50 + \ln (1 + 3e^{-164/T} + 5e^{-442/T} + 5e^{-29200/T} + e^{-62100/T}) - \ln p$$

$$\ln Q (\text{N}^{++}) = \frac{5}{2} \ln T + 0.30 + \ln (2 + 4e^{-252/T}) - \ln p$$

$$\ln Q (\text{C}^{++}) = \frac{5}{2} \ln T + 0.07 - \ln p$$

$$\ln Q (\text{e}^-) = \frac{5}{2} \ln T - 14.24 - \ln p$$

$$\ln Q (\text{N}_2^+) = \frac{7}{2} \ln T - 0.42 - \ln (1 - e^{-3180/T}) + \ln (2 + 2e^{-36600/T} + 4e^{-12970/T}) - \ln p$$

$$\ln Q (\text{A}) = \frac{5}{2} \ln T + 1.866 - \ln p$$

$$\ln Q (\text{A}^+) = \frac{5}{2} \ln T + 1.866 + \ln (4 + 2e^{-2060/T}) - \ln p$$

$$\ln Q (\text{N}^{++}) = \frac{5}{2} \ln T + 1.866 + \ln (5 + 3e^{-1600/T} + e^{-2260/T} + e^{-20000/T} + e^{-47600/T}) - \ln p$$

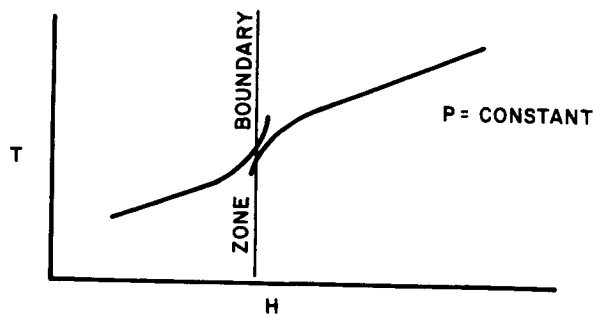
Note: for the Partition Functions, pressure is expressed in atmospheres.

#### e. Method of Calculation

Either of two methods are frequently used for solving the reaction equations to ascertain the composition at a state point. One of these methods uses the concept of minimization of free energy while the other attempts the simultaneous solution directly. The work of Hansen (ref. I-10) using the latter approach, is particularly noteworthy as illustrating how simple calculations for air can be made with good engineering accuracy.

Since the trajectory variables yield pressure and enthalpy, whereas the partition functions involve temperature and pressure, a rapidly convergent method was necessary. This was especially true in light of the concept of directly computing the composition along each trajectory. With computation speed and simplicity in mind, the approach used by Hansen, whereby the calculation is divided into zones, was selected. In each zone, only the important thermodynamic reactions would be solved simultaneously, thereby reducing the calculation to relatively simple algebraic relationships. The main difficulty with this approach lies at the zone boundaries, where small gaps in the calculations appear.

Preliminary computations indicated the desirability of accurately predicting the delineation of the zones. This can be seen intuitively as the edges of the zones demonstrate certain changes in the behavior of the gas. At the edges of the zones, the derivatives of the concentrations are essentially zero and hence a plot of  $(Z)$ , the compressibility factor, against temperature, holding pressure constant, would indicate inflection points at the zone edges. This can be seen in Hansen's results. A plot of temperature versus enthalpy, with pressure constant, will also exhibit inflection points at the zone edges. The results of the temperature calculations follow the general pattern depicted in the sketch below.

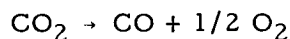
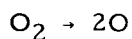


TEMPERATURE VERSUS ENTHALPY NEAR A ZONE EDGE

To minimize the effects of the zone edges, calculations were made to estimate the achievable tolerances of convergence. It was found that in order to achieve convergence to within 2 percent of the enthalpy at the zone edges, specific tables for each mixture would be desirable which denoted the enthalpies and pressures corresponding to the zone edges.

Examination of the results of other calculations led to the following choice of zones:

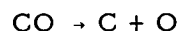
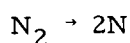
1) Zone No. 1 -- Thermodynamic Reactions



In zone 1, therefore, two simultaneous equations resulted.

At the end of zone 1,  $\text{O}_2$  and  $\text{CO}_2$  are fully dissociated.

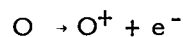
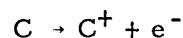
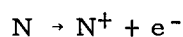
2) Zone No. 2 -- Thermodynamic Reactions



In zone 2, two simultaneous equations resulted, as argon was not coupled.

At the end of zone 2, all molecules are fully dissociated.

3) Zone No. 3 -- Thermodynamic Reactions

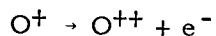
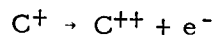


At the end of zone 3, all atoms are fully ionized.

Argon was omitted in zone 3 as it was unnecessary, as few points of the Mars cases fell in this zone.



4) Zone 4 -- Thermodynamic Reactions

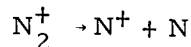
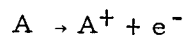
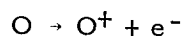
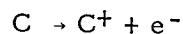
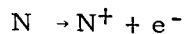
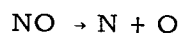
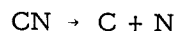


At the end of zone 4 all particles are doubly ionized. Argon was omitted in zone 4, as no Mars entry cases fell in this zone. The thermodynamic reactions were assumed to control the temperature and density calculation having specified the pressure and enthalpy. With the solution for the temperature in hand, the concentrations for the remaining species were evaluated;

5) Zone No. 1 -- Minor Reactions

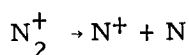
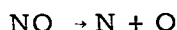
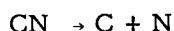
No other reactions were used in this zone, as the limits are such that relatively little radiation could be expected from this zone. It should be noted that the specified concentrations of  $\text{N}_2$  and A were not changed in the first zone.

6) Zone No. 2 -- Minor Reactions



The concentrations of CN and NO were assumed small and found by the expressions for their equilibrium constants, relating the concentrations to those for C and N obtained from the thermodynamic solution. Treatment of the small concentrations of ionized species necessitated the addition of the charge conservation relationship. The amount of ionization of argon was assumed small, so that the argon concentration was unchanged in zone 2.

### 7) Zone No. 3 -- Minor Reactions



These concentrations were computed assuming them to be small and simply relating them to the previously computed concentrations through their respective equilibrium constants.

An iterative solution was required to match the enthalpy and pressure specified. The enthalpy is found by

$$\frac{\text{MH}}{\text{RT}_0} = \sum X_i \frac{\text{MH}_i}{\text{RT}_0}$$

where

$$\frac{\text{MH}_i}{\text{RT}_0} = \frac{E_{o_i}}{\text{RT}_0} + \frac{T^2}{T_0} \left( \frac{\partial \ln Q_i}{\partial T} \right)_p$$

### f. Reference Conditions

The enthalpies have been normalized with respect to  $\text{RT}_0/\text{M}$ , where  $T_0 = 273.16^\circ\text{K}$  and the molecular weight is

$$\text{M} = 28 X_N + 32 X_O + 44 X_C + 40 X_A$$

where  $R$  is the universal gas constant,  $M$  is the molecular weight of the cold gas, and  $X_N$ ,  $X_O$ ,  $X_C$ ,  $X_A$  are the mole fractions of  $\text{N}_2$ ,  $\text{O}_2$ ,  $\text{CO}_2$ , and  $A$  in the atmosphere. The reference  $P_0$ , is 1 atmosphere, or 2116 lb/ft<sup>2</sup>. The reference density now depends on the molecular weight of the atmospheric constituents.

### g. Zone Tables

Eleven zone tables were developed covering the range of carbon dioxide and nitrogen mixtures of interest. These tables are summarized in table I-19. A special table was also prepared for air. It was found that the zones for the argon mixtures could be satisfactorily handled by considering an equivalent concentration of nitrogen for the total nitrogen and argon concentrations.

TABLE I-19

ZONE TABLES

$$X_N = 0.97$$

$$X_C = 0.02$$

$$X_O = 0.01$$

P	T <sub>1</sub>	T <sub>2</sub>	T <sub>3</sub>
100	4800	12,800	31,300
10	4300	10,700	25,500
1	3800	9200	21,400
0.1	3500	8000	18,400
0.01	3200	7100	16,000
0.001	2900	6400	14,200
0.0001	2720	5800	12,800
P	(HM/RT <sub>O</sub> ) <sub>1</sub>	(HM/RT <sub>O</sub> ) <sub>2</sub>	(HM/RT <sub>O</sub> ) <sub>3</sub>
100	81.3	716	2757
10	73.2	659	2544
1	64.9	618	2389
0.1	59.0	587	2274
0.01	55.1	564	2179
0.001	50.2	547	2109
0.0001	47.2	534	2055

TABLE I-19 (Cont'd)

$$X_N = 0.94$$

$$X_O = 0.01$$

$$X_C = 0.05$$

P	$T_1$	$T_2$	$T_3$
100	5100	12,700	31,300
10	4500	10,700	25,600
1	4000	9100	21,400
0.1	3600	8000	18,400
0.01	3300	7100	16,000
0.001	3000	6300	14,200
0.0001	2700	5700	12,700
P	$(HM/RT_o)_1$	$(HM/RT_o)_2$	$(HM/RT_o)_3$
100	94.7	724	2800
10	84.7	670	2588
1	76.3	625	2425
0.1	69.6	598	2309
0.01	64.7	575	2213
0.001	59.6	556	2141
0.0001	54.6	541	2082

TABLE I-19 (Cont'd)

$$X_N = 0.915$$

$$X_C = 0.075$$

$$X_O = 0.01$$

P	T <sub>1</sub>	T <sub>2</sub>	T <sub>3</sub>
100	5200	12,700	31,400
10	4600	10,600	25,600
1	4100	9100	21,400
0.1	3700	7900	18,400
0.01	3300	7000	16,000
0.001	3000	6300	14,200
0.0001	2800	5700	12,700
P	(HM/RT <sub>O</sub> ) <sub>1</sub>	(HM/RT <sub>O</sub> ) <sub>2</sub>	(HM/RT <sub>O</sub> ) <sub>3</sub>
100	103	734	2841
10	93.2	676	2620
1	84.8	635	2456
0.1	78.0	603	2338
0.01	71.1	580	2241
0.001	66.0	564	2168
0.0001	62.7	550	2106

TABLE I-19 (Cont'd)

$$X_N = 0.89$$

$$X_C = 0.01$$

$$X_C = 0.10$$

P	T <sub>1</sub>	T <sub>2</sub>	T <sub>3</sub>
100	5300	12,600	31,400
10	4700	10,600	25,600
1	4100	9100	21,500
0.1	3700	7900	18,400
0.01	3400	7000	16,000
0.001	3100	6200	14,200
0.0001	2800	5600	12,700
P	(HM/RT <sub>o</sub> ) <sub>1</sub>	(HM/RT <sub>o</sub> ) <sub>2</sub>	(HM/RT <sub>o</sub> ) <sub>3</sub>
100	112	739	2882
10	102	686	2653
1	91.3	644	2492
0.1	84.5	612	2367
0.01	79.5	590	2269
0.001	74.2	569	2194
0.0001	69.1	555	2132

TABLE I-19 (Cont'd)

$$X_N = 0.84$$

$$X_O = 0.01$$

$$X_C = 0.15$$

P	T <sub>1</sub>	T <sub>2</sub>	T <sub>3</sub>
100	5500	12,500	31,500
10	4800	10,500	25,600
1	4200	9000	21,500
0.1	3800	7800	18,400
0.01	3400	6900	16,000
0.001	3100	6200	14,100
0.0001	2900	5600	12,600
P	(HM/RT <sub>O</sub> ) <sub>1</sub>	(HM/RT <sub>O</sub> ) <sub>2</sub>	(HM/RT <sub>O</sub> ) <sub>3</sub>
100	130	756	2953
10	117	700	2718
1	107	660	2554
0.1	99.6	627	2426
0.01	92.5	604	2325
0.001	87.2	588	2244
0.0001	83.8	574	2181

TABLE I-19 (Cont'd)

$$X_N = 0.79$$

$$X_C = 0.2$$

$$X_O = 0.01$$

P	$T_1$	$T_2$	$T_3$
100	5600	12,400	31,500
10	4900	10,400	25,700
1	4300	8900	21,500
0.1	3900	7800	18,400
0.01	3500	6900	16,000
0.001	3200	6100	14,100
0.0001	2900	5500	12,600
P	$(HM/RT_O)_1$	$(HM/RT_O)_2$	$(HM/RT_O)_3$
100	145	772	3024
10	133	717	2791
1	122	675	2616
0.1	115	646	2484
0.01	108	623	2380
0.001	102	602	2298
0.0001	96.7	587	2232



TABLE I-19 (Cont'd)

$$X_N = 0.69$$

$$X_O = 0.01$$

$$X_C = 0.3$$

P	T <sub>1</sub>	T <sub>2</sub>	T <sub>3</sub>
100	5800	12,200	31,600
10	5000	10,200	25,800
1	4400	8800	21,600
0.1	3900	7700	18,400
0.01	3500	6800	16,000
0.001	3200	6100	14,100
0.0001	2000	5500	12,500
P	(HM/RT <sub>o</sub> ) <sub>1</sub>	(HM/RT <sub>o</sub> ) <sub>2</sub>	(HM/RT <sub>o</sub> ) <sub>3</sub>
100	177	804	3172
10	162	747	2929
1	151	709	2745
0.1	141	678	2601
0.01	134	654	2492
0.001	128	637	2405
0.0001	124	621	2331

TABLE I-19 (Cont'd)

$$X_N = 0.49$$

$$X_O = 0.01$$

$$X_C = 0.50$$

P	T <sub>1</sub>	T <sub>2</sub>	T <sub>3</sub>
100	6100	11,900	31,900
10	5300	10,000	25,900
1	4600	8600	21,600
0.1	4100	7600	18,400
0.01	3700	6700	16,000
0.001	3300	6000	14,000
0.0001	3000	5500	12,500
P	(HM/RT <sub>O</sub> ) <sub>1</sub>	(HM/RT <sub>O</sub> ) <sub>2</sub>	(HM/RT <sub>O</sub> ) <sub>3</sub>
100	241	869	3479
10	224	815	3199
1	210	774	2993
0.1	199	747	2835
0.01	192	722	2716
0.001	183	702	2614
0.0001	176	691	2537

TABLE I-19 (Cont'd)

$$X_N = 0.14$$

$$X_O = 0.01$$

$$X_C = 0.85$$

P	T <sub>1</sub>	T <sub>2</sub>	T <sub>3</sub>
100	6500	11,800	32,200
10	5600	10,000	26,200
1	4900	8600	21,800
0.1	4300	7600	18,500
0.01	3800	6700	15,900
0.001	3400	6100	14,000
0.0001	3100	5500	12,400
P	(HM/RT <sub>O</sub> ) <sub>1</sub>	(HM/RT <sub>O</sub> ) <sub>2</sub>	(HM/RT <sub>O</sub> ) <sub>3</sub>
100	351	996	4001
10	330	942	3685
1	313	900	3441
0.1	299	871	3252
0.01	287	843	3099
0.001	277	828	2987
0.0001	269	808	2892

TABLE I-19 (Cont'd)

$$X_N = 0.01$$

$$X_O = 0.01$$

$$X_C = 0.98$$

P	T <sub>1</sub>	T <sub>2</sub>	T <sub>3</sub>
100	6800	11,900	32,300
10	5900	10,000	26,200
1	5100	8700	21,800
0.1	4500	7600	18,500
0.01	4000	6800	15,900
0.001	3600	6100	14,000
0.0001	3300	5500	12,400
P	(HM/RT <sub>O</sub> ) <sub>1</sub>	(HM/RT <sub>O</sub> ) <sub>2</sub>	(HM/RT <sub>O</sub> ) <sub>3</sub>
100	397	1048	4198
10	375	989	3858
1	354	951	3606
0.1	339	917	3405
0.01	326	894	3244
0.001	316	873	3126
0.0001	309	853	3026

TABLE I-19 (Concl'd)

$$X_N = 0.78$$

$$X_O = 0.21$$

$$X_C = 0.01$$

P	T <sub>1</sub>	T <sub>2</sub>	T <sub>3</sub>
100	5900	12,500	31,600
10	5100	10,500	25,800
1	4500	9100	21,700
0.1	4000	7900	18,600
0.01	3600	7000	16,200
0.001	3300	6300	14,300
0.0001	3000	5700	12,800
P	(HM/RT <sub>O</sub> ) <sub>1</sub>	(HM/RT <sub>O</sub> ) <sub>2</sub>	(HM/RT <sub>O</sub> ) <sub>3</sub>
100	144	655	2737
10	130	603	2522
1	120	569	2366
0.1	112	538	2244
0.01	105	516	2148
0.001	99.8	501	2071
0.0001	94.8	468	2011

In general, any mixture ratio can be analyzed by specifying the table which has the concentrations most closely representative of the mixture of interest. Several special cases are not possible; zero concentrations of carbon dioxide and/or zero concentrations of nitrogen. Zero concentrations of oxygen and/or argon can be specified. The reason for the exception is due to singularities in the algebraic relationships used in solving the equilibrium concentrations. Additional programing was deemed unnecessary, as these two concentrations ( $\text{CO}_2$ ,  $\text{N}_2$ ) can be made small enough, on the order of 0.001, so that they have a negligible effect on the results.

### 3. Pressure Distribution

#### a. Symbols

A	streamtube area ( $\text{ft}^2$ )
$C_p$	specific heat at constant pressure
h, H	static and total enthalpy (Btu/lb)
$K_c$	radius of curvature of streamlines
M	Mach number
n	distance normal to streamlines
$P_e$	pressure at edge of entropy layer and/or at edge of boundary layer ( $\text{lb}/\text{ft}^2$ )
R	gas constant; also body radius
$R_c$	reference radius (feet)
s	distance along streamlines
T	temperature ( $^{\circ}\text{K}$ )
u	local velocity
$V_{\infty}$	free stream velocity
x	axial coordinate
y	radial coordinate
$\gamma$	ratio of specific heats
$\delta$	streamline deflection angle
$\rho$	density ( $\text{slugs}/\text{ft}^3$ )
$\theta$	body surface slope

## Subscripts

e	conditions edge of entropy layer
o	conditions at start of entropy layer calculation
s	stagnation conditions
w	conditions at the shock wave
$\infty$	free stream conditions.

## b. Derivation of Equations\*

The effect of nose bluntness on the hypersonic flow around bodies lies in the formation of a high-entropy, low density layer near the surface of the body. This layer is caused by the streamlines near the body passing through the normal or near normal portion of the shock, whereas the streamlines away from the body have passed through a shock inclined at a small angle. Since the entropy rise across the normal portion is higher than across the inclined portion, and since entropy is constant along streamlines, the formation of the so-called "entropy layer" is obtained. This entropy layer has recently received considerable attention by various authors (ref. I-11 to I-14).

The existence of the entropy layer can be demonstrated through an investigation of the blast-wave solution. The problem of a violent spherical explosion was treated numerically by G. I. Taylor (ref. I-15) and analytically by L. I. Sedov (ref. I-16). S. C. Lin (ref. I-17) extended the solution to the case of a violent cylindrical explosion. He pointed out that, through the use of the hypersonic equivalence principle of Hayes, the solution should apply to the wake of an unyawed axisymmetric body in hypersonic flight. Cheng and Pallone (ref. I-18) and Lees and Kubota (ref. I-19) extended this analogy to the flow field about two-dimensional and axisymmetric blunt-nosed slender bodies, respectively.

Einbinder (ref. I-20) has analyzed the blast-wave solution for various  $\gamma$  and has demonstrated the existence of a high-temperature, low-density region near the core. Freeman (ref. I-21) has examined this solution in the limit as  $\gamma \rightarrow 1$  and has found that the whole flow is concentrated near the shock wave, the only particles in the region between the shock and the center being those that were originally very near the center. He also found that, except in the region near the shock, the temperature is large.

---

\*The derivation follows that given by Salathe, E.P., Entropy-Layer Theory For Pressure Distributions in Hypersonic Flow, Avco Doc. RAD-TM-62-79 (1962).

Since for sufficiently high-flight velocities and sufficiently slender bodies the flow variables in the inner and outer regions of the shock layer must differ considerably, a reasonable description of the flow field can be achieved by considering the two sections separately and matching them at their common boundary.

Consider the hypersonic flow over an axisymmetric blunt body. It is convenient to use the "natural coordinate system" in which one coordinate (s) is measured along the streamlines, the other (n) is perpendicular to it. The one-dimensional flow equations are applicable to a streamtube formed by two adjacent streamlines.

The equations of one-dimensional flow written for the streamtube formed by the stream surfaces n and n + Δn have the form

$$\text{Continuity:} \quad \rho u \Delta A = \text{constant} \quad (20)$$

$$\text{s Momentum:} \quad \rho u \frac{\partial u}{\partial s} = - \frac{\partial p}{\partial s} \quad (21)$$

$$\text{n Momentum:} \quad \frac{\rho u^2}{K_c} = - \frac{\partial p}{\partial n} = \rho u^2 \frac{\partial \delta}{\partial s} \quad (22)$$

$$\text{Energy:} \quad h + \frac{1}{2} u^2 = H \quad (23)$$

$$\text{State:} \quad P = \rho R T \quad (24)$$

Here, ΔA is the area of the streamtube between the stream surfaces n and n + Δn.

From equations (20) to (24), the one-dimensional isentropic relationships along a streamtube can be derived. A simplification in the relationship between the streamtube area and the pressure is sought. By continuity,

$$\frac{d\rho}{\rho} + \frac{du}{u} = - \frac{d\Delta A}{\Delta A} \quad (24a)$$

and by the energy equation

$$\frac{2 du}{u} = - \frac{dh}{H - h} = - \frac{2 C_p T}{u^2} \frac{dT}{T} = - \frac{2}{(\gamma - 1) M^2} \frac{dT}{T} \quad (24b)$$



Using the isentropic relationships

$$\frac{d\rho}{\rho} = \frac{1}{\gamma} \frac{dp}{P} \quad (25)$$

and

$$\frac{dT}{T} = \frac{(\gamma - 1)}{\gamma} \frac{dp}{P}$$

then equations (24a), (24b), and (25) combine to yield,

$$\frac{dp}{P} = \frac{\gamma M^2}{(1 - M^2)} \frac{d\Delta A}{\Delta A} \quad (26)$$

The assumption is now made that  $M^2 \gg 1$ , such that  $M^2/1 - M^2 = -1$ . This assumption is justified at the outer edge of the entropy layer where the Mach number is higher than at the body surface. For bodies which have rapid expansions near the nose, as a hemisphere cylinder, the above approximation should be quite good close to the nose. The use of this method is now, however, clearly restricted to a supersonic region, and the method using the results is discussed in the following section.

The pressure and area ratios are now related by

$$\frac{\Delta A}{\Delta A_o} = \left( \frac{P_e}{P_{eo}} \right)^{-\frac{1}{\gamma}} \quad (27)$$

The area of the streamtube is related to  $y$  by

$$\Delta A = 2\pi \cos \delta y dy \quad (28)$$

so that in the limit as the streamtube thickness approaches zero,

$$\cos \delta y dy = \left( \frac{P_e}{P_{eo}} \right)^{-\frac{1}{\gamma}} \cos \delta_o y_o dy_o \quad (29)$$

Neglecting the variation of  $\delta$  across the entropy layer, this equation can be integrated to yield

$$y_e = \sqrt{\frac{\bar{A}_{eo}}{\pi} \left(\frac{P_e}{P_{eo}}\right)^{-\frac{1}{\gamma}} \frac{\sec \theta}{\sec \theta_o} + R^2} \quad (30)$$

where  $\bar{A}_{eo} = \pi (y_{eo}^2 - R_o^2)$ . Equation (30) relates the growth of the entropy layer to the pressure impressed upon it by the outer layer. A number of methods, e.g., tangent wedge, shock expansion, and Newtonian theory, can be used to analyze the outer layer, considering it to be attached to an "effective body", the body plus the entropy layer. For simplicity, the Newtonian pressure relationship without centrifugal correction is used, given by

$$P_e = P_\infty + \rho_\infty V_\infty^2 \frac{\left(\frac{dy_e}{dx}\right)^2}{1 + \left(\frac{dy_e}{dx}\right)^2} \quad (31)$$

where  $y_e(x)$  is the height of the entropy layer given by equation (30). Since the pressure is assumed constant across the entropy layer, the body surface pressure is also defined by equation (31). Combining equations (30) and (31), a differential equation for the pressure is obtained.

$$\begin{aligned} & \sqrt{\frac{P_e - P_\infty}{\rho_\infty V_\infty^2 - P_e + P_\infty} \left[ \frac{\bar{A}_{eo}}{\pi} \left(\frac{P_e}{P_{eo}}\right)^{-\frac{1}{\gamma}} \frac{\sec \theta}{\sec \theta_o} + R^2 \right]} \\ &= - \frac{\bar{A}_{eo}}{2\gamma\pi} \left(\frac{P_e}{P_{eo}}\right)^{-\frac{\gamma+1}{\gamma}} \frac{\sec \theta}{\sec \theta_o} \frac{d}{dx} \left(\frac{P_e}{P_{eo}}\right) \\ &+ \frac{\sec \theta}{\sec \theta_o} \frac{\bar{A}_{eo}}{2\pi} \left(\frac{P_e}{P_{eo}}\right)^{-\frac{1}{\gamma}} \tan \theta \frac{d\theta}{dx} + R \tan \theta. \end{aligned} \quad (32)$$

The initial area of the entropy layer  $\bar{A}_{eo}$  can be related to the drag of the nose.

The energy in any transverse plane of the flow field is given by

$$E = 2\pi \int_R^{y_w} \frac{P}{(\gamma - 1)} y dy + 2\pi \int_R^{y_w} \frac{\rho V^2}{2} y dy \quad (33)$$

where  $y_w$  is the value of  $y$  at the shock. The first term represents the thermal energy and the second represents the kinetic energy of the flow. The thermal energy is much larger than that in the outer layer and accounts for the greatest portion of the energy. Hence equation (33) is approximately given by

$$E = 2\pi \int_R^{y_{eo}} \frac{1}{(\gamma - 1)} P y dy = 2\pi \frac{P_{eo}}{\gamma - 1} \left( \frac{y_{eo}^2 - R_o^2}{2} \right) = \frac{\bar{A}_{eo} P_{eo}}{(\gamma - 1)} \quad (34)$$

as the pressure is assumed constant across the entropy layer. Since the energy is supplied by the drag,

$$\frac{\bar{A}_{eo} P_{eo}}{\gamma - 1} = D \quad (35)$$

or

$$\bar{A}_{eo} = \frac{D}{P_{eo}} (\gamma - 1) .$$

For the particular case of a blunt nosed cone, for which  $\theta = \text{constant}$ , equation (32) can be written, using equation (35), in the form

$$\frac{dP_e/P_s}{dx} = \frac{\gamma}{B} \left( \frac{P_e}{P_s} \right)^{\frac{\gamma+1}{\gamma}} \left\{ \frac{R_o}{R_c} \tan \theta + \tan^2 \theta \left( \frac{x}{R_c} - \frac{x_o}{R_c} \right) \right. \\ \left. - \sqrt{\frac{\left( \frac{P_e}{P_s} - \frac{P_\infty}{P_s} \right)}{\left( 1 - \frac{P_e}{P_s} + \frac{P_\infty}{P_s} \right)}} \left\{ 2B \left( \frac{P_e}{P_s} \right)^{-\frac{1}{\gamma}} + \left[ \frac{R_o}{R_c} + \tan \theta \left( \frac{x}{R_c} - \frac{x_o}{R_c} \right) \right]^2 \right\} \right\}$$

where

$$B = (\gamma - 1) \left( \frac{P_{eo}}{P_s} \right)^{\frac{1-\gamma}{\gamma}} \int_0^{R_o/R_c} \frac{P_e}{P_s} \frac{R}{R_c} \frac{dR}{R_c} .$$

The initial value of pressure,  $P_{eo}$ , is determined from upstream conditions as described below.

### c. Calculation Model

The calculation model for the pressure distribution is premised on the use of equation (36) for conical sections. Each vehicle shape is divided into a series of conical sections and sharp corners. A Prandtl-Meyer expansion is used to relate the pressures fore and aft of the corners.

Over the blunt face, Newtonian theory is used until the pressure gradient equals that given by a Prandtl-Meyer expansion. This method has been suggested by Lees and Kabota (ref. I-22) and used extensively. It is sometimes called the Newtonian-Prandtl-Meyer approximation. The match point between the Newtonian and Prandtl-Meyer solutions has been evaluated, and the pressure at this point,  $P^*/P_s$  is given by the expression

$$\frac{P_\infty}{P_s} = \frac{P_e^*}{P_s} - \left( \frac{\gamma}{\gamma-1} \right)^2 \frac{\frac{P_e^*}{P_s} \left[ \left( \frac{P_s}{P_e^*} \right)^{\frac{\gamma-1}{\gamma}} - 1 \right]^2}{\left( 1 - \frac{P_e^*}{P_s} \right) \left\{ \frac{2}{\gamma-1} \left[ \left( \frac{P_s}{P_e^*} \right)^{\frac{\gamma-1}{\gamma}} - 1 \right] - 1 \right\}} . \quad (37)$$

Starting at the stagnation point, the pressure ratio is given by,

$$\frac{P_e}{P_s} = \sin^2 \theta + \frac{P_\infty}{P_s} \cos^2 \theta \quad (38)$$

for

$$\frac{\pi}{2} \geq \theta \geq \theta^*$$

where  $\theta^*$  is given by

$$\frac{P_e^*}{P_s} = \sin^2 \theta^* + \frac{P_\infty}{P_s} \cos^2 \theta^* .$$

Then for  $\theta^* \geq \theta \geq \theta_C$ , a Prandtl-Meyer expansion is used giving

$$\frac{dP_e/P_s}{d\theta} = \gamma \frac{P_e}{P_s} \frac{\frac{2}{\gamma-1} \left[ \left( \frac{P_s}{P_e} \right)^{\frac{\gamma-1}{\gamma}} - 1 \right]}{\sqrt{\frac{2}{\gamma-1} \left[ \left( \frac{P_s}{P_e} \right)^{\frac{\gamma-1}{\gamma}} - 1 \right] - 1}} \quad (39)$$

On the other hand, if  $\theta_C > \theta^*$ , then following station 2 as shown in figure I-7, a linear pressure variation from station 2 to station 3, is assumed with sonic pressure assumed ahead of the corner at station 3. When equation (36) is used, going from station 2 to station 3 substitute conditions at 0 with conditions at 2. Going around the corner from station 3 to station 4, a Prandtl-Meyer is used. From station 4 to station 5, equation (36) is used substituting conditions at 0 with conditions at 4. Going from the cylinder to the flare, a reverse Prandtl-Meyer is used to approximate the oblique shock. Along the succeeding sections, the above technique is simply repeated. Along the boat-tail sections, negative cone angles are inserted. The geometric relationships between stations are similar to those given in the coefficients section.

The above approach has been successfully used for angle-of-attack calculations by redefining the body geometry with respect to the new stagnation point.

#### 4. Convective Heating

##### a. Symbols

a,b	Nose bluntness parameters
M	Molecular weight
P	Pressure (lb/ft <sup>2</sup> )
q	Heat rate (Btu/ft <sup>2</sup> -sec)
R	Body radius (feet)
R <sub>C</sub> , R <sub>N</sub> , R <sub>S</sub> , $\theta_N$ ,	Body geometry parameters defined in figure I-6
S	Distance along streamline (feet)
u	Local velocity (ft/sec)
V <sub>∞</sub>	Flight velocity (ft/sec)

$\alpha$	Angle of attack
$\phi$	Meridian angle
$\gamma$	Ratio of specific heats
$\rho$	Density (slugs/ft <sup>3</sup> )
Subscripts	
e	Edge of boundary layer
S	Stagnation conditions
T	Turbulent flow
$\infty$	Free stream conditions
( )*	Sonic point conditions.

#### b. Stagnation Point\*

The thermodynamic and transport properties used in this study have been generated recently at Avco RAD. In all cases, the best molecular data presently available have been used.

The thermodynamic properties for mixtures of CO<sub>2</sub> and N<sub>2</sub> have been generated by a technique which is based on the minimization of free energy. Complete descriptions of the technique and of the machine program are given in Avco RAD reports (refs. I-23 and I-24).

For these heat-transfer studies, the transport properties have been calculated to 20,000°K for pressures from 0.1 to 100 atm. The species included in these calculations are as follows: C, CO, CO<sub>2</sub>, C<sub>3</sub>O<sub>2</sub>, O, O<sub>2</sub>, N<sub>2</sub>O<sub>4</sub>, N<sub>2</sub>O<sub>5</sub>, C<sup>+</sup>, CO<sup>+</sup>, O<sup>+</sup>, O<sub>2</sub><sup>+</sup>, e<sup>-</sup>, CN, C<sub>2</sub>N<sub>2</sub>, C<sub>4</sub>N<sub>2</sub>, N, N<sub>2</sub>, NO, NO<sub>2</sub>, N<sub>2</sub>O, N<sup>+</sup>, and NO<sup>+</sup>.

---

\*A detailed discussion of these effects is given by Van Tassell, W., Convective Heating in Planetary Atmospheres, Avco Doc. RAD TM-63-72 (1963).

The transport properties have been calculated by the techniques outlined by Yos (ref I-25), using the best-available collision cross sections published.

Heat-transfer rates and boundary-layer profiles have been found from a similar solution of the laminar boundary-layer equations. A detailed description of the solution is also given in reference I-26.

The atomic composition was assumed to be constant throughout the boundary layer. In essence, this means that multicomponent diffusion was neglected. All fluid properties were continuously variable throughout the boundary layer. The effects of chemical reactions were included by employing the reaction-conductivity concept. All calculations assumed a wall temperature of 300°K. Argon calculations were incomplete, so the molecular weight correlation evolved from the above studies was assumed for the argon mixture also.

The results for four mixture ratios are shown in figures I-7 thru I-10. It should be noted that stagnation enthalpy ratios,  $H/RT_0$ , are a function of the composition, and hence the corresponding flight velocity is a function of the composition. A correlation of the stagnation point heating with flight velocity was evolved, and is given by

$$q_s = K \sqrt{\rho_\infty} \left( \frac{v_\infty}{10^4} \right)^B \sqrt{\frac{1}{v_\infty} \left( \frac{du}{ds} \right)_s} \text{ Btu/ft}^2\text{-sec}$$

where

$$K = (1.1 + 0.075M) \times 10^4$$

$$B = 3.909 - 0.0229 M$$

$$M = \text{molecular weight}$$

$$\left( \frac{du}{ds} \right)_s = \text{velocity gradient at stagnation point.}$$

The range of K and b are

M	$10^{-4}K$	B
28	3.2	3.259
44	4.4	2.899

The stagnation point velocity gradient was computed using Vinokur's (ref. I-27) results where the gradient is given as a function of the minor and major axes of an elliptical nose. The relation given for the gradient by Vinokur has been correlated as:

$$\sqrt{\frac{a}{V_{\infty}} \left( \frac{du}{ds} \right)_s} = K_1 \left( \frac{\rho_{\infty}}{\rho_s} \right)^C$$

where

$$C = 0.25 + 0.285 \left( \frac{b}{a} \right)^{2.7}$$

and

$$K_1 = 1.0 + 0.66 \left( \frac{b}{a} \right)^3$$

To utilize Vinokur's results, a nose section consisting of  $R_N$  and  $R_S$  is assumed to be equivalent to an elliptical nose with axes (a) and (b) given by

$$a = R_N \sin \theta_N + R_S (1 - \sin \theta_N)$$

$$b = R_N (1 - \cos \theta_N) + R_S \cos \theta_N$$

The approach above cannot be applied if the flow is subsonic on the forecone. In these cases, the schlieren photographs supplied by JPL were utilized. The data were used by correlating the standoff distance with an effective  $b/a$ , and using Vinokur's result to scale the effect of density ratio.

At angle of attack (three dimensional stagnation point) test data must be relied upon, at present, for accurate stagnation point location. In the absence of comprehensive data for all the shapes considered, a consistent analysis based on the Newtonian stagnation point location, was performed.



Using the method of reference I-28, the stagnation point heating is given as

$$\frac{q_{s', \alpha}}{q_{s', \alpha=0}} = \left( \frac{R_{\alpha=0}}{2\pi} \int_0^{2\pi} \frac{d\phi}{R(\phi)} \right)^{1/2}$$

where  $R_{\alpha=0}$  is the nose radius at the stagnation point at zero angle of attack and  $\phi$  is the position angle about the stagnation point, and  $R(\phi)$  is the radius of curvature at the angle  $\phi$ . As the integral is very difficult to evaluate, it was modified as follows

$$\frac{q_{s', \alpha}}{q_{s', \alpha=0}} = \left( \frac{(s^*/R_C)_{\alpha=0}}{2\pi} \int_0^{2\pi} \frac{d\phi}{(s^*/R_C)} \right)^{1/2}$$

where  $(s^*/R_C)_{\alpha=0}$  is the distance to the sonic point at zero angle of attack and  $s^*/R_C$  is the distance to the sonic point at angle of attack and varies with  $\phi$ . The  $s^*/R_C$  variations were obtained with  $\phi$  and the integral evaluated (both done graphically). The angle of attack effect obtained using the radius of curvature integral is seen to be discontinuous where the stagnation point leaves the nose radius, and occurs on the shoulder radius segment.

### c. Convective Heating Distributions

The theoretical analysis of a laminar boundary layer with a pressure gradient is considerably simplified if "local similarity" is assumed. A complete discussion of this approach to boundary layer analysis is given in reference I-29. Some estimates of the errors involved in using this analysis under conditions where the flow properties are changing rapidly (i. e., around a sharp corner) are given in reference I-29. The indications are that the similarity theory is adequate for engineering analyses of a wide variety of configurations. The variation in heat transfer is given as a function of the stagnation point heat transfer rate, i. e.,

$$\frac{q}{q_s} = \frac{1}{2} \left[ \left( \frac{P_e}{P_s} \right) \left( \frac{u_e}{V_\infty} \right) \left( \frac{R}{R_C} \right) / \sqrt{\frac{\xi}{R_C^3}} \sqrt{\frac{R_C}{V_\infty}} \left( \frac{du}{ds} \right)_s \right] \left( \frac{1 + .096 \sqrt{\beta}}{1.068} \right)$$

where

$$\xi/R_C^3 = \int_0^{s/R_C} \left( \frac{P_e}{P_s} \right) \left( \frac{u_e}{V_\infty} \right) \left( \frac{R}{R_C} \right)^2 d s/R_C$$

$$\beta = 2 \frac{d \ln u}{d \xi}$$

and  $u/V_\infty$  (the local velocity) is given by

$$\frac{u_e}{V_\infty} = \sqrt{1 - \left( \frac{P_e}{P_s} \right)^{(\gamma-1)/\gamma}},$$

The velocity gradient term is evaluated by means of Newtonian theory,

$$\frac{du}{ds} = \frac{V_\infty}{R_N} \sqrt{2 \frac{\rho_\infty}{\rho_s} \left( 1 - \frac{P_\infty}{P_s} \right)}$$

for use within the above relation for heating rate distribution. The applicability of this technique is shown in reference I-30.

An approximate theory is utilized for evaluating the turbulent heat transfer rate for a highly cooled boundary layer for the case of blunted bodies of revolution in high speed flight. The turbulent distribution is given by

$$\frac{q_T}{q_T^*} = \frac{\left( \frac{P_e}{P_s} \right)^{\frac{\gamma+7}{10\gamma}} \left( \frac{u_e}{V_\infty} \right)^{0.8} (s^*/R_C)^{0.2}}{\left( \frac{2}{\gamma-1} \right)^{\frac{\gamma+7}{10(\gamma-1)}} \left( \frac{\gamma-1}{\gamma+1} \right)^{0.4} (s/R_C)^{0.2}}$$

where  $q_T^*$  is the heating rate at the sonic point where  $\frac{P_e}{P_s} = \left( \frac{2}{\gamma+1} \right)^{\frac{\gamma}{\gamma-1}}$   
 $s^*/R_C$  is the distance along the body to the sonic point.

The turbulent sonic point heating correlation used is that suggested for air,

$$q_T^* = (XKT) \rho_\infty^{0.8} \left( \frac{V_\infty}{10^4} \right)^{3.18} \text{ Btu/ft}^2\text{-sec}$$

The angle of attack effects on body pressure distribution and subsequently by the heating distributions can be evaluated by means of an equivalent body whose contour is obtained by rotating the body about a new axis of symmetry through the stagnation point. The heating distribution can be computed at angle of attack on the windward-most facing elements (the body streamlines in the plane formed by the body axis and wind axis) by means of the similarity method (ref. I-28).

Two simplified models for vehicle oscillatory motion were used in the heating analysis. For all cases with initial vehicle spin, a lunar-motion dynamics model was utilized which assumed the spin frequency was equal to the pitch frequency. Thus, a single longitudinal meridian would always face the free stream velocity vector and the heat shield is designed to the heating found on the windward ray of the vehicle at an angle of attack which equals the envelope value. With spin, the lunar motion model is justified since the vehicle natural frequency may be of the same magnitude as the spin rate twice during the heat pulse and at high heating rates relative to the peak rate.

With zero spin, the angle of attack is varying from the envelope value to zero, and the averaged heating rate is going to be less than the heating determined by a lunar motion assumption. A comparison of the convective heating at a point on the M1 afterbody for the two dynamics models is shown in figure I-11.

The complete determination of the heating at some point on the afterbody requires the angle of attack envelope (along with a dynamics model), the stagnation point heating ( $q_s$ ) and the heating distribution as functions of time; the number of calculations needed for the required parameter variation would be excessive. It was found that a sufficient reduction in the calculations with little loss in accuracy could be achieved by assuming the heating distribution for the angle of attack at peak convective heating to apply over the entire trajectory.

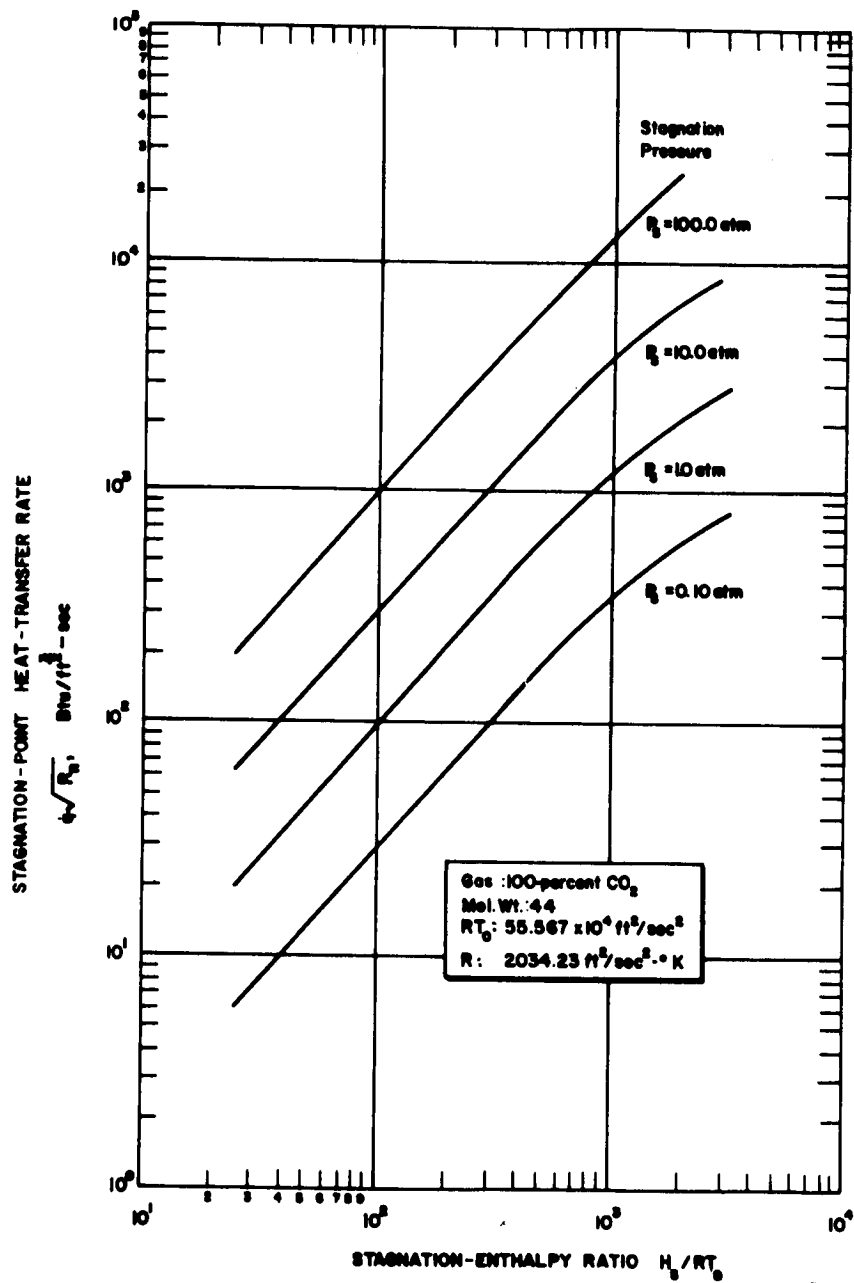


Figure 1-7 CONVECTIVE HEATING AT A STAGNATION POINT (100-PERCENT  $CO_2$ )

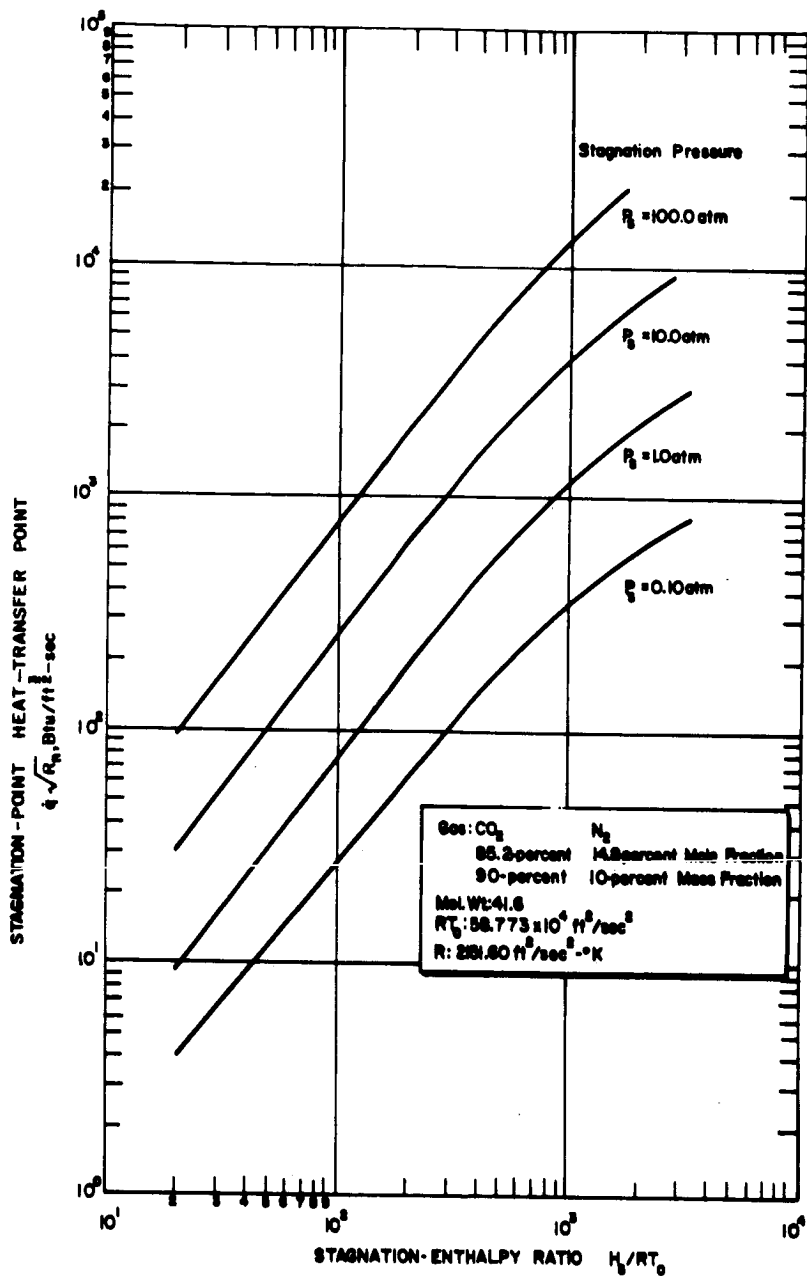


Figure 1-8 CONVECTIVE HEATING AT A STAGNATION POINT (90-PERCENT  $\text{CO}_2$  AND 10-PERCENT  $\text{N}_2$ )

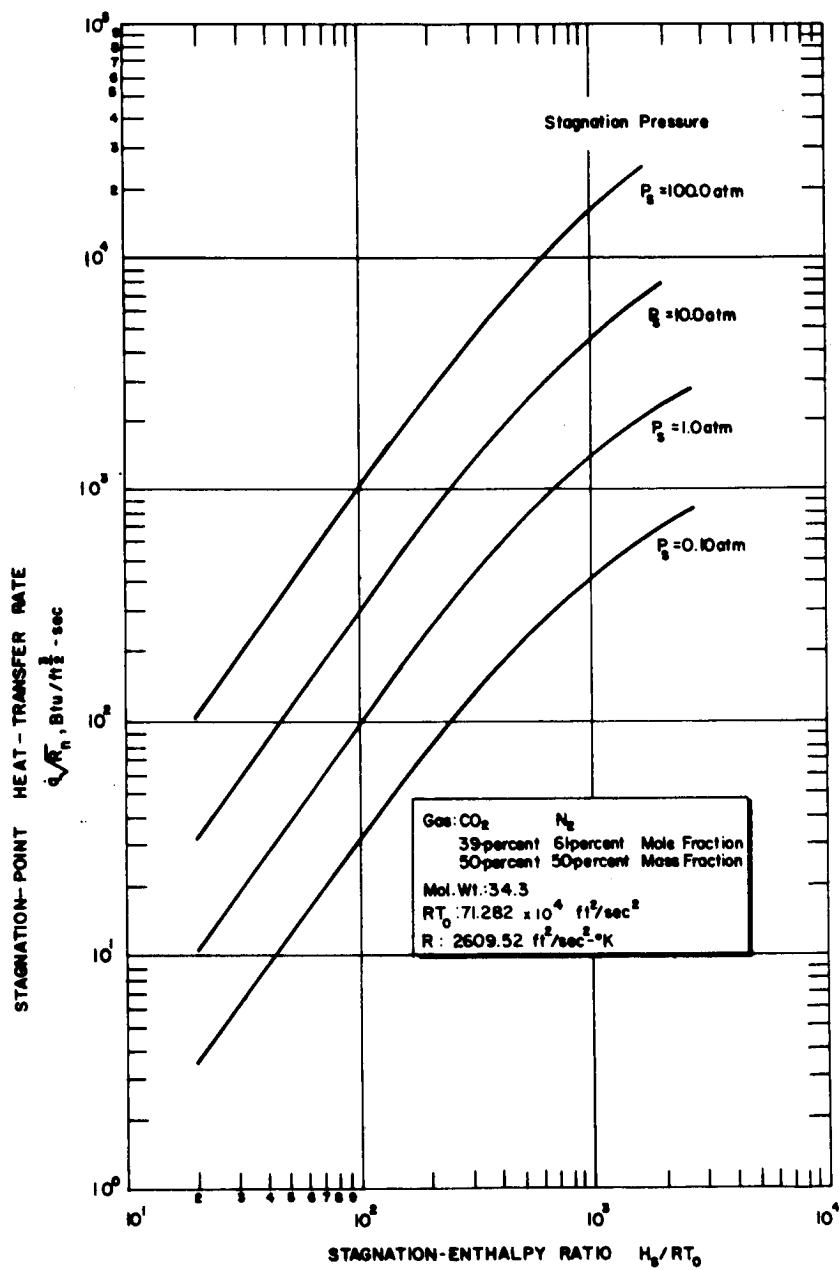


Figure 1-9 CONVECTIVE HEATING AT A STAGNATION POINT (50-PERCENT  $\text{CO}_2$  AND 50-PERCENT  $\text{N}_2$ )

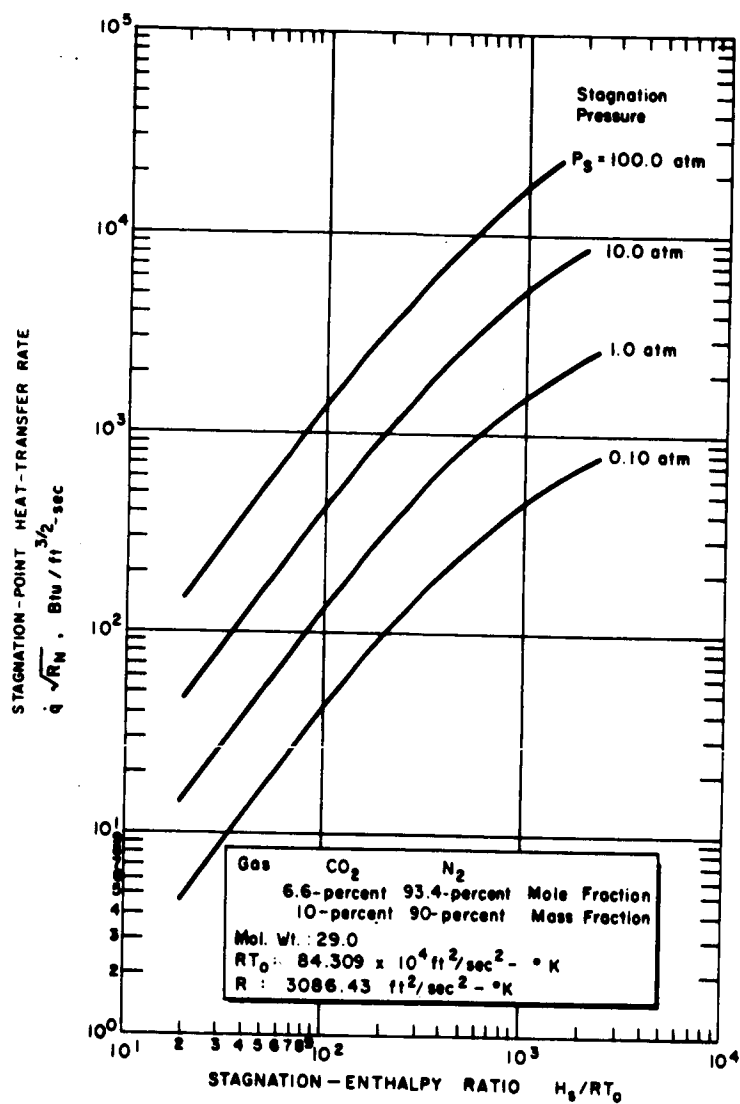
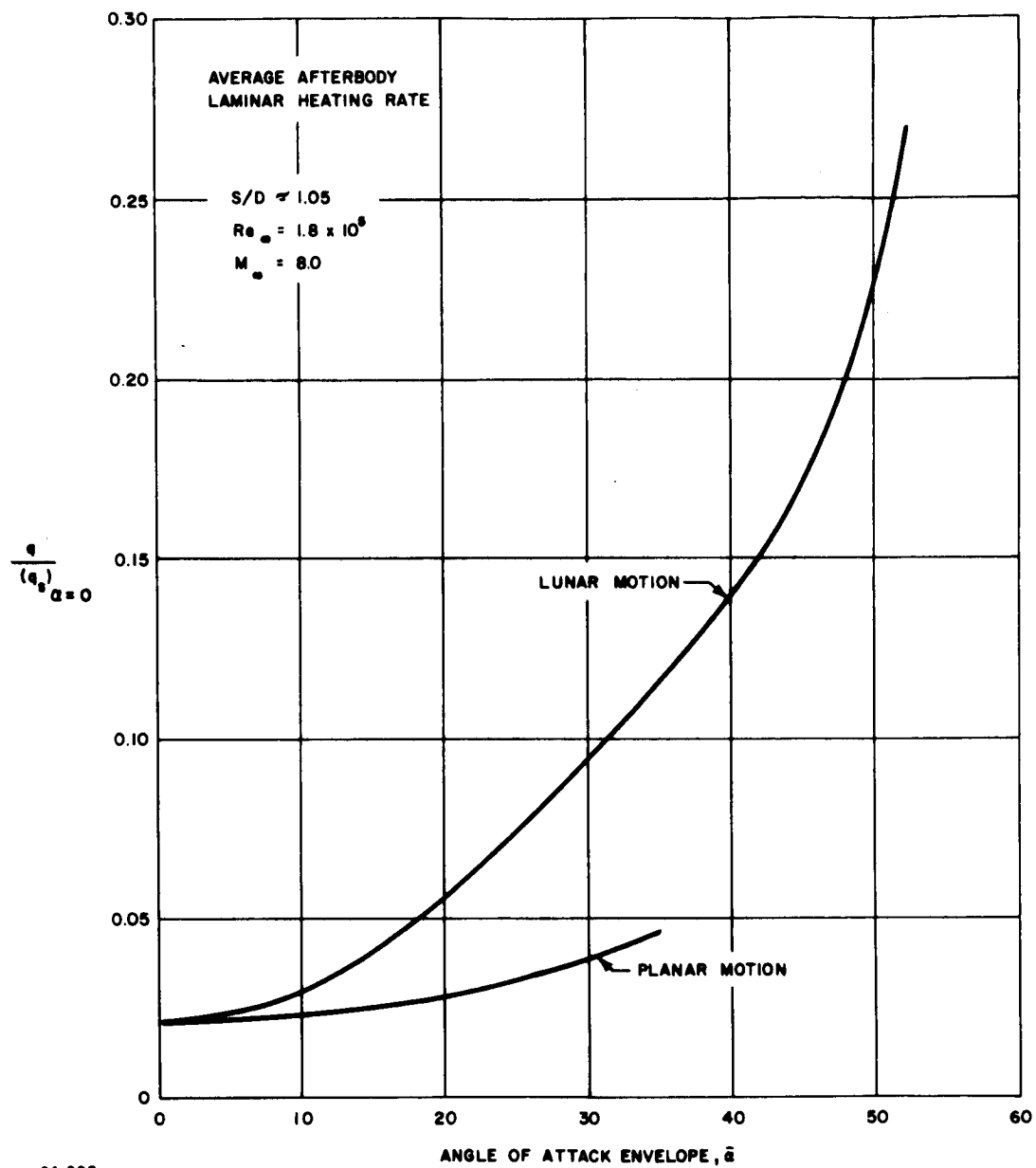


Figure I-10 CONVECTIVE HEATING AT A STAGNATION POINT (10-PERCENT CO<sub>2</sub> AND 90-PERCENT N<sub>2</sub>)



64-223

Figure I-11 EFFECT OF DYNAMICS ON CONVECTIVE HEATING



## 5. Radiative Heating

### a. Symbols

$A_s$	Surface area of the radiating volume
$B$	Planck's blackbody function
$c$	Speed of light
$C_i, T_i, n_i$	Empirical constants determined from shock tube experiments and theoretical considerations
$d_n$	Degeneracy of the absorbing state
$E$	Radiative power
$f_e$	Electronic oscillator strength for absorption
$h$	Planck's constant
$I$	Radiant intensity
$I_{BB}$	Blackbody intensity
$K$	Mass absorption coefficient
$N_i$	Number of molecules or atoms of species $i$ or the concentration of absorbing molecules
$q_r$	Radiative heat rate (Btu/ft <sup>2</sup> -sec)
$r_o$	Classical electron radius
$T$	Temperature of the slab
$V$	Flight velocity
$x_i$	Fraction of molecules in the absorbing state
$Z$	Geometrical variable normal to the body
$\delta$	Shock detachment distance
$\theta$	Angle between the normal to the plane and each ray; also, azimuthal angle to the normal.

$\mu$	Reduced mass of the molecule
$\nu_{0,0}$	Wave number of the (0,0) vibration transition
$\nu$	Frequency in wave numbers
$\xi$	Flux radiated per unit volume and distance normal to the surface
$\rho$	Density
$\sigma$	Stefan-Boltzman constant
$\tau_\lambda$	Optical thickness

#### Subscripts

b	Conditions at the body
E	Equilibrium conditions
NE	Nonequilibrium conditions
RAD	Includes equilibrium and nonequilibrium effects
p	Peak value
s	Stagnation point conditions
w	Shock wave conditions
$\infty$	Free stream conditions

#### b. General Equation of Radiative Transfer

In a gaseous medium of low density such as that found in the region behind the shock wave of an entry vehicle, the scattering of radiative energy may be neglected. Therefore, a pencil of radiation traversing this medium will be weakened only by absorption by the molecules in its path. We may define the absorption coefficient  $K_\lambda$  as the expected number of absorptions which will occur between photons and the atmosphere per unit path length of travel. The emission coefficient  $j_\lambda$  may be defined as the amount of energy that will be emitted from an element of mass into a solid angle in the wavelength interval  $(\lambda, \lambda + d\lambda)$ . If we assume that the conditions are such that we can define at each point in the radiating volume a local temperature  $T$ , then by Kirchoff's law we have:

$$j_{\lambda} = K_{\lambda} B_{\lambda}(T) . \quad (40)$$

The change in intensity across a small cylinder of height  $ds$  and cross section  $d\sigma$  in the wavelength interval  $(\lambda, \lambda + d\lambda)$  in time  $dt$  and confined to a unit solid angle  $d\omega$  is:

$$\frac{dI_{\lambda}}{ds} d\sigma d\lambda d\omega dt ,$$

The energy difference is due to a rate of emission greater than that of absorption.

The amount of energy absorbed will be

$$K_{\lambda} ds I_{\lambda} d\lambda d\sigma d\omega dt$$

while the amount emitted is:

$$j_{\lambda} d\sigma ds d\lambda d\omega dt ,$$

taking an energy balance

$$\frac{dI_{\lambda}}{ds} = -K_{\lambda} I_{\lambda} + j_{\lambda} . \quad (41)$$

Combining equations (40) and (41)

$$- \frac{dI_{\lambda}}{ds} \frac{1}{K_{\lambda}} = I_{\lambda} - B_{\lambda}(T) . \quad (42)$$

### c. Plane Parallel Slab Approximation

If we assume that the volume of radiating gas is that of a plane parallel slab of finite thickness and of infinite extent, equation (42) may be written:

$$\mu \frac{dI_{\lambda}(\tau_{\lambda}, \mu, \phi)}{d\tau_{\lambda}} = I_{\lambda}(\tau_{\lambda}, \mu, \phi) - B_{\lambda}(\mu, \phi) \quad (43)$$

where:

$$\mu = \cos \theta$$

$\theta$  = the angle between the normal to the plane and each ray

$\tau_\lambda$  = the optical thickness as defined by:

$$\tau_\lambda = \int_Z^0 K_\lambda dz \quad .$$

The physical situation which is to be described is that of a radiating volume of gas supplying the radiative heat flow to an entry vehicle. This radiating volume is approximated by the plane parallel slab described above. Defining a positive and negative direction from a plane within the parallel layer, the solution to equation (43), assuming that the intensity at both boundaries is 0, is: (e. g. see reference I-31)

$$I(\tau, +\mu, \phi) = \int_{t=\tau}^{\tau_1} B e^{-(t-\tau)/+\mu} \frac{dt}{+\mu} \quad (44)^*$$

$$I(\tau, -\mu, \phi) = \int_{t=0}^{\tau} B e^{-(\tau-t)/-\mu} \frac{dt}{-\mu} \quad (45)$$

Defining the radiative heat flux as the net flow of radiation across a unit area

$$F = \int_{\Omega} I \cos \theta d\Omega \quad (46)$$

\*For simplicity, the  $\lambda$  subscripts will be suppressed for the remaining portion of the analysis.

where  $\Omega$  is the solid angle or:

$$F = \int_0^{2\pi} \int_0^{\pi/2} I \cos \theta \sin \theta d\theta d\phi$$

$$F = 2\pi \int_0^1 I_\mu d\mu \quad (47)$$

The net flux may be divided into the flow of energy in the positive and negative Z directions across a unit area at  $Z = r$  thus:

$$F = F_+ - F_- \quad (48)$$

substituting equation (44) and (45) into equation (47)

$$F_+(\tau) = 2\pi \int_{t=\tau}^{\tau} \int_{\mu=0}^1 B \int_{\mu=0}^1 e^{-(t-\tau)/+\mu} d\mu dt \quad (49)$$

$$F_-(\tau) = 2\pi \int_{t=0}^{\tau} B \int_{\mu=0}^{-1} e^{-(\tau-t)/-\mu} d\mu dt \quad (50)$$

Using the exponential integral  $E_n(x)$  for a positive real argument,

$$E_n(x) = \int_0^1 e^{-x/\mu} \mu^{n-1} \frac{d\mu}{\mu} .$$

We may rewrite equation (49) and (50) as:

$$F_+ (\tau) = 2\pi \int_{t=\tau}^{\tau_1} B E_2 (t - \tau) dt \quad (51)$$

$$F_- (\tau) = 2\pi \int_{t=0}^{\tau} B E_2 (\tau - t) dt . \quad (52)$$

Since the temperature throughout the volume is assumed to be constant, the Planck intensity function is a constant and may be written:

$$B = \frac{\sigma T^4}{\pi} .$$

Combining equations (48), (51), and (52):

$$F (\tau) = 2\sigma T^4 \left[ \int_{t=\tau}^{\tau_1} E_2 (t - \tau) dt - \int_{t=0}^{\tau} E_2 (\tau - t) dt \right] . \quad (53)$$

Since we desire the flow of energy across the boundary at  $Z = 0$ ,

$$F (0) = 2\sigma T^4 \int_{t=0}^{\tau_1} E_2 (t) dt . \quad (54)$$

Noting that  $\frac{d}{dx} E_{n+1} (x) = - E_n (x)$  (ref. I-31),

then:

$$F(0) = 2\sigma T^4 \int_{t=0}^{\tau_1} -\frac{d}{dt} E_3(t) dt = 2\sigma T^4 \int_{t=\tau_1}^0 \frac{d}{dt} E_3(t) dt$$

$$F(0) = 2\sigma T^4 [E_3(0) - E_3(\tau_1)] = \sigma T^4 (1 - 2E_3(\tau_1)) \quad (55)$$

where  $E_3(0) = 1/2$ .

The flux has been defined as the flow of radiant energy across a unit area. Therefore,  $F(0)$ , in the physical situation being described, is the heat flux to a unit area of a vehicle whose tangent plane is the plane at  $Z = 0$ .

$$F(0) = q_R = \sigma T^4 [1 - 2E_3(\tau_1)] \quad (56)$$

Using the recursion formular for  $E_n(x)$

$$n E_{(n+1)}(x) = e^{-x} - x E_n(x)$$

$$q_R = \sigma T^4 [1 - e^{-\tau} + \tau E_2(\tau)] \quad (57)$$

This is the exact solution to equation (43) where the gas is at a constant temperature and density. The approximations that were made in reference I-32 will now be made in order to compare the solutions.

If  $\tau \ll 1$ ; we may expand  $e^{-\tau}$  and neglect the higher order terms

$$q_R \simeq \sigma T^4 \tau [1 + E_2(\tau)] \quad (58)$$

Since  $E_2(\tau)$  approaches 1.0 as  $\tau$  approaches 0, equation (58) can be approximated by:

$$q_R \simeq \sigma T^4 2\tau \quad (59)$$

or spectrally:

$$q_R(\lambda) \approx 2\tau \frac{2\pi h c^2}{\lambda^5} \left( e^{+hc/kT\lambda} - 1 \right)^{-1} . \quad (60)$$

One other factor has to be considered in equation (60). Returning to the expression of Kirchoff's Law (equation (40)), it should be noted that the emission coefficient  $j$  includes the induced emission while also depending on the incident intensity. To account for this induced emission, the absorption coefficient should be multiplied by the factor  $(1 - e^{(-hc/kT\lambda)})$ .

A detailed argument for accounting for the induced emission in this manner may be found in reference I-33. Equation (60) now becomes:

$$q_R(\lambda) \approx 2Kl \frac{2\pi h c^2}{\lambda^5} e^{-hc/kT\lambda} . \quad (61)$$

Equation (60) is the heat flux to a unit area of a body from a plane parallel slab under the assumption of an optically thin gas. Equation 1 of reference I-32 is assumed to be the solution to the same physical situation. This assumption can be tested by comparing the two equations.

Inserting  $\sigma = \frac{2\pi^5 k^4}{15 h^3 c^2}$  into equation 1 of reference I-32 and changing from frequency to wavelength, the following equation results:

$$\frac{dI}{d\lambda} = 2Kl \frac{2\pi c^2 h}{\lambda^5} e^{-hc/kT\lambda} . \quad (62)$$

It is seen that equation (62) is identical to equation (60), thus the quantity  $\frac{dI}{d\lambda}$  in reference I-32 is the radiative heat flux  $q_R$  as has been defined above. In the case of a constant temperature and density, the absorption coefficient is constant. Therefore, the optical thickness may be written as:

$$\tau = Kl \quad (63)$$



Substituting this in equation (59) the following equation results

$$q_R = 2 K' l \sigma T^4 \quad (64)$$

where  $K'$  is the absorption coefficient reduced by the induced emission  
 $K' = K(1 - e^{-hc/KT_\lambda})$  (65)  
 and averaged over all wavelengths.

Then

$$\frac{q_R}{l \sigma T^4} = 2 K' \quad (66)$$

The right side of equation (65) is defined equal to  $(\frac{\epsilon}{L})$  in reference I-32. Tables of this quantity are listed in reference I-32 and these are the values that are almost exclusively used, at the present, to compute radiant heating. From this definition, and equation (65), it follows that

$$\frac{\epsilon}{L} = \frac{q_R}{l \sigma T^4} = 2 K' \quad (67)$$

#### d. Radiation Model

Calculations of the equilibrium radiative heat flux for the variety of vehicle shapes, entry conditions, and atmospheric models of this study, were carried out using the following equations and assumptions.

Any attempt to compute a radiative heat flux must deal with both the macroscopic or geometric aspects of the transfer of radiant energy and the microscopic or absorption and emission of the radiant energy by the individual molecules or atoms.

With respect to the macroscopic aspect of the radiant transfer, the so-called "plane parallel" approximation was used. This consists of replacing the actual curved shock layer by a slab of radiating gas having a thickness equal to the detachment distance of the shock in a direction normal to the vehicle surface and extending to infinity perpendicular to this normal. For blunt nosed vehicles of the type considered in this study, the plane parallel layer geometry is a good approximation. This is because the radiation from the "wings" of the slab is attenuated to some extent by the intervening layer of gas and the radiant flux absorbed by the vehicle has a cosine dependence. The reason for the use of the plane parallel slab approximation is the simplification that it introduces into the transfer equation.

The appropriate equation for the above case is defined as:

$$-\cos \theta \frac{dI}{d\tau} = K [I - B] \quad (68)$$

and

$$r = \int_Z^{\delta} K dz \quad (69)$$

$\delta$  is the detachment distance

$Z$  is the geometric variable normal to the body.

From the definition of the intensity ( $I$ ), the radiant flux crossing a unit area is

$$q_R = \int_{\Omega} I \cos \theta d\Omega \quad (70)$$

where:

$\Omega$  is the solid angle.

Solving equations (68), (69), and (70) with the additional restrictions that the temperature and density in the slab be constant results in

$$q_R = \sigma T^4 [1 - 2 E_3(\tau)] \quad (71)$$

where:

$$E_3(\tau) = \int_0^1 e^{-\tau/\mu} \mu d\mu \quad (72)$$

and

$\sigma$  is the Stephan-Boltzmann constant

T is the temperature of the slab.

Equation (71) is the equation used in the present study. Note that it accounts for absorption.

The microscopic aspect of radiation has to be appealed to in order to obtain values of the mass absorption coefficient K. There are two processes of emission and absorption of radiation; that due to the rotational, vibration, and electronic transitions in molecules, and the Kramer's radiation in atoms. A number of mathematical models have been formulated for the absorption coefficient for molecules (see ref. I-34). For the molecular species and temperatures of interest, the different models give essentially the same results. The one large uncertainty in all these models is the value of the electronic oscillator strength,  $f_e$ , which is defined as:

$$f_e = \frac{8\pi^2 \mu c}{3h d_n} \tilde{\nu} |R_e(r)|^2 \quad (73)$$

where

$\mu$  is the reduced mass of the molecule

$c$  is the speed of light

$h$  is Planck's constant

$\tilde{\nu}$  is the frequency in wave numbers

$d_n$  is the degeneracy of the absorbing state.

The quantity  $R_e(r)$  is the electronic transition moment and for many molecules varies for the different vibrational transitions. This quantity could, in theory, be calculated from quantum mechanical considerations, but in practice the complexity and number of the calculations render such a process impossible. Therefore, the value of  $f_e$  is obtained from experimental measurements of the intensity or of the radiative lifetime of the excited molecule. Both of these experimental methods are difficult and result in uncertainties in the electronic oscillation strength. These, in turn, are reflected in the absorption coefficient.

Presently, Kramer's free-free radiation is on a fairly firm basis but the free-bound is not. Most calculations of the free-bound Kramer's radiation have used a formula postulated by Unsold (ref. I-35). Recently Biberman and Norman (ref. I-36 and I-37) have obtained corrections for the Unsold formula using the quantum defect method of Burgess and Seaton (ref. I-38).

Kivel and Bailey (reference I-32) have presented an empirical equation for the emissivity per unit length whose form has been dictated by the reasoning of references I-34 and I-35. This equation gives the emissivity per unit length of a plane parallel slab of gas at a constant temperature and density. From the previous arguments, it may be seen that for a plane parallel slab, the relation between the absorption coefficient  $K$  and the emissivity per unit length  $\epsilon/L$  is:

$$K = \frac{1}{2} \frac{\epsilon}{L} \quad (74)$$

The expression for the absorption coefficient used in the present study uses equation (74) combined with the equation presented in reference I-32.

$$K = 1/2 C_i \left( \frac{N_i}{5.4 \times 10^{19}} \right) \frac{e^{-T_i/T}}{(T \times 10^{-4})^{n_i}} \quad (75)$$

where

$N_i$  is the number of molecules or atoms of species  $i$

and

$C_i$ ,  $T_i$  and  $n_i$  are empirical constants determined from shock tube experiments and theoretical considerations.

The values of  $C_i$ ,  $T_i$  and  $n_i$  listed in reference I-32 were used in this study with several exceptions. The primary differences lie in the treatment of the cyanogen, carbon dioxide, and  $N_2^+$  bands. The results of Fairbairn (ref. I-39) were used for the cyanogen, wherein values for the oscillator strength of CN red, ( $A^2 \pi \rightarrow X^2 \Sigma$ ) (red) and CN violet, ( $B^2 \Sigma \rightarrow X^2 \Sigma$ ) were suggested as  $f = 0.0068$  and  $f = 0.032$ , respectively. However, it should be noted these values are appropriate only if the lower estimate of  $D_0 = 7.6$  ev, the dissociation energy for cyanogen, is used. The value for the red system may be low due to the incomplete spectrum from which it was measured.

Several CO<sub>2</sub> bands were investigated by evaluating their Franck-Condon factors and determining the form of the spectral absorption coefficient. Approximate curve fits were then obtained in a form similar to that used by Kivel and Bailey. Finally, the oscillator strengths were estimated by use of the data of James (ref. I-40) for CO<sub>2</sub> mixtures. Only the dominant band system  $a^3\pi - X^1\Sigma^+$  was used in the study.

The N<sub>2</sub><sup>+</sup> band system was modified as detailed analysis of the Franck-Condon factors and of the vibrational and rotational transitions yielded emissivities considerably higher than predicted by reference I-32. The analysis is discussed in section B.6. If the oscillator strength of reference I-32 for N<sub>2</sub><sup>+</sup> is correct, then the estimates made indicate that the radiation may be four to six times larger than predicted by reference I-32. A conservative estimate of the N<sub>2</sub><sup>+</sup> band system was used, being six times the value given by reference I-32.

A tabular summary of the emissivity expressions used in this study is given in table I-20.

#### e. Nonequilibrium Heating

At the present time, methods for estimating the equilibrium radiant heat flux exist. On the other hand, there is not any satisfactory analytical method for estimating so-called nonequilibrium radiant heating.

First, due to the confusion resulting from the association of the term nonequilibrium radiation with nonequilibrium chemical effects, a brief discription of nonequilibrium radiation is deemed appropriate.

When an ambient gas is disturbed by a high-velocity strong shock wave, the energy is initially transmitted to the molecules in the ambient gas in the form of translational and rotational energy, after which the electronic energy states are quickly excited. It is only after these excited molecules have experienced a large number of collisions that the vibrational modes are excited. This distribution of the energy takes a finite amount of time, called the relaxation time, which varies for different molecular species. Another phenomena takes place during this time, the dissociation and recombination of a portion of the molecules present. Both of these phenomena act to produce the nonequilibrium radiation in the following way:

When a molecule is acted upon by a shock wave, its electronic states initially have a disproportionately large amount of energy for the reasons discussed above. This excess energy in the electronic states is a consequence of the higher vibrational states of the molecule not yet being excited. This means that more molecules will populate the

TABLE 1-20

TABLE OF CONSTANTS FOR THE EMISSIVITY EXPRESSIONS

$$\frac{\epsilon_i}{L} = C_i \left( \frac{N_i}{5.4 \times 10^{19}} \right) \frac{e^{-T_i/T}}{(T \times 10^{-4})^{n_i}}$$

Species (i)	$C_i$ (cm <sup>-1</sup> )	$T_i$ (°K)	$n_i$
O <sub>2</sub> S-R	$1 \times 10^4$	70,500	5
NO $\beta + \gamma$	$1 \times 10^3$	65,000	5
N <sub>2</sub> 2nd pos.	$2 \times 10^5$	129,500	4
N <sub>2</sub> 1st pos.	$1.5 \times 10^3$	90,000	4
CN Red	$2.34 \times 10^2$	13,000	4
CN Violet	$3.2 \times 10^3$	36,000	4
NO vibration - rotation	$4 \times 10^{-4}$	2,700	4
CO <sub>2</sub>	$9 \times 10^3$	96,000	4
CO	$3.6 \times 10^2$	70,000	4
O	$2.2 \times 10^5$	158,000	3
N	$1.2 \times 10^6$	169,000	3
NO	$8.4 \times 10^4$	108,000	3
O <sub>2</sub>	$6.0 \times 10^5$	145,000	3
N <sub>2</sub>	$1.1 \times 10^6$	180,000	3
N <sup>+</sup>	$2.9 \times 10^6$	343,000	3
O <sup>+</sup>	$1.1 \times 10^7$	407,000	3
C	$3.1 \times 10^5$	131,000	3
C <sup>+</sup>	$0.66 \times 10^5$	282,000	3
N <sub>2</sub> <sup>+</sup>	$6.0 \times 10^4$	36,000	4
A	$1 \times 10^7$	183,000	3
A <sup>+</sup>	$1.8 \times 10^6$	318,000	3

higher electronic states than an equilibrium Boltzmann distribution would predict. Since, in many cases, the average time for a molecule to change to a more stable lower electronic state by means of radiating away the excess energy is less than the vibrational relaxation time, an excess of radiation over the equilibrium amount will result during this period. Chemical dissociation and recombination also require a finite time to reach equilibrium. Since the intensity of radiation from a molecule is greater than from an atom at the same temperature, and since the ratio of molecules to atoms is greater before than after chemical equilibrium has been reached behind the shock, there will also be an excess of radiation due to the additional molecules present. The "overshoot" radiation above the equilibrium radiation due to both these phenomenas is called the nonequilibrium radiation. From this brief discussion, some of the difficulties in formulating an analytical approach may be appreciated. Chief among these difficulties is that the relaxation times, rate of relaxation, and the chemical rate constants are either not known or are known only approximately at the high temperatures of interest.

From the brief introduction given above, an important fact may be deduced about nonequilibrium radiation. That is, it is a function of time. In the case of a vehicle descending through an atmosphere, the radiation may be thought of as originating from a number of infinitesimal slabs of gas traveling from the shock to the vehicle with the velocity of the vehicle. Therefore, the nonequilibrium region may be transformed from a time to a space coordinate. In other words, in the shock layer, the thickness of the nonequilibrium layer is a function of the relaxation times, the rate of chemical reaction, and the velocity of the vehicle. Since, for a given molecular or atomic specie, the relaxation time and reaction rate depend on the available energy (vehicle velocity) and the number of molecules present, the thickness of the nonequilibrium layer may be reduced to a function of the ambient pressure and the velocity of the vehicle. This simple dependance is pointed out in reference I-42 in which the results of a number of shock tube experiments are interpreted. In that report, the nonequilibrium thickness for shock-heated air is presented as a function of ambient pressure and shock velocity. These results have been correlated and extrapolated, and a simple model formulated.

The nonequilibrium thickness is defined as the distance from the bow wave to the point where the nonequilibrium radiative intensity is within 10 percent of the equilibrium intensity. The correlation obtained from reference I-42 is

$$\delta_{NE} = \frac{2.3 \times 10^{-6}}{\rho_{\infty} \left( \frac{V_{\infty}}{10^4} \right)^{4.3}} \quad (76)$$

where

$\delta_{NE}$  = nonequilibrium thickness (feet)

$\rho_{\infty}$  = ambient density (slug/ft<sup>3</sup>)

$V_{\infty}$  = flight velocity (ft/sec).

The distance to the peak nonequilibrium intensity,  $\delta_p$ , was also correlated as

$$\delta_p = \frac{0.23 \times 10^{-6}}{\rho_{\infty} \left( \frac{V_{\infty}}{10^4} \right)^{3.3}} \quad (77)$$

Using equations (76), and (77), a calculation model was evolved based on the estimated radiative pulse shape shown in figure I-12.

The total radiation flux to the body, assuming an optically thin slab can now be written as

$$\begin{aligned} q_{RAD} &= q_E \left[ 1 - \frac{1}{2} \frac{\delta_p}{\delta} - \frac{1}{2} \frac{\delta_{NE}}{\delta} + \frac{I_{NE}}{I_E} \frac{\delta_{NE}}{2\delta} \right] ; \delta > \delta_{NE} \\ q_{RAD} &= q_E \left[ 1 - \frac{1}{2} \frac{\delta_p}{\delta} - \frac{1}{2} \frac{\delta_{NE}}{\delta} + \frac{I_{NE}}{I_E} \frac{\delta_{NE}}{2\delta} - \frac{1}{2} \frac{(\delta_{NE} - \delta)^2}{(\delta_{NE} - \delta_p)\delta} \left( \frac{I_{NE}}{I_E} - 1 \right) \right] ; \delta_p < \delta < \delta_{NE} \\ q_{RAD} &= \frac{q_E}{2} \frac{I_{NE}}{I_E} \frac{\delta}{\delta_p} ; \delta < \delta_p \end{aligned} \quad (78)$$

where

$q_{RAD}$  = total radiative heat flux (Btu/ft<sup>2</sup>/sec)

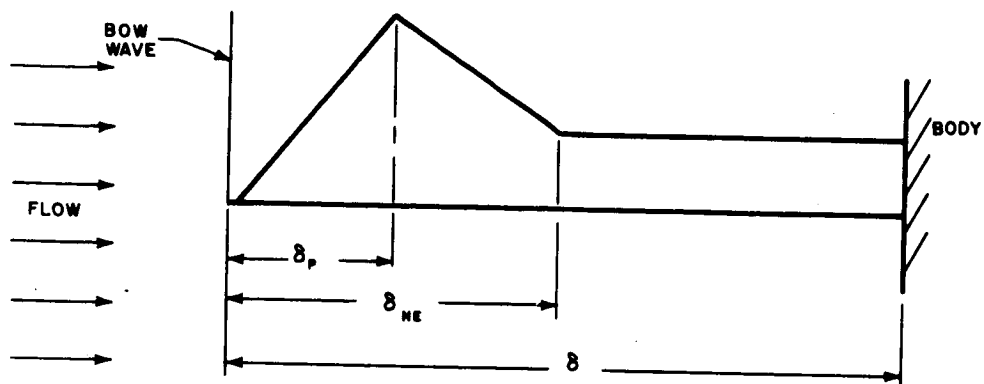
$q_E$  = equilibrium radiative heat flux (Btu/ft<sup>2</sup>-sec).

(For an optically thin gas,  $q_E = \left( \frac{I_E \delta}{2} \right)$ ).

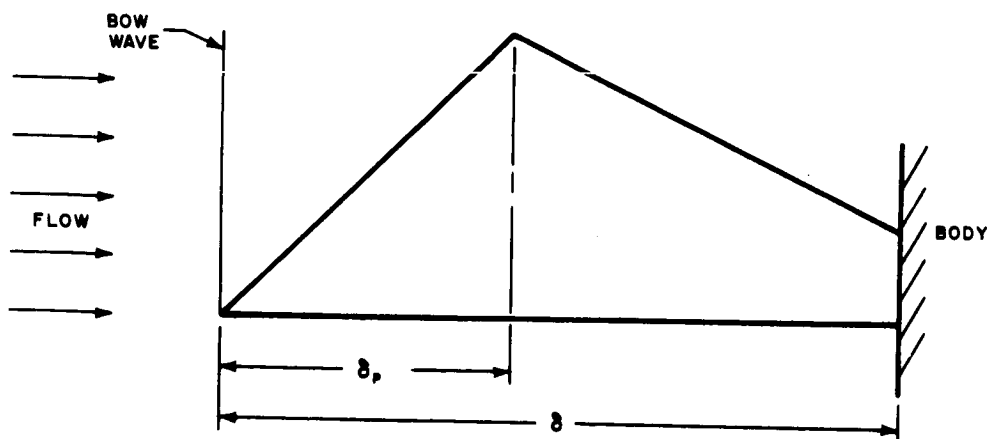
Data on the ratio of  $I_{NE}/I_E$  have been summarized by Page (ref. I-43), and a value of 10 appears to bound the bulk of the data.

#### f. Radiation Distributions





A. PULSE MODEL WITH NO TRUNCATION



B. PULSE MODEL WITH TRUNCATION

64-224

Figure I-12 RADIATIVE HEAT PULSE MODEL

The computation of the radiative heating component at other stations about the vehicle than the stagnation point was done under the following assumptions:

- 1) The gas cap volume can be approximated by an optically thin, one dimensional slab of gas lying tangent to the body with a thickness equal to the shock layer at that point.
- 2) The distribution of the radiation across the gas layer is given by a second degree polynomial

$$I = I_b + K_1 \xi + K_2 \xi^2 \quad (79)$$

where

$\xi$  is the distance normal to the surface

$I$  is the radiation intensity

$I_b$  is the radiation intensity at the body.

The first coefficient  $K_1$ , relates the rate of change in intensity normal to the surface. In general the pressure and enthalpy gradients normal to the surface can be given as

$$\frac{\partial P}{\partial \xi} = \frac{\rho_b V_b^2}{R_{cb}} \quad (81)$$

$$\frac{\partial h}{\partial \xi} = T \frac{\partial S}{\partial \xi} + \frac{V_b^2}{R_{cb}} \quad (82)$$

Since the entropy gradient is negative, the enthalpy gradient will always be negative on blunt, conical bodies. The radiative intensity being much more sensitive to enthalpy than to pressure, it was therefore assumed that a conservative estimate on the radiative heating would result if the enthalpy gradient normal to the surface was taken as zero. Consequently,  $K_1$  in equation (79) is zero.

The second coefficient is now found by determining the local shock angle, so that

$$I = I_b + (I_w - I_b) \frac{\xi^2}{\delta_{wb}^2} \quad (83)$$

Rather than solve the oblique shock equations, a normal shock solution with a normal velocity of  $V_N = V_\infty \sin \theta_w$  was used. This also results in conservatism when the shock is weak, but in which case the radiation is negligible.

The radiation to the body is found by integrating equation (81), yielding

$$q_{Rb} = \left( \frac{2}{3} I_b + \frac{1}{3} I_w \right) \frac{\delta_{wb}}{2} \quad (84)$$

Equation (84) was used to obtain the radiation heating distributions. The necessary inputs are the shock shape and pressure distribution about the body. The intensity at the body was found from a knowledge of the stagnation point conditions using the gas dynamic computation, described earlier, and the pressure distribution. The enthalpy distribution is found by the isentropic relationship,

$$\frac{dh}{h} = - \frac{P}{\rho h} \frac{dP}{P}$$

or

$$\frac{d \ln h}{d \ln P} = \frac{\gamma - 1}{\gamma} \quad (85)$$

Assuming  $\frac{\gamma - 1}{\gamma}$  is constant around the body,

$$\frac{h}{H_s} = \left( \frac{P}{P_s} \right)^{\frac{\gamma - 1}{\gamma}} \quad (86)$$

For a strong shock,

$$\frac{P_s}{P_\infty} = \frac{\gamma + 1}{\gamma - 1} \quad (87)$$

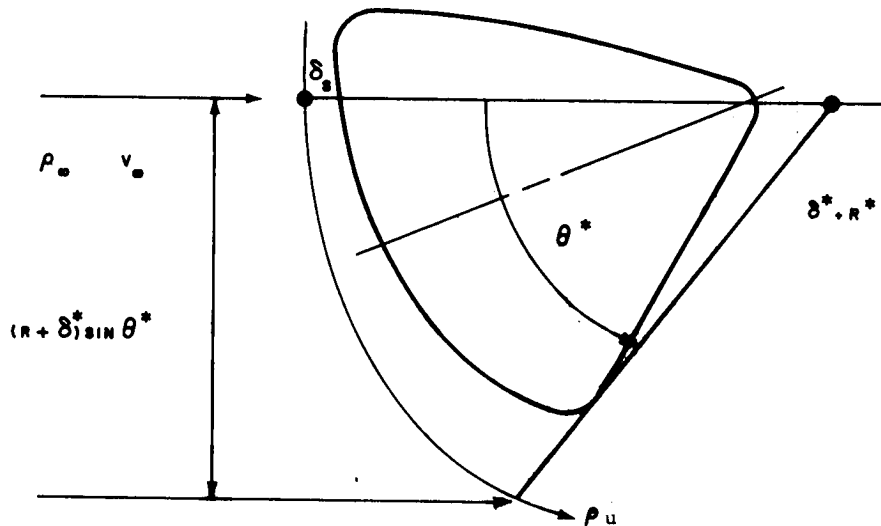
or

$$\frac{\gamma - 1}{\gamma} = \frac{2}{\frac{P_s}{P_\infty} + 1} \quad (88)$$

The stagnation density ratio is computed from the gas dynamics calculations, and therefore  $\left(\frac{\gamma-1}{\gamma}\right)$  is known.

To compute the radiative heating distributions, a shock shape is needed. Vinokur's results (ref. I-27) were used at zero angle of attack at the stagnation point, evaluating the nose bluntness parameters (b) and (a) in the same manner as for the stagnation point convective heating. For the shapes with large forecone angles, the schlieren photographs supplied by JPL were used to correlate the standoff distance with nose shape. The effect of density ratio was then accounted for by Vinokur's results.

The standoff distance at the sonic point was determined from a mass balance using a similar approach as in reference I-31 Referring to the sketch below:



The shock was approximated by a spherical section from the stagnation to the sonic point. The mass flow into the shock is estimated by

$$W = \frac{\rho_{\infty} V_{\infty}}{2} (R^* + \delta^*) \sin \theta^*$$

as shown in the above sketch. The mass flow distribution across the shock layer was fitted with a polynomial. A fourth-order polynomial was found to predict standoff distances in good agreement with available experimental shock shapes. The resultant mass flow distribution is then

$$\overline{\rho u} = \frac{4}{5} \rho_e u_e + \frac{1}{5} \rho_w u_w$$

where  $\rho_w, u_w$  are conditions at the shock. Since the shock conditions are dependent on shock angle, an iterative solution is required. The standoff distance at the sonic point is then given by

$$\delta^* = \frac{R^* \sin \theta^*}{2 \left( \frac{\overline{\rho u}}{\rho_\infty V_\infty} \right) - \sin \theta^*}$$

Having solved for  $\delta^*$  and the corresponding wave angle, the complete shock was determined using the form

$$y^2 = Ax + Bx^2$$

For configurations which consisted of spherically blunted cones, it was possible to use a more simple solution for the shock shape between the stagnation and sonic points.

The method is described in reference I-30. This method is applicable when the sonic points remain on the spherical portion of the nose. The stagnation point shock standoff distance used in conjunction with this method was determined from Vinokur's results. For angles of attack for which the sonic points were not on the spherical nose, the sonic point shock standoff distance was determined as described above.

## 6. Heating Block Evaluation

### a. Evaluation of Radiant Heating Calculations

A comparison has been made between the gas emissivities computed and more exact theoretical methods in order to establish the degree

of confidence expected. The equation used to compute the gas emissivity per unit path length is that presented by Kivel and Bailey, (ref. I-32)

$$\frac{\epsilon}{L} = C_i \left( \frac{N_i}{5.4 \times 10^{19}} \right) \frac{e^{-T_i/T}}{(T \times 10^{-4})^{n_i}} \quad (89)$$

where

$N_i$  = the number of molecules or atoms of species  $i$

$C_i$ ,  $T_i$  and  $n_i$  are empirical constants determined from shock tube experiments and theoretical considerations.

The theoretical models that are used to evaluate the accuracy of equation (89) may be divided into two groups. The first set of equations to be considered is that which computes the emissivity of diatomic molecules; the second group includes the models that evaluate the Kramer's radiation from atoms and ions.

#### 1) Diatomic molecules

The following set of equations developed by Kivel, et al (ref. I-32) were used for comparison with equation (89) for the diatomic molecules of interest. The spectral absorption coefficient is given by:

$$K_\lambda = \pi r_o f_e N_i X_i \phi \frac{hc}{kT} \exp - \left[ \frac{hc}{kT} \left( \nu_{00} - \frac{1}{\lambda} \right) \right] \quad (90)$$

where

$r_o$  = the classical electron radius

$f_e$  = the electronic oscillator strength for absorption

$N_i$  = the concentration of the absorbing molecules

$x_i$  = the fraction of molecules in the absorbing state

$\nu_{00}$  = the wave number of the (0, 0) vibration transition

and

$$\phi = \frac{k T}{h c} \frac{1}{Q_v'' Q_r'' |B_e' - B_e''|} \sum_{\epsilon_r' \geq 0} q_{v'v''} \exp - \left[ \frac{\epsilon_v' - \epsilon_r'}{k T} \right]$$

where

$$Q_v'' = \left[ 1 - \exp - \left( \frac{h c \omega_e''}{k T} \right) \right]^{-1} \text{ is the vibrational partition function}$$

for the absorbing state (the '' refers to the absorbing state and the ' refers to the emitting state).

$$Q_r'' = K T / h c B_e'' \text{ is the rotational partition function for the absorbing state.}$$

$$q_{v'v''} = \int \psi_{v'} \psi_{v''} dr \text{ is the Franck-Condon factor for the}$$

transition from  $v'$  to  $v''$

$$\epsilon_v' = h c \left( \frac{1}{\lambda_{v'}} - \frac{1}{\lambda_o'} \right) \text{ is the vibrational energy relative to}$$

the ground vibrational state for the emitting state

$$\epsilon_r' = (B_e' / B_e' - B_e'') h c \left( \frac{1}{\lambda} - \frac{1}{\lambda_{v'v''}} \right) \text{ is the rotational energy}$$

for the emitting state

$$\frac{1}{\lambda_v} = \omega_e (v + 1/2) - \omega_e x_e (v + 1/2)^2 + \omega_e y_e (v + 1/2)^3$$

is the wave number of the  $v$ th vibrational level

$$\frac{1}{\lambda_{v'v''}} = \nu_{00} + \left( \frac{1}{\lambda_{v'}} - \frac{1}{\lambda_o'} \right) - \left( \frac{1}{\lambda_{v''}} - \frac{1}{\lambda_o''} \right)$$

is the wave number for the vibrational transition between the states  $v'$  and  $v''$ .

$\omega_e$ ,  $\omega_e x_e$ ,  $\omega_e y_e$ ,  $B_e$  and  $\bar{\nu}_{00}$  are the basic molecular spectroscopic constants. The notation of Herzberg (ref. I-5) is used.

Since the geometry of equation (89) is that of a plane parallel layer of thickness  $L$ , we may relate the absorption coefficient  $K$  to the emissivity per unit length  $\epsilon/L$  as follows: The Planck radiation meanfree path  $\lambda_p$  is the reciprocal of the integrated absorption coefficient  $K$  and is given by:

$$\lambda_p = \frac{\int_{4\pi} I_{BB} d\omega}{\int_{4\pi} \xi d\omega} \quad (91)$$

where:

$I_{BB}$  is the blackbody intensity

$\xi$  is the flux radiated per unit volume

and

$\omega$  is the unit solid angle.

Thus,

$$\int_{4\pi} \xi d\omega = \frac{E A_s}{V} \quad (92)$$

where

$E$  = the radiative power

$A_s$  = the surface area of the radiating volume  $V$ .

Since the geometry is that of a plane parallel semi-infinite slab of thickness  $L$



$$\int_{4\pi} \xi \, d\omega = \frac{2\epsilon \sigma T^4}{L} \quad (93)$$

where

$\epsilon$  = the emissivity of the gas

$\sigma$  = the Stephan-Boltzman constant.

Therefore,

$$\lambda_p = \frac{1}{K} = \frac{4\sigma T^4}{2(\epsilon/L)\sigma T^4} = \frac{2}{(\epsilon/L)} \quad (94)$$

Equation (90) rests on a firmer theoretical basis than equation (89) since it takes into account the vibrational and rotational transitions of the molecule. Equation (89) attempts to account for these by the semi-empirical term  $\frac{C_i}{(T \times 10^{-4})^{n_i}}$ . In equation (90), the rotational structure is "smeared out" over each vibrational band. At the temperatures and pressures of interest, this is thought to be a good approximation. One difficulty with the smeared out approximation is that at very high temperatures the centers of the rotational lines of certain molecules reach the blackbody limit, while the "wings" of the line continue to radiate as predicted. The result of this is that equation (90) would over predict the radiation for this case. One more qualification which applies both to equations (89) and (90) should be mentioned. The electronic oscillator strength,  $f_e$ , which is contained explicitly in equation (90) and implicitly in equation (89), is a quantity which must be determined independently through experiment. Due to the difficult nature of these experiments, there is an uncertainty in the value of  $f_e$  for many of the diatomic molecules of interest. Also,  $f_e$  varies somewhat with the different vibrational transitions. Unfortunately, experimental data on this variation are sketchy.

A comparison of the emissivity per unit length for the diatomic molecules of interest computed by means of equation (89) and by means of equations (90) and (94) are given in table I-21. The comparisons are presented for three temperatures and pressures which are typical of the range of interest for the peak radiant heating for a Mars or Venus entry. The atmospheric composition that was chosen was:  $X_{N_2} = 0.889$ ,  $X_{CO_2} = 0.1$ ,  $X_{O_2} = 0.001$ ,

TABLE I-21

## COMPARISON OF IMPROVED AND APPROXIMATE RADIATION THEORIES

Species	Temperature (°K)	$N_1$ $5.4 \times 10^{19}$	$f_e$	$\epsilon/L$ Improved Equation (90)	$\epsilon/L$ Approximate Equation (89)	<u>Improved</u> <u>Approximate</u>
CN	11312	1.142 (-7)*	0.027	7.62 (-6)	7.73 (-6)	0.98
(Violet)	9882	1.139 (-5)		8.14 (-4)	8.36 (-4)	0.97
	6632	2.169 (-4)		1.19 (-2)	1.32 (-2)	0.90
CN	11312	1.142 (-7)	0.027	2.25 (-6)	2.95 (-6)	0.84
(Red)	9882	1.139 (-5)		3.38 (-4)	4.26 (-4)	0.79
	6632	2.169 (-4)		1.73 (-2)	2.11 (-2)	0.82
NO	11312	1.203 (-7)	0.008	4.90 (-7)	6.58 (-7)	0.75
( $\beta$ )	9882	8.613 (-6)		2.87 (-5)	4.03 (-5)	0.71
	6632	3.931 (-4)		3.09 (-4)	5.38 (-4)	0.57
NO	11312	1.203 (-7)	0.001	1.07 (-7)	8.22 (-8)	1.30
( $\gamma$ )	9882	8.613 (-6)		5.76 (-6)	5.04 (-6)	1.14
N <sub>2</sub>	11312	4.797 (-6)	0.025	9.29 (-7)	9.53 (-7)	0.97
(1st Pos.)	9882	6.308 (-4)		7.67 (-5)	6.80 (-5)	1.13
	6632	5.894 (-2)		4.27 (-4)	3.61 (-4)	1.18
N <sub>2</sub>	11312	4.797 (-6)	0.09	2.81 (-6)	5.57 (-6)	0.50
(2nd Pos.)	9882	6.306 (-4)		1.43 (-4)	2.40 (-4)	0.59
	6632	5.894 (-2)		1.06 (-4)	1.80 (-4)	0.59
CO <sup>+</sup>	11312	1.318 (-8)	0.0278	4.84 (-8)	8.53 (-8)	0.57
(Comet-Tail)	9882	2.625 (-7)		1.22 (-6)	2.01 (-6)	0.60
	6632	1.257 (-6)		7.57 (-6)	1.13 (-5)	0.68
N <sub>2</sub> <sup>+</sup>	11312	3.484 (-9)	0.18	7.07 (-7)	1.57 (-7)	4.52
(1st Neg.)	9882	2.754 (-8)		6.57 (-6)	1.35 (-6)	4.88
	6632	1.203 (-9)		2.95 (-7)	4.87 (-8)	6.06

\*Numbers in parentheses refer to power of 10

where  $X$  is the mole fraction. Since the number of molecules per cubic centimeter enters equations (89) and (90) as a linear function, the choosing of an atmosphere does not limit the comparison. An atmosphere was chosen only to indicate the relative importance of the molecules. It should be noted that the comparison in table I-21 in no way attempts to determine the correct oscillator strength. This must be determined experimentally.

Reference to table I-21 reveals that the approximate method correlates well with the more sophisticated method for the case of the dominate radiator, CN. On the other hand, it may be seen, that for atmospheres containing a very high percent of nitrogen, the agreement will not be as favorable. The worst discrepancy in the latter case would be in the  $N_2^+$  molecule for which the approximate theory predicts a value from 4.5 to 6 too low. At the high temperature, the centers of the rotational lines of this molecule might be reaching their blackbody limit as discussed above. In this case, the discrepancy might not be as bad as shown at the high temperature. At the lower temperature, this is not so and the discrepancy appears to be real. Since the smearing out of the rotational lines could only cause an overprediction in equation (90), the factor of 2 discrepancy in the  $N_2$  (2nd pos.) would also seem to be real.

When one considers an atmosphere containing a very high percentage of  $CO_2$ , the dominate diatomic radiator would be expected to be CO. Reference I-32 does not contain any constants for this molecule; to obtain the constants equation (90) was solved for three of the band systems of CO and the best constants to fit the data were determined. The constants so obtained are given in table I-22. The value of  $C_i$  is given independent of the electronic oscillator strength,  $f_e$ . Once  $f_e$  has been determined experimentally, it may simply be multiplied by the constant given in table I-22. For the comparisons between equation (89) and (90) given in table I-22, an arbitrary value of 0.01 was used for  $f_e$ .

## 2) Kramer's radiation

Above 8000°K, an important source of radiation arises from the deceleration (free-free) and capture (free-bound) of electrons by atoms or ions. This radiation is called Kramer's radiation. The total Kramer's radiation (free-free plus free-bound) for nitrogen has been measured experimentally by Morris (ref. I-41) at a pressure of 1 atmosphere and within a temperature range from 8000 to 12000°K. Comparison of the experimental data of Morris with the values predicted by equation (89) using the constants of

TABLE I-22

CONSTANTS FOR EQUATION (89) AND COMPARISON WITH EQUATION (90) FOR THE CO MOLECULE

Band System	Temperature (°K)	$\frac{C_i}{f_e}$	$T_i$	$n_i$	( $\epsilon/L$ ) Equation (90)	( $\epsilon/L$ ) Equation (89)
$b^3\pi - X^1\Sigma^+$	11312				1.69 (-8)	1.80 (-8)
	9882	1.89 (6)	1.21 (4)	4	1.12 (-6)	1.12 (06)
	6632				1.09 (-5)	7.95 (-6)
$A^1\pi - X^1\Sigma^+$	11312				1.91 (-7)	2.53 (-6)
	9882	2.27 (7)	9.3 (7)	4	1.69 (-5)	1.70 (-5)
	6632				5.42 (-4)	6.27 (-4)
$a^3\pi - X^1\Sigma^+$	11312				3.74 (-7)	6.22 (-7)
	9882	7.22 (5)	7.09 (4)	4	4.62 (-5)	7.04 (-5)
	6632				5.18 (-3)	2.40 (-3)

reference I-32 reveals the following discrepancies. At a temperature of 12000°K, equation (89) predicts the Kramer's radiation from nitrogen to be a factor of two too high. At 8000°K, equation (89) gives values about a factor of three too low, with the crossover point being ~9000°K. Since the concentration of the nitrogen atoms enters equation (89) as a linear function, the same discrepancies would be expected to exist at the pressures of interest, especially since these are of the order of 1 atmosphere, at the peak radiant heating for Mars and Venus entry.

At present, the theoretical model presented by Lindenmeier (ref. I-44) which computes the free-bound radiation, is being modified. Preliminary results seem to give good comparison with the experimental data. Another theoretical model for the free-bound radiation, that of Biberman and Norman (ref. I-45) has been compared with the experimental data. This theory predicts values approximately 30 percent too low.

The free-free radiation is on good theoretical grounds. At the higher temperatures (~11,000°K) the free-free contributes only negligibly to the Kramer's radiation.

One further complication in computing the Kramer's radiation from nitrogen is the contribution due to the negative nitrogen ion. At present, this mechanism is little understood but work is underway to clear up this difficulty. This source of radiation seems to explain this discrepancy between the theory of Biberman and Norman and the experimental data.

The only other major contributor to the Kramer's radiation for the atmospheres under consideration is that due to Argon. A comparison between the radiation computed by means of equation (89) and by the method of Bibermann and Norman which is given by the following equation, is presented in table I-23. The equations below include the free-free as well as the free-bound radiation. The intensity  $I_\lambda$ , for  $\lambda \leq \lambda_c$  is given by:

$$I_\lambda = \frac{1.63 \times 10^{-35}}{\lambda^2 T^{1/2}} N_e N_I \left\{ \xi_\lambda \exp \left[ -\frac{hc}{kT} \left( \frac{1}{\lambda} - \frac{1}{\lambda_c} \right) \right] - \xi_\lambda \exp (-hc/\lambda kT) \right\} \quad (95)$$

and for  $\lambda \geq \lambda_c$

$$I_{\lambda} = \frac{1.63 \times 10^{-35}}{\lambda^2 T^{1/2}} N_e N_i \left[ \xi_{\lambda} - \xi_{\lambda} \exp \left( - \frac{h c}{\lambda k T} \right) \right] \quad (96)$$

where:

$N_e$  and  $N_i$  are the concentration of electrons and ions, respectively.

$\lambda_c$  is the limiting wave length above which the energy levels can be regarded as being continuous.

and

$\xi_{\lambda}$  is a correction function to the Unsold-Kramer's formula using the quantum defect method of Burgess and Seaton (ref. I-46).

Equations (95) and (96) were solved for Argon at a temperature of 16000°K and a pressure of 1.1 atmospheres. The results were compared to experimental data of Olsen (ref. I-47) at the same temperature and pressure. The results agreed within 10 percent, thus giving a degree of confidence in equations (95) and (96). The emissivity per unit length was computed by equations (95) and (96) and compared to those computed by equation (89). The results are given in table I-23.

TABLE I-23

A COMPARISON OF THE KRAMERS' RADIATION FROM ARGON

Temperature °K	$N_e$ (atoms/cm <sup>3</sup> )	$N_i N_e$ (part/cm <sup>3</sup> )	$\epsilon / L$ (eq. 94 & 95)	$\epsilon / L$ (eq. 89)
16000.0	5.0 (16)*	4.0 (34)	9.56 (-4)	2.44 (-3)
10000.0	4.288 (16)	1.351 (30)	7.43 (-9)	2.71 (-7)
8000.0	6.433 (16)	1.473 (28)	2.60 (-7)	8.84 (-6)

\*Numbers in parentheses refer to power 10

The pressure corresponding to the temperature of 16,000°K in table I-23 is 1.1 atmospheres, while for the 8000 and 10000°K temperature the corresponding pressure is 0.05 atmosphere. Preliminary experimental data of Morris and Bach (ref. I-48) in the temperature range of 8000 to 12000°K and a pressure of 1 atmosphere are a factor of 10 lower than the comparative results of equation (89). The experimental data do not extend below 3000A. For wavelengths below 3000A, the emissivity has been assumed to be constant. Since the emissivity should have a  $\nu^{-3}$  dependence, the extrapolated experimental data should be an upper limit.

One final approximation should be mentioned. This program computes the radiant heat flux from the plane parallel layer as:

$$q_R = [1 - 2E_3(\tau)] \sigma T^4 \quad (97)$$

where

$$\tau = \sum_i K_i \delta = \sum_i 1/2 (\epsilon/L)_i \delta \quad \text{is the optical thickness}$$

$\delta$  is the shock detachment

and

$[1 - 2E_3(\tau)]$  is an expression previously derived which accounts for the self absorption of the gas in the plane parallel layer.

The correct expression for the plane parallel layer should be:

$$q_R = \int_0^\infty [1 - 2E_3(\tau_\lambda)] \frac{C_1}{\lambda^5} \exp\left(-\frac{C_2}{\lambda T}\right) d\lambda \quad (98)$$

where

$\tau_\lambda$  = the spectral optical thickness

$C_1$  = the first radiation constant

$C_2$  = the second radiation constant

and

$\lambda$  = the wavelength.

Equations (97) and (98) give similar results as long as the spectral absorption coefficient  $\tau_\lambda < 0.5$  for all wavelengths, i.e., as long as no part of the spectral emission approaches the blackbody limit. Since the spectral radiation varies strongly with wavelength, part of the spectrum may be strongly self absorbed while the rest of the spectrum may not be self absorbed. In this case, since equation (98) only accounts for self absorption of the integrated spectrum, it would over-predict the radiation.

Atomic line radiation has been excluded from the calculations since at the temperatures of interest it is negligible in comparison to the molecular and Kramers' radiation. This is because at these temperatures the line width is only a few Angstroms and is highly self-absorbing.

A comparison of the radiative predictions using the model described previously and the results of James (ref I-40) is shown in figure I-13. The comparison is based on an equilibrium computation, whereas the amount of nonequilibrium under the test conditions is considerable. Using the correlations noted earlier, the ratios of nonequilibrium distance to the standoff distance and the ratio of total intensity to equilibrium intensity were computed for the test conditions and are tabulated below:

Velocity (ft/sec)	$\delta_{NE}/\delta$	$I_{TOT}/I_E$
26248	0.6	3.7
21326	1.3	6.3
16405	3.5	6.8

The question arises as to how much of the observed radiation stems from nonequilibrium conditions. The results of Allen, et al (ref. I-49) indicate that a considerable amount of radiation over the nose cap can come from the expanded stagnation gas, in which case a greater fraction of equilibrium conditions could exist than one might estimate from the computations above. It appears, however, that a good deal of conservatism exists in the radiative predictions as the equilibrium calculations agree fairly well with James data (ref. I-40) and the nonequilibrium correction is quite large.

#### b. Evaluation of Gasdynamics Calculation

A number of comparisons of concentration calculations have been made with the results of other investigators. Figures I-14 and I-15 are comparative results derived from reference I-50 obtained for 9 percent



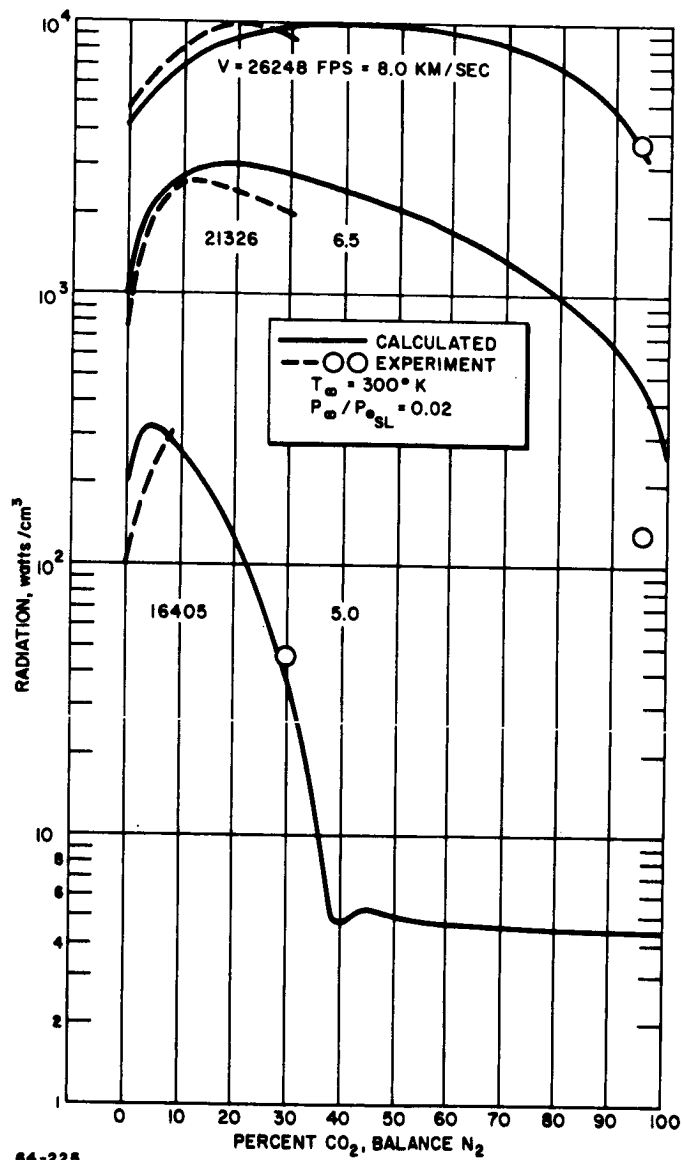


Figure I-13 COMPARISON OF RADIATION PREDICTIONS WITH EXPERIMENT

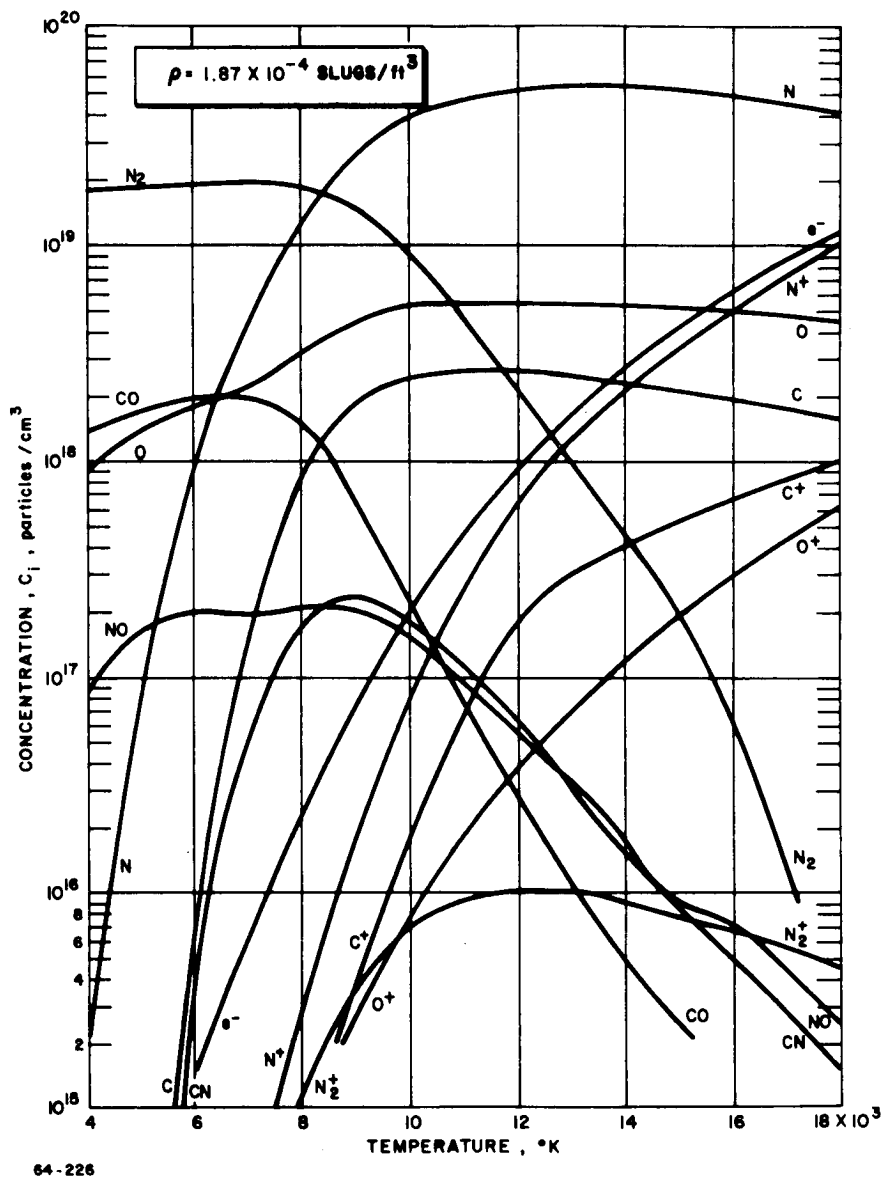
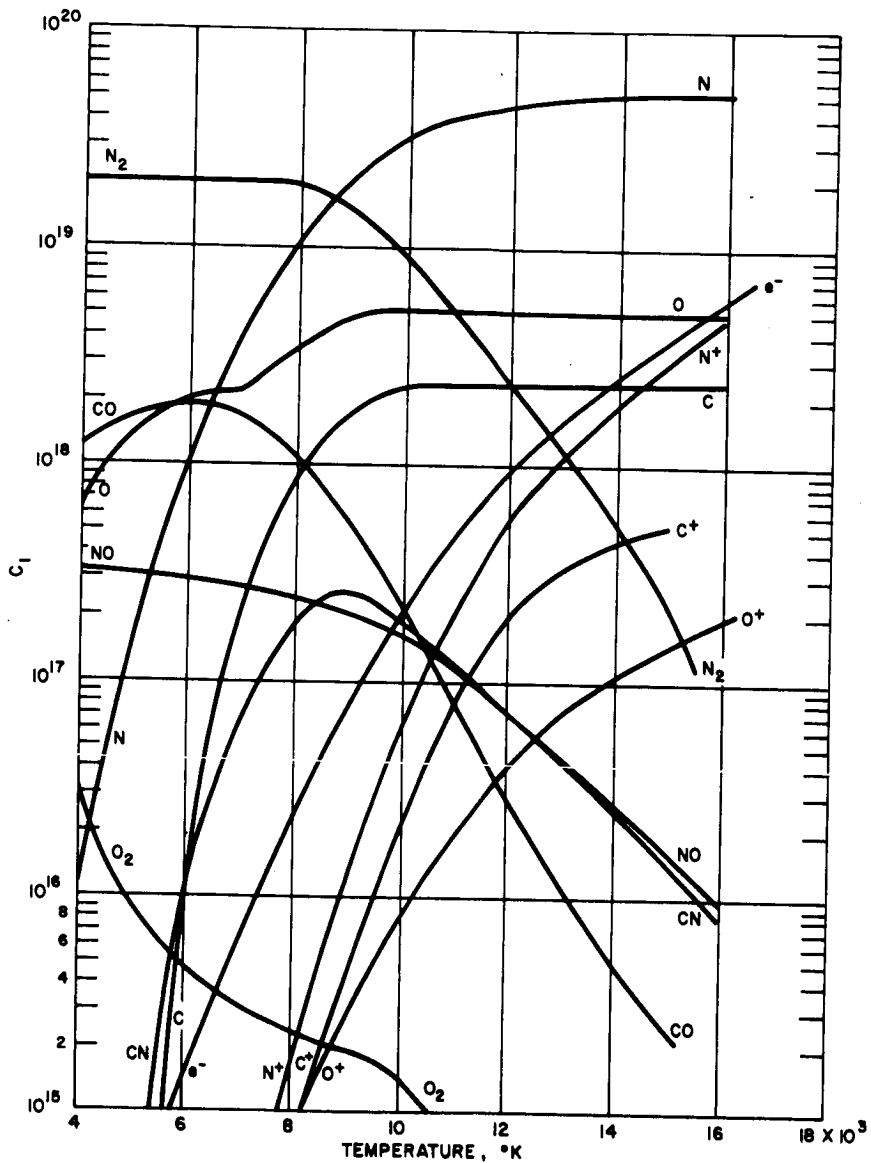


Figure I-14 CALCULATED RESULTS FOR 9-PERCENT CO<sub>2</sub> AND 91-PERCENT CO<sub>2</sub>



64-227

Figure 1-15 RESULTS FOR 9-PERCENT  $\text{CO}_2$  AND 91-PERCENT  $\text{N}_2$  FROM  
VENUS-MARS CAPSULE STUDY, VOLUME II

CO<sub>2</sub> and 91 percent N<sub>2</sub>. The results of figure I-15 were replotted from a published figure and hence could contain uncertainties. The prominent features correlate well however, with the peak CN concentrations being within a few percent of each other and both occurring at 9000°K. Comparisons of the concentrations for pure CO<sub>2</sub> with the result of Raymond (ref. I-51), and for pure nitrogen of Treanor (ref. I-52) were close with less than 5 percent difference in the major specie concentrations.

The calculations for the argon mixtures were checked with a thermochemical program at Avco RAD, Program No. 1291. A typical comparison is shown below for 64 percent CO<sub>2</sub>, 35 percent A, and 1 percent N<sub>2</sub>, at flight conditions of  $V = 23177$  ft/sec and  $\rho = 5.323 \times 10^{-7}$  slug/ft<sup>3</sup>.

	Present Calculation	Program 1291
X(CO)	0.2715 E - 0	0.2854 E - 0
X(O)	0.1008 E + 1	0.1014 E + 1
X(A)	0.3500 E - 0	0.3500 E - 0
X(C)	0.3683 E - 0	0.3596 E - 0
X(A <sup>+</sup> )	0.2179 E - 4	0.171 E - 4
X(e <sup>-</sup> )	0.5407 E - 2	0.5101 E - 2

#### c. Evaluation of Pressure Distribution Calculation

The three-dimensional case of a sphere cylinder is shown in figure I-16 for  $M_\infty = \infty$ . It is compared with perfect-gas characteristics of Chushkin and Shulishnina (ref. I-53) with  $\gamma = 1.4$ . The results for  $\gamma = 1.15$  are also included to show approximately the effect of a real gas. The axisymmetric blast-wave solution is also plotted.

Figures I-17 through I-20 show the results at  $M_\infty = \infty$  for spherically blunted cones with half angles of 5, 10, 20, and 30 degrees, respectively. These are also compared with the perfect-gas characteristics of Chushkin and Shulishnina.

The drag coefficients were taken from Chushkin's results and were 0.880 for the cylinder, 5- and 10-degree cones, 0.883 for the 20-degree cone, and 0.894 for the 30-degree cone. The agreement between

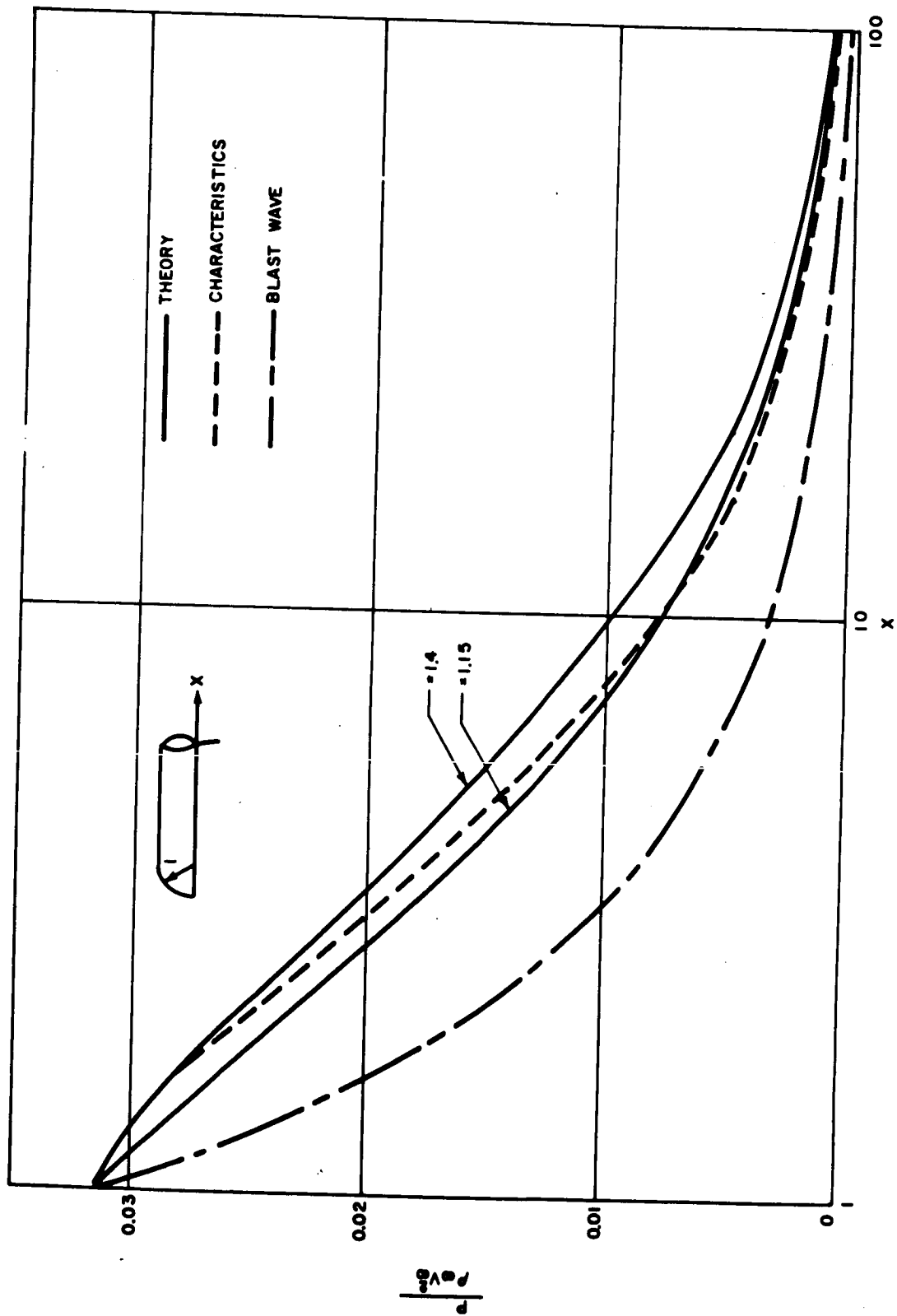


Figure 1-16 PRESSURE DISTRIBUTION ON A BLUNTED CYLINDER,  $M_\infty = \infty$

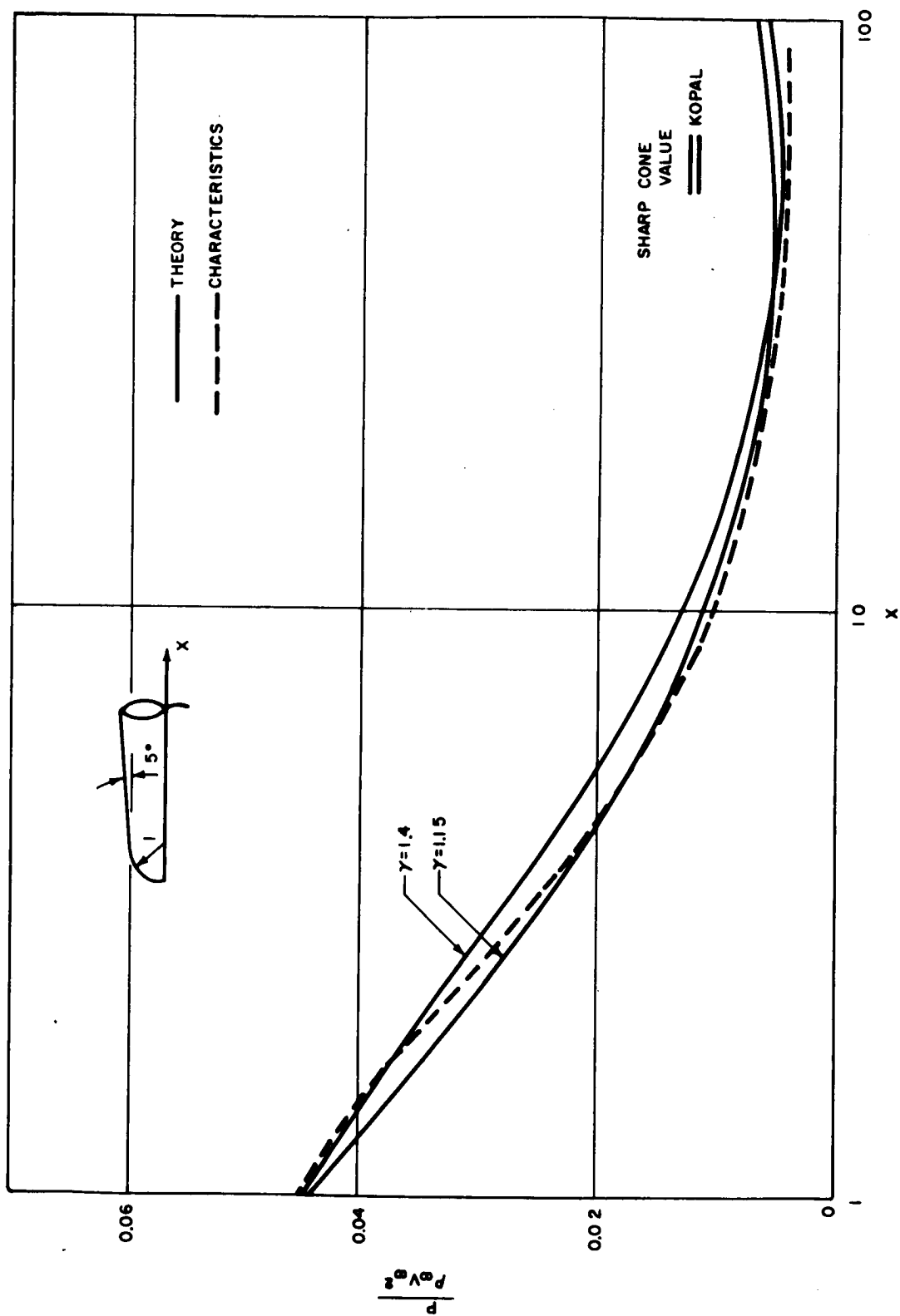


Figure 1-17 PRESSURE DISTRIBUTION ON A BLUNTED 5-DEGREE CONE,  $M_{\infty} = \infty$

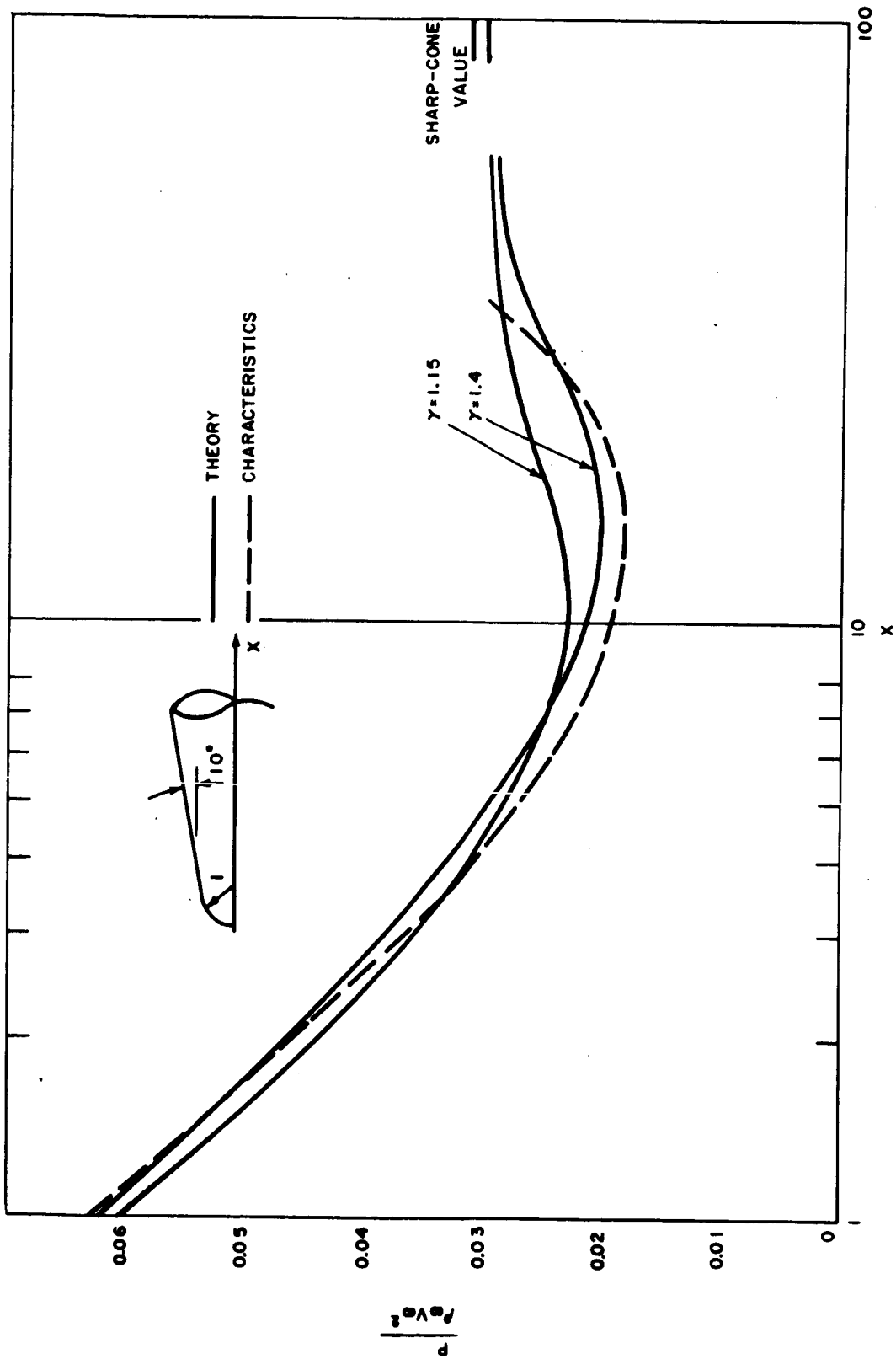


Figure 1-18 PRESSURE DISTRIBUTION ON A BLUNTED 10-DEGREE CONE,  $M_\infty = \infty$

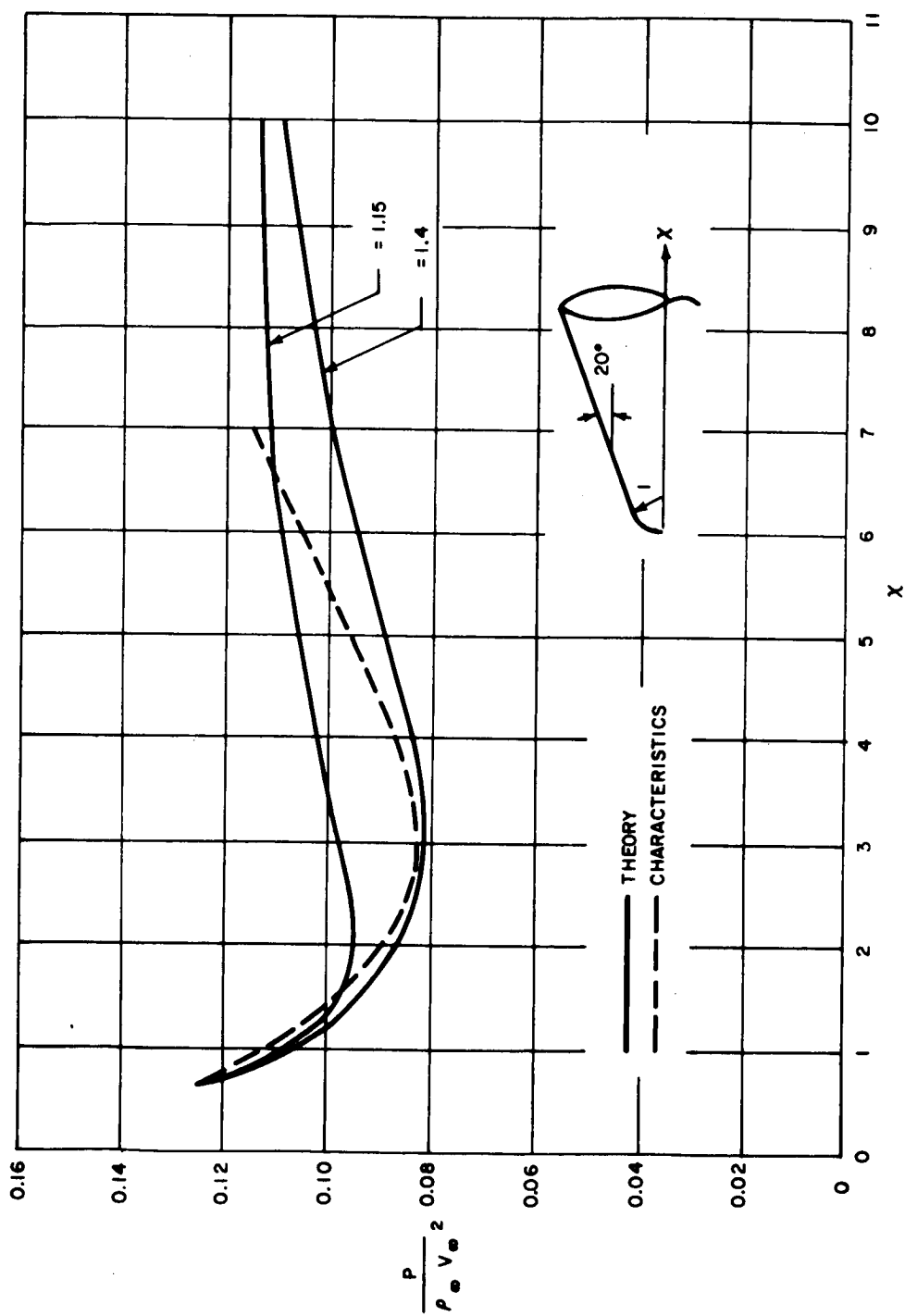


Figure 1-19 PRESSURE DISTRIBUTION ON A BLUNTED 20-DEGREE CONE,  $M_{\infty} = \infty$



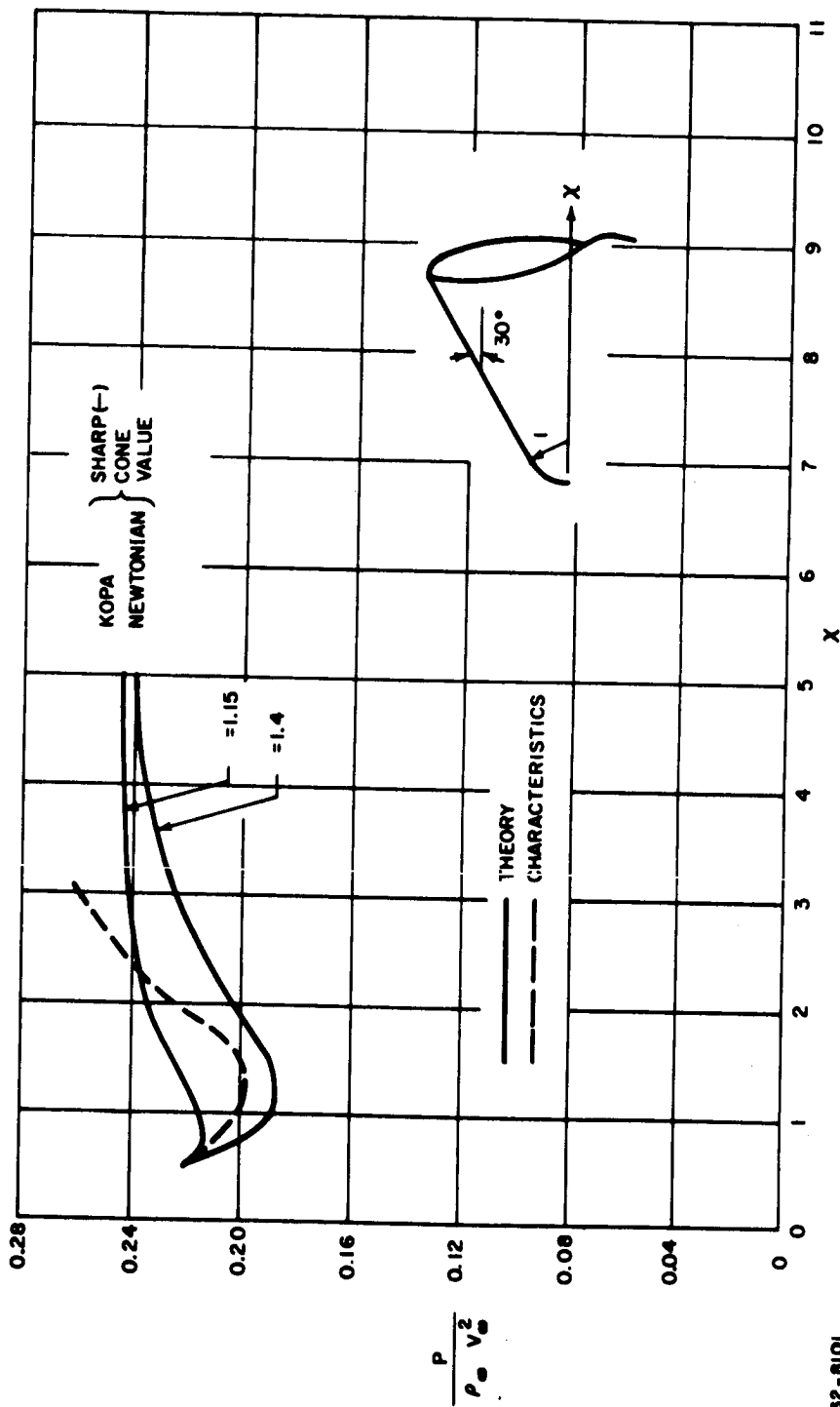


Figure 1-20 PRESSURE DISTRIBUTION ON A BLUNTED 30-DEGREE CONE,  $M_{\infty} = \infty$

62-8101

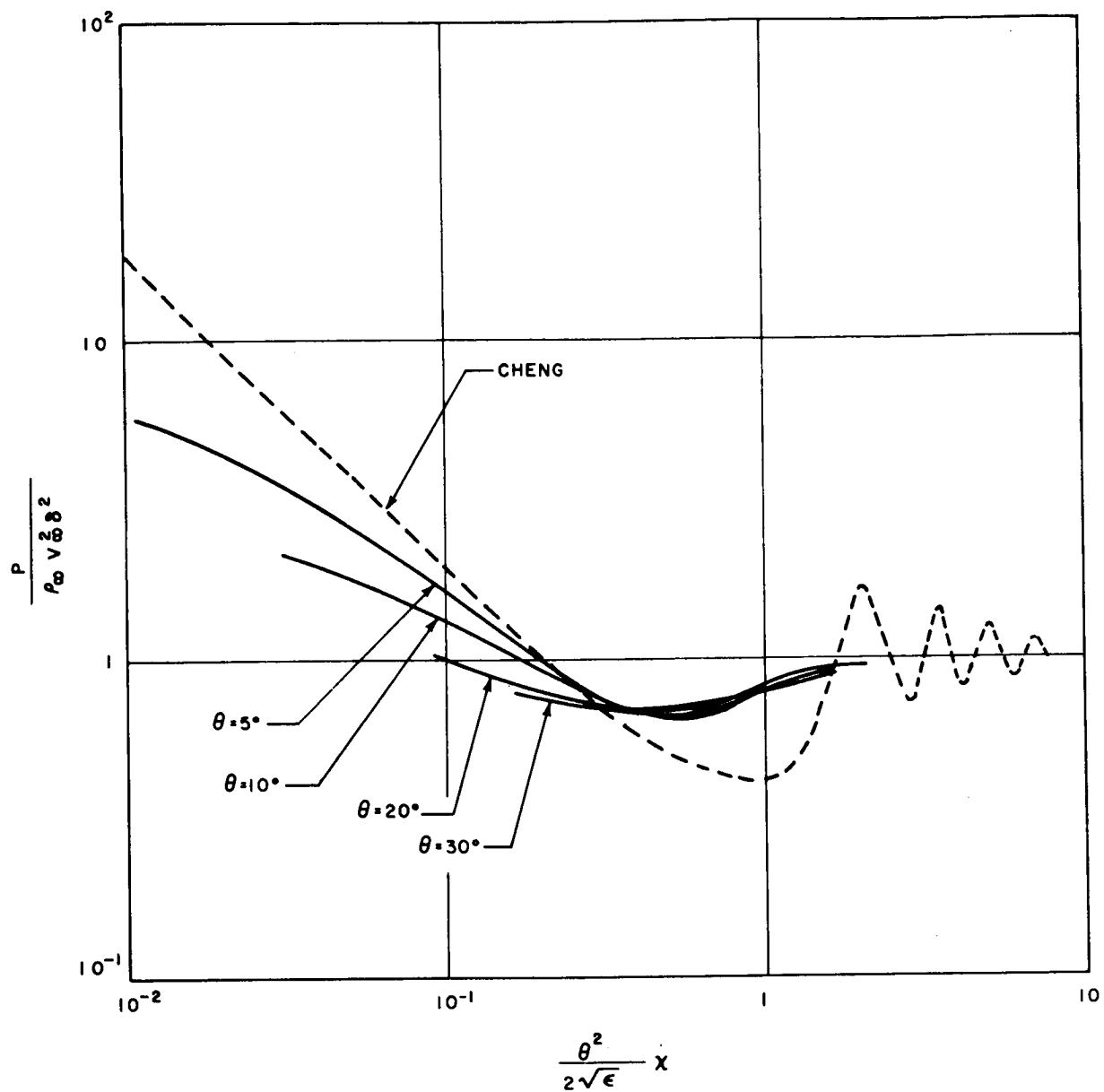


Figure 1-21 COMPARISON WITH CHENG,  $\gamma=1.4$

theory and characteristics appears to be very good up to the 20-degree cone. However, at large values of  $x$ , the theory approaches the sharp-cone pressure which is shown for  $\gamma = 1.4$  while for the 10- and 20-degree cones the characteristic pressure continues to rise. The exact sharp-cone values as given by Kopal (ref. I-54) and the Newtonian sharp-cone values are shown on the graphs.

A solution for pressure distributions on blunt-nosed cones was also obtained by Cheng (ref. I-55). His results when plotted in the form  $y/\delta^2$  versus  $(\theta^2/2\sqrt{\epsilon})x$  give a universal curve for all cone angles, Mach numbers, and altitudes. This curve is plotted in figure I-21 along with the results from the present theory. The results show considerable disagreement with Cheng's theory, and no trend is evident toward a universal curve in terms of his parameters.

Cheng's solution shows an oscillatory behavior in the pressure distribution at large values of  $x$ . It overshoots the sharp-cone value, then decreases, performing a damped oscillation about this value. This behavior has been observed experimentally by Bertram (ref. I-56) and is a consequence of the inertia of the outer layer. The outer layer is separated from the body by the entropy layer but at a sufficient distance downstream the body has expanded and the entropy layer contracted to such an extent that the body exerts a direct influence upon the outer layer. It pushes the layer out, causing the pressure to increase. However, the inertia of the layer causes it to continue beyond the sharp cone value. The increased pressure then pushes the layer back toward the body. This process continues as a damped oscillation until equilibrium is reached. Since the centrifugal term was not included in the present theory, the inertia of the layer is not accounted for. Consequently, no pressure overshoot occurs, and the pressure tends smoothly to the sharp-cone value.

#### d. Evaluation of Convective Heating

A comparison of the present results and available experimental data compiled from Gruszczynski and Warren (ref. I-57) is shown in figure I-22. The analytical results are only shown for the extremes in both pressure and mixture; namely,

$$P_s = 0.1 \text{ and } 100 \text{ atm, and}$$

$$\text{Mixture} = 100\text{-percent CO}_2, \text{ and } 10\text{-percent CO}_2 \text{ and } 90\text{-percent N}_2.$$

The resulting comparison shows good agreement.

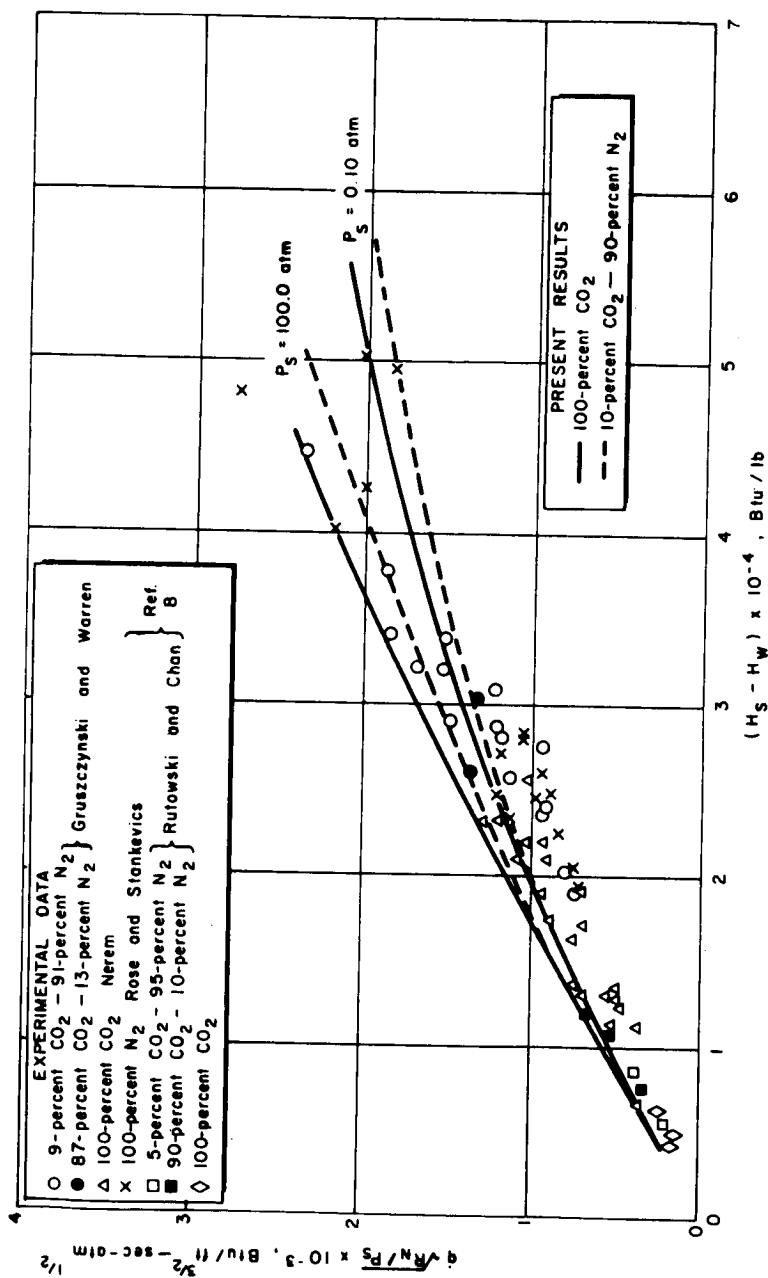


Figure 1-22 COMPARISON OF ANALYTICAL AND EXPERIMENTAL RESULTS FOR STAGNATION POINT HEATING IN CO<sub>2</sub> - N<sub>2</sub> MIXTURES

The analysis of the aerodynamic heat transfer for arbitrary gas mixtures can be separated into two fundamental problems; i.e.,

- 1) Evaluation of thermodynamic and transport properties of gas mixtures, and
- 2) Boundary-layer analysis of heat transfer in gas mixtures.

The methods used in the evaluation of properties has been shown to be adequate when the results are compared with available experimental data. From these methods, it is possible to determine the necessary thermodynamic and transport properties of any arbitrary mixture of gases.

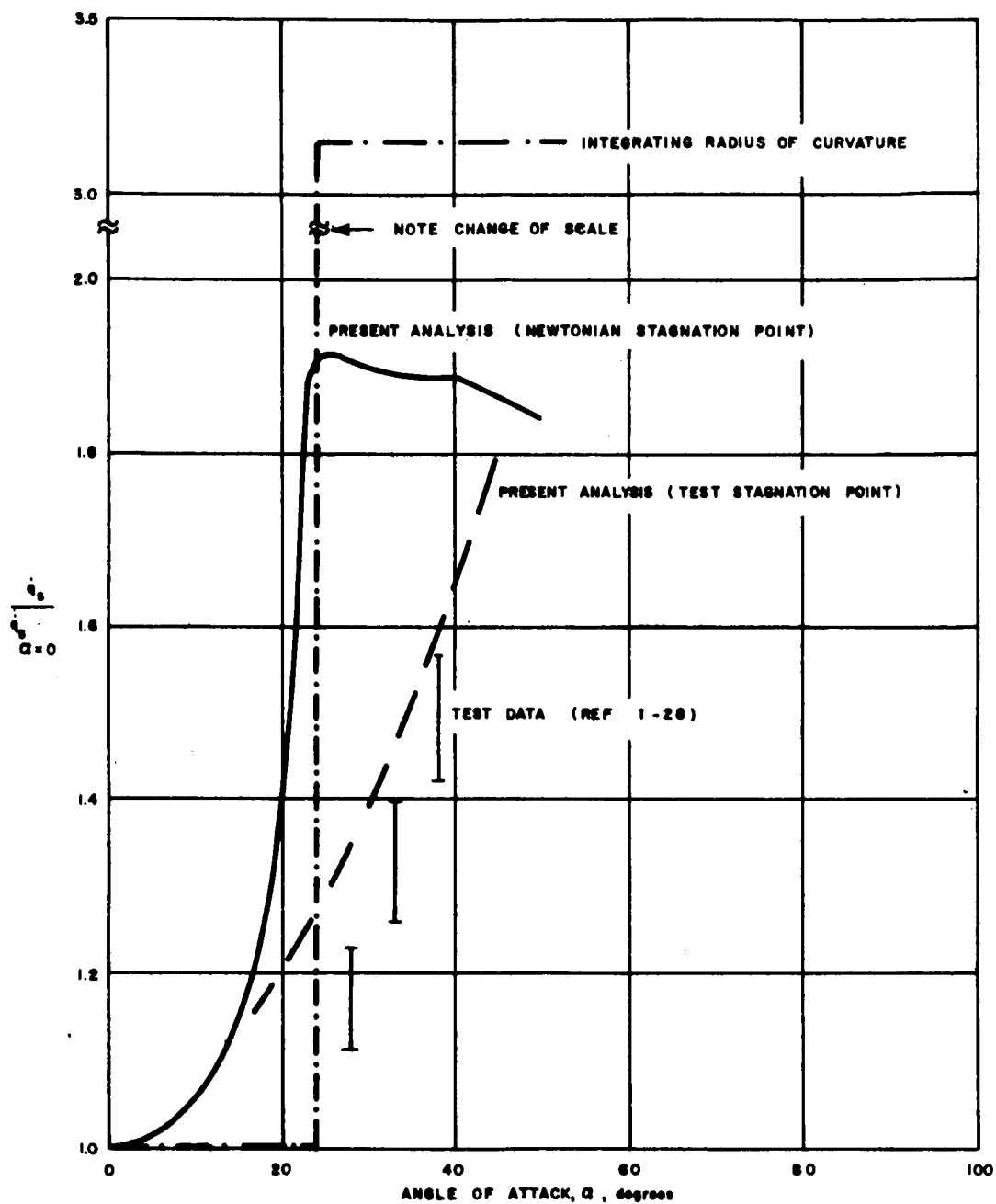
The laminar boundary-layer analysis used in this study has been proven to be a valuable tool for the case of air. It has been developed to the point where it is possible to investigate the boundary-layer behavior for any gas. The study presented in this report is for a stagnation point only; however, the method is also applicable to any geometry that can be considered to generate a "similar" boundary layer (i.e., flat plate). The comparison of these analytical results with available experimental data has shown relatively good agreement.

A comparison of experimental angle of attack effects on the stagnation point heating with predictions is shown in figure I-23. The effect of the location of the stagnation point is clearly discernable from these results.

#### e. Evaluation of the Shock Shape Calculations

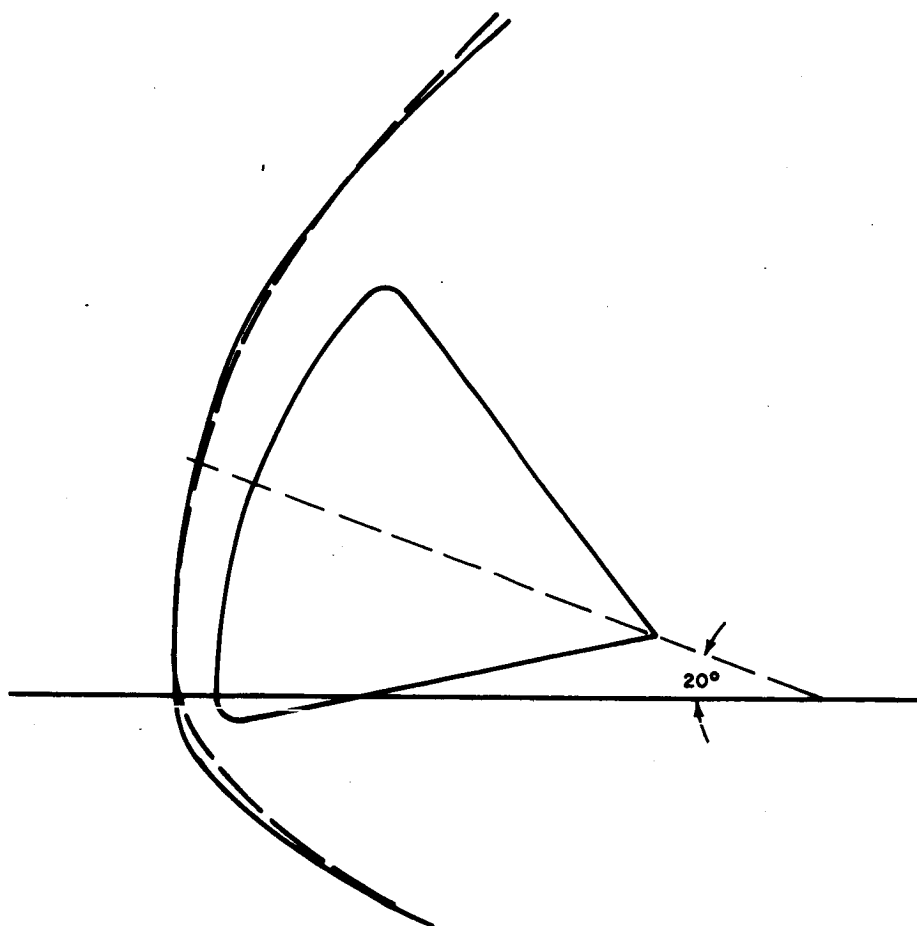
The use of the hyperbolic form  $y^2 = Ax^2 + Bx$  to approximate shock shapes has been investigated by James and Terry (ref. I-58). A comparison with experimental results on the M1 shape is shown in figure I-24, for a 20-degree angle of attack.

The approximate nature of the solution has led to consistent trends in the results. However, a complete evaluation of the approach requires comparative schlieren photographs for the remainder of the vehicles.



64-228

Figure 1-23 STAGNATION POINT HEATING (M1 CONFIGURATION)



$M = 13.09$

$\rho_0 / \rho_\infty = 10.6$

———— THEORETICAL  
 - - - - - ACTUAL

64-229

Figure I-24 COMPARISON OF THEORETICAL AND ACTUAL SHOCK SHAPES  
 (M1 CONFIGURATION)

## C. TRAJECTORY BLOCK

### 1. Introduction

The purpose of this block is to determine the angle of attack envelope, heating and loads history for entry capsules into the planets. The program utilized in this block has two options namely (1) four degree of freedom solution with coefficients which vary with angle of attack, and (2) linearized solution with coefficients which vary with Mach number.

The trajectory calculation provides the angle of attack envelopes, and the flight conditions for evaluating the aerodynamic heating and loads. The heating computations were connected directly to the trajectory program to provide the convective and radiative heat pulse.

### 2. Force Equations

#### a. Symbols

a	acceleration, ft/sec <sup>2</sup>
A	reference area, ft <sup>2</sup>
C <sub>D</sub>	drag coefficient
C <sub>L</sub>	lift coefficient
D	drag force, pounds
F	force, pounds
g	acceleration due to gravity at the surface, ft/sec <sup>2</sup>
L	lift force, pounds
m	Mass, slugs
R	radius of planet at surface, feet
t	time, seconds
V	velocity, ft/sec
X <sub>0</sub> , Y <sub>0</sub> , Z <sub>0</sub>	inertial cartesian coordinates
Z	altitude of the vehicle, feet
$\beta$	heading angle



$\gamma$	flight path angle
$\rho$	ambient density, slug/ft <sup>3</sup>
$\lambda$	roll angle
$\xi, \eta, R$	inertial spherical coordinates
$\Omega$	resultant angular rotation about the origin

#### Subscripts

o	initial conditions
SL	conditions at surface
$\xi, \eta, R$	component along $\xi, \eta, R$ axes
R	resultant value
W	wind

#### Superscripts

( $\rightarrow$ )	vector
( $\cdot$ )	differentiation with respect to time.

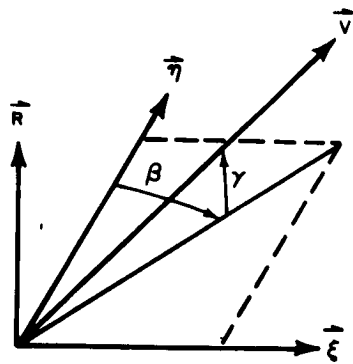
#### b. Inertial Coordinate System for the Force Equations

An inertial cartesian coordinate system, with origin at the center of planet, is assumed. The location of the entry vehicle is then given by specifying  $\xi, \eta, R$  as shown in figure I-25. As shown, the Z axis passes through the northern pole, the vector  $\vec{\eta}$  points northward, the vector  $\vec{\xi}$  eastward, and the vector  $\vec{R}$  points radially outwards from the center of the planet.

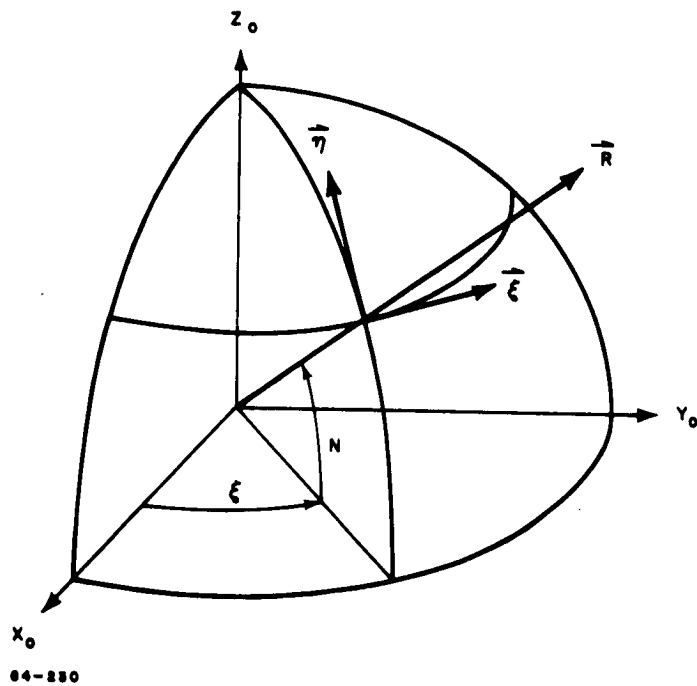
The velocity vector is specified by its scalar value, the heading angle measured east from north, and the elevation angle measured positive above the local horizontal. The details of the velocity vector coordinates are shown in the insert of figure I-25.

#### c. The Acceleration Vector

By the laws of mechanics, the motion of the center of gravity of a vehicle can be found by summing the forces acting on the vehicle.



VELOCITY VECTOR DETAIL



04-230

Figure 1-25 INERTIAL COORDINATE SYSTEM FOR PLANETARY ENTRY

$$\Sigma \vec{F} = m \vec{a} \quad (1)$$

and, hence, we must ascertain the form of the acceleration vector. According to vector mechanics,

$$\vec{a} = \frac{d\vec{V}}{dt} = \frac{\delta \vec{V}}{\delta t} + \vec{\Omega} \times \vec{V} \quad (2)$$

where  $\vec{\Omega}$  is the resultant angular rotation about the origin. The components of  $\vec{\Omega}$  are:

$$\begin{aligned} \Omega_{\xi} &= -\dot{\eta} \\ \Omega_{\eta} &= \dot{\xi} \cos \eta \\ \Omega_R &= \dot{\xi} \sin \eta \end{aligned} \quad (3)$$

Hence, the total rotational vector is

$$\vec{\Omega} = -\vec{\xi}_u \dot{\eta} + \vec{\eta}_u \cos \eta \dot{\xi} + \vec{R}_u \sin \eta \dot{\xi} \quad (4)$$

The velocity vector has the components

$$\begin{aligned} V_{\xi} &= R \cos \eta \dot{\xi} \\ V_{\eta} &= R \dot{\eta} \\ V_R &= \dot{R} \end{aligned} \quad (5)$$

Hence, the total velocity vector is

$$\vec{V} = \vec{\xi}_u R \cos \eta \dot{\xi} + \vec{\eta}_u R \dot{\eta} + \vec{R}_u \dot{R} \quad (6)$$

The acceleration vector is given by equation (2), which upon substitution of (4) and (6) yields,

$$\begin{aligned} \vec{a} &= \vec{\xi}_u (\ddot{R} \dot{\xi} \cos \eta - \dot{\eta} \dot{\xi} R \sin \eta + R \ddot{\xi} \cos \eta) \\ &+ \vec{\eta}_u (R \ddot{\eta} + \dot{R} \dot{\eta}) + \vec{R}_u \ddot{R} \end{aligned}$$

$$+ \begin{vmatrix} \vec{\xi}_u & \vec{\eta}_u & \vec{R}_u \\ -\dot{\eta} & \dot{\xi} \cos \eta & \dot{\xi} \sin \eta \\ R \dot{\xi} \cos \eta & R \dot{\eta} & \dot{R} \end{vmatrix} \quad (7)$$

Completing the cross product and collecting terms, the acceleration is

$$\begin{aligned} \vec{a} &= \vec{\xi}_u (2 \dot{R} \dot{\xi} \cos \eta - 2 R \dot{\eta} \dot{\xi} \sin \eta + R \ddot{\xi} \cos \eta) \\ &+ \vec{\eta}_u (2 \dot{R} \dot{\eta} + R \ddot{\eta} + R \dot{\xi}^2 \cos \eta \sin \eta) \\ &+ \vec{R}_u (\ddot{R} - R \dot{\xi}^2 \cos^2 \eta - R \dot{\eta}^2) . \end{aligned} \quad (8)$$

The three component forces are given by

$$\begin{aligned} \frac{F_R}{m} &= \ddot{R} - R \cos^2 \eta \dot{\xi}^2 - R \dot{\eta}^2 \\ \frac{F_{\xi}}{m} &= 2 \dot{R} \dot{\xi} \cos \eta - 2 R \dot{\eta} \dot{\xi} \sin \eta + R \ddot{\xi} \cos \eta \\ \frac{F_{\eta}}{m} &= 2 \dot{R} \dot{\eta} + R \ddot{\eta} + R \dot{\xi}^2 \cos \eta \sin \eta . \end{aligned} \quad (9)$$

#### d. Drag Vector

During entry into the atmosphere, account must be made of the lift and drag. The drag forces are defined to lie along the total relative wind velocity vector. The velocity of the vehicle relative to the atmosphere is

$$\vec{V}_R = \vec{V} - \vec{V}_W \quad (10)$$

where  $\vec{V}_W$  is the wind vector in an inertial frame of reference. Hence, account must be taken of the rotation of the atmosphere as well as the relative winds. The wind vector has components

$$\begin{aligned} V_{W\xi} &= R \cos \eta \omega_e + V_{WE} \\ V_{W\eta} &= V_{WN} \\ V_{WR} &= 0 \end{aligned} \quad (11)$$

The relative velocity vector is now

$$\vec{V}_R = \vec{\xi}_u \overbrace{(R \cos \eta \dot{\xi} - R \cos \eta \omega_e - V_{WE})}^{V_{R\xi}} + \eta_u \overbrace{(R \dot{\eta} - V_{WN})}^{V_{R\eta}} + \vec{R}_u \overbrace{\dot{R}}^{V_{RR}} \quad (12)$$

The drag vector is defined as

$$\vec{D} = \frac{-\vec{V}_R}{V_R} D \quad (13)$$

where

$$V_R = \sqrt{V_{R\xi}^2 + V_{R\eta}^2 + V_{RR}^2}$$

so that the drag components are

$$\begin{aligned} D_\xi &= - \frac{V_{R\xi}}{V_R} D \\ D_\eta &= - \frac{V_{R\eta}}{V_R} D \\ D_R &= - \frac{V_{RR}}{V_R} D \end{aligned} \quad (14)$$

The drag force acting on the vehicle is then

$$D = C_D A \frac{1}{2} \rho V_R^2 \quad (15)$$

where

$\rho$  = ambient density

$V_R$  = relative wind speed

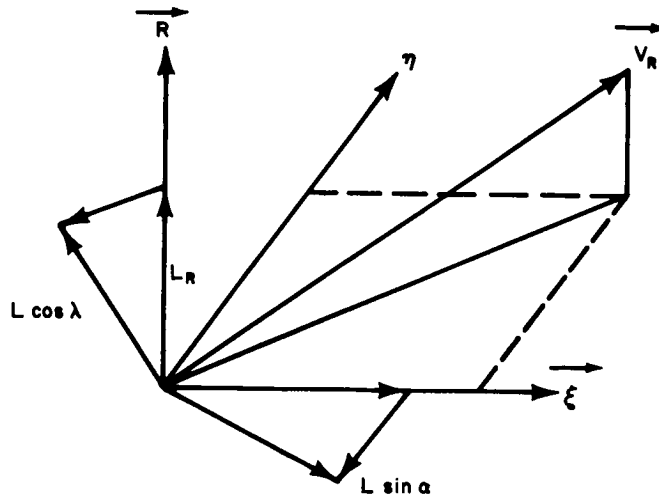
$A$  = reference area

$C_D$  = drag coefficient.

e. Lift Vector

The lift vector is defined as normal to the relative wind velocity vector. The roll angle  $\lambda$  will be introduced to indicate the angular position of the lift vector measured from the plane of the relative velocity and radius vectors.

Adopting the roll convection shown in the sketch below,



the lift components are

$$L_R = L \cos \lambda \frac{\sqrt{V_{R\xi}^2 + V_{R\eta}^2}}{V_R}$$

$$L_\xi = -L \cos \lambda \frac{V_{R\xi}}{\sqrt{V_{R\xi}^2 + V_{R\eta}^2}} + L \sin \lambda \frac{V_{R\eta}}{\sqrt{V_{R\xi}^2 + V_{R\eta}^2}} \quad (16)$$

$$L_\eta = -L \cos \lambda \frac{V_{R\eta}}{\sqrt{V_{R\xi}^2 + V_{R\eta}^2}} - L \sin \lambda \frac{V_{R\xi}}{\sqrt{V_{R\xi}^2 + V_{R\eta}^2}}$$

The total lift is

$$L = C_L A \frac{1}{2} \rho V_R^2 \quad (17)$$

where

$C_L$  = lift coefficient

$A$  = reference area

$\rho$  = ambient density

$V_R$  = relative wind speed.

## f. Entry Trajectories

The treatment of the motion of a vehicle during atmospheric entry is simplified by considering a coordinate system which uses the elevation and heading angles,  $\gamma$  and  $\beta$ .

$$V_{\xi} = V \cos \gamma \sin \beta = R \cos \eta \dot{\xi} \quad (18)$$

$$V_{\eta} = V \cos \gamma \cos \beta = R \dot{\eta}$$

$$V_R = V \sin \gamma = \dot{R}$$

The equations of motion (9) can now be written,

$$\begin{aligned} \frac{F_R}{m} &= \dot{V} \sin \gamma + V \cos \gamma \dot{\gamma} - \frac{V^2 \cos^2 \gamma}{R} \\ \frac{F_{\xi}}{m} &= \frac{V^2 \sin \gamma \cos \gamma \sin \beta}{R} - \frac{V^2 \cos^2 \gamma \cos \beta \tan \eta \sin \beta}{R} \\ &\quad + \dot{V} \cos \gamma \sin \beta - V \sin \beta \sin \gamma \dot{\gamma} + V \cos \gamma \cos \beta \dot{\beta} \end{aligned} \quad (19)$$

$$\begin{aligned} \frac{F_{\eta}}{m} &= \frac{V^2 \sin \gamma \cos \gamma \cos \beta}{R} + \dot{V} \cos \gamma \cos \beta - V \sin \gamma \cos \beta \dot{\gamma} \\ &\quad - V \cos \gamma \sin \beta \dot{\beta} + \frac{V^2 \cos^2 \gamma}{R} \sin^2 \beta \tan \eta \end{aligned}$$

By observation, we note that  $\dot{V}$  and  $\dot{\gamma}$  can be eliminated by combining the latter two equations of (19), such that

$$\frac{F_{\xi}}{m} \cos \beta - \frac{F_{\eta}}{m} \sin \beta = V \cos \gamma \dot{\beta} - \frac{V^2 \cos^2 \gamma \tan \eta \sin \beta}{R} \quad (20)$$

Eliminating  $\dot{\beta}$  from the latter two equations of (19),

$$\frac{F_{\xi}}{m} \sin \beta + \frac{F_{\eta}}{m} \cos \beta = \frac{V^2 \sin \gamma \cos \gamma}{R} + \dot{V} \cos \gamma - V \sin \gamma \dot{\gamma} \quad (21)$$

Combining equation (21) and the first equation of (19), to eliminate  $\dot{\gamma}$  and then  $\dot{V}$ , yields

$$\frac{F_R}{m} \sin \gamma + \frac{F_{\xi}}{m} \sin \beta \cos \gamma + \frac{F_{\eta}}{m} \cos \beta \cos \gamma = \dot{V} \quad (22)$$

and

$$\frac{F_R}{m} \cos \gamma - \frac{F_\xi}{m} \sin \beta \sin \gamma - \frac{F_\eta}{m} \cos \beta \sin \gamma = V \dot{\gamma} - \frac{V^2 \cos \gamma}{R} . \quad (23)$$

To transform the force components, account must be taken of the effect of the wind on the defined coordinate system. To simplify the approach,  $\gamma_R$  and  $\beta_R$  are introduced such that,

$$\begin{aligned} V_{R\xi} &= V_R \cos \gamma_R \sin \beta_R \\ V_{R\eta} &= V_R \cos \gamma_R \cos \beta_R \\ V_{RR} &= V_R \sin \gamma_R . \end{aligned} \quad (24)$$

The drag and lift components can now be written as,

$$\begin{aligned} D_\xi &= -D \cos \gamma_R \sin \beta_R \\ D_\eta &= -D \cos \gamma_R \cos \beta_R \end{aligned} \quad (25)$$

$$\begin{aligned} D_R &= -D \sin \gamma_R \\ L_R &= L \cos \lambda \cos \gamma_R \end{aligned} \quad (26)$$

$$\begin{aligned} L_\xi &= -L \cos \lambda \sin \gamma_R \sin \beta_R + L \sin \lambda \cos \beta_R \\ L_\eta &= -L \cos \lambda \sin \gamma_R \cos \beta_R - L \sin \lambda \sin \beta_R . \end{aligned}$$

Substituting the various force components into equation (22), yields

$$\begin{aligned} -\frac{D}{m} [\sin \gamma_R \sin \gamma + \cos \gamma_R \cos \gamma \sin \beta_R + \cos \gamma_R \cos \gamma \cos \beta \cos \beta_R] \\ + \frac{L}{m} [\cos \lambda (\cos \gamma_R \sin \gamma - \cos \gamma \sin \gamma_R \sin \beta \sin \beta_R - \cos \gamma \sin \gamma_R \cos \beta \cos \beta_R) \end{aligned} \quad (27)$$

$$+ \sin \lambda (\cos \gamma \sin \beta \cos \beta_R - \cos \gamma \cos \beta \sin \beta_R)]$$

$$+ g_R \sin \gamma + g_\xi \cos \gamma \sin \beta + g_\eta \cos \gamma \cos \beta = \dot{V} ,$$



or

$$\begin{aligned}
 & - \frac{D}{m} [\sin \gamma_R \sin \gamma + \cos \gamma_R \cos \gamma \cos (\beta - \beta_R)] \\
 & + \frac{L}{m} [\cos \lambda (\cos \gamma_R \sin \gamma - \cos \gamma \sin \gamma_R \cos (\beta - \beta_R)) + \sin \lambda \cos \gamma \sin (\beta - \beta_R)] \\
 & + g_R \sin \gamma + g_\xi \cos \gamma \sin \beta + g_\eta \cos \gamma \cos \beta = \dot{V} .
 \end{aligned}$$

In the case of zero wind and  $g_\xi = g_\eta = 0$ , i.e., nonrotating spherical planet and no local winds, equation (27) reduces to

$$- \frac{D}{m} + g_R \sin \gamma = \dot{V} . \quad (28)$$

Substitution for the force components in equation (23) yields

$$\begin{aligned}
 & \frac{D}{m} [-\sin \gamma_R \cos \gamma + \cos \gamma_R \sin \beta_R \sin \gamma \sin \beta + \cos \gamma_R \cos \beta_R \cos \beta \sin \gamma] \\
 & + \frac{L}{m} [\cos \lambda (\cos \gamma \cos \gamma_R + \sin \gamma_R \sin \beta_R \sin \gamma \sin \beta + \sin \gamma_R \cos \beta_R \sin \gamma \cos \beta)] \\
 & + \frac{L}{m} [\sin \lambda (-\cos \beta_R \sin \beta \sin \gamma + \sin \beta_R \cos \beta \sin \gamma)] \\
 & + g_R \cos \gamma - g_\xi \sin \beta \sin \gamma - g_\eta \cos \beta \sin \gamma = V \dot{\gamma} - \frac{V^2 \cos \gamma}{R} .
 \end{aligned} \quad (29)$$

For a spherical nonrotating planet and zero winds, equation (29) reduces to

$$V \dot{\gamma} = \frac{L}{m} \cos \lambda + \frac{V^2 \cos \gamma}{R} + g_R \cos \gamma \quad (30)$$

The remaining equation (20) becomes, after substitution of the forces,

$$\begin{aligned}
 & \frac{D}{m} [ - \cos \gamma_R \sin \beta_R \cos \beta + \cos \gamma_R \cos \beta_R \sin \beta ] \\
 & + \frac{L}{m} \cos \lambda [ - \sin \gamma_R \sin \beta_R \cos \beta + \sin \gamma_R \cos \beta_R \sin \beta ] \\
 & + \frac{L}{m} \sin \lambda [ + \cos \beta_R \cos \beta + \sin \beta_R \sin \beta ] + g_\xi \cos \beta - g_\eta \sin \beta \\
 & = V \cos \gamma \dot{\beta} - \frac{V^2 \cos^2 \gamma}{R} \sin \beta \tan \eta .
 \end{aligned} \tag{31}$$

For a spherical nonrotating planet with zero winds,

$$V \cos \gamma \dot{\beta} = \frac{L}{m} \sin \lambda + \frac{V^2}{R} \cos^2 \gamma \sin \beta \tan \eta . \tag{32}$$

Summarizing the three equations of motion for a spherical, nonrotating planet replacing  $g_R = -g$

$$\dot{V} = - \frac{D}{m} - g \sin \gamma \tag{33}$$

$$V \dot{\gamma} = \frac{L}{m} \cos \lambda + \frac{V^2 \cos \gamma}{R} - g \cos \gamma$$

$$V \cos \gamma \dot{\beta} = \frac{L}{m} \sin \lambda + \frac{V^2}{R} \cos^2 \gamma \sin \beta \tan \eta$$

An important observation of the resultant equations (33) is that the first two equations are independent of the third when the roll angle is specified. The first two equations describe the motion of the vehicle in the plane of the velocity and radius vectors. These two equations form the basis for the calculation of the flight path during entry for this study.

Considering the two force equations to be solved, the following supplementary relationships permit their solution:

$$g = g_{SL} \left( \frac{R_{SL}}{R} \right)^2$$

$$R = R_{SL} + z \quad (34)$$

$$\frac{dz}{dt} = V \sin \gamma$$

$$\rho = \rho(z)$$

where

$g_{SL}$  = acceleration due to gravity at the surface

$R_{SL}$  = radius of the planet at the surface

$z$  = altitude of the vehicle

$\rho$  = ambient density of the atmosphere.

As axisymmetric ballistic vehicles are of primary interest, with zero lift at zero angle of attack, lift occurs only as a result of the dynamic motions of the vehicle about its center of gravity. Fortunately, the oscillatory motions of the entry vehicle tend to cancel out the effects of lift on the flight path. Hence, the drag coefficient is obtained as a function of time and depends on the angle of attack of the vehicle. An option in the dynamics calculation permits the drag coefficient to be specified as a function of Mach number, at zero angle of attack, below peak dynamic pressure if the angle of attack is low.

The side force equation has been neglected as it is primarily dependent on the magnitude of the lift vector component which is normal to the velocity and gravitation vectors. A side component of the lift vector can occur due to the angle of attack motions of the vehicle, but it also tends to be canceled out by the oscillatory nature of this motion.

The basic assumptions used in evolving the force equations are:

- 1) Spherical planet
- 2) Nonrotating planet
- 3) Zero winds
- 4) Inverse square gravitational field.

Additional assumptions used in programing the force equations are:

- 1) The side force equation has a negligible effect on the flight path
- 2)  $C_L \cos \lambda$  is effectively zero for axisymmetric ballistic vehicles.

The initial conditions, specified as entry conditions, are the entry altitude  $z_e$ , velocity  $V_e$ , and flight path angle  $\gamma_e$ . In addition, the surface radius  $R_{SL}$  and acceleration due to gravity  $g_{SL}$  are required. The variation of density with altitude must be given to be able to compute the drag force. In the event that aerodynamic coefficients are specified as a function of Mach number, then the variation speed of sound with altitude is also needed.

### 3. Atmospheric Data

#### a. Symbols

a	speed of sound, ft/sec
$C_P$	specific heat, Btu/lb
g	acceleration due to gravity, ft/sec
L	temperature gradient, °K/ft
M	Mach number, molecular weight
p	pressure, lbs/ft <sup>2</sup>
R	universal gas constant, radius of planet
T	temperature, °K

$X_O, X_N, X_C, X_A$  mole fraction of oxygen, nitrogen, carbon dioxide, and argon respectively.

$z$  altitude, feet

$\beta^{-1}$  scale height, feet

$\rho$  ambient density, slug/ft<sup>3</sup>

#### Subscripts

SL conditions at surface of planet

ST stratosphere

TH base of thermosphere

#### b. Atmosphere generation

The generation of the variation of density with altitude was simplified by introducing the hydrostatic relationships used in meteorology. This was done to avoid the necessity of placing complete tables of density variations with altitude for each new atmosphere conceived. Since one of the trajectory options provides for the variation of coefficients with Mach number, when the vehicle is below peak dynamic pressure, the speed of sound variation with altitude is also needed. The compositions considered include atmospheres of arbitrary fractions of nitrogen, oxygen, carbon dioxide, and argon. The atmosphere is then identified by specifying the mole fractions  $X_N, X_C, X_A, X_O$  of these constituents.

In the troposphere, the temperature variation with altitude is linear for earth, and may be linear for other planets as well, in which case,

$$T = T_{SL} - L_{SL} \left( \frac{g_{SL} z}{C_P} \right) \quad (35)$$

where  $\frac{-g_{SL}}{C_P}$  is the adiabatic lapse rate and hence  $L_{SL}$  represents the

estimated temperature gradient in terms of a fraction of the adiabatic value. The specific heat at constant pressure is

$$\frac{C_P}{R} = \frac{3.5 X_N + 3.5 X_O + 4.0 X_C + 2.5 X_A}{M} \quad (36)$$

where  $R$  is the universal gas constant and  $M$  is the molecular weight, given by

$$M = 28 X_N + 32 X_O + 44 X_C + 40 X_A.$$

To obtain the density variation with altitude, the hydrostatic equation is used,

$$dp = - \rho g dz \quad (37)$$

and the ideal gas equation expressed as

$$\frac{dp}{p} = \frac{d\rho}{\rho} + \frac{dT}{T}. \quad (38)$$

Note that it is assumed the molecular weight is constant with altitude.

Combining the ideal gas and hydrostatic equations,

$$\frac{d\rho}{\rho} = - \frac{dT}{T} - \frac{Mg dz}{RT}. \quad (39)$$

Using the expression for temperature as a function of altitude, equation (35), and the inverse square gravity relationship, the integration of equation (39) yields

$$\rho = \rho_{SL} \frac{T_{SL}}{T} \exp - \left\{ \frac{M g_{SL}}{R \left( T_{SL} + \frac{g_{SL} L_{SL}}{C_p} R_{SL} \right)} \left[ \frac{z R_{SL}}{(R_{SL} + z)} - \frac{g_{SL} L_{SL} R_{SL}^2 \ln \left( \frac{R_{SL} \left( T_{SL} - \frac{L_{SL} g_{SL}}{C_p} z \right)}{T_{SL} (R_{SL} + z)} \right)}{C_p \left( T_{SL} + \frac{L_{SL} g_{SL}}{C_p} R_{SL} \right)} \right] \right\} \quad (40)$$

The location of the beginning of the stratosphere is known by specification of the stratosphere temperature  $T_{ST}$ , so that by equation (35),

$$z_{ST} = \frac{C_p (T_{SL} - T_{ST})}{L_{SL} g_{SL}} \quad (41)$$

The stratosphere is taken to be a layer of gas at uniform temperature so that proceeding along similar lines as for the troposphere layer, the following relationships are obtained:

$$\rho = \rho_{ST} e^{\beta_{ST} z_{ST}} e^{-\beta z}$$

where

$$\beta = \frac{M g_{SL} R_{SL}}{R T_{ST} (R_{SL} + z)} \quad (42)$$

$$\beta_{ST} = \beta(z_{ST})$$

$$\rho_{ST} = \rho(T_{ST}, z_{ST}) \text{ as given by equation (40).}$$

Provision is included for a thermosphere, identified by the pressure at its base  $P_{TH}$  and a linear temperature gradient  $L_{TH}$  in the layer. The density variation with altitude is found in a manner analogous to that used for the troposphere. The resultant expression is

$$\rho = \frac{P_{TH} M}{RT} \exp - \left\{ \frac{M g_{SL}}{R [T_{ST} - L_{TH} (R_{SL} + z_{TH})]} \left[ \frac{R_{SL}^2 (z - z_{TH})}{(R_{SL} + z)(R_{SL} + z_{TH})} \right. \right. \\ \left. \left. + \frac{L_{TH} R_{SL}^2}{T_{ST} - L_{TH} (R_{SL} + z_{TH})} \ln \left( \frac{T_{ST} + L_{TH} (z - z_{TH})}{T_{ST} (R_{SL} + z)/(R_{SL} + z_{TH})} \right) \right] \right\} \quad (43)$$

where

$$T = T_{ST} + L_{TH} (z - z_{TH}) . \quad (44)$$

The altitude at which the thermosphere begins is found by the stratosphere calculations to occur when the pressure decreases to  $P_{TH}$ .

The speed of sound is readily found by means of its dependence on temperature, specific heat and molecular weight,

$$a = \sqrt{\frac{C_P T}{\frac{C_P M}{R} - 1}} . \quad (45)$$

Summarizing, the relationships have been developed, for model atmospheres consisting of:

- a. A troposphere with a linearly decreasing temperature with increasing altitude
- b. A stratosphere with constant temperature
- c. A thermosphere with a linearly increasing temperature with increasing altitude
- d. A constant molecular weight gas.

The parameters which define the atmosphere are the mole fractions of its constituents, the surface acceleration due to gravity and radius of the planet at the surface, the atmospheric temperature and density at the surface, the stratosphere temperature, the pressure at the base of the thermosphere, and the temperature gradients in the troposphere and thermosphere.



#### 4. Dynamics

##### a. Symbols

$A$	Reference area, $\text{ft}^2$
$C_N$	Normal force coefficient
$C_m$	Pitching moment coefficient
$C_{m_\alpha}$	Pitching moment derivative (per radian)
$C_{L_\alpha}$	Lift coefficient derivative (per radian)
$C_{m_q}$	$\frac{\partial C_m}{\partial \left( \frac{Qd}{2V} \right)}$ , pitch damping coefficient (per radian)
$d$	Vehicle diameter, feet
$H$	Total angular momentum, $\text{ft-lb-sec}$
$\vec{i}, \vec{j}, \vec{k}$	Unit vectors along the body axes
$I_X, I_Y, I_Z$	Moments of inertia about body axes, $\text{slug-ft}^2$
$K$	Space motion factor
$L$	Aerodynamic roll moment, $\text{ft-lb}$
$m$	Mass of vehicle, slugs; aerodynamic pitching moment, $\text{ft-lb}$
$P$	Spin rate, $\text{rad/sec}$ .
$q$	Dynamic pressure, $\text{lb/ft}^2$
$Q$	Pitch rate, $\text{rad/sec}$
$R$	Yaw rate, $\text{rad/sec}$
$V$	Velocity, $\text{ft/sec}$
$X_o, Y_o, Z_o$	Inertial axes
$X_B, Y_B, Z_B$	Body axes
$\alpha$	Angle of attack, degrees

$\beta$	Side Slip angle
$\alpha'$	Total angle of attack
$\psi, \theta, \phi$	Euler angle between body and inertial axes
$\sigma$	nondimensional radius of gyration, ft, $\sigma = \sqrt{\frac{I_Y}{md^2}}$
$\omega$	Total angular rate, rad/sec
$\rho$	Ambient density, slug/ft <sup>3</sup>
$\omega_n$	Natural frequency of vehicle, rad/sec

#### Subscripts

$\infty$	Ambient conditions
----------	--------------------

#### Supersubscripts

( $\vec{\phantom{x}}$ )	Vector quantity
-------------------------	-----------------

#### b. Derivation of equations

Two options are provided for the dynamics computations, due to the fact that entry problems of ballistic vehicles can be classified in a gross manner by virtue of their aerodynamic characteristics. Slender vehicles possess a highly positive lift curve slope which has a dominant effect on the dynamic motion of such bodies. Very blunt bodies, on the other hand, depend upon a delicate balance of the pitch damping and lift curve slopes to achieve satisfactory dynamic performance. As a result of these two basic differences, the blunt, high drag vehicle will tend to have larger amplitude motions during the lower altitude portions of their flight in comparison to their slender counterparts.

Hand in hand with the differences in dynamic behavior described above is the difference in the variation of the aerodynamic coefficients with Mach number between the slender and the very blunt vehicle. The high drag vehicle generally has a much smaller drag coefficient variation, supersonically, with Mach number than the slender vehicle. Consequently, the larger amplitude motion of the blunt vehicle points to placing emphasis on the drag coefficient variation with angle of attack, whereas as the smaller amplitude motion of the slender bodies points to emphasis of the drag coefficient variation with Mach number.

The solution to the body motions from entry to peak dynamic pressure (both options) is approximated as follows:

- a. Mach number variation of the coefficients are assumed negligible.

- b. The effect of flight path curvature is assumed negligible.
- c. The drag variation with angle of attack is accounted for.
- d. The damping due to plunging motion is accounted for.

The assumption of negligible flight path curvature, permits a simplification in the derivation of the moment equations, as the inertial reference frame can be oriented along the velocity vector. The coordinate system used in deriving the moment equations is shown in figure I-26. The inertial axes are  $X_O$ ,  $Y_O$ ,  $Z_O$ , and the body axes  $X_B$ ,  $Y_B$ ,  $Z_B$ . The Euler angles are  $\psi$ ,  $\theta$ ,  $\phi$ , which specify the position of the body axes with respect to the inertial axes. The origin of the body axes is at the center of gravity of the body. The Euler angle sequences consists of a yaw  $\psi$ , a pitch  $\theta$ , and a roll  $\phi$  taken in that order about their respective body axis, and denoted by operation (1), (2) and (3) in figure I-26.

Letting  $\vec{i}$ ,  $\vec{j}$ ,  $\vec{k}$  represent unit vectors along the body axes, the total angular rate is given by

$$\vec{\Omega} = \vec{i} P + \vec{j} Q + \vec{k} R . \quad (46)$$

The Euler angular rates are then given by the following relationships

$$\dot{\psi} = (R \cos \phi + Q \sin \phi) \sec \theta \quad (47)$$

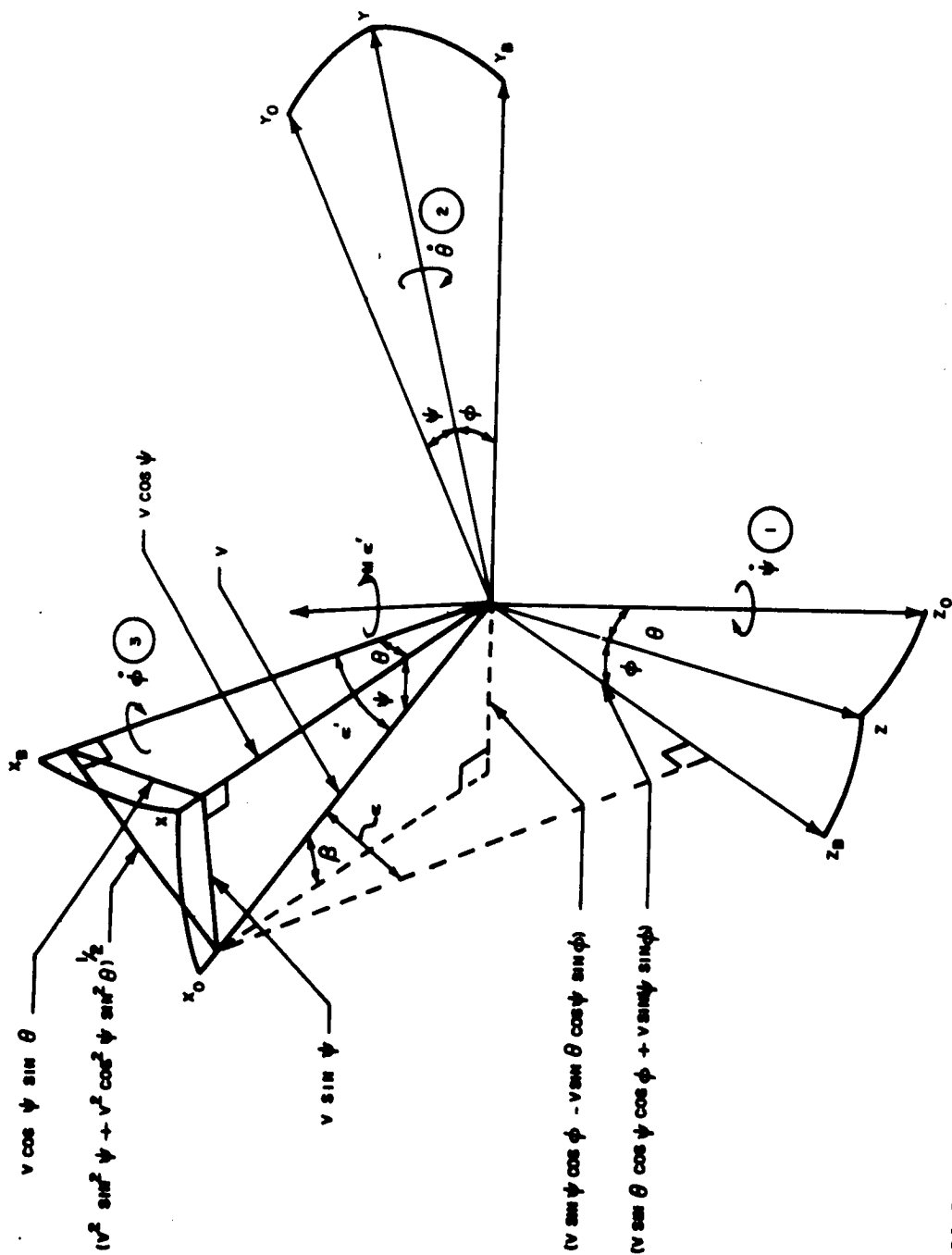
$$\dot{\theta} = (Q \cos \phi - R \sin \phi) \quad (48)$$

$$\dot{\phi} = P + \psi \sin \theta . \quad (49)$$

These rates must be integrated to give the Euler angles which are then used to compute the total angle of attack,  $\alpha'$ , and the aerodynamic coefficients. The magnitude of the total angle of attack  $\alpha'$  can be expressed simply by considering the velocity vector  $V$  resolved into components  $V \sin \psi$  and  $V \cos \psi$  normal and parallel to the intermediate body axis position  $OX$  in figure I-26. If the latter component is itself resolved into components  $V \cos \psi \sin \theta$  and  $V \cos \psi \cos \theta$  normal and parallel to  $OX_B$  respectively, then by means of the inset triangle, the total angle of attack  $\alpha'$  is given by

$$\sin \alpha' = \sqrt{\sin^2 \psi + \cos^2 \psi \sin^2 \theta} . \quad (50)$$

It follows by similar reasoning that the effective angles of pitch and yaw  $\alpha$  and  $\beta$  for the body axis system at completion of the Euler sequence will likewise be specified by the projection of  $\vec{V}$  on axes  $OZ_B$  and  $OY_B$ , respectively. Hence,  $\sin \alpha$  and  $\sin \beta$  are given by the direction cosines of  $\vec{V}$  (or  $OX_O$ ) on body axes  $OZ_B$  and  $OY_B$ , and these are:



64-231

Figure 1-26 COORDINATE SYSTEM FOR DYNAMICS ANALYSIS

$$\sin \alpha = \sin \theta \cos \psi \cos \phi + \sin \psi \sin \phi \quad (51)$$

$$\sin \beta = \sin \psi \cos \phi - \sin \theta \cos \psi \sin \phi \quad (52)$$

Solutions of these equations for  $\alpha$  and  $\beta$  enables the static moment contributions in pitch and yaw to be obtained by use of the pitching moment coefficient appropriate to each angle. However, it is not admissible to perform a separate table lookup for each angle, since the airflow sees only the total angle  $\alpha'$ . It is therefore necessary to obtain  $C_m$  at  $\alpha'$  and then resolve this into two components in the pitch and yaw planes.

The total moment vector lies perpendicular to the plane containing  $\vec{V}$  and  $\vec{i}$  and hence

$$\vec{M} = M' \frac{(\vec{V} \times \vec{i})}{|\vec{V} \times \vec{i}|} \quad (53)$$

where  $m'$  is the scalar value of the moment. The velocity vector is easily deduced by observation of figure I-26, as

$$\vec{V} = V (\vec{i} \cos \alpha' - \vec{j} \sin \beta + \vec{k} \sin \alpha) . \quad (54)$$

Hence, the moment vector is

$$\vec{M} = M' \frac{(\vec{j} \sin \alpha + \vec{k} \sin \beta)}{\sin \alpha'} \quad (55)$$

From equation (54) it is apparent that the transformations to obtain the moment components in the pitch and yaw plane are  $\sin \alpha / \sin \alpha'$  and  $\sin \beta / \sin \alpha'$ . Similarly, the pitching rate vector  $\vec{\dot{\alpha}}'$  is given by

$$\vec{\dot{\alpha}}' = \dot{\alpha}' \left( \vec{j} \frac{\sin \alpha}{\sin \alpha'} + \vec{k} \frac{\sin \beta}{\sin \alpha'} \right) \quad (56)$$

so that the transformations to obtain Q and R are also  $\sin \alpha / \sin \alpha'$  and  $\sin \beta / \sin \alpha'$ . The derivation of the moment equations is simplified if the unit vector  $\vec{j}'$  which lies along  $\vec{M}$  is introduced and  $\vec{k}'$  which is normal to the two vectors,  $\vec{i}$  and  $\vec{j}'$ . Then,

$$\vec{M} = \frac{d\vec{H}}{dt} = \frac{\partial \vec{H}}{\partial t} + \vec{\Omega} \times \vec{H} \quad (57)$$

where

$$\vec{\Omega} = \vec{i} P + \vec{j}' \dot{\alpha}' \quad (58)$$

$$\vec{H} = \vec{i} P I_x + \vec{j}' (\dot{\alpha}' + \dot{\gamma}_L) I_y \quad (59)$$

The introduction of the flight path curvature into the moment equation (58) would at first appear contradictory to the assumptions mentioned earlier. However, its inclusion here is not to account for changes in the flight path but to keep the coupling between the lift generated at angle of attack and the body dynamics. The importance of this coupling resulting in damping due to the plunging motion of the vehicle, has been established by many investigators, e. g., Friedrich and Dore (ref. I-59), and Allen (ref. I-60).

The moment vector, after performing the vector algebra, is

$$\vec{M} = \vec{j}' I_y (\ddot{\alpha}' + \ddot{\gamma}') + \vec{k}' P \dot{\alpha}' (I_y - I_x) \quad (60)$$

The  $\ddot{\gamma}'$  term is principally determined by the lift vector, which lies in the plane of the total angle of attack, and the previously mentioned investigators have shown that

$$\ddot{\gamma}' \approx \frac{\dot{L}}{m V_\infty} = \frac{C_{L_\alpha} q A \dot{\alpha}'}{m V_\infty} \quad (61)$$

With the above approximation for  $\ddot{\gamma}'$ , the moment vector is given by

$$\vec{M} = \vec{j}' I_y \left( \ddot{\alpha}' + \frac{C_{L_\alpha} q A \dot{\alpha}'}{m V} \right) + \vec{k}' P \dot{\alpha}' (I_y - I_x) \quad (62)$$

The unit vectors  $\vec{j}'$  and  $\vec{k}'$  are readily shown to be

$$\vec{j}' = \vec{j} \frac{\sin \alpha}{\sin \alpha'} + \vec{k} \frac{\sin \beta}{\sin \alpha'} \quad (63)$$

$$\vec{k}' = -\vec{j} \frac{\sin \beta}{\sin \alpha'} + \vec{k} \frac{\sin \alpha}{\sin \alpha'} \quad (64)$$

Hence, the moment expression takes the form:

$$\begin{aligned} \vec{M} = \vec{j} & \left[ I_y \left( \ddot{\alpha}' + \frac{C_{L_\alpha} q A \dot{\alpha}'}{m V} \right) \frac{\sin \alpha}{\sin \alpha'} - \frac{\sin \beta}{\sin \alpha'} (I_y P \dot{\alpha}' - I_x P \dot{\alpha}') \right] \\ & + \vec{k} \left[ I_y \left( \ddot{\alpha}' + \frac{C_{L_\alpha} q A \dot{\alpha}'}{m V} \right) \frac{\sin \beta}{\sin \alpha'} + \frac{\sin \alpha}{\sin \alpha'} (I_y P \dot{\alpha}' - I_x P \dot{\alpha}') \right] \end{aligned} \quad (65)$$

while also,

$$\begin{aligned} \vec{M} = \vec{j}' \left( C_m q Ad + C_{mq} \dot{a}' \frac{q Ad^2}{2V} \right) + \vec{k} \frac{\sin \beta}{\sin \alpha'} \left( C_m q Ad + C_{mq} \dot{a}' \frac{q Ad^2}{2V} \right) \\ = j \frac{\sin \alpha}{\sin \alpha'} \left( C_m q Ad + C_{mq} \dot{a}' \frac{Ad^2}{2V} \right) + k \frac{\sin \beta}{\sin \alpha'} \left( C_m q Ad + C_{mq} \dot{a}' \frac{q Ad^2}{2V} \right) \end{aligned} \quad (66)$$

Hence, the final expression for the moment components is

$$I_y \dot{Q} = q Ad \left\{ C_m \frac{\sin \alpha}{\sin \alpha'} + Q \left[ \frac{d}{2V} C_{mq} - \frac{I_y C_{L\alpha}}{m V d} \right] \right\} + (I_y - I_x) PR \quad (67)$$

$$I_y \dot{R} = q Ad \left\{ C_m \frac{\sin \beta}{\sin \alpha'} + R \left[ \frac{d}{2V} C_{mq} - \frac{I_y C_{L\alpha}}{m V d} \right] \right\} + (I_x - I_y) PQ \quad (68)$$

The third, or L, moment equation is set arbitrarily to zero since the study is confined to an idealized axisymmetric body with  $I_Y = I_Z$ , no offset center of gravity and no fins. A constant spin rate is assumed to exist, so that  $P = 0$ .

A predictor-corrector scheme (sometimes called the modified Adams-Boshforth method) is used for the numerical integration. It possesses an intrinsic advantage in that an estimate for the truncation error is available at each stage. If this error is large, then the integration interval is decreased by some pre-assigned factor and if it is small then the interval is increased by some factor. In this sense the method chooses its own interval for integration. This scheme is not self starting; a Runge-Kutta procedure is used with intervals which are small.

Below peak dynamic pressure, the dynamic calculations described above can be used if desired. In the event, the motion is of large angle of attack at peak dynamic pressure, and the aerodynamic coefficients do not change markedly with Mach number, then the above approach to estimate the vehicle's performance below peak dynamic pressure is reasonable. If, however, at peak dynamic pressure, the angle of attack envelope is small enough to utilize linearized coefficients, then provision is made to optionally switch over to a linear analysis which couples the force and moment equations and accounts for Mach number effects.

Before proceeding to a description of the linearized solution, the basic elements of the first option are now recapitulated:

- a. No Mach number effects (a way in which Mach effects can be introduced is discussed later)
- b. An idealized axisymmetric body is assumed, with  $I_Y = I_Z$
- c. Constant Spin Rate;  $P = 0$
- d. The moment and force equations are coupled two ways:
  - 1) The drag variation due to angle of attack is included
  - 2) The effect of lift on the body dynamics is approximately accounted for.

A summary of the equations programed for solution follows:

a.  $\Sigma L = 0$

b.  $\Sigma M = q Ad \left[ C_m \frac{\sin \alpha}{\sin \alpha'} + \left( \frac{d}{2V} C_{mq} - \frac{I_y C_{La}}{m V d} \right) (Q) \right]$

c.  $\Sigma N = q Ad \left[ C_m \frac{\sin \beta}{\sin \alpha'} + \left( \frac{d}{2V} C_{mq} - \frac{I_y C_{La}}{m V d} \right) (R) \right]$

d.  $\sin \alpha' = (\sin^2 \psi + \cos^2 \psi \sin^2 \theta)^{1/2}$

e.  $\sin \alpha = (\sin \theta \cos \psi \cos \phi + \sin \psi \sin \phi)$

f.  $\sin \beta = (\sin \psi \cos \phi - \sin \theta \cos \psi \sin \phi)$

g.  $C_m = - \left( \frac{X_{CP}}{d} - \frac{X_{CG}}{d} \right) C_N$

h.  $\dot{Q} = \frac{\bar{M}}{I_y}$

i.  $\dot{R} = \frac{\bar{N}}{I_z}$

j.  $\bar{M} = \Sigma M + (I_z - I_x) PR$

k.  $\bar{N} = \Sigma N + (I_x - I_y) PQ$

l.  $\dot{\psi} = (R \cos \phi + Q \sin \phi) \sec \theta$

m.  $\dot{\theta} = (Q \cos \phi - R \sin \phi)$

n.  $\dot{\phi} = P + \dot{\psi} \sin \theta$



### c. Linearized Equations of Motion

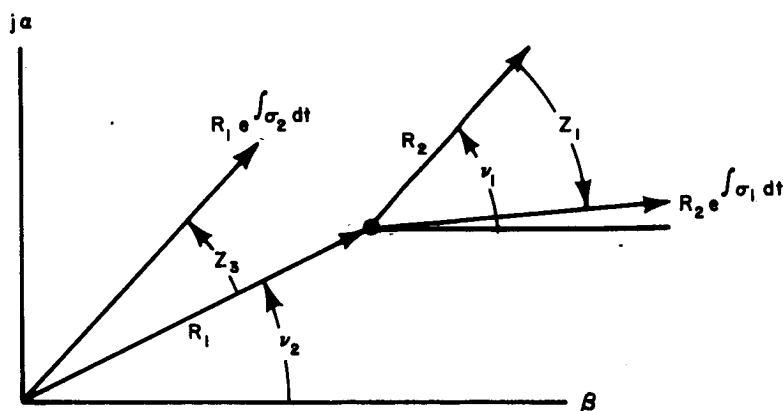
For vehicles which have small angles of attack, the use of linearized methods can simplify the necessary inputs and the computer program. Consequently, an option is provided wherein a linearized solution to a vehicle which is pitching and spinning can be used.

A number of investigators considered the linearized solution of an axysymmetric vehicle with spin. Nicolaides (ref. I-61) and Nelson (ref. I-62) have considered the motion for vehicles at constant velocity. Garber (ref. I-63) and Migotsky (ref. I-64) have considered the motion of an entry vehicle with spin. In general, the solutions indicate that the motion is epicyclic consisting of two vectors which rotate in different directions and with different rates. The solution for the angle of attack and side slip angles is given by Garber in equations (74) and (75) of reference I-63. These formulas are summarized below:

$$\alpha = e^{\int \sigma_1 dt} [A_1 \cos Z_1 + A_2 \sin Z_1] + e^{\int \sigma_2 dt} [A_3 \cos Z_2 + A_4 \sin Z_2] \quad (69)$$

$$\beta = e^{\int \sigma_1 dt} [B_1 \cos Z_1 + B_2 \sin Z_1] + e^{\int \sigma_2 dt} [B_3 \cos Z_2 + B_4 \sin Z_2] \quad (70)$$

The solution is more readily understood if one considers the following diagram:



The total angle of attack is generated by the two vectors  $R_1$  and  $R_2$  revolving at different directions and at different rates. The initial positions of these vectors can be specified as  $\nu_1$  and  $\nu_2$ . At  $t = 0$  the vectors have magnitude  $R_1$  and  $R_2$ , however, at subsequent times their values are  $R_1 e^{\int \sigma_1 dt}$  and  $R_2 e^{\int \sigma_2 dt}$  as a result of damping.

At a subsequent time the angular position of the two vectors are  $Z_1 - \nu_1$  and  $Z_3 + \nu_2$  so that the angle of attack expression takes the form of

$$\alpha = R_1 e^{\int \sigma_2 dt} \sin (Z_3 + \nu_2) - R_2 e^{\int \sigma_1 dt} \sin (Z_1 - \nu_1) \quad (71)$$

and the side slip vector takes the form of

$$\beta = R_1 e^{\int \sigma_2 dt} \cos (Z_3 + \nu_2) + R_2 e^{\int \sigma_1 dt} \cos (Z_1 - \nu_1) . \quad (72)$$

The total angle of attack is given by

$$\alpha_R^2 = \alpha^2 + \beta^2 . \quad (73)$$

Letting

$$\sigma_1 = \lambda - \Delta\lambda \quad (74)$$

and

$$\sigma_2 = \lambda + \Delta\lambda \quad (75)$$

the total angle of attack expression can be written as

$$\alpha_R^2 = e^{2 \int \lambda dt} \left\{ R_1^2 e^{2 \int \Delta\lambda dt} + R_2^2 e^{-2 \int \Delta\lambda dt} + 2 R_1 R_2 \cos (Z_1 + Z_3 + \nu_1 - \nu_2) \right\} .$$

Considering the envelope value, only the total angle of attack envelope reduces to the form

$$\frac{\alpha_R}{\alpha_{R_0}} = e^{\int \lambda dt} \frac{\left( R_1 e^{\int \Delta\lambda dt} + R_2 e^{-\int \Delta\lambda dt} \right)}{R_1 + R_2} \quad (77)$$

where  $\alpha_{R_0}$  is the angle of attack at  $T = 0$ . The form of equation (77) can be further simplified by substituting

$$K = \frac{R_1 - R_2}{R_1 + R_2} \quad (78)$$

so that

$$\frac{a_R}{a_{R_0}} = e^{\int \lambda dt} \frac{\left[ \frac{\int \Delta \lambda dt}{(1+K)e} + \frac{-\int \Delta \lambda dt}{(1-K)e} \right]}{2} \quad (79)$$

This result is the same as that obtained by Migotsky. For the case of zero spin, the result reduces to the work of Sommer and Tobak (ref. I-65). The expression  $\Delta \lambda$  is

$$\Delta \lambda = \frac{\frac{I_x}{I_y} \frac{P}{2} \frac{\rho AV}{m} \left[ C_{L\alpha} + \frac{C_{mq}}{2\sigma^2} \right]}{4 \sqrt{\omega_n^2 + \left( \frac{I_x P}{2I_y} \right)^2}} \quad (80)$$

and the expression for  $\lambda$  is

$$\lambda = -\frac{1}{4} \frac{\rho AV}{m} \left( C_{L\alpha} - \frac{C_{mq}}{2\sigma^2} \right) - \frac{1}{2} \frac{d}{dt} \frac{\sqrt{\omega_n^2 + \left( \frac{I_x P}{2I_y} \right)^2}}{\sqrt{\omega_n^2 + \left( \frac{I_x P}{2I_y} \right)^2}} \quad (81)$$

Substituting these expressions into the angle of attack envelope formulas, one obtains,

$$\frac{a_R}{a_{R,o}} = \left( \frac{a_R}{a_{R,o}} \right)_{P=0} \left[ \frac{1 + \left( \frac{I_x P}{2 I_y \omega_n} \right)_0^2}{1 + \left( \frac{I_x P}{2 I_y \omega_n} \right)^2} \right]^{1/4} \frac{\left[ (1+K) e^{\int \Delta \lambda dt} + (1-K) e^{-\int \Delta \lambda dt} \right]}{2} \quad (82)$$

The quantity K is called the "space motion factor". Nelson (ref. I-62) describes the influence of K on the nature of the resultant motion in detail.

A summary of the equations programed follows:

$$a. \quad \left( \frac{a_R}{a_{R,o}} \right)_{P=0} = \left[ \frac{-C_{m_{a,0}} q_0}{-C_{m_a} q} \right]^{1/4} e^{\frac{1}{2} \int_0^t P_1 V dt}$$

$$b. \quad P_1 = - \frac{\rho A}{2m} \left( C_{L_a} - \frac{C_{m_q}}{2 \sigma^2} \right)$$

$$c. \quad q = \frac{1}{2} \rho V^2$$

$$d. \quad \frac{a_R}{a_{R,o}} = \left( \frac{a_R}{a_{R,o}} \right)_{P=0} \left[ \frac{1 + \left( \frac{I_x P}{2 I_y \omega_n} \right)_0^2}{1 + \left( \frac{I_x P}{2 I_y \omega_n} \right)^2} \right]^{1/4} \left[ \frac{(1+K) e^{\int_0^t \Delta \lambda dt} + (1-K) e^{-\int_0^t \Delta \lambda dt}}{2} \right]$$

$$e. \quad \sigma^2 = \frac{I_y}{m d^2}$$

$$f. \quad \omega_n^2 = - \frac{C_{m_a} q A d}{I_y}$$

$$g. \Delta \lambda = \frac{\frac{I_x}{I_y} \frac{P}{2} \frac{\rho AV}{m} \left[ C_{L\alpha} + \frac{C_{mq}}{2\sigma^2} \right]}{4 \sqrt{\omega_n^2 + \left( \frac{I_x P}{2I_y} \right)^2}}$$

## 5. Trajectory Block Evaluation

### a. Angle-of-Attack Effects

The significance of the effects of angle-of-attack variations is largely dependent on the shapes. The M1 vehicle exhibits a large variation of the hypersonic drag coefficient with angle of attack, as shown in the table below.

$\alpha$	$C_D$
0	1.45
30	1.20
60	0.44
90	0.54
120	0.85
150	0.84
180	0.60

Early results showed that with high spin rates, large angles of attack resulted at peak dynamic pressure. To verify these results, six-degree-of-freedom solutions were run which indicated that much smaller angles of attack were occurring. Consequently, it was deemed necessary to account for the angle of attack variation of the drag coefficient, coupling the moment and force equations. At the same time the damping due to the plunging motion of the vehicle was added as discussed earlier. A comparison of the results at peak dynamic pressure of the coupled and uncoupled solutions is shown in the table I-24.

TABLE I-24

## CONDITIONS AT PEAK DYNAMIC PRESSURE

	Uncoupled		Coupled	
	Angle of Attack (degrees)	Dynamic Pressure lb/ft <sup>2</sup>	Angle of Attack (degrees)	Dynamic Pressure lb/ft <sup>2</sup>
M1-AB-1	28	150	23	168
M1-A3-2	21	802	25	850
M1-A3-3	28	127	22	145
M1-A3-6	126	149	40	267

A typical comparative summary of results obtained by a particle trajectory, a six-degree-of-freedom solution and the modified four degree-of-freedom solution programed for this study is shown in table I-25.

The results shown in table I-25 indicate that accounting for the drag variation with angle of attack had a serious effect on the peak heating and loads, especially for the entry case M1-A1-2 where the flight path angle is  $\gamma_e = -90$  degrees. It was a result of these differences which led to the development of the coupled, four-degree-of-freedom solution used for the final calculations.

Comparisons with six-degree-of-freedom solutions were done for several cases. In these comparisons (shown in table I-25) the six-degree-of-freedom and approximate solutions utilized the same aerodynamic coefficients. For both solutions, identical atmospheres and a spherical non-rotating planet was assumed.

The comparisons are shown in figures II-2 and II-4 of Volume II. The angle of attack envelopes show excellent agreement down to peak dynamic pressure. Below peak dynamic pressure, the angle-of-attack envelopes both exhibit a limit cycle behaviour. However, the six-degree-of-freedom solution exhibited larger envelopes as the spin rate was increased.

TABLE I-25

## TRAJECTORY COMPARISONS

Flight Event	M1-A1-1			M1-A1-2		
	Particle Trajectory	Six Degree of Freedom	Four Degree of Freedom	Particle Trajectory	Six Degree of Freedom	Four Degree of Freedom
Angle of Attack at Peak Stagnation Heating (degrees)	-----	-----	31	-----	-----	41
Angle of Attack at Peak Dynamic Pressure (degrees)	-----	27	25	-----	35	33
Peak Stagnation Point Convective Heating (Btu/ft <sup>2</sup> -sec)	69	-----	79	167	-----	200
Peak Stagnation Point Radiative Heating (Btu/ft <sup>2</sup> -sec)	6.3	-----	7.9	84	-----	122
Peak Dynamic Pressure (lb/ft <sup>2</sup> )	204	232	228	1200	1431	1421
Altitude at Mach 2.5 (feet)	73,200	72,100	73,700	24,100	21,200	22,500

TABLE I-26

## LINEAR SOLUTION COMPARISONS

Flight Event	M1-A1-1			M1-A1-6		
	Linear	4 degree	6 degree	Linear	4 degree	6 degree
Angle of Attack at Peak Dynamic Pressure	25	25	27	39	39	39
Minimum Angle of Attack Envelope Value (degrees)	12	20	24	26	27	33
Mach Number for Rapid Divergence	1.75	Limit Cycle	Limit Cycle	4.15	Limit Cycle	Limit Cycle

## b. Linear Solution

One of the major difficulties with the linear solution is its limited applicability. For the study of slender missiles with small angle of attack oscillations, the linear approach is highly useful. However, in the present study, two factors led to serious limitations in the use of the linear approximation:

- 1) The entry conditions studied considered an angle of attack of 179 degrees, which in the predominant number of vehicles considered led to angles of attack at peak dynamic pressure outside the range of applicability of linear coefficients.
- 2) The majority of the vehicles studied were relatively blunt and had poor aerodynamic characteristics at low Mach numbers. This type of vehicle relies primarily on the nonlinearity of the coefficients to prevent it from tumbling at low speed; the nature of its dynamic motion is often referred to as a limit cycle. The vehicle that limit cycles is dynamically unstable at small angles of attack, but develops a stable oscillation at high angle of attack. Consequently, a linear analysis could fail completely in characterizing the vehicle's performance, giving misleading results.

A number of comparative cases were calculated to illustrate the nature of the solution obtained by the linear approximation. The results shown in table I-26 are typical of the differentiation the linearized and four and six degree of freedom calculations.

## c. Summary Evaluation

The approximate four-degree-of-freedom solutions yielded good agreement with six-degree-of-freedom calculations, in every respect, for the flight conditions and shapes compared. The computer time for the approximate method is about 20 percent and the computer storage is about 30 percent of that required for the full six-degree-of-freedom solution.

Limitations of the approximate method could arise at very large spin rates at angle of attack such that a ballistic vehicle could generate sustained lift and change the trajectory. It may be recalled, that in the approximate solution, the effects of lift on the flight path were omitted.

Another limit comes from the approximation which neglects the angle-of-attack contribution due to trajectory curvature. Hence, an entry condition of zero angle of attack, with zero rates, will result in zero angle of attack throughout; similarly a 180-degree angle of attack with



zero rates would maintain the 180-degree angle of attack throughout. The probability of entry under these conditions is essentially zero; nevertheless, these cases are frequently done in studies. As a result of this behavior, a benefit is incurred by being able to use the program for particle trajectories, if so desired.

## D. STRUCTURES BLOCK

### 1. Introduction

The purpose of the structures block is to provide a means of calculating realistic elemental weight of major structural members. Analytical expressions were developed from an analytical or empirical description of a critical mode of structural failure to adequately describe the elemental weights. The major structural members considered in this study are:

- 1) The external structure which is the aerodynamic load bearing structure supporting the thermal protection system (heat shield) during entry
- 2) The internal structure which serves as the load-carrying member for the residual weight and parachute reaction system
- 3) The retardation (parachute) system which serves as a high-drag load-carrying decelerator
- 4) The impact attenuation system which serves as the energy absorber during impact.

The latter three major structural members will constitute the internal package systems described herein

#### 1) External Structure

A typical configuration for the external load-bearing structure analysis is shown in figure I-27. It is evident from this figure that the structure can best be described by three primary structural sections: (1) a spherical cap (2) a cone, and (3) a cylinder. No general expressions for describing the thickness and weight of rings, toroidal sections, or any other structural fasteners will be attempted here. The reason for this is that the stresses in most structures are directly related to the method of loading and an exact geometry which is usually dictated by design considerations.

Also shown in figure I-27 is the nomenclature for definition of pertinent sections in defining the shapes generated.

The analysis, and consequently the weight expression, for the external structure employed the use of two types of shell construction: (1) sandwich (honeycomb) shell, and (2) stiffened shell. The sandwich shell construction provides an excellent stability-strength to

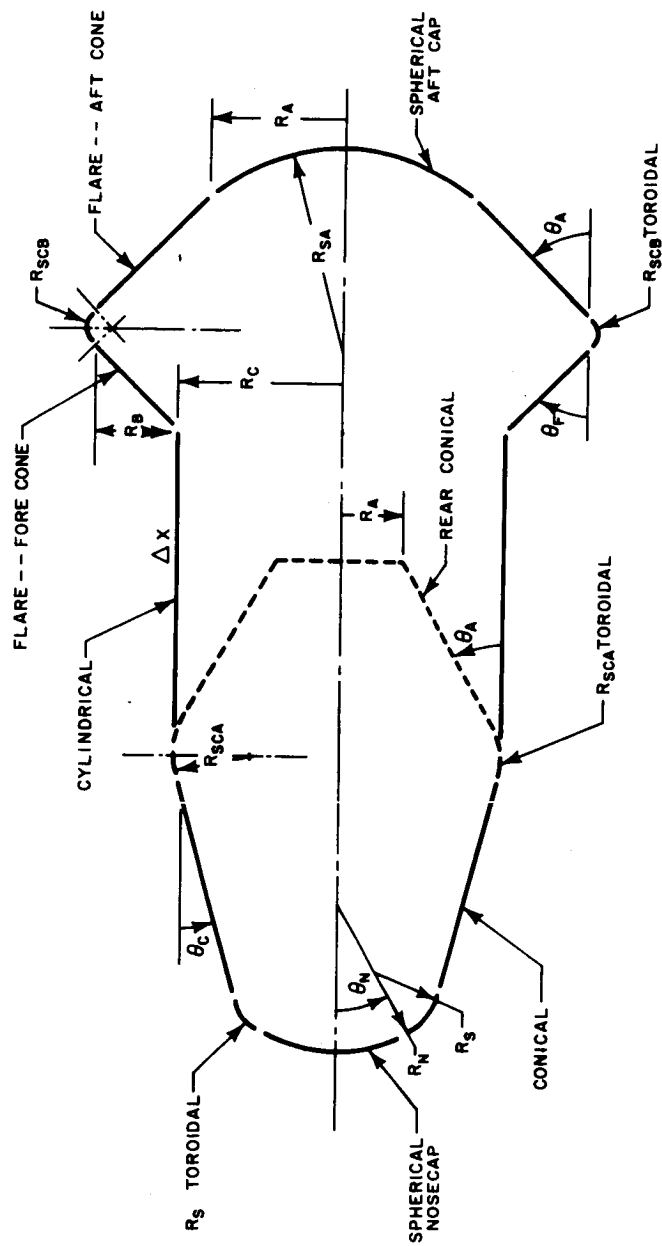


Figure 1-27 SHAPE PARAMETERS

64-232

weight ratio for both static and dynamic loading conditions. The selection of a stiffened (monocoque) shell was incorporated to make the program more general, in that a larger range of shell materials could be handled and a radiative (hot structure) design concept could be investigated in comparison to a heat shield-substructure (cold structure) design concept.

## 2) Internal Package Systems

As stated earlier, the internal package systems consist of an internal structure, retardation system, and an impact attenuation system. The analysis of each system is fully described in its representative section in the following text. The selection of the internal structural configuration is based on the determination of an internal weight to adequately represent a structure supporting the internal package. It is impossible to evolve a general expression for any type of structure to support any type of loading. Therefore, a specific type of structure had to be selected to fit within the geometry specified and to be a function of the loads and force imposed on the capsule during the flight performance. A cylindrical shape was selected to represent the structural support for the residual weight and the impact attenuation system, and a cone shape to represent the structural support and redistribution scheme for the parachute reaction system.

The retardation systems considered in this study consist of a two-chute system; a drogue chute deployed, usually, at Mach 2.5 and a main chute deployed at Mach 0.8. The selection of this retardation system evolved from a series of studies conducted on other systems indicating that a lightweight design would result from a two-chute system. Another reason is that this parachute system is within the state-of-the-art of recovery systems.

Since the contractual work statement specified the use of a passive (crushable material) impact attenuation system, and that the capsule must be capable of impacting up to 45 degrees from the vertical, the analysis and design scheme followed in order. To simplify the design interface with the internal structure and to develop a more general design approach, a spherical cap segment was employed. Analysis of the impact attenuation considered several crushable types of materials commonly used as impact attenuators.

## 2. Spherical Cap Sandwich Shell

### a. Introduction

Analyses of a spherical sandwich cap have been derived and the optimum and nonoptimum weight expression developed. The analyses considered five modes of failure in the derivation of these expressions; they are

- 1) General instability
- 2) Yielding -- face sheets
- 3) Core crushing
- 4) Dimpling -- face sheets
- 5) Wrinkling.

However, only the first three modes of failure were used in the developed expression. Since dimpling of face sheets depends only on the cell size, this criteria can be satisfied through core crushing in that it is a function of a ratio of ribbon thickness to cell size. Wrinkling of the face sheets was not considered a critical mode of failure since core crushing criteria and minimum allowable core density would give the core sufficient strength such that the face sheets would fail in general instability first.

Since little test data and theoretical analysis is known on buckling of sandwich spherical caps, derivation of the general instability criteria was limited to transformation of isotropic (homogenous) buckling data to sandwich shells. Transformation of these data employed the use of equivalent bending and extensional rigidity functions for homogeneous and sandwich shells. A comparison with a more rigorous transformation by expansion of the strain energy expression proves that this method is adequate. Optimum expressions are developed for the core thickness and face sheet thickness with respect to the total sandwich cap unit weight. These expressions were derived so that optimum design would be obtained if face sheet yielding or minimum gage were not the critical criterion. Hence, optimum weight will only occur when face sheet material has a high yield stress capability.

b. Nomenclature

B	Extensional rigidity, $\frac{Et}{(1 - \nu^2)}$
D	Bending rigidity, $\frac{EI}{(1 - \nu^2)}$
E, $E_f$	Young's modulus of elasticity (psi)
H	Height of spherical cap (inches)
K	Constant for unit weight of adhesive in sandwich construction (lb/ft <sup>2</sup> )
P	Uniform applied pressure load (psi)
$q_{CR}$	Classical spherical shell buckling pressure load, $\frac{2E}{[3(1 - \nu^2)]^{1/2}} \left(\frac{t}{R}\right)^2$ (psi)
R	Radius of spherical cap (inches)
t	Thickness of isotropic shell (inches)
$t_f$	Thickness of face sheet (inches)
$t_c$	Thickness of core (inches)
W	Unit weight of sandwich shell (lb/ft <sup>2</sup> )
$\nu, \nu_f$	Poisson's ratio homogeneous shell and face sheets
$\lambda$	Geometric parameter, $2 [3(1 - \nu^2)]^{1/4} \left(\frac{H}{t}\right)^{1/2}$
$\rho_f$	Density of face sheet (lb/ft <sup>3</sup> )
$\rho_c$	Density of core (lb/ft <sup>3</sup> )
$\rho_R$	Density of core material (lb/ft <sup>3</sup> )

$\sigma_{cyf}$  Compressive yield stress of face sheet (psi)

$\sigma_{cyR}$  Compressive yield stress of core material (psi)

### c. Derivation of Core Thickness

Although a number of experiments have been performed on snap buckling of isotropic (homogeneous) spherical caps, no test results appear to be available on buckling of sandwich spherical caps. Therefore, test results on homogeneous shells are generally used as the basis for design. To use these results, it is necessary to interpret the parameters used for homogeneous spherical caps in terms of parameters of sandwich shells. This is accomplished by transformation of isotropic bending and extensional rigidity parameters to sandwich shell equivalent parameters.

Usually, most general instability test data and theoretical analyses of homogeneous shells are presented in terms of nondimensional parameters (ref. I-66 to I-68), a geometric parameter  $\lambda$ , and a pressure ratio parameter  $P/q_{CR}$ , of

$$\lambda = 2 [3(1 - \nu^2)]^{1/4} \left(\frac{H}{t}\right)^{1/2}$$

and

$$P/q_{CR} = \frac{P [3(1 - \nu^2)]^{1/2}}{2E} \left(\frac{R}{t}\right)^2$$

where

$P$  = uniform applied pressure

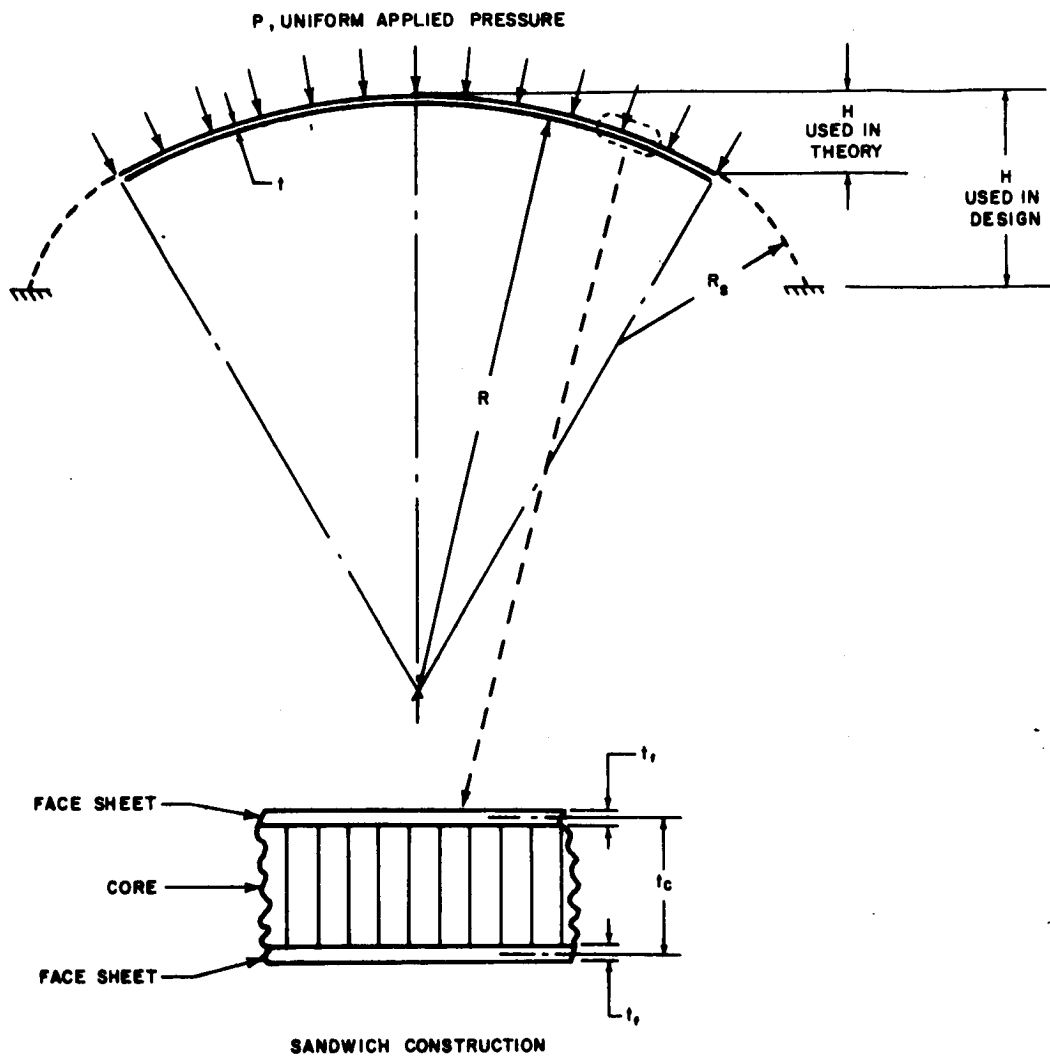
$q_{CR}$  = classical spherical shell buckling pressure

$t$  = shell thickness

$H, R$  = geometric parameters, defined in figure I-28.

We see that  $\lambda$  may be rewritten as

$$\lambda = \sqrt{2} \left(\frac{B}{D}\right)^{1/4} (1 - \nu^2)^{1/4} H^{1/2}$$



04-288

SANDWICH CONSTRUCTION

Figure 1-28 SPHERICAL CAP GEOMETRY



if

$$B = \frac{E t}{(1 - \nu^2)} \quad \text{Extensional Rigidity}$$

and

$$D = \frac{E t^3}{12 (1 - \nu^2)} \quad \text{Bending Rigidity}$$

The equivalent extensional and bending rigidities for a sandwich shell, neglecting the core and moment of inertia of the face sheets, are

$$B = \frac{2 E_f t_f}{(1 - \nu_f^2)}$$

$$D = \frac{E_f t_f t_c^2}{2 (1 - \nu_f^2)}$$

where  $t_f$  and  $t_c$  are defined in accordance with figure I-28.

Hence, for a sandwich shell,  $\lambda$  becomes

$$\lambda = 2 (1 - \nu_f^2)^{1/4} \left( \frac{H}{t_c} \right)^{1/2} .$$

Similarly, the pressure ratio parameters may be rewritten as

$$P/q_{CR} = \frac{PR^2}{4 (BD)^{1/2} (1 - \nu^2)^{1/2}}$$

Again applying the sandwich shell extensional and bending rigidities, this pressure ratio parameter becomes

$$P/q_{CR} = \frac{PR^2 (1 - \nu_f^2)^{1/2}}{4 E_f t_c t_f} .$$

The above transformation can be more rigorously derived by comparisons of the strain energy expansion for homogeneous and sandwich shells (ref. I-66). In both methods of transformation, it is assumed that the core is sufficiently rigid so that transverse shear

deformation has a negligible influence on the buckling load. The expressions, and consequently the correlations, would not be expected to hold for relatively weak sandwich cores.

Figure I-29 presents test data on snap buckling of homogeneous spherical caps under external pressure (ref. I-67). The lower bound of these test data can be represented by the relationship

$$P/q_{CR} = \frac{1.1}{\lambda^{2/3}} \quad .$$

Applying this relationship to the above derivation for sandwich shells, we find

$$P = \frac{2.78 E_f (t_c)^{4/3} t_f}{H^{1/3} R^2 (1 - \nu_f^2)^{2/3}} \quad .$$

Hence the core thickness becomes

$$t_c = 0.465 (1 - \nu_f^2)^{1/2} \left( \frac{P}{E_f t_f} \right)^{3/4} H^{1/4} R^{3/2}, \text{ in.} \quad .$$

In terms of face sheet thickness, the above expression may be written as

$$t_c = 0.36 (1 - \nu_f^2)^{2/3} \left( \frac{P}{E_f} \right)^{1/4} \frac{H^{1/3}}{t_c^{4/3}} R^2, \text{ in.}$$

The geometric parameters H and R in the above equations for core and face sheet thickness can be expressed in terms of the general program geometric parameter as

$$H = R_c \left\{ \frac{R_N}{R_c} (1 - \cos \theta_N) + \frac{R_S}{R_c} \cos \theta_N \left[ 1 - \frac{\sin \theta_c}{\sin (90^\circ + \theta_N)} \right] \right\} \quad .$$

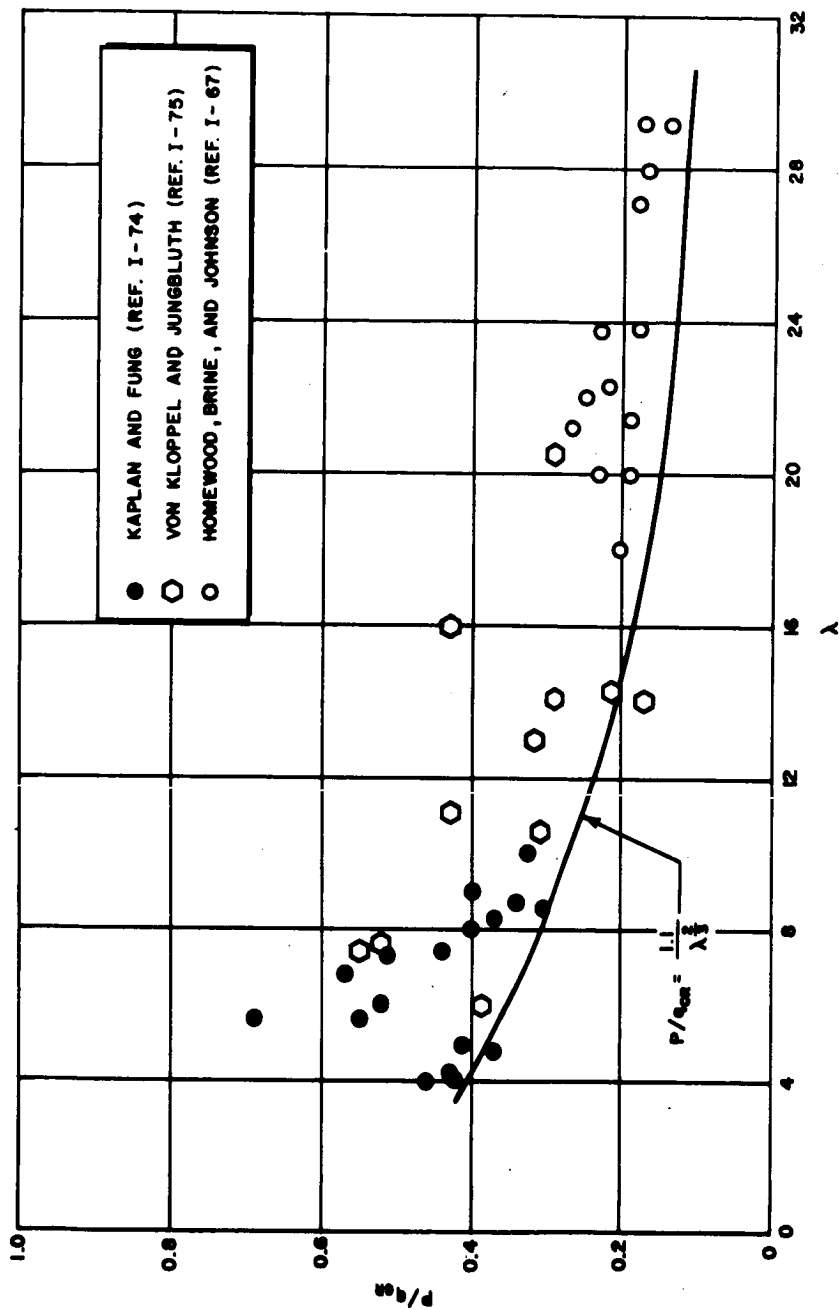


Figure 1-29 EXPERIMENTAL BUCKLING OF SPHERICAL SHELLS

64-234

Note that the above expression for H includes the height of the short toroidal section defined by  $R_S$ . This results in a conservative solution for the spherical cap and accounts for uncertainties in buckling of spherical-toroidal caps.

d. Derivation of Optimum Expressions

1) Optimization of weight with respect to face sheet thickness

The unit area weight expression for a honeycomb sandwich structure can be written as follows:

$$W = \frac{1}{12} \rho_f (2 t_f) + \frac{1}{12} \rho_c (t_c) + K, \text{ lb/ft}^2$$

where  $\frac{1}{12}$  is used to convert the inch unit of  $t_f$  and  $t_c$  to foot units, and K is unit weight of adhesive material.

Or,

$$W = \frac{1}{6} \rho_f t_f + \frac{1}{12} \rho_c t_c + K, \text{ lb/ft}^2 .$$

Let

$$K_{11} = \frac{1}{6} \rho_f$$

and

$$K_{22} = \frac{\rho_c}{12} \left[ 0.465 (1 - \nu_f^2)^{1/2} \left( \frac{P_{CR}}{E_f} \right)^{3/4} H^{1/4} \left( \frac{R_N}{R_C} \right)^{3/2} \right] R_C^{3/2} .$$

Now the unit area weight expression can be written as

$$W = K_{11} t_f + \frac{K_{22}}{t_f^{3/4}} + K, \text{ lb/ft}^2.$$

Optimum weight (minimum) can be determined from the condition

$$\frac{\partial W}{\partial t_f} = 0;$$

$$\frac{\partial W}{\partial t_f} = K_{11} - \frac{3}{4} K_2 \frac{1}{t_f^{7/4}} = 0.$$

Thus,

$$t_{f \text{ opt}} = \left[ \frac{3 K_{22}}{4 K_{11}} \right]^{4/7}, \text{ in.}$$

## 2) Optimization of weight with respect to core thickness

The optimum core thickness expression will be that which is required to complement the optimum face sheet thickness for the stability requirement. This thickness can therefore be expressed as

$$\frac{1}{12} \rho_c t_{c \text{ opt}} = \frac{K_{22}}{t_{f \text{ opt}}^{3/4}}$$

$$t_{c \text{ opt}} = \frac{12}{\rho_c} \frac{K_{22}}{t_{f \text{ opt}}^{3/4}}$$

$$t_{c \text{ opt}} = \frac{12 K_{22}}{\rho_c} \left[ \frac{1}{\left( \frac{3 K_{22}}{4 K_{11}} \right)^{4/7}} \right]^{3/4}$$

or,

$$t_{c \text{ opt}} = \frac{12 K_{22}}{\rho_c} \left[ \frac{4 K_{11}}{3 K_{22}} \right]^{3/7}, \text{ in.}$$

### 3) Optimum weight expression

The optimum weight expression is merely the sum of the optimum face sheet weight, core weight, and adhesive weight on a unit area basis.

$$W_{\text{opt}} = \frac{1}{6} \rho_f t_{f_{\text{opt}}} + \frac{1}{12} \rho_c t_{c_{\text{opt}}} + K, \text{ lb/ft}^2.$$

$$W_{\text{opt}} = K_{11} \left[ \frac{3K_{22}}{4K_{11}} \right]^{4/7} + \frac{\rho_c}{12} \left\{ \frac{12K_{22}}{\rho_c} \left[ \frac{4K_{11}}{3K_{22}} \right]^{3/7} \right\} + K$$

$$W_{\text{opt}} = 2.36 K_{11} \left[ \frac{3K_{22}}{4K_{11}} \right]^{4/7} + K, \text{ lb/ft}^2.$$

#### c. Limitations

##### 1) Yielding criteria

The face sheet thickness must satisfy yielding criteria based on simple membrane stress for spherical shells

$$\sigma_{CY_f} = \frac{PR}{4t_f}, \text{ psi}$$

or

$$t_f = \frac{PR}{4\sigma_{CY_f}}, \text{ in.}$$

This equation assumes that one half of the external pressure load is transmitted to the inner face sheet. Hence validity of this criteria is only applicable for large  $R/t_c$  shells, i.e., thin shell theory.

## 2) Core crushing

An empirical equation was developed to fit the test data for most aluminum and steel core materials. The equation arrived at is

$$\rho_c = 0.22 \rho_R (P/\sigma_{CYR})^{0.588}$$

where

$\rho_c$  = required core density (lb/ft<sup>3</sup>)

$\rho_R$  = density of core material (lb/ft<sup>3</sup>)

P = applied pressure load

$\sigma_{CYR}$  = compressive yield stress of core material (psi)

This empirical equation was derived assuming that one half of the uniform pressure load is being transmitted by the core to the inner face sheet.

However, after the program was completed, an analytical solution was found in reference I-71 that closely agrees with the test data. A comparison with the above expression indicated that the reference I-71 equation is a little more conservative. The difference in the expression did not warrant a change in the program.

## 3) Practical considerations

From the standpoint of practical design consideration, the face sheet thickness and core thickness must satisfy the minimum allowable manufacturing gage,  $t_{f \min}$  and  $t_{c \min}$ . The selection

of these values depends on the material and the method of sandwich fabrication, i. e., bonding or brazing and core design.

Due to the mode of failure and the shell theory used to describe this mode, the core thickness must be limited to a maximum,  $t_{c \max}$ . This limitation is necessary to substantiate the

assumption that transverse shear deformation has a negligible influence on the buckling load.

Also from the standpoint of practical design, the selection of core density must be within the acceptable manufacturing limitation, i. e.,  $\rho_{c_{\min}}$ .

f. Weight Expressions

For nonoptimum design (i. e., if  $t_c$  and  $t_f$  are governed by instability and/or yielding criteria), the unit weight expression can be written as follows:

$$W = 1/6 \rho_f t_f + 1/12 \rho_c t_c + K, \text{ lb/ft}^2$$

where

$\rho_f$  = face sheet density

$\rho_c$  = core density

$K$  = adhesive weight

The total weight of the spherical cap is then determined by

$$W_T = NWA, \text{ lb}$$

where

$N$  = represents the practical considerations of design, i. e., ratio of actual design weight to bare weight, usually about 1.7 average for sandwich type construction.

$A$  = Total surface area.



### 3. Conical and Cylindrical Sandwich Shells

#### a. Introduction

Governing equations for the weight expressions of conical and cylindrical sandwich shells have been derived. Derivation of these equations considered five modes of failure:

- 1) Shell general instability
- 2) Face sheet yielding
- 3) Core crushing
- 4) Face sheet dimpling
- 5) Shell wrinkling.

Shear effects on these modes of failure were neglected since their contributions in thin shell theory are small as compared to bending. However, this imposes certain restrictions on the design, such as maximum core thickness.

Each mode of failure is investigated with respect to the critical shell parameter. The results indicated that only the first three modes are needed in the derivation of the weight expressions. Since face sheet dimpling criteria depends on cell size only, it can be satisfied by core crushing, which is a function of the ratio of ribbon thickness to cell size. Wrinkling criteria will not be critical as long as the core has sufficient strength to satisfy core crushing; hence general instability will usually govern.

The derived expressions for the pertinent geometric parameter based on the above criterion were then optimized with respect to weight to obtain the minimum unit structural weight. However, if yielding or minimum thicknesses are the governing criteria, then the optimum will obviously be the weight corresponding to these criteria.

#### b. Nomenclature

- B      Extensional rigidity,  $\frac{2 E t_f}{(1 - \nu_f^2)}$
- D      Bending rigidity,  $\frac{E t_f t_c^2}{2 (1 - \nu_f^2)}$

$E_f$	Young's Modulus of Elasticity - face sheet (psi)
$K$	Constant for adhesive unit weight (lb/ft <sup>2</sup> )
$K_1$	$\frac{k^3 (1 - \beta + \beta^2/3 + \beta^2/2 \pi^2) - (1 - \bar{\gamma}) (1 - \beta)^2}{2 (1 - \beta/2)^2}$
$K_2$	$k$ , inches
$k$	$R_0 (1 - \beta/2)/\sin a$ , inches
$\beta$	geometric parameter, $(L/R_0) \cos a$
$L$	Slant length of cone, inches
$R_0$	Base radius of cone, inches
$P$	Nondimensional instability pressure parameter
$P_{CR}$	Critical pressure load, psi
$t_f$	Face sheet thickness, inches
$t_c$	Core thickness, inches
$t_1, t_3, t_4$	Geometric constants, function of geometric parameter $\beta$
$a$	Base cone angle of shell, degrees
$W$	Unit weight of sandwich shell, lb/ft <sup>2</sup>
$\bar{\gamma}$	Ratio of axial to lateral pressure distribution
$\lambda$	$\frac{m\pi}{L}$
$\nu_f$	Poisson's Ratio of face sheet
$\rho_f$	Density of face sheet
$\rho_c$	Density of core.

c. Derivation of Core Thickness

This derivation is based on a general instability criteria developed in reference I-70. From page 16 of this reference, we find the nondimensional pressure parameter,

$$P = \frac{2 t_f}{k} \cdot \frac{S^3 \left[ \frac{3+S}{1+S} + 1 \right]}{\left( \frac{3+S}{1+S} \right)^{1/2} \left[ \left( \frac{3+S}{1+S} \right)^{1/4} + \frac{S}{2} \right]}$$

Let

$$P_1 = \frac{S^3 \left[ \frac{3+S}{1+S} + 1 \right]}{\frac{3+S}{1+S}^{1/2} \left[ \frac{3+S}{1+S}^{1/4} + \frac{S}{2} \right]}$$

Now a new and simpler expression relating  $P_1$  to  $S$  can be developed by making a plot of values of  $P_1$  versus the value given by the right side of the present expression.

From the plot shown on figure I-30 and from the values shown in table I-27, this new expression can be written as follows:

$$P_1 = (1.3) S^{2.84}$$

where the constant 1.3 is the intercept of the  $P_1$  line,  $\ln(+0.255) = 1.3$  (determined from the curve fit), and where the power of  $S$  is the slope of the plotted line;

$$\frac{\ln 6.65}{\ln 2.34} = 2.84$$

As a check, the values of  $P_1$  and  $S$  are calculated from this new expression and are shown in table I-28. A number of observations can now be made in the diagnosis of table I-28.

- 1) The percent error for  $P_1$  when  $S = 0.1$  will not be as high as 10 percent. The 10 percent value is high due to the inaccuracy of the five-place log tables in this low region.
- 2) The new equation fits the terms well for  $0 < S \leq 1.0$ . Note the equation is inadequate for  $S=0$ ; which must be handled as a special case.

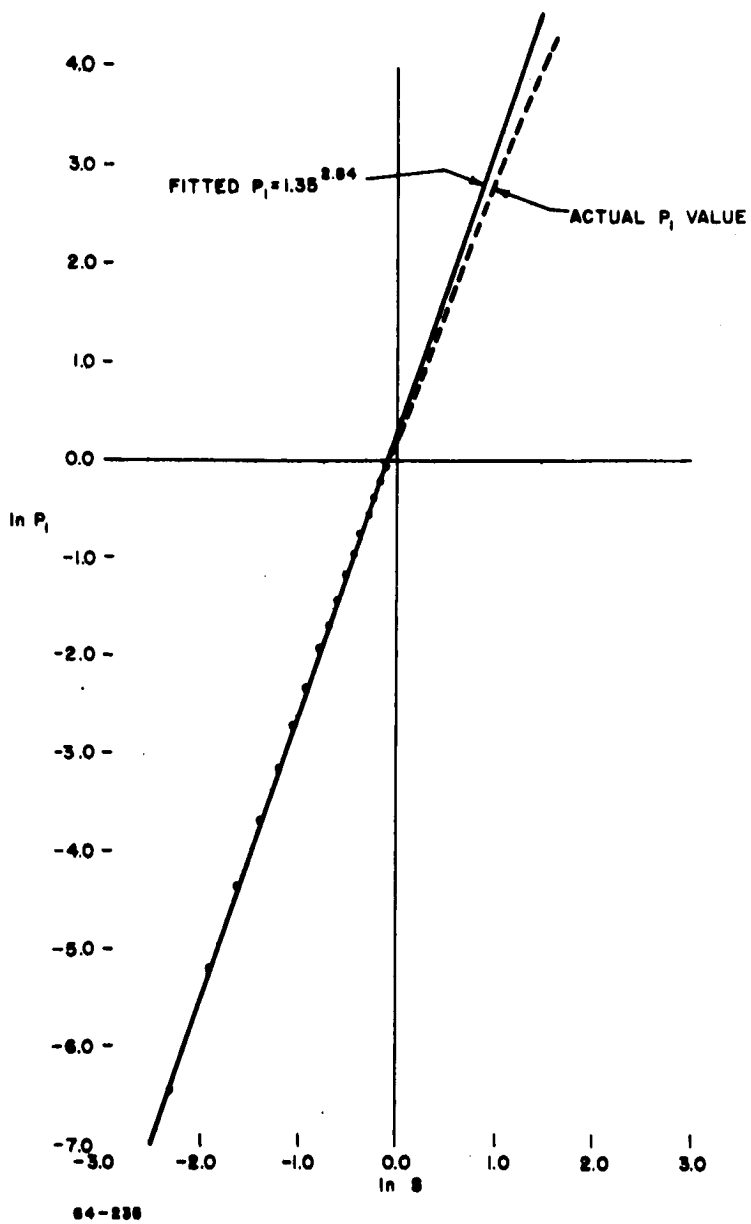


Figure 1-30  $\ln P_1$  VERSUS  $\ln S$

3) The new equation does not fit the terms well beyond  $S = 1.0$ .

It is appropriate to comment that in a number of practical cases handled, the calculated value of  $S$  has always bounded  $0 < S \leq 1.0$  as described.

With the new expression  $P_1 = (1.3) S^{2.84}$ , it is now possible to write equation (22) of reference I-70 in the following simplified form:

$$P = \frac{2 t_f}{k} \frac{S^3 \left[ \frac{3+S}{1+S} + 1 \right]}{\left( \frac{3+S}{1+S} \right)^{1/2} \left[ \left( \frac{3+S}{1+S} \right)^{1/4} + \frac{S}{2} \right]}$$

$$= \frac{2 t_f}{k} (1.3) S^{2.84}$$

where

$$S = 2 \left( \frac{\lambda K_1 t_c^{1/2}}{k^{3/2} K_2} \right) \left( \frac{2 t_1 t_3 t_4}{2 t_3 - v_f^2} \right)^{1/4}$$

Let

$$A = \left( \frac{\lambda K_1}{k^{3/2} K_2} \right) \left( \frac{2 t_1 t_3 t_4}{2 t_3 - v_f^2} \right)^{1/4}$$

The expression for  $S$  can now be written as

$$S = 2 A t_c^{1/2}$$

Substituting this back into the above expression for  $P$ ,

$$P = \frac{2 t_f}{k} [1.3 (2 A t_c^{1/2})^{2.84}]$$

and

$$t_c = 0.127 \left( \frac{P k}{t_f A^{2.84}} \right)^{0.704}, \text{ in.}$$

It is evident from the expression for  $t_c$ , that the expression for face sheet thickness  $t_f$  can be written as

$$t_f = \frac{P k}{18.6 (A t_c^{1/2})^{2.84}}, \text{ in.}$$

1) Special case  $S = 0$

For the case of a cylinder with a lateral load and no axial load, the following relationships,

$$\bar{\gamma} = 0 \quad \beta = 0 \quad K_1 = 0,$$

and therefore

$$S = 0$$

indicate that the expressions developed previously are not applicable to this special case.

In accordance with reference I-70, the following special relationships are established.

From page 10 of reference I-70,

$$\begin{aligned} P_B &= \frac{\left[ \frac{3+S}{1+S} + 1 \right]}{\left( \frac{3+S}{1+S} \right)^{1/2} \left[ \left( \frac{3+S}{1+S} \right)^{1/4} + \frac{S}{2} \right]} \\ &= \frac{3+1}{(3)^{1/2} (3)^{1/4}} = 1.75 \end{aligned}$$

and

$$P_B = \frac{P_{CR} K_2}{2 t_4 \lambda^2 D H^{1/4}}$$

where

$$K_2 = k = \frac{R_o \left(1 - \frac{\beta}{2}\right)}{\sin \alpha} = R_o, \lambda = \frac{\pi}{L},$$

$$D = \frac{E_f t_f t_c^2}{2(1 - \nu_f^2)}, H = \frac{(2 t_3 - \nu_f^2)}{8 t_1 t_3 t_4 \lambda^4 k^2} \left(\frac{B}{D}\right),$$

$$t_1 = t_3 = t_4 = .5, B = \frac{2 E_f t_f}{(1 - \nu_f^2)}.$$

Making the above substitutions, we arrive at the expression

$$t_c = .404 \left( \frac{P_{CR} R_o^{3/2} L}{E_f t_f} \right)^{2/3} \cdot (1 - \nu_f^2)^{1/2}, \text{ in.}$$

It is evident from the expression for  $t_c$ , that the expression for face sheet thickness  $t_f$  can be written as follows:

$$t_f = .258 \left( \frac{P_{CR}}{E_f} \right) (1 - \nu_f^2)^{3/4} \left( \frac{R_o}{t_c} \right)^{3/2} L, \text{ in.}$$

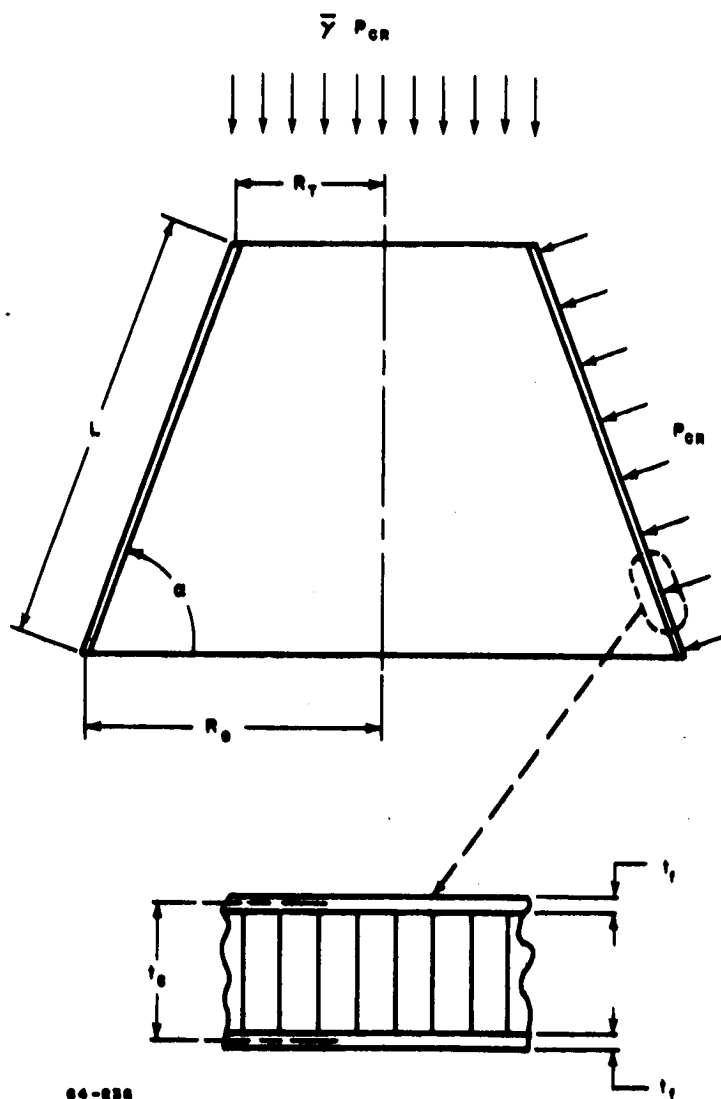
## 2) Definition of geometric parameters in terms of the general program parameters

Reference to figure I-31 indicates that only four parameters,  $\alpha$ ,  $R_o$ ,  $R_T$ , and  $a$ , need be defined to handle any type of section.

The following are the typical sections needed to define any capsule shape.

### a) Conical section

$$L = \frac{R_C}{\sin \theta_C} \left[ 1 - \left( \frac{R_N}{R_C} - \frac{R_S}{R_C} \right) \sin \theta_N - \frac{R_S}{R_C} \cos \theta_C \right]$$



04-236

Figure 1-31 CONICAL SANDWICH SHELL GEOMETRY



$$R_o = R_C$$

$$R_T = (R_N - R_S) \sin \theta_N + R_S \cos \theta_C$$

$$\alpha = 90^\circ - \theta_C$$

b) Cylindrical section

$$L = \Delta X$$

$$R_o = R_C$$

$$R_T = R_C$$

$$\alpha = 90^\circ$$

c) Flare fore cone section

$$L = \frac{R_C}{\sin \theta_F} \cdot \left( \frac{R_B}{R_C} - 1 \right)$$

$$R_o = R_B$$

$$R_T = R_C$$

$$\alpha = 90^\circ - \theta_F$$

d) Flare aft cone section

$$L = \frac{R_C}{\sin \theta_A} \cdot \left( \frac{R_B}{R_C} - \frac{R_A}{R_C} \right)$$

$$R_o = R_B$$

$$R_T = R_A$$

$$\alpha = 90^\circ - \theta_A$$

e) Rear conical section

$$L = \frac{R_C}{\sin \theta_A} \cdot \left( 1 - \frac{R_A}{R_C} \right)$$

$$R_o = R_C$$

$$R_T = R_A$$

$$\alpha = 90^\circ - \theta_A$$

d Derivation of Optimum Expressions

1) Optimization of weight with respect to core thickness

The unit area weight expression for a honeycomb sandwich structure can be written as follows:

$$W = \frac{1}{6} \rho_f t_f + \frac{1}{12} \rho_c t_c + K, \text{ lb /ft}^2$$

Let

$$C_1 = \frac{1}{6} \rho_f \left( \frac{Pk}{18.6 A^{2.84}} \right) = \left( \frac{Pk \rho_f}{111.8 A^{2.84}} \right)$$

and

$$C_2 = \frac{1}{12} \rho_c$$

Now the unit area expression can be written as

$$W = \frac{C_1}{(t_c)^{1.42}} + t_c C_2 + K$$

Optimum weight (minimum) can be obtained from the condition

$$\begin{aligned} \frac{\partial W}{\partial t_c} &= 0 \\ \frac{\partial W}{\partial t_c} &= - \frac{1.42 C_1}{(t_c)^{2.42}} + C_2 = 0 \\ t_{c_{opt}} &= \left( \frac{1.42 C_1}{C_2} \right)^{0.414} \end{aligned}$$

$$t_{c_{opt}} = 1.156 \left( \frac{C_1}{C_2} \right)^{0.414}, \text{ in.}$$

## 2) Optimization of weight with respect to face sheet thickness

The optimum face sheet thickness will be that which is required to complement the optimum core thickness for the stability requirement. This thickness can therefore be expressed as follows:

$$\begin{aligned} \frac{1}{6} \rho_f t_{f_{opt}} &= \frac{C_1}{t_{c_{opt}}^{1.42}} \\ t_{f_{opt}} &= \frac{6 C_1}{\rho_f} \left[ \frac{1.156}{C_2} \right]^{-1.42} \\ t_{f_{opt}} &= \frac{4.89}{\rho_f} [C_1^{0.414} \cdot C_2^{0.586}], \text{ in.} \end{aligned}$$

## 3) Optimum weight expression

The optimum weight expression is merely the sum of the optimum face sheet weight, core weight, and adhesive weight on a unit area base.

$$\begin{aligned} w_{opt} &= \frac{1}{6} \rho_f t_{f_{opt}} + \frac{1}{12} \rho_c t_{c_{opt}} + K \\ w_{opt} &= \frac{C_1}{(t_c)^{1.42}} + t_c C_2 + K \\ w_{opt} &= 1.971 [C_1^{0.414} C_2^{0.586}] + K, \text{ lb/ft}^2 \end{aligned}$$

## 4) Special case of a cylinder

### a) Optimization of weight with respect to core thickness

The unit area weight expression for a honeycomb sandwich structure can be written as follows:

$$W = \frac{1}{6} \rho_f t_f + \frac{1}{12} \rho_c t_c + K, \text{ lb/ft}^2$$

Let

$$X_1 = \frac{\rho_f P_{CR} R_C^{3/2} \Delta X (1 - \nu_f^2)^{3/4}}{23.2 E_f}$$

and

$$X_2 = \frac{\rho_c}{12}$$

$$W = \frac{X_1}{t_c^{3/2}} + t_c X_2 + K$$

$$\frac{\partial W}{\partial t_c} = -\frac{3}{2} \left[ \frac{X_1}{(t_{c_{opt}})^{5/2}} \right] + X_2 = 0$$

$$t_{c_{opt}}^{5/2} = 1.5 \left[ \frac{X_1}{X_2} \right]$$

$$t_{c_{opt}} = 1.176 \left[ \frac{X_1}{X_2} \right]^{2/5}$$

b) Optimization of weight with respect to face sheet thickness

The optimum face sheet thickness expression will be that which is required to complement the optimum core thickness for the instability requirement. This thickness can be expressed therefore as follows:

$$\frac{\rho_f t_{f_{opt}}}{6} = \frac{X_1}{(t_{c_{opt}})^{3/2}}$$

$$t_{f_{opt}} = \frac{6 X_1}{\rho_f \left[ 1.176 \left( \frac{X_1}{X_2} \right)^{4/5} \right]^{3/2}}$$

$$t_{f_{opt}} = \frac{4.7 [X_1^{2/5} X_2^{3/5}]}{\rho_f}$$

c) Optimum weight expression

The optimum weight expression is merely the sum of the optimum face sheet weight, core weight, and adhesive weight on a unit area basis.

$$w_{opt} = \frac{1}{6} \rho_f t_{f_{opt}} + \frac{1}{12} \rho_c t_{c_{opt}} + K$$

$$w_{opt} = \frac{X_1}{t_c^{3/2}} + t_c X_2$$

$$w_{opt} = \frac{X_1}{\left[ 1.176 \left( \frac{X_1}{X_2} \right)^{2/5} \right]^{3/2}} + 1.176 \left( \frac{X_1}{X_2} \right)^{2/5} X_2$$

$$w_{opt} = 1.959 [X_1^{2/5} X_2^{3/5}] + K, \text{ lb/ft}^2$$

e. Limitations

1) Yielding criteria

The derivation of face sheet yielding criteria is developed in reference I-70. In accordance with the theory set forth on page 8 of reference I-70, and the loading conditions to which entry cones are subjected, the maximum value of  $\bar{\sigma}_y$  is obtained when  $r = R_o$ ; hence

$$\bar{\sigma}_y = \frac{P_{CR}}{2(t - t_c) \sin \alpha} \left[ 3r^2 + \frac{R_o^4}{r^2} (1 - \bar{\gamma})^2 (1 - \beta)^4 \right]^{1/2}$$

$$\sigma_{c_{y_f}} = \frac{P_{CR}}{4t_{c_{y_f}} \sin \alpha} \left\{ 3R_o^2 + \frac{R_o^4}{R_o^2} (1 - \bar{\gamma})^2 \left[ 1 - \left( 1 - \frac{R_T}{R_o} \right)^4 \right] \right\}^{1/2}$$

where

$$\beta = 1 - \frac{R_T}{R_o}$$

and  $R_T$  = the radius of the smaller end of the cone. Thus,

$$\sigma_{c_{y_f}} = \frac{P_{CR} R_o}{4t_{c_{y_f}} \sin \alpha} \left[ 3 + (1 - \bar{\gamma})^2 \left( \frac{R_T}{R_o} \right)^4 \right]^{1/2}$$

and then,

$$t_{c_{y_f}} = \frac{P_{CR} R_o}{4\sigma_{c_{y_f}} \sin \alpha} \left[ 3 + (1 - \bar{\gamma})^2 \left( \frac{R_T}{R_o} \right)^4 \right]^{1/2}$$

## 2) Core crushing

The derivation and limitations of core crushing expression is defined under the spherical cap limitation section.

## 3) Allowable thickness

The minimum and maximum allowable limitation are set forth in the spherical cap limitation section.

b. Weight Expressions

For nonoptimum design, i. e., if  $t_c$  and  $t_f$  are governed by minimum gage and/or yielding criteria, the unit weight expression can be written as follows:

$$W = \frac{1}{6} \rho_f t_f + \frac{1}{12} \rho_c t_c + K, \text{ lb/ft}^2$$

and hence the total weight becomes

$$W_T = NWA$$

where

N represents the practical consideration of design, i. e., ratio of actual design weight to bare weight (face sheet and core). This factor is usually about 1.7 average for sandwich type construction

A = total surface area.

TABLE I- 27  
VALUES FOR PLOT OF  $\ln P_1$  VERSUS  $\ln S$

S	$P_1$	$\ln S$	$\ln P_1$
0	0	-	-
0.10	0.001689	-2.30259	-6.43021
0.15	0.005603	-1.89712	-5.18838
0.20	0.013040	-1.60944	-4.33985
0.25	0.025010	-1.38629	-3.68849
0.30	0.042470	-1.20397	-3.15903
0.35	0.066270	-1.04982	-2.71404
0.40	0.097150	-0.91629	-2.33150
0.45	0.136100	-0.79851	-1.92347
0.50	0.183600	-0.69315	-1.69500
0.55	0.240400	-0.59784	-1.42696
0.60	0.306800	-0.51083	-1.18156
0.65	0.384200	-0.43078	-0.95659
0.70	0.472200	-0.35667	-0.75036
0.75	0.571500	-0.28768	-0.55949
0.80	0.683000	-0.22314	-0.38126
0.85	0.806500	-0.16252	-0.21505
0.90	0.943100	-0.10536	-0.05858
0.95	1.092800	-0.05129	+0.08874
1.00	1.256300	0.00000	+0.22816
2.00	7.736000	+0.69315	+2.04588
3.00	21.133400	+1.09861	+3.05085
4.00	42.047600	+1.38629	+3.73880
5.00	70.62240	+1.60944	+4.25735



TABLE I-28

EVALUATION OF CURVE FIT FOR  $P_1$

S	$P_1$	Error From Previously Calculated $P_1$ (percent)
0.10	0.001859	10
0.20	0.013350	2.4
0.30	0.042560	0.2
0.40	0.096300	0.9
0.50	0.181600	1.1
0.60	0.304700	0.7
0.70	0.472100	0.0
0.80	0.689800	0.9
0.90	0.963800	2.2
1.00	1.300000	3.5
2.00	9.300300	20.4
3.00	29.441800	34.8

#### 4. Spherical Cap Membrane

##### a. Introduction

Governing equations have been developed for the weight expression of membrane spherical nosecaps. The derivation of these expressions used snap buckling test data under external pressure for isotropic (homogeneous) spherical shells presented in reference I-67. A curve fit was made to the lower bound of these test data; hence conservative results will be indicated.

Only general instability (snap buckling) and yielding modes of failure were considered in the derivation. However, the resulting shell thickness will be subjected to practical minimum gage allowables.

##### b. Nomenclature

E Young's modulus of elasticity (psi)

H Height of spherical cap (inches)

P Applied uniform pressure (psi)

$q_{CR}$  Classical spherical shell buckling pressure load,

$$\frac{2E}{3(1-\nu^2)^{1/2}} \left(\frac{t}{R}\right)^2 \quad (\text{psi})$$

R Radius of spherical cap (inches)

t Thickness of spherical cap (inches)

$\lambda$  Geometric parameter of spherical cap

$$2[3(1-\nu^2)]^{1/4} \left(\frac{H}{t}\right)^{1/2} .$$

$\nu$  Poisson's Ratio

$\sigma_{CY}$  Compressive yield stress (psi)

$\rho$  material density (lb/ft<sup>3</sup>)

$W_{SC}$  Unit weight of spherical cap (lb/ft<sup>2</sup>)

### c. Derivation of Shell Thickness

Derivation of the shell thickness is based on a series of static tests on snap buckling of spherical caps under uniform pressure (ref. I-67). These results are presented in terms of a nondimensional geometric parameter  $\lambda$  and a pressure ratio  $P/q_{CR}$  where

$$\lambda = 2[3(1 - \nu^2)]^{1/4} \left(\frac{H}{t}\right)^{1/2}$$

and

$$P/q_{CR} = \frac{P[3(1 - \nu^2)]^{1/2}}{2E} \left(\frac{R}{t}\right)^2$$

$$q_{CR} = \frac{2E}{[3(1 - \nu^2)]^{1/2}} \left(\frac{t}{R}\right)^2, \text{ classical theory.}$$

The results of these tests are illustrated in figure I-29. The relationship developed in that section to enclose the lower bound of tests will be employed here. This relationship is

$$P/q_{CR} = \frac{1.1}{(\lambda)^{2/3}}.$$

Substituting the expression for  $\lambda$  into this relation and equating to the pressure ratios, results in

$$\begin{aligned} P/q_{CR} &= \frac{1.1}{2^{2/3} [3(1 - \nu^2)]^{1/2}} \left(\frac{t}{H}\right)^{1/3} \\ &= \frac{P[3(1 - \nu^2)]^{1/2}}{2E} \left(\frac{R}{t}\right)^2, \end{aligned}$$

or,

$$t = 1.20 \left(\frac{P}{E}\right)^{3/7} (1 - \nu^2)^{2/7} \left(\frac{H}{R}\right)^{1/7} R, \text{ in.}$$

In terms of the general program geometric parameters, the spherical cap parameters, height  $H$  and radius  $R$ , are expressed as

$$H = R_C \left\{ \frac{R_N}{R_C} (1 - \cos \theta_N) + \frac{R_S}{R_C} \cos \theta_N \left[ 1 - \frac{\sin \theta_C}{\sin 90^\circ + \theta_N} \right] \right\}, \text{ in.}$$

$$R = R_N, \text{ in.}$$

Note that H in the above expression includes the height of the toroidal section defined by  $R_S$  (figure I-28). This results in a conservative solution for the spherical cap and accounts for the uncertainties in buckling of spherical-toroidal caps.

#### d. Limitations

##### 1) Yielding criteria

The shell thickness must satisfy the yielding criteria defined by the simple membrane theory for spherical shells

$$\sigma_{CY} = \frac{PR}{2t}, \text{ psi.}$$

or

$$t_{CY} = \frac{PR}{2\sigma_{CY}}, \text{ in.}$$

##### 2) Practical considerations

From the standpoint of practical design considerations, the thickness of the shell must be limited to acceptable minimum gage material or  $t_{\min}$ .

#### e. Weight Expressions

The unit weight expression for the spherical cap can be expressed simply as

$$W_{SC} = \frac{t}{12} \rho, \text{ lb/ft}^2.$$

where

$\rho$  = material density (lb/ft<sup>3</sup>)

$t$  = shell thickness (inches) .

Hence the total weight then becomes

$$W_{TSC} = W_{SC} A_{SC}$$

where

$A_{SC}$  = total surface area (ft<sup>2</sup>).

## 5. Conical and Cylindrical Ring-Stiffened Shells

### a. Introduction

Analysis is presented herein for the derivation of ring-stiffened conical and cylindrical shell weight expressions. The derivation considered three modes of failure:

- 1) General instability
- 2) Local instability
- 3) Yielding.

Of these, only the first two modes of failure were considered critical. Experience in the design of ring-stiffened shells indicated that yielding of uniform shells is never a critical condition, and general or local instability usually governs.

General instability is failure of the shell as a whole, i.e., rings and skin all fail simultaneously. Local instability is the failure of the shell between stiffeners. It is assumed in the analysis that optimum design is when the shell fails simultaneously, in general and local instability. The analysis is limited to the derivation present in reference I-72 for elastic stability of orthotropic conical and cylindrical shells subjected to axisymmetric loading conditions.

In review of trajectory data for Mars and Venus entry capsules, the effects of high g loads on the capsules must be included in the structural analysis of a ring-stiffened shell. This effect was neglected in the sandwich shell analysis since the units are small ; however, in ring-stiffened shells, the unit weights could become very large in particular if the shell is used as a thermal heat sink concept. Therefore, an

equivalent pressure load due to the structure and heat shield unit inertia weights has been incorporated.

Considering the general size and shape of the entry capsule under investigation, as well as the probable selection of materials in design application, only a Z-type stiffener was employed in the following analysis.

b. Nomenclature

$A_{ST}$	Cross-sectional area of stiffener ( $\text{in}^2$ )
$a$	Base radius of conical shell (inches)
$D$	Bending rigidity of shell $\frac{E t^3}{12(1 - \nu^2)}$
$D_\theta$	Equivalent bending rigidity $\frac{I_\theta E}{d_\theta}$
$d_\theta$	Stiffener spacing (inches)
$E$	Modulus of elasticity (psi)
$b, h, H$	Stiffener geometry parameters
$g_e$	Entry deceleration (g)
$I$	Average effective moment of inertia of stiffener (inches)
$k$	$\frac{a(1 - \beta/2)}{ \sin \alpha }$ (inches)
$K_1$	$\frac{(1 - \beta + \beta^2/3 + \beta^2/2 \pi^2) - (1 - \bar{\gamma})(1 - \beta)^2}{2(1 - \beta/2)^2}$
$L$	Slant length of cone (inches)
$n$	Stiffener proportionality factor
$m$	Skin effective width factor
$P$	Pressure nondimensional parameter

$P_L$	Total lateral pressure (psi)
$S$	Geometric nondimensional parameter
$t$	Shell skin thickness (inches)
$t_1, t_3, t_4$	Geometric constants, function of geometric parameter $\beta$
$\alpha$	Cone base angle
$\beta$	$(L/a)  \cos \alpha $
$\bar{\gamma}$	Ratio of axial to lateral pressure of conical shell
$\nu$	Poisson's ratio
$\rho$	Material density (lb/ft <sup>3</sup> )
$W_{ST}$	Unit weight of shell skin (lb/in <sup>2</sup> )
$W_{HS}$	Unit weight of heat shield (lb/in <sup>2</sup> )
$W_e$	Effective width of skin (inches)

c. Derivation of Shell Thickness

i) General instability

This derivation is based on the general instability requirements set forth in reference I-72. From reference I-72, the shell must satisfy the general instability expression

$$P = \frac{\left[ \frac{3+S}{1+S} + 1 \right]}{\left( \frac{3+S}{1+S} \right)^{1/2} \left[ \left( \frac{3+S}{1+S} \right)^{1/4} + \frac{S}{2} \right]}$$

where

$$P = \frac{A}{\left( \frac{D\theta}{D} \right)^{3/4} t^{5/2}}$$

if

$$A = 6(1 - \nu^2) \left( \frac{P_L}{E} \right) \left( \frac{L k^{3/2}}{\pi t_4} \right) \left[ \frac{8 t_1 t_3 t_4}{12(2 t_3 - \nu^2)} \right]^{1/4}$$

and

$$S = B \left( \frac{D_\theta}{D} \right)^{1/4} t^{1/2}$$

if

$$B = 2\pi \left( \frac{K_1 k^{1/2}}{L} \right) \left[ \frac{8 t_1 t_3 t_4}{12(2 t_3 - \nu^2)} \right]^{1/4} .$$

Hence, for general instability, the value A and B become constants depending on geometry (figure I-32) and loading.

The parameters  $D_\theta/D$ , bending rigidity ratio, and  $t$ , shell thickness, are then the only unknown values required. The parameter  $D_\theta$  relates the bending rigidity of a ring-stiffened shell to an equivalent isotropic shell or

$$D_\theta = \frac{I_\theta E}{d_\theta}$$

where

$I_\theta$  = average effective moment of inertia of the skin and stiffener in the circumferential direction

$d_\theta$  = stiffener spacing.

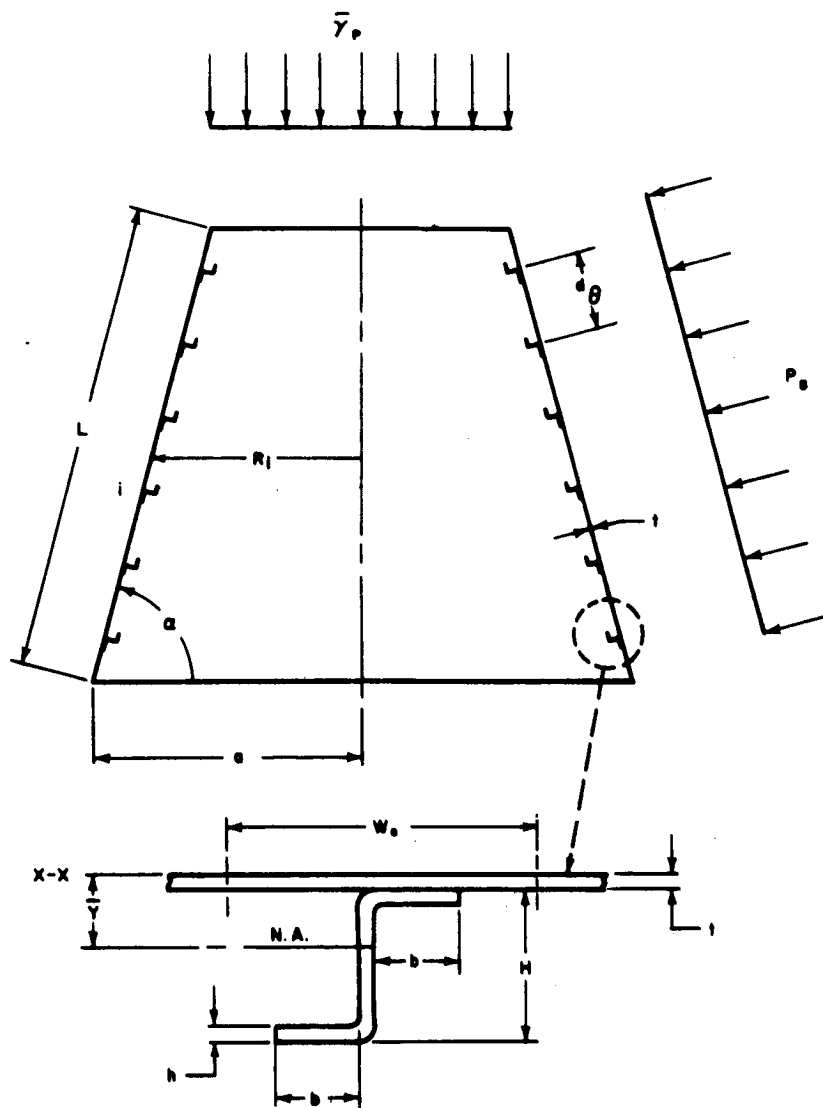
This ratio,  $D_\theta/D$ , becomes equal to unity for nonstiffened shells.

## 2) Local instability

For local instability, i.e., stability between stiffeners, the above set of equations for general instability can be readily employed if

$$D_\theta/D = 1.0$$





64-237

# STIFFENER GEOMETRY

Figure 1-32 CONE GEOMETRY

and

$$L = d_{\theta} .$$

Now the values A and B in these expressions become a function of  $d_{\theta}$ . However, there still remain two unknown values,  $t$  shell thickness, and  $d_{\theta}$  stiffener spacing, and only one equation. Hence, the solution then depends on some criteria to establish one of these unknowns. This same situation also exists for general instability where  $D_{\theta}/D$  and  $t$  are the unknown values. The proposed design (computation) approach is to first assume a value of  $t$ , either based on minimum gage (i.e., if it is a cold structure, since experience has shown that it is close to minimum gage for optimization) or by the required thermal thickness (i.e., hot structures no heat shield). Then solution of  $d_{\theta}$  and  $D_{\theta}/D$  can be readily obtained subjected to the practical design considerations and limitations (reference section e). Once  $D_{\theta}$  is known, the stiffener size (H) can be obtained and consequently the weight expression.

### 3) Pressure load, $P_L$

Due to the high g load history experienced on the capsules under consideration, the weight of the shell becomes a significant effect in the determination of the shell buckling criteria. Therefore, the effect of the shell inertia weight must be included in this lateral pressure load.

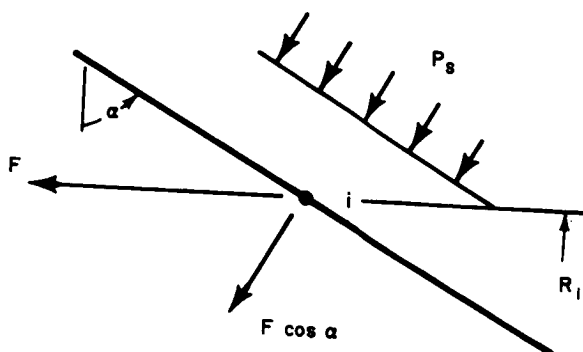
Let

$$P_L = P_S + P_{i_{ST}} + P_{i_{HS}}$$

where

$$\begin{aligned} P_S &= \text{aerodynamic pressure load} \\ P_{i_{ST}} &= \text{inertia pressure load of shell} \\ P_{i_{HS}} &= \text{inertia pressure load of heat shield.} \end{aligned}$$

From the conical shell geometry presented in figure I-32 the following inertia load system will exist at point i



where

$$F = W_{ST} g_e + W_{HS} g_e$$

$$W_{ST} = \text{unit weight of shell (lb/in}^2\text{)}$$

$$= \frac{\rho t}{1728}$$

$$W_{HS} = \text{unit weight of heat shield (lb/in}^2\text{)}$$

$$g_e = \text{entry axial deceleration.}$$

Hence,

$$P_{iST} = \frac{\rho t}{1728} g_e \cos \alpha$$

$$P_{iHS} = W_{HS} g_e \cos \alpha .$$

Note that for hot structures, i.e., no heat shield,

$$P_{iHS} = 0 .$$

#### 4) Definition of geometric parameters in terms of the general program parameters

Reference to figure I-32 indicates that only three parameters,  $L$ ,  $a$ , and  $\alpha$ , are necessary to define any type of conical

section. The following are the typical sections needed to define any of the capsules under consideration.

a) Conical section

$$a = R_c$$

$$L = \frac{R_c}{\sin \theta_c} \left[ 1 - \left( \frac{R_N}{R_c} - \frac{R_S}{R_c} \right) \sin \theta_N - \frac{R_S}{R_c} \cos \theta_c \right]$$

$$\alpha = \theta_c - 90^\circ.$$

b) Cylindrical

$$a = R_c$$

$$L = \Delta X$$

$$\alpha = 90^\circ$$

c) Flare fore cone

$$a = R_B$$

$$L = \frac{R_c}{\sin \theta_F} \left( \frac{R_B}{R_c} - 1 \right)$$

$$\alpha = \theta_F - 90^\circ.$$

d) Flare aft cone

$$a = R_B$$

$$L = \frac{R_c}{\sin \theta_A} \left( \frac{R_B}{R_c} - \frac{R_A}{R_c} \right)$$

$$\alpha = 90^\circ - \theta_A.$$

e) Rear conical

$$a = R_c$$

$$L = \frac{R_c}{\sin \theta_A} \left( 1 - \frac{R_A}{R_c} \right)$$

$$\alpha = 90^\circ - \theta_A .$$

d. Stiffener Geometry

Considering the general size of the capsules under consideration and the types of material probable in design application, a Z-type stiffener was selected in this study. Figure I-32 represents the geometry of such a stiffener. From the stiffener geometry, the following geometric considerations can be established:

$$\begin{aligned} A_T &= h (2b + H) + W_e t, \text{ in}^2 \\ &= \text{total cross-sectional area} \end{aligned}$$

$$\begin{aligned} A_{SF} &= h (2b + H), \text{ in}^2 \\ &= \text{total stiffener area} \end{aligned}$$

$$\bar{y} = \frac{\sum A y}{\sum A} = \frac{W_e t^2/2 + h (2b + H) (H/2 + t)}{h (2b + H) + W_e t}, \text{ in.}$$

$\bar{y}$  = location of neutral axis

$$\begin{aligned} I_{x-x} &= \sum A \bar{y}^2 + \sum I_o \\ &= \frac{W_e t^3}{4} + h (2b + H) (H/2 + t)^2 + \frac{W_e t^3}{12} \\ &+ \left[ \frac{(b + h) H^3}{12} - b \frac{(H - 2h)^3}{12} \right], \text{ in.}^4 \end{aligned}$$

$I_{x-x}$  = moment of inertia about x-x.

In the above geometric relation, four parameters, H, b, h, and  $W_e$  are required to define the stiffener. These parameters must be reduced to one in order to find a solution. Since in most shell designs, the stiffener thickness is approximately equal to the skin thickness, then let

$$h = t.$$

Also, Z - type stiffeners can be efficiently designed such that the web and flange fail under compression at the same time by proper proportioning. Hence, let

$$b = nH.$$

Finally, the effective width,  $W_e$ , may be expressed as a function of skin thickness t in most practical designs, thus

$$W_e = mt.$$

Substituting these relations into the geometric expressions for area and moments of inertia, the following equations result

$$A_T = tH (2n + 1) + mt^2$$

$$A_{ST} = th (2n + 1)$$

$$\bar{y} = \frac{mt^3/2 + tH (2n + 1) (H/2 + t)}{A_T}$$

$$I_{x-x} = \frac{mt^4}{3} + tH (2n + 1) (H/2 + t)^2 + \frac{(nH + t)H^3}{12} - \frac{nH (H - 2t)^3}{12}.$$

Then the average effective moment of inertia becomes

$$I_\theta = I_{x-x} - A_T \bar{y}^2.$$

e. Limitations

1) Yielding criteria

Experience has shown that yielding of this skin is almost never a critical criteria in the design of a ring-stiffened shell. Hence, it is felt that addition of the yielding criteria to the program would not significantly contribute to a realistic weight expression.

2) Stiffener spacing

The general instability criteria set forth in reference I-72 is limited to equally spaced stiffeners. Thus the ratio of cone length,  $L$ , to stiffener space,  $d_\theta$ , must always equal a whole number in the program or

$$\frac{L}{d_\theta} = N, \text{ whole number (i.e., equal spacing).}$$

3) Practical considerations

Due to practical manufacturing limitations of stiffener spacing, the program must be limited to a minimum spacing  $d_{\theta \min}$ , in the design approach. This spacing will depend on the type of stiffener and the relative size of both the stiffener and shell.

The program must also be limited to practical minimum shell thickness,  $t_{\min}$ , from the standpoint of manufacturing and availability.

f. Weight Expression

The unit weight of shell skin can be simply expressed as

$$W_{ST} = \rho \frac{t}{12}, \text{ lb/ft}^2,$$

and consequently, the total weight of the skin becomes

$$W_{TST} = W_{ST} A_S, \text{ lb}$$

where  $A_S$  = total surface area,  $\text{ft}^2$ .

The total stiffener weight may be expressed as

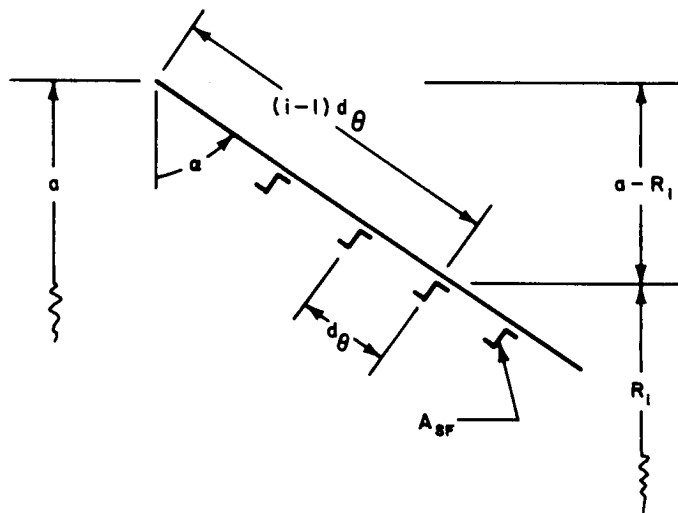
$$W_{SF} = 2\pi\rho A_{SF} \sum_{i=1}^{i=L/D_\theta + 1} (R_i) \quad , \quad \text{lb}$$

where

$R_i$  = radius of (i)th stiffener

$A_{SF}$  = cross-sectional area of stiffener ( $\text{in}^2$ ).

From the geometry presented in figure I-32 the following relation can be developed for the ith radius,  $R_i$  :



$$R_i = a - (i - 1) d_\theta \sin (90^\circ - \alpha) .$$



Hence,

$$W_{SF} = 2\pi\rho A_{SF} \sum_{i=1}^{i=(L/d_\theta+1)} [\alpha - (i-1) d_\theta \sin(90^\circ - \alpha)]$$

for  $\alpha < 90^\circ$

$$W_{SF} = 2\pi\rho A_{SF} (L/d_\theta + 1) \alpha$$

for  $\alpha = 90^\circ$ .

## 6. Internal Structure

### a. Introduction

The internal structure has been idealized as a conical section and cylindrical section as illustrated in figure I-33. The conical section (or cone as used in derivation) supports the parachute system package and reacts the snatch loads at parachute deployment. The cylindrical section (hereafter cylinder) provides the packaging volume for the residual weight. This idealized selection of the internal structure was developed to show a realistic weight allocation for the internal structure which would be a function of loads and forces imposed on the capsule during its performance. This configuration does not indicate an actual design concept since in actual design the internal structure would be dictated by the residual weight components and layouts.

The following derivations employ simple buckling theory for cylinders and tensile yield criteria for the cone. These derivations result in equations for the section thickness and, consequently, the total weight expressions.

### b. Nomenclature

C	Practical consideration factor for ring, brackets, etc.
E	Modulus of elasticity (psi)
$g_x$	Entry or impact g level (earth g)
HR	Internal cylinder geometry proportionality factor
PD	Maximum parachute snatch load (pounds)
$R_P$	Radius of internal cylinder (feet)
$t_{\text{cone}}$	Thickness of internal cone (inches)
$t_{\text{cyl}}$	Thickness of internal cylinder (inches)
$W_{\text{RES}}$	Residual weight (pounds)
$W_{\text{INT}}$	Weight of internal package, $W_{\text{INSTR}} + W_{\text{CU}} + W_{\text{RES}}$ (pounds)
$W_{\text{INSTR}}$	Weight of internal structure (pounds)
$W_{\text{CU}}$	Weight of crushable material (pounds)

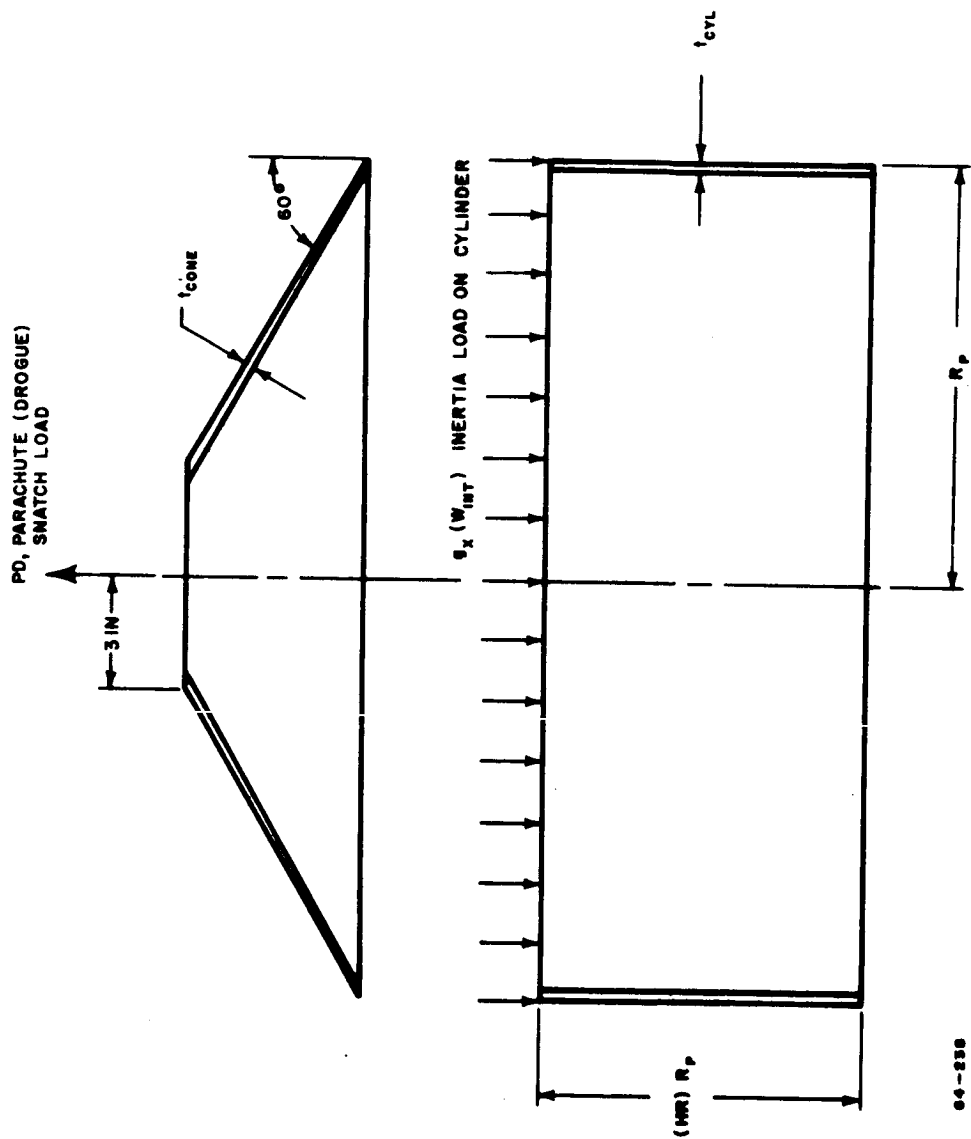


Figure I-33 IDEALIZED CONICAL AND CYLINDRICAL SECTION

$\rho_{\text{cyl}}$	Density of internal cylinder material (lb/ft <sup>3</sup> )
$\rho_{\text{cone}}$	Density of internal cone material (lb/ft <sup>3</sup> )
$\sigma_{\text{ty}}$	Tensile yield Stress (psi)
$\nu$	Poisson's ratio.

### c. Derivation of Cone Thickness

The cone is of constant cross-sectional area and is assumed to react the drogue maximum snatch load in tension. As shown in figure I-33 the cone is cut off at a 3-inch radius to allow for parachute attachment fittings. The cone angle is also arbitrarily fixed at 60 degrees so that a solution could be developed based on only the cylinder radius,  $R_p$ .

Since the cone is assumed as a constant area, and the stress level is allowed to reach tensile yield, then

$$\sigma_{\text{ty}} = \frac{PD}{A}$$

where

PD = drogue maximum snatch load (pounds)

$$A = 2\pi R_p t_{\text{cone}}$$

Hence

$$t_{\text{cone}} = \frac{PD}{2\pi R_p \sigma_{\text{ty}}}, \text{ in.}$$

This thickness must be limited by practical consideration to minimum gage,  $t_{\text{min}}$ .

Referring to figure I-33, let the residual weight,  $W_{\text{RES}}$ , be packaged in the cylinder of radius  $R_p$  and height  $(HR)R_p$ , then

$$W_{RES} = (R_P)^3 (HR) \rho_{RES}$$

where

$$\rho_{RES} = \text{density of residual weight (lb/ft}^3\text{)}.$$

and hence the cylinder radius becomes

$$R_P = \left[ \frac{W_{RES}}{\pi(HR) \rho_{RES}} \right]^{1/3}, \text{ ft.}$$

#### d. Derivation of Cylinder Thickness

To develop a conservative approach to the cylinder weight expression, the entire internal package inertia weight load is assumed reacted at the end of the cylinder. The cylinder is then analyzed for a buckling mode of failure. From reference 1-73 the critical buckling stress is

$$\sigma_{CR} = \frac{K \pi^2 E}{12 (1 - \nu^2)} \left( \frac{t_{cyl}}{L} \right)^2, \text{ psi.}$$

For short and/or transition cylinders, the constant K is approximately equal to 4. If the analysis is limited to metal material,  $\nu$  becomes equal to 0.3. Hence the critical buckling stress is therefore

$$\sigma_{CR} = 3.62 \frac{E_{cyl}}{(HR)^2} \left( \frac{t_{cyl}}{12 R_P} \right)^2, \text{ psi.}$$

Now if the critical buckling stress is equated to the applied inertia stress,

$$\sigma = \frac{F_{inertia}}{A_{cyl}} = \frac{g_x W_{INT}}{2 \pi (12 R_P) t_{cyl}}, \text{ psi.}$$

Then

$$t_{cyl} = \left[ \frac{g_x W_{INT} (12 R_P) (HR)^2}{(2 \pi) 3.62 E_{cyl}} \right]^{1/3}, \text{ in.}$$

or

$$t_{cyl} = 0.35 \left[ \frac{g_x W_{INT} (HR)^2 12 R_P}{E_{cyl}} \right]^{1/3}, \text{ in.}$$

where

$g_x$  = maximum entry or impact g deceleration, earth g

$W_{INT}$  = total internal package weight

$$= W_{RES} + W_{CU} + W_{INSTR.}$$

For most capsules under investigation (in particular Mars capsules), HR in the above equation is unity; thus the cylinder thickness becomes

$$t_{cyl} = 0.35 \left[ \frac{g_x W_{INT} (12 R_P)}{E_{cyl}} \right]^{1/3}, \text{ in.}$$

This thickness is subjected by practical limitation to minimum gage,  $t_{min}$ .

#### e. Weight Expressions

The weight of the cone becomes simply the density times the volume, or

$$W_{cone} = \rho_{cone} t_{cone} A_{S_{cone}}$$

$$W_{cone} = \rho_{cone} t_{cone} R_P^2 (2\pi) (1.731) (12) (12)$$

$$W_{cone} = \rho_{cone} t_{cone} R_P^2 (2\pi) (20.77) (12), \text{ lb.}$$

where

$$\rho_{cone} = \text{density of cone material (lb/ft}^3\text{)}.$$

Similarly, the weight of the cylinder becomes

$$W_{cyl} = \rho_{cyl} t_{cyl} A_{S_{cyl}}$$

or

$$W_{cyl} = \rho_{cyl} t_{cyl} (2\pi) (144) R_p^2 (HR)$$

where

$$\rho_{cyl} = \text{density of cylinder material (lb/ft}^3\text{)}.$$

The total weight of the internal structure  $W_{INSTR}$ , becomes the sum of the cone weight and cylinder weight plus a factor to account for rings, stiffeners, brackets, etc.

Thus,

$$W_{INSTR} = C(W_{CONE} + W_{CYL})$$

where

$C$  = factor for practical design considerations, an average of 1.5 for most monocoque structures.

## 7. Retardation (Parachute) System

### a. Introduction

The parachute system considered consists of a drogue parachute, usually deployed supersonically, and a main parachute of larger area and of lighter construction deployed subsonically. Sizing of the main parachute systems considered that the external heat shield and structure was jettisoned at drogue chute deployment.

The relative sizing of the two chutes has been done in terms of their respective canopy and line weights. For the main chute systems, all of the chute weight is considered to be in the canopy and lines. The drogue chute canopy and lines are considered to be only a part of the chute system weight. The remaining weight in the drogue chute system is made up of ejection gas generator-mortar, fitting, etc.

Selecting of parachute material and material densities included the effects of sterilization and aerodynamic heating degradation on the strength properties. Hence, different properties were employed for  $\gamma_e = -90$  - degree and  $\gamma_e = -20$  - degree trajectories to fully evaluate the effects of entry conditions on elemental weights.

b. Derivation of Parachute Size and Weight

For a given equilibrium descent velocity at Mars sea level, the main parachute may be sized by equating the drag force to the Martian suspended weight of capsule and the parachute. Since the entry capsule heat shield and external structure as well as the drogue chute has been assumed jettisoned at this time, the suspended capsule weight becomes

$$W_{\text{suspended}} = W_E - W_{\text{HS}} - W_{\text{ST}} - W_{\text{DSY}}$$

where

$$W_E = \text{total entry weight (pounds)}$$

$$W_{\text{HS}} = \text{heat shield weight (pounds)}$$

$$W_{\text{ST}} = \text{external structure weight (pounds)}$$

$$W_{\text{DSY}} = \text{total drogue chute system weight (pounds)}$$

Now equating the Martian weight to the aerodynamic drag force at equilibrium descent velocity (i. e., sea level) and neglecting the capsule drag, we get

$$\frac{g_{\text{SL}}}{g_{\oplus}} (W_E - W_{\text{HS}} - W_{\text{ST}} - W_{\text{DSY}}) = \frac{1}{2} \rho_{\text{SL}} V_{\text{SL}}^2 A_{\text{MC}} \quad (1)$$

where

$$g_{\text{SL}} = \text{Mars sea level gravitational constant}$$

$$g_{\oplus} = \text{earth gravitational constant} \\ = 32.17 \text{ ft/sec}^2$$

$$\rho_{\text{SL}} = \text{Mars sea level atmospheric density (slug/ft}^3\text{)}$$

$$C_{\text{DM}} = \text{Drag coefficient of main chute (ft}^2\text{)}$$

$$A_{\text{MC}} = \text{area of main chute (ft}^2\text{)}$$

$$V_{\text{SL}} = \text{main chute terminal velocity (ft/sec).}$$

However, from the weight consideration

$$W_{\text{MC}} = W_{\text{MA}} A_{\text{MC}}$$



or

$$A_{MC} = \frac{W_{MC}}{W_{MA}} \quad (2)$$

where

$W_{MC}$  = total weight of main chute (pounds)

$W_{MA}$  = unit weight of main chute (lb/ft<sup>2</sup>).

Considering the drogue chute, we may say in a similar manner that

$$W_{DSY} - W_{\text{ejection mortar}} - W_{\text{package fittings}} = K_1 W_{MC} = A_{DC} W_{DA}$$

or

$$A_{DC} = \frac{K_1 W_{MC}}{W_{DA}} \quad (3)$$

where

$A_{DC}$  = area of drogue chute (ft<sup>2</sup>)

$W_{DA}$  = unit weight of drogue (lb/ft<sup>2</sup>)

$K_1 = \frac{\text{weight of drogue canopy and lines}}{\text{weight of main canopy and lines}}$

If

$K_2 = \frac{\text{weight of drogue total chute system}}{\text{weight of drogue canopy and lines}}$

or

$$K_2 = \frac{W_{DSY}}{K_1 W_{MC}},$$

then

$$W_{DSY} = K_1 K_2 W_{MC} \quad (4)$$

Substituting equations (2) and (3) into equation (1) and solving for  $W_{MC}$  we obtain

$$W_{MC} = \frac{\frac{2g_{SL}}{32.17} \frac{W_{MA}}{\rho_{SL} V_{SL}^2 C_{DM}} (W_E - W_{HS} - W_{ST})}{1 + \left[ \frac{2K_1 K_2 g_{SL}}{32.17} \right] \left[ \frac{W_{MA}}{\rho_{SL} V_{SL}^2 C_{DM}} \right]} \quad (5)$$

#### c. Derivation of Drogue Maximum Load

The maximum drogue chute load (i. e., snatch load at opening) can be obtained from the aerodynamic drag equation

$$PD = F_D C_{DD} A_{DC} q_D \quad (6)$$

where

$F_D$  = dynamic load factor

$C_{DD}$  = drag coefficient of drogue chute

$A_{DC}$  = area of drogue chute ( $ft^2$ )

$q_D$  = dynamic pressure on drogue chute ( $lb/ft^2$ )

This load is required for structural sizing of the internal cone structure supporting the parachute system.

#### d. Material Selection

The following data are applicable to ring sail-type main parachute systems:

$C_{DM}$	$W_{MA}$ ( $lb/ft^2$ )	$q^*_{max}$ allowable ( $lb/ft^2$ )	Material	Maximum Deployment Mach No.
0.70	0.013	6 to 8	0.6 oz/yd <sup>2</sup> Nylon	0.8
0.75	0.0186	20 to 25	1.1 oz/yd <sup>2</sup> Nylon	0.8

\*Unsterilized

A study of trajectory information indicates that at Mach 0.8 the dynamic pressure will not exceed  $2.5 \text{ lb/ft}^2$  (i. e., for capsules of  $M/C_D A \leq 0.2$ ) in any atmosphere studies for  $\gamma_e = -20$  degrees. Allowing for a material strength reduction of 40 to 50 percent, with a corresponding decrease in  $q_{\max}$  allowable, we see that the  $0.6 \text{ oz/yd}^2$  nylon material is acceptable for the  $\gamma_e = -20$  -degree trajectories. However, for the  $\gamma_e = -90$  -degree trajectories  $q_{\max}$  was about  $6 \text{ to } 7 \text{ lb/ft}^2$  and therefore sterilized  $1.1 \text{ oz/yd}^2$  nylon must be used on these trajectories.

Due to the higher Mach number opening of the drogue parachute (i. e., Mach 2.5 versus 0.8 for this main), higher temperatures will be felt by the canopy and line materials. HT -1 (Dupont NOMEX) material has been selected for the drogue chute as compared to nylon for the main chute. As a consequence, the unit weight of the chute material will be higher. However, a much smaller material strength degradation will be encountered after heat sterilization.

For Hemisflo-type drogue chutes, the following data apply;

$C_{DD}^{(1)}$	$k_D^{(2)}$ (lb/ft <sup>2</sup> )	Actual <sup>(3)</sup> $q_{\max}$ at $M = 2.5$	Allowable <sup>(4)</sup> $q_{\max}$ at $M = 2.5$	$\gamma_e$ (degrees)	Material
0.34	0.1104	50 - 65	80	-90	HT - 1
0.34	0.0276	9 - 14	20	-20	HT - 1

Notes:

- (1) Mean value, based on constructed area
- (2) Only includes canopy and lines
- (3) Based on trajectory data
- (4) Reduction to allow for sterilization.

#### e. Drogue Ejection System Weight

Since the drogue chute must be ejected, an inertia weight-gas generator-driven mortar system was considered in the program. The packaging weight for the drogue system (i. e., canopy, lines, fitting, etc.) usually accounts for about 30 percent weight increase over the weight of just the canopy and lines. The drogue mortar structure, gas generator, pressure sealing sabot, and associated hardware has accounted for an additional 50 percent on several small drogue systems investigated. Hence a typical value of  $K_2$  will be 1.8.

## 8. Impact Attenuation System

### a. Introduction

The idealized model as presented in figure 1-34 for the impact attenuation system was selected to simplify the impact design approach and to meet the requirement that the capsule must be designed to impact up to 45 degrees from the vertical with a passive system. Hence, the most desirable design approach would be a spherical segment using crushable material attenuator.

Derivation of the weight expression is based upon the assumption that all the crushable material is crushed under the designed g load. This results in the highest loads imposed upon the payload and hence a conservative approach. Only known test data of available crushable materials are considered in the determination of material density.

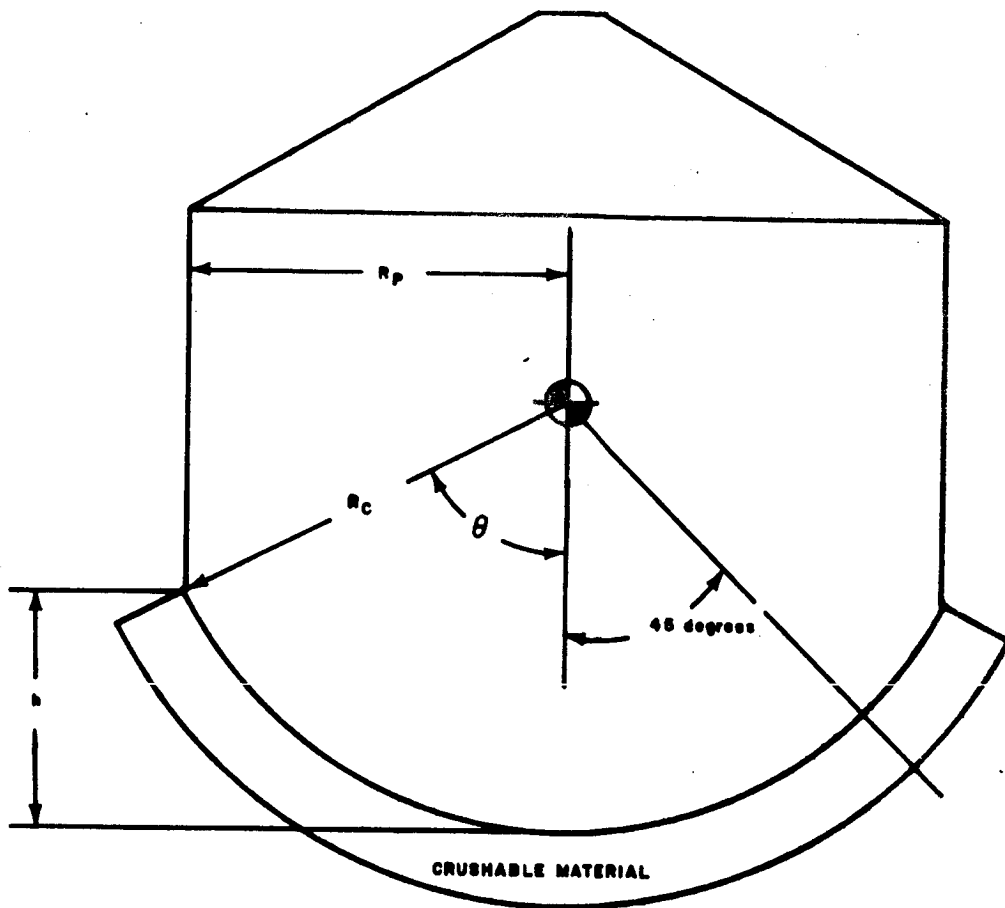
### b. Nomenclature

A	area	in <sup>2</sup>
G	acceleration	earth g
R <sub>p</sub>	radius	feet
V	velocity	ft/sec
m	mass	slugs (lb-sec <sup>2</sup> /ft)
s	crushing stress	lb/in. <sup>2</sup>
t	thickness	inches
w	weight	pounds
$\alpha$	empirical constant	---
$\beta$	empirical constant	---
$\gamma$	density	lb/ft <sup>3</sup>
$\epsilon$	usable strain	---

### Subscripts

cu crushable material

INT payload (internal structure + residual weight + crushable material)



64-239

Figure I-34 IMPACT ATTENUATION SYSTEM--IDEALIZED MODEL

### c. Derivation of Crushing Stress

The crushing stress,  $s$ , of the crushable material used is computed based on the following considerations. The highest loads will be transmitted to the payload if all of the crushable material is being crushed. This could conceivably occur in the event of impact into fairly soft sand, for example. In this event,

$$F = s (\pi R_p^2) .$$

From Newton's Law,

$$F = W_{INT} G .$$

thus,

$$s = \frac{W_{INT} G}{\pi R_p^2 (144)} \quad (7)$$

### d. Derivation of Density of Crushable Material

The density of the crushable material is computed from empirical formulas which have been derived to fit known data. It was decided to attempt the curve fitting with formulas of the type

$$\gamma = \frac{s^\beta}{a} . \quad (8)$$

The results can be seen on figure I-35. The solid lines represent the known data and the dotted lines are the best fits using the above equation. For the three materials shown, the empirical constants are tabulated below. Included in this table are values of  $\epsilon$ , the usable strain of the materials. This quantity is used in subsequent discussions.

For $\gamma$ in lb/ft <sup>3</sup> and $s$ in psi			
Material	$a$	$\beta$	$\epsilon$
Al honeycomb	4.15	0.554	0.75
Plastic foams	4.6	0.662	0.5
Balsa wood	65,000	1.81	0.75

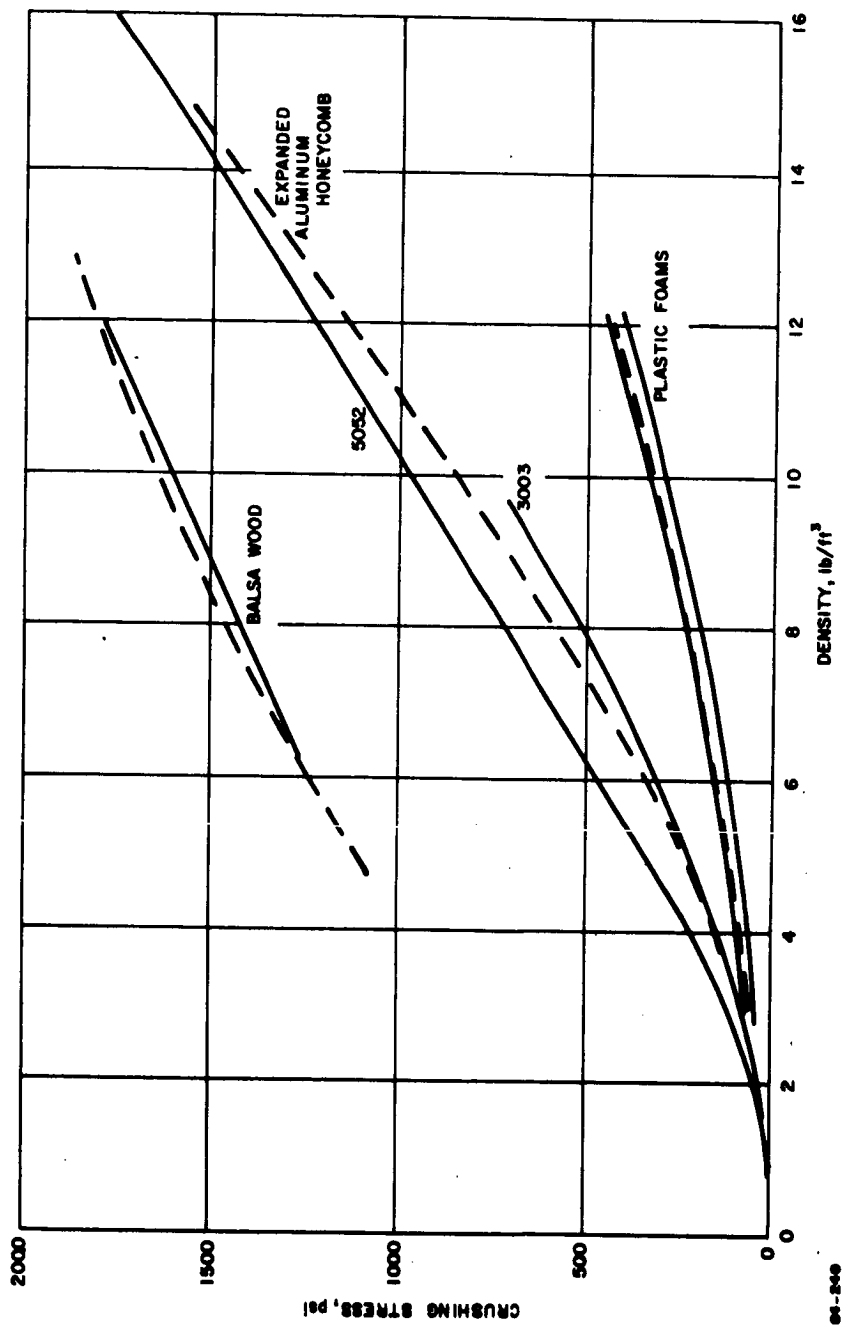


Figure 1-35 CRUSHING STRENGTH OF IMPACT MATERIAL

### e. Derivation of Crushing Thickness

The thickness of material required is computed by analyzing the dynamics of impact. Thus, using figure I-36.

$$F = s \cdot A(y) = m \left( - \frac{d^2 y}{dt^2} \right) .$$

From geometry,

$$A(y) = \pi \left[ 2 R_c \frac{y}{\epsilon} - \left( \frac{y}{\epsilon} \right)^2 \right] .$$

Since

$$\frac{d^2 y}{dt^2} = V \cdot \frac{dV}{dy} ,$$

then

$$V \frac{dV}{dy} = - \frac{\pi s}{m} \left[ 2 R_c \frac{y}{\epsilon} - \left( \frac{y}{\epsilon} \right)^2 \right] .$$

Integrating, using the initial conditions that  $V = V_o$  when  $y = 0$ ,

$$V_o^2 - V^2 = \frac{2 \pi \epsilon s}{m} \left[ R_c \left( \frac{y}{\epsilon} \right)^2 - \frac{1}{3} \left( \frac{y}{\epsilon} \right)^3 \right] .$$

Now, when  $V = 0$ ,  $y = y_m$  and  $y_m/\epsilon = t$

$$V_o^2 = \frac{2 \pi \epsilon s R_c^3}{m} \left( \frac{t}{R_c} \right)^2 \left[ 1 - \frac{1}{3} \frac{t}{R_c} \right] .$$

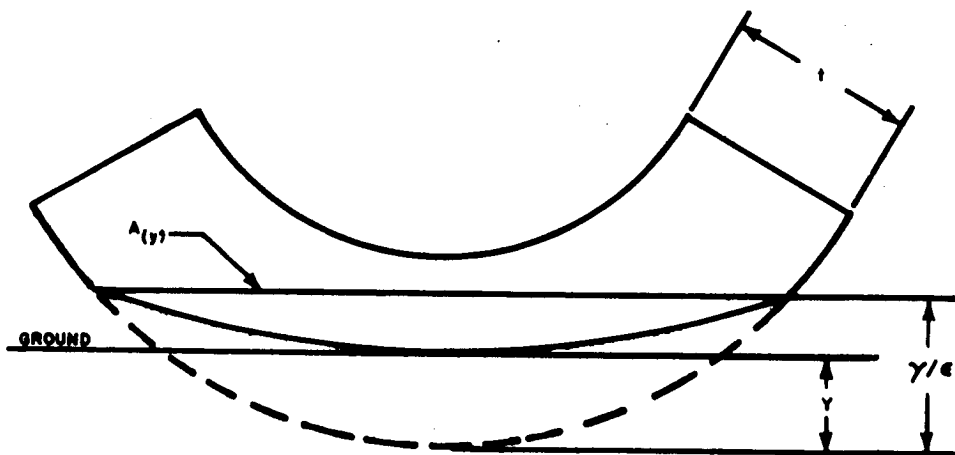
If  $\frac{t}{R_c} \ll 1$  ,

(9)

$$t = \sqrt{\frac{m_{INT}}{2 \pi \epsilon s R_c}} V_o .$$

For the particular geometry shown in figure I-34, employing the assumption that impact must be designed up to 45 degrees from the vertical, it is apparent that





64-241

Figure I-36 CRUSHING THICKNESS MODEL

$$R_c = \sqrt{\frac{5}{4}} R_p .$$

Now, equation (9) may be rewritten as

$$t = 0.23 \sqrt{\frac{W_{INT}}{12 R_p \epsilon S}} V_o . \quad (10)$$

#### f. Weight Expression

Recalling again figure I-34, it follows that

$$\theta = 63.4^\circ .$$

Hence, the total surface area becomes

$$A = 2 \pi R_c h = 2 \pi R_c^2 (1 - \cos \theta)$$

or

$$A = 4.3416 (R_p)^2 \text{ 144} .$$

The weight of crushable material is simply the density times the volume or

$$\begin{aligned} W_{CU} &= A t \gamma \\ &= 2.51 \times 10^{-3} R_p^2 t \gamma \text{ (144)} . \end{aligned} \quad (11)$$

### 9. Evaluation

A method has been presented for the purpose of parametrically evaluating a structural weight for entry capsules into the atmospheres of Mars and Venus. The major contribution of the structural analysis pertinent to the input for systems considerations is to develop structural weights depicting the relative merits of various shapes, sizes, materials, and types of construction. The constraints developed for this study are very general and

consist of such considerations as methods of fabrication, limitations of manufacturing techniques, and material requirements. The critical environment under investigation in this phase of the study would be the planetary entry environment; the trajectory analysis has to be generated to establish the loading conditions on the vehicle.

The analyses employed in this investigation are defined by general types of failure modes. This type of failure is described by general structural considerations and does not require a detailed design for analysis. The modes of failure under consideration are membrane stresses in a shell structure and shell buckling due to general instability. In this investigation, the primary structural problems are restricted to stresses in shells of revolution subjected to axisymmetric loading due to aerodynamic pressure distributions.

There are several areas of uncertainties in the analysis, and in general sandwich shell theory, that must be noted. Among the pertinent ones are:

- a. Inadequate general instability test data to substantiate sandwich shell theory
- b. Inadequate definition of core crushing phenomena and test data substantiation
- c. General instability test data for complete shell of combined sections
- d. Inadequate data on practical consideration factor for large sandwich shells.

Only through a large-scale test program will these facts be fully understood.

The equations used to describe the effects of the load on the structures under consideration are derived from classical theory and are comprehensive. However, due to the nature of the program, it is necessary to account for additional structural weight by use of an experience factor, or practical considerations.

The practical considerations involved in evaluating a realistic weight for the external and internal structure are based primarily on an experience factor of work in the field of reentry systems. The equations used to solve for structural sizes and the corresponding structural weight of the external sandwich and internal structures do not account for the usual problems which arise in practice. These problems encompass such areas as providing local structural members for detail consideration of load distribution, discontinuity stresses, and unsymmetrical effects.

Because this study effort could not include such a detailed structural design, practical design consideration factors were employed.

The external structure, being of sandwich type construction, must be provided with special types of fittings for joining parts together and supporting componentry. Based on experience derived here, the following relationships have been established as a guide.

The factor, accounting for practical considerations, to be used in multiplying the analytical weight expression is variable in accordance to physical characteristics of a particular type of structure. These factors and the type of structure of which they apply are presented here.

$\frac{W_{TOTAL}}{W_{skin, core, bond}}$	= 1.20	A structure with no cutouts, but with provisions of assembly to adjoining structures.
--	--------	---

$\frac{W_{TOTAL}}{W_{skin, core, bond}}$	= 2.20	A structure with a number of large cutouts, sharp bends, and with provisions of assembly to adjoining structures.
--	--------	---

$\frac{W_{TOTAL}}{W_{skin, core, bond}}$	= 1.7	An average of the above factors.
--	-------	----------------------------------

For ring-stiffened type construction, a summary of entry vehicle designs indicated that the above ratio, total gross weight of structure to only skin weight, covered a range from 1.5 to 1.85 depending on the vehicle under consideration. The average of these values again turns out to be 1.7.

## E. HEAT SHIELD BLOCK

### 1. Introduction

A vehicle entering the atmospheres of Mars and Venus will encounter radiative heating from the shock wave gas cap and convective heating from the boundary layer of considerable magnitude. Of primary importance, therefore, is the design of the thermal protection system. From a thermodynamic point of view, this involves determining the thermal protection system weight required to limit the inner structure of the vehicle to some prescribed temperature.

The mathematical model employed in the heat shield calculation must account for the differences in material response to laminar, turbulent and/or radiative heating. Further, it has been found that the thermal response of materials is a function of the levels of the convective and radiative heating, their relative proportions and the enthalpy and pressure of the gas.

The materials chosen for both Mars and Venus are charring ablators and hence a detailed analysis involves the thermal degradation, char and char loss of the material. The amount of combustion, due to the varying atmospheric composition, and the absorption of the thermal pulse in depth are also aspects which must be included in a detailed analysis.

The approach used herein, was to modify an approximate computational scheme for which considerable experience in its use and applicability exists. The development of the original method is given in reference I-82. This calculation had to be modified to handle radiative heating and large effects of structural capacitance. The calculation model is based on a non-charring model treating radiation heating as a surface phenomenon. The effects of these assumptions were then evaluated by comparison with detailed numerical calculations simulating the material response in detail. By use of the approximate method, large savings in computer time and program complexity were achieved, in calculating the large number of cases required for this parametric study.

### 2. Calculation Model

#### a. Symbols

$C_p$	Specific heat of heat shield; Btu/lb
$f$	Vaporization fraction
$H_v$	Heat of vaporization
$H_g/RT_0$	Dimensionless stagnation enthalpy

$H_g$	Stagnation enthalpy of atmosphere
$h_w$	Enthalpy at wall temperature
$k$	Thermal conductivity of heat shield: Btu/hr-ft-°F
$q_c$	Convective heat rate, Btu/ft <sup>2</sup> -sec.
$q_R$	Radiative heat rate, Btu/ft <sup>2</sup> -sec.
$Q_c$	Total convective heating, Btu/ft <sup>2</sup>
$Q_R$	Total radiative heating, Btu/ft <sup>2</sup>
$\dot{s}$	Linear ablation rate, ft/sec.
$t$	Time, seconds
$T$	Temperature, °F
$W_a$	Total ablative weight, lbs/ft <sup>2</sup>
$\dot{w}_a$	Ablation rate, lbs/sec.
$W_{ins}$	Total insulation weight, lbs/ft <sup>2</sup>
$\rho$	Density of heat shield, lbs/ft
$a$	Absorptivity of surface material
$\epsilon$	Emissivity of heat shield material

#### b. Radiation Shield and Structure

The physical model of the thermal system is shown in figure I-37. The boundary layer is assumed to be transparent and the shield surface opaque to the gas cap radiation, such that all the energy from the gas cap strikes the surface of the radiation shield. The radiation shield is assumed to be a homogeneous material with constant thermophysical properties. These properties are assumed to be typical for a self insulating radiation shield (i. e., low thermal conductivity and high surface emissivity) so that the primary means of thermal protection is by surface reradiation at the wall temperature. The problem is solved in two parts. First, the radiation shield requirement without a supporting structure is obtained. Secondly, the thermal protection system requirements are obtained accounting for the supporting structure, employing some of the parameters developed in the previous analysis.

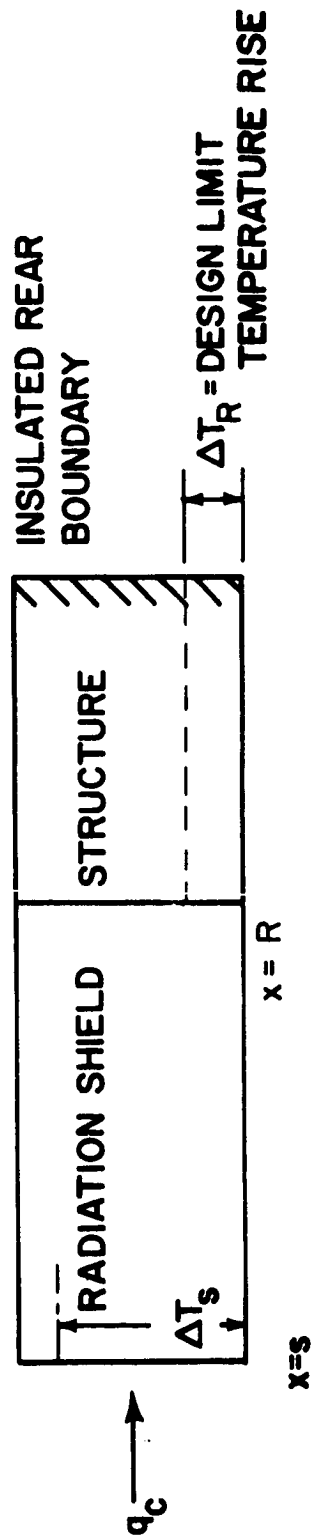


Figure 1-37 RADIATION SHIELD PLUS STRUCTURE

A typical thermal environment is shown in figures I-38 and 39. It is assumed that a thermal protection system is required for an entry altitude of 800,000 until the vehicle impacts. The relative magnitude of the radiative and convective pulses will vary depending on entry conditions, planetary atmospheres, and vehicle design. For this type of reentry environment, the actual problem which involves variable surface temperature is simulated by an equivalent problem. The equivalent problem relates to a slab with a constant surface temperature history, but produces the same transient backface temperature history as the real problem. The analytical solution to the equivalent problem is known, and may be used to avoid numerical calculations. To use this solution, a series of assumptions are made which relate the conditions of the real environment to those satisfying the equivalent problem.

As shown in figure I-37, the surface of the shield is located at  $x = s$  and the rear at  $x = R$ . Initially, the structure is ignored. The surface,  $x = s$ , is exposed to a transient cold wall convective heat rate,  $q_c(t)$ , and a transient radiative heat rate,  $q_R(t)$ . The rear of the shield,  $x = R$ , is assumed to be insulated. The hot-wall convective pulse must be obtained by multiplying the cold-wall pulse by the enthalpy difference across the thermal boundary layer. The enthalpy of the atmosphere at stagnation and wall temperatures are  $H_g$  and  $h_w$ , respectively.  $H_g$  is given as some function of time, and a functional relationship between  $h_w$  and the surface temperature,  $T_s$ , is given. Since the radiative pulse is assumed to strike the shield undisturbed and the shield is assumed to be opaque,  $q_R$  is only multiplied by the absorptivity ( $\alpha$ ) of the surface material. The thermophysical properties,  $K$ ,  $\rho$ ,  $C_p$ ,  $\epsilon$ , and  $\alpha$  are assumed constant. The term  $t_f$  is the duration of the flight time, where  $t$  is selected as zero at entry. The heat shield is assumed to be at some prescribed temperature,  $T_o$ , at  $t = 0$ . It is then required to find the radiation shield weight required to ensure that the backface temperature ( $x = R$ ) just reaches some specified design temperature limit,  $T_R$ , during flight. Mathematically, the problem is to solve the following equation:

$$\frac{\partial T}{\partial t} = \frac{K}{\rho C_p} \frac{\partial^2 T}{\partial x^2} \quad (1)$$

subject to the following initial and boundary conditions.

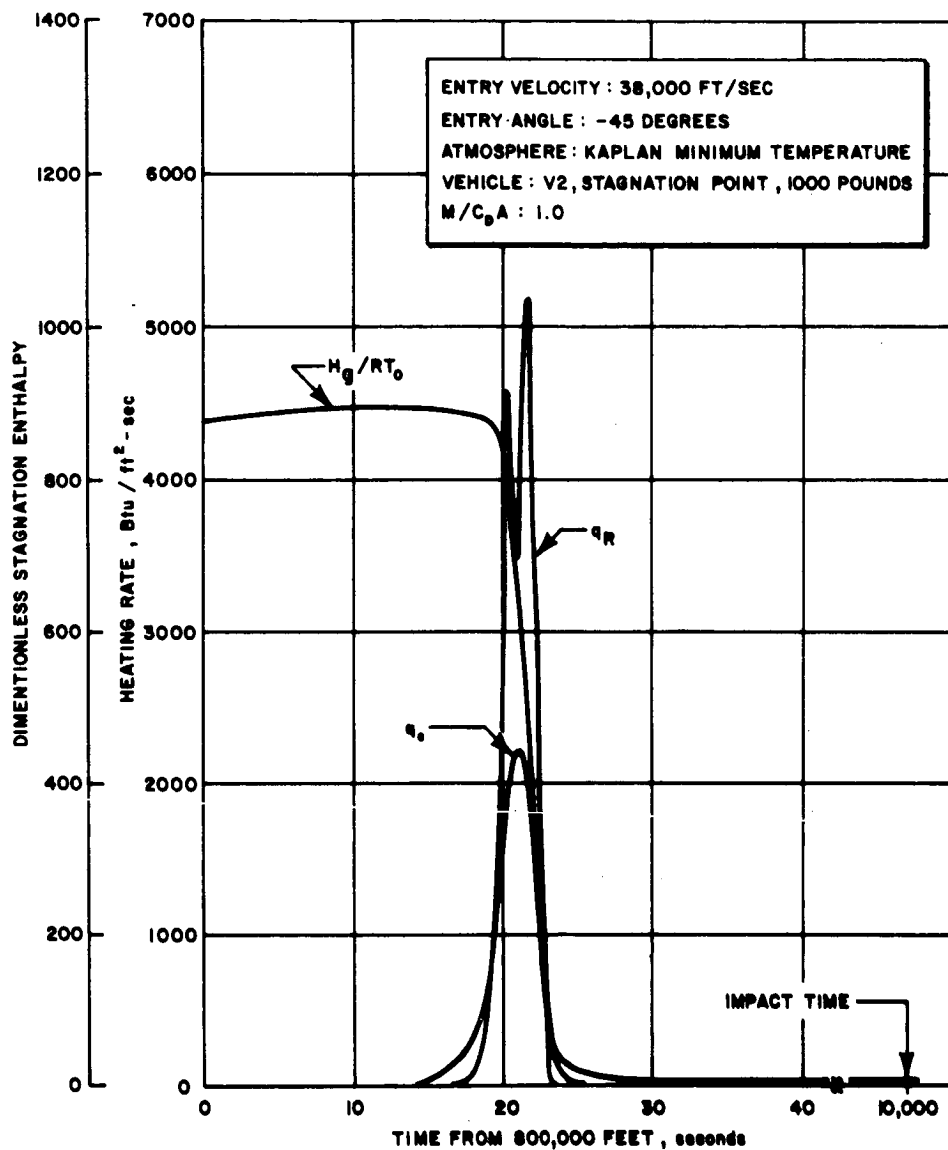
At  $t = 0$ :

$$T(x, 0) = T_o \quad (2)$$

At  $x = s$

$$q_c \left[ \frac{H_g - h_w}{H_g} \right] + \alpha q_R - \sigma \epsilon (T_s + 460)^4 = - \left( K \frac{\partial T}{\partial x} \right)_{x=s} \quad (3)$$





64-848

Figure I-38 TYPICAL VENUS HEATING ENVIRONMENT

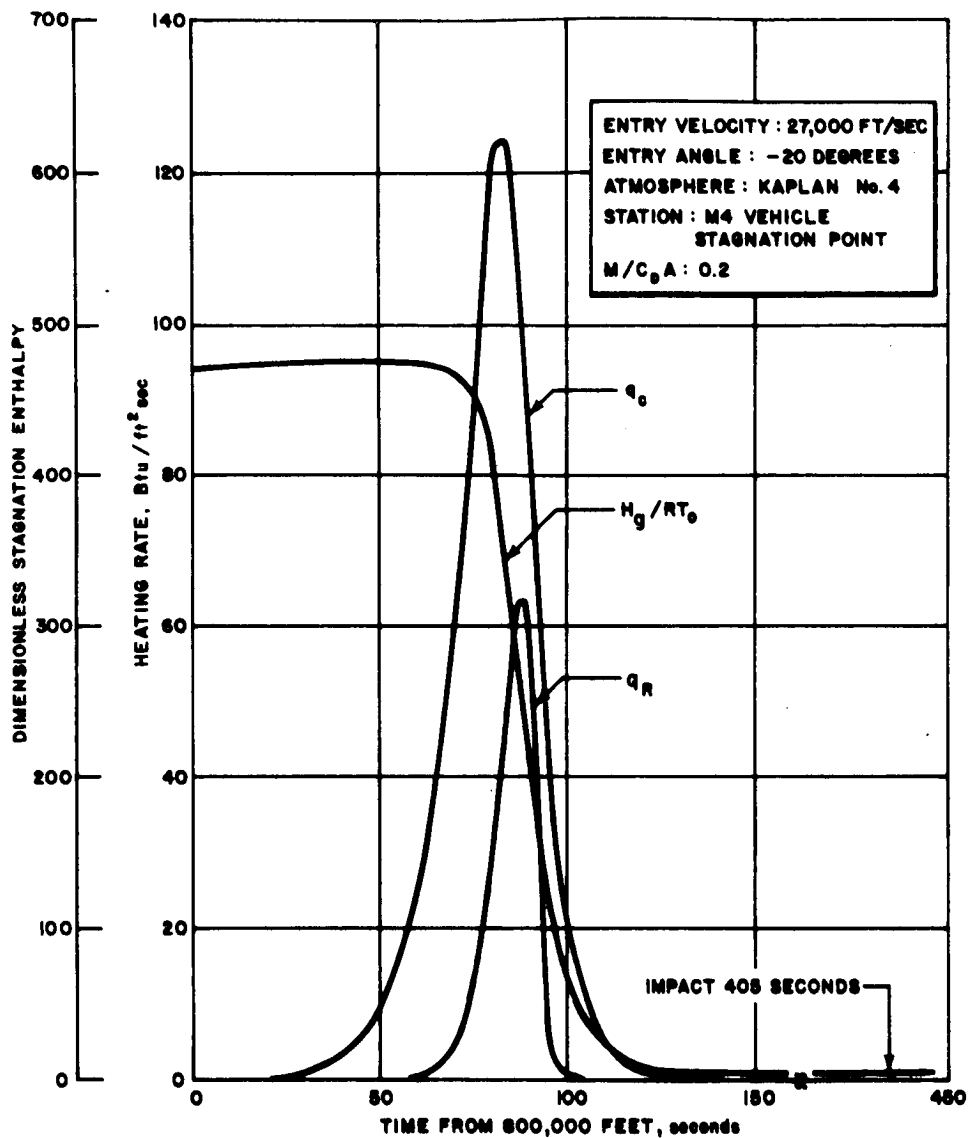


Figure 1-39 TYPICAL MARITIAN HEATING ENVIRONMENT

At  $x = R$

$$\left(\frac{\partial T}{\partial x}\right)_{x=R} = 0 \quad (4)$$

To do this,  $q_C$  and  $q_R$  are replaced by equivalent heat rates  $q'_C$  and  $q'_R$  which start at an initial time,  $t_i$ , defined as

$$t_i = t_{q(\max)} - \frac{2 \int_0^{t_{q_{\max}}} q_C dt + 2\alpha \int_0^{t_{q_{\max}}} q_R dt}{\dot{q}_{\max}} \quad (5)$$

In Equation (5),  $q_{\max}$  is the maximum value that the sum of  $q_C$  and  $\alpha \dot{q}_R$  can achieve over the trajectory and  $t_{q(\max)}$  corresponds to the time when this occurs. A condition placed on the transformation of  $q_C$  and  $q_R$  to  $q'_C$  and  $q'_R$  is that the total heats  $Q_C$  and  $Q_R$  are the same for both pulses, i. e.,

$$\begin{aligned} Q_C &= \int_{t_i}^{t_f} q'_C dt = \int_0^{t_f} q_C dt \\ \alpha Q_R &= \alpha \int_{t_i}^{t_f} q'_R dt = \alpha \int_0^{t_f} q_R dt \end{aligned} \quad (6)$$

The variable enthalpy,  $H_g$  is replaced by its time average,  $H'_g$ ,

$$H'_g = \frac{1}{t_f - t_i} \int_{t_i}^{t_f} H_g dt \quad (7)$$

The sum of the equivalent heat rates  $q'_C$  and  $q'_R$  are then chosen such that the rate of heat conduction into the bar is  $q_k$ ,

$$q'_c \left[ 1 - \frac{h'_w}{H'_g} \right] + \alpha q'_R - \sigma \epsilon (T'_s + 460)^4 = q_k \quad (8)$$

$q_k$  is then the heat rate that would produce a constant surface temperature history,  $T'_s$ . As a consequence, the hot wall and emissivity corrections are independent of time, and the problem is linearized.

The problem is now one of finding the temperature response in a finite bar, one end of which is held at a constant temperature, the other end of which is insulated. The solution to this problem is given by Carslaw and Jaeger (ref. I-76):

$$\frac{\Delta T(x, t)}{\Delta T_s} = 1 - \frac{4}{\pi} \sum_{n=0}^{\infty} \frac{(-1)^n}{2n+1} \left\{ \exp \left[ - \frac{(2n+1)^2 \pi^2 \frac{K}{\rho C_P} t}{4(R-s)^2} \right] \right\} \cos \frac{(2n+1)\pi(R-x)}{2(R-s)} \quad (9)$$

Integrating equation (8) over the time interval from  $t_i$  to  $t_r$ , where  $t_r$  is the time at which the backface reaches its design limit temperature,  $T_R$ , the total heat conducted into the material is found to be:

$$Q_c \left[ 1 - \frac{h'_w}{H'_g} \right] + \alpha Q_R - \epsilon \sigma (T'_s + 460)^4 (t_r - t_i) = W C_P \Delta T_M \quad (10)$$

In equation (1)  $Q_c$  and  $\alpha Q_R$  are given by equation (6). The corrections

$\left( 1 - \frac{h'_w}{H'_g} \right)$  and  $\epsilon \sigma (T'_s + 460)^4$  are constants which are functions only of surface temperature,  $T'_s$ . On the right side of equation (10),  $W$  is the weight of the shield required to limit the backface temperature rise to the specified limit,  $\Delta T_R$ , over the interval  $(t_r - t_i)$ , and  $\Delta T_M$  is the average temperature rise in the bar where these conditions are met.

At this instant, some unique value of  $\frac{K \rho t}{C_P W^2}$  exists and there is a temperature distribution in the bar given by equation (9) from which  $\Delta T_M$  could be calculated if  $t_r$  and  $T'_s$  were known.

Consider, first, the case where the rear face reaches a maximum temperature (just equal to the design limit) at some time  $t_r < t_f$  and subsequently falls below this value. In order for this to happen when using equation (9), the entire bar must have equilibrated at a uniform temperature

$T_R$  at time  $t_R$ . Hence, at this instant  $T'_s = T_R$ . Furthermore, from equation (9) the condition corresponds very nearly to a value of unity for  $\frac{K \rho t}{C_p W^2}$ .

Thus,

$$W = \sqrt{\frac{\rho K}{C_p}} \sqrt{t_R - t_i} \quad (11)$$

substituting equation (11) into equation (10) and solving for

$$\sqrt{t_R - t_i} = \frac{\sqrt{\rho K C_p \Delta T_M^2 + 4 \epsilon \sigma (T_s + 460)^4 [Q_c \left(1 - \frac{h'_w}{H'_g}\right) + a Q_R]}}{2 \epsilon \sigma (T_s + 460)^4} - \frac{\Delta T_M \sqrt{\rho K C_p}}{2 \epsilon \sigma (T_s + 460)^4}$$

Hence, the required weight  $W$  can be obtained from substituting equation (11) into equation (12).

Consider next the case where the design limit temperature is reached precisely at the instant  $t_f$ , and the bar subsequently reaches a larger equilibrium value at time  $t_R > t_f$ . This case is the more probable of the two conditions, since the average surface temperature experienced during entry is much larger than the allowable backface temperature rise,  $T_s \gg T_R$ . To solve for this condition by hand calculation or machine calculation an iteration procedure is required, since there are essentially two unknowns in equation (10) viz.,  $T_s$  and  $W$ . Consequently, some choice must be made for a value of  $T_s$  to start the iteration. The following procedure involves the selection of different values to  $T_s$  until a solution of equation (10) is obtained.

Since the primary means of protection is through surface radiation, assume for the first approximation,  $T'_s$ , that  $h'_w/H'_g$  and  $W_{c_p} \Delta T_M$  are both zero. Solution of equation (10) for  $T'_s$  then gives the maximum possible value for  $T'_s$ ,

$$T'_s = \sqrt[4]{\frac{Q_c + a Q_R}{\epsilon \sigma (t_f - t_i)}} - 460, \quad (13)$$

knowing  $T'_s$ , and  $T_R$  the ratio  $\frac{\Delta T_R}{\Delta T'_s}$  can be formed. To facilitate the iteration procedure, equation (9) was solved for the value of  $\frac{\Delta T_R}{\Delta T'_s}$ ; also,  $\frac{\Delta T_M}{\Delta T'_s}$  was obtained by integration of  $\frac{1}{\Delta x} \int \frac{\Delta T_x}{\Delta T'_s} ds$  where  $s \leq x \leq R$ . These results are presented as a function of  $\frac{K\rho t}{C_p W^2}$  in figure I-40. For

abbreviation let:

$$\frac{K\rho(t_f - t_i)}{C_p W'^2} = r' \quad (14)$$

Then,

$$W' = \sqrt{\frac{K\rho(t_f - t_i)}{C_p r'}} \quad (15)$$

Equation (15) gives the maximum possible value for  $W$ . Using  $T'_s$  and the functional relation between  $h'_w$  and  $T'_s$ , a hot wall correction may now be applied to  $Q_c$ :  $Q_c(1 - h'_w/H'_g)$ . This represents the minimum possible hot wall input. Using this input and the first approximations  $W'$  and  $\Delta T'_M$ , a second approximation for  $T''_s$  may be found from equation (10):

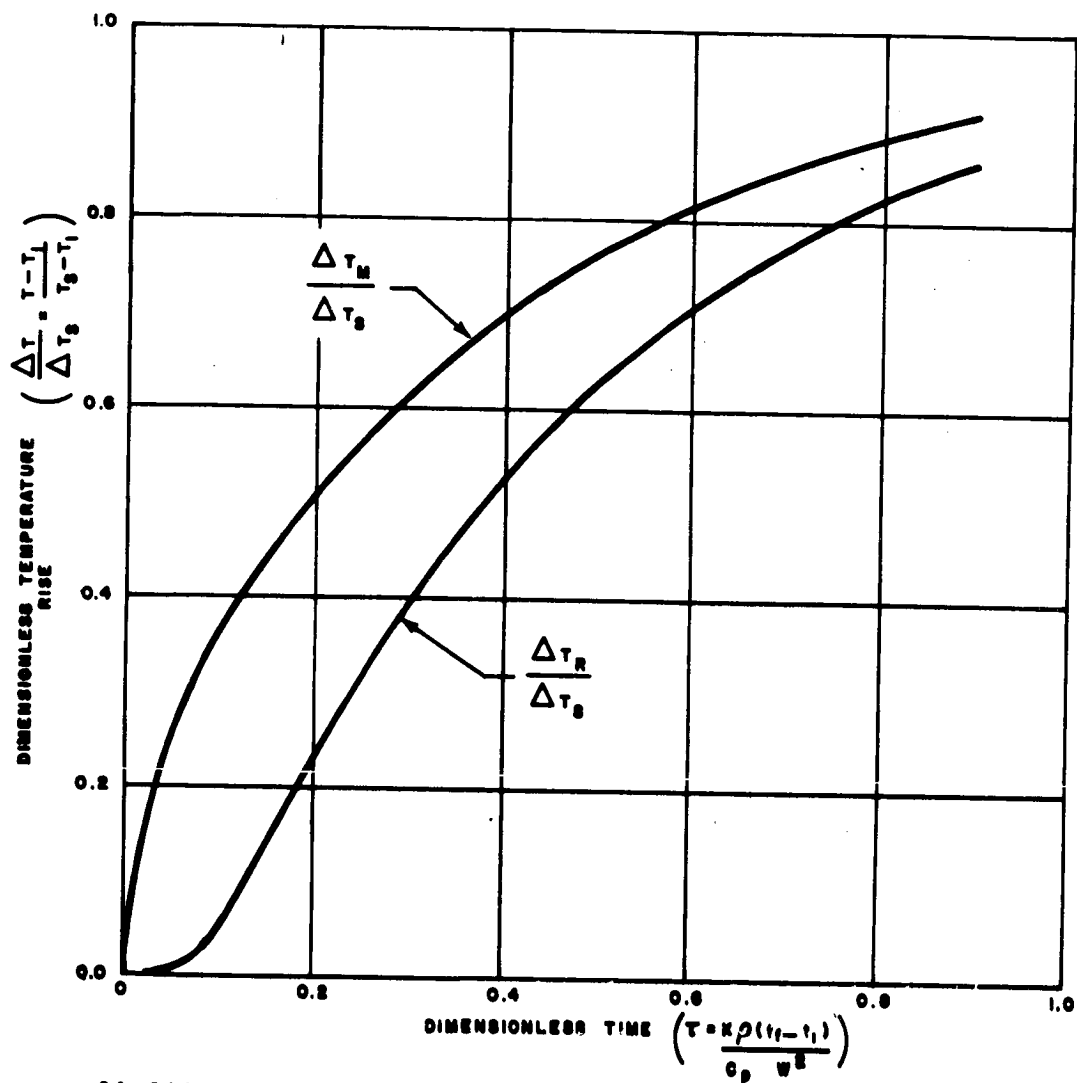
$$Q_c \left[ 1 - \frac{h'_w}{H'_g} \right] + a Q_R - \epsilon \sigma (T''_s + 460)^4 (t_f - t_i) = W' C_p \Delta T'_M \quad (16)$$

Solving for  $T''_s$ :

$$T''_s = \left[ \sqrt[4]{\frac{Q_c \left( 1 - \frac{h'_w}{H'_g} \right) + a Q_R - W' C_p \Delta T'_M}{\epsilon \sigma (t_f - t_i)}} - 460 \right] \quad (17)$$

Equation (17) gives a minimum value for  $T''_s$ . The procedure is repeated by forming the new ratio  $\Delta T_R/\Delta T''_s$ , entering figure I-40 and finding the

new value of  $r'' = \frac{K\rho(t_f - t_i)}{W''^2}$  to be solved for  $W''$  and also the new value of  $\frac{\Delta T'_M}{\Delta T'_s}$  to be used with  $r'''$  in solving for  $W'''$ . The process is repeated until a suitable convergence is obtained usually by the third iteration.



64-244

Figure 1-40 REAR AND MEAN TEMPERATURE RISE IN A FINITE MEDIUM WITH CONSTANT SURFACE TEMPERATURE AND INSULATED REAR BOUNDARY

The final weight found is designated as  $W^N$ .

### c. Ablation System

The ablation system as shown in figure I-41 is composed of a single heat shield material, satisfying both insulation and ablation requirements. The term ablation here, may be described as the surface recession of a material due to the absorption of heat through a phase or degradation reaction. Again, the boundary layer is assumed to be transparent and the shield surface opaque to the gas cap radiation. It is further assumed that this remains unchanged with the injection of ablation products into the boundary layer; thus all the energy from the gas cap will still strike the ablating surface.

The approximate procedure of an ablation system is divided in two sections, namely, the ablation weight and insulation weight.

#### 1) Ablation weight

Using the same heat input and air enthalpy as illustrated in figures I-38 and 39. it is assumed that when the heat rate reaches some value at time  $t_{ia}$  the material begins to ablate with a constant surface temperature  $T_A$ . An instantaneous heat balance at the surface of the material is then

$$q_c \left( 1 - \frac{h_w}{H_g} \right) + \alpha q_R - \epsilon \sigma (T_A + 460)^4 = - \left( K \frac{\partial T}{\partial x} \right)_{x=s} + \dot{W}_A (q^* - C_p \Delta T_A) \quad (18)$$

where  $q^*$  is the effective heat of ablation.

At any instant  $t_{ia}$  just prior to the onset of ablation (and just subsequent to its termination,  $t_{fa}$ ),  $\dot{W}_A = 0$ . An estimate of  $t_{ia}$  and  $t_{fa}$  can be made by setting  $- \left( K \frac{\partial T}{\partial x} \right)_{x=s} = 0$ . For such conditions,  $t_{ia}$  and  $t_{fa}$  may be found from the given  $q_c$ ,  $q_R$  and  $H_g$  versus time relationships at those points where:

$$q_c \left[ 1 - \frac{h_w}{H_g} \right] + \alpha q_R = \epsilon \sigma (T_A + 460)^4 \quad (19)$$

As  $t_{ia}$  approaches  $t_q(\max)$  the maximum surface temperature will just reach the ablation temperature and then decrease. Under these conditions, equation (19) may be improved by deriving another expression which accounts for the amount of heat conducted into the solid. The expression may then be used to determine what level of cold wall and radiative heat flux is needed to cause ablation or what is the limiting total heat flux that a radiation shield can withstand without exceeding some prescribed design limiting surface temperature.



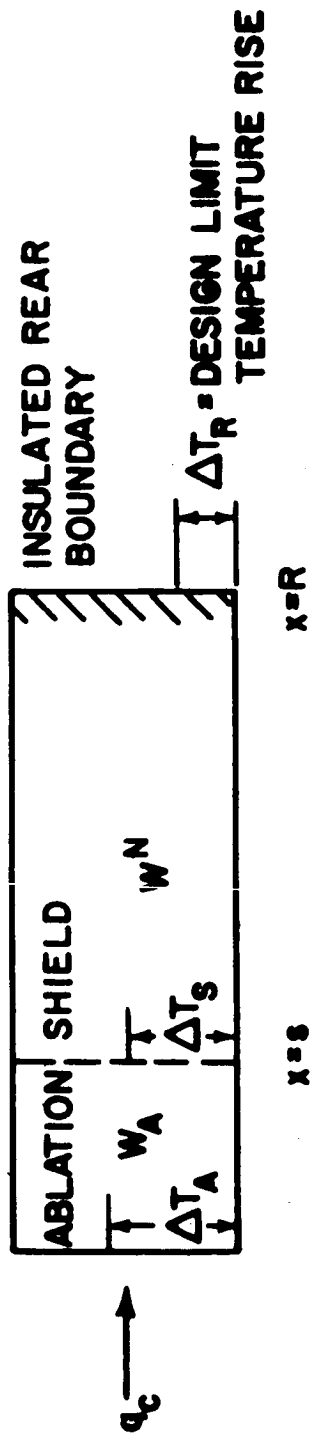


Figure 1-41 SIMPLE ABLATION SHIELD

For a radiation shield it can be assumed that the effective heat flux and surface temperature reach their maximum values simultaneous with the maximum total heat rate. At peak heating, the instantaneous heat balance at the surface with no ablation is:

$$\left[ q_c \left( 1 - \frac{h_w}{H_g} \right) + a q_R \right]_{\max} = \left( -K \frac{\partial T}{\partial x} \Big|_{x=s} \right)_{\max} + \epsilon \sigma (T_A + 460)^4 \quad (20)$$

The maximum effective heat flux may be approximated by assuming the shape of the effective heat flux history is sinusoidal of the form

$$-K \frac{\partial T}{\partial x} \Big|_{x=s} = q_{\text{eff}(\max)} \sin^2 \left( \frac{\pi t}{2[t_{q_{\max}} - t_i]} \right) \quad (21)$$

where  $t_q(\max)$  and  $t_i$  are defined in equation (5)

Solving the one-dimensional heat conduction equation with equation (21) as a boundary condition and assuming the slab is essentially semi-infinite gives the following relationship between the surface temperature,  $T_s$ , at peak heating and the maximum effective flux (ref I-79).

$$\left( -K \frac{\partial T}{\partial x} \Big|_{x=s} \right)_{\max} = 1.82 \sqrt{\frac{K \rho C_p}{2(t_{q_{\max}} - t_i)}} \Delta T_s \quad (22)$$

Putting (22) into (20) results in a relationship between the maximum surface temperature and maximum total heat flux.

Then, if

$$\left[ q_c \left( 1 - \frac{h_w}{H_g} \right) + a q_R \right]_{\max} > 1.82 \sqrt{\frac{K \rho C_p}{2(t_{q_{\max}} - t_i)}} \Delta T_A + \epsilon \sigma (T_A + 460)^4 \quad (23)$$

ablation will occur.  $T_A$  is the ablation temperature.

The steady state mass ablation rate ( $\dot{W}_a$ ) can be found from the following:

$$\dot{w}_a = \frac{q_c \left[ 1 - \frac{h_w}{H_g} \right] + \alpha q_R - \epsilon \sigma (T_A + 460)^4}{C_p (T_A - T_o) + X f_1 [Hv_1 + \eta_1 (H_g - h_w)] + (1-X) f_2 [Hv_2 + \eta_2 (H_g - h_w)]} \quad (24)$$

at any instant of time between  $T_{ia}$  and  $t_{fa}$ . In equation (24) the subscripts refer to the solid (1) and resin (2), X refers to the solid fraction, f to the vaporization fraction,  $\eta$  to the transpiration coefficient, and  $H_v$  to heat absorbed by a phase change or reaction. Since the boundary layer and ablation products are assumed transparent to the gas cap radiation, only convective heating is blocked by transpiration. Therefore, equation (24) is unrealistic for large ablation rates since mathematically more energy can be blocked than is convected to the surface. Modifying the equation for the situation when this might occur yields:

$$\dot{w}_a = \frac{\alpha q_R - \epsilon \sigma (T_A + 460)^4}{C_p (T_A - T_o) + X f_1 H_v_1 + (1-X) f_2 H_v_2} \quad (25)$$

The total ablation weight loss is then:

$$W_a = \int_{t_{ia}}^{t_{fa}} \dot{w}_a dt$$

where  $\dot{w}_a$  at any time is the larger value found from equation (24) and (25).

## 2) Insulation weight

The heat stored in the material just at the instant the ablation ceases is  $Q_K$ ,

$$Q_K = W_{ins} C_p \Delta T_M \quad (26)$$

In equation (26),  $W_{ins}$  is the "insulation weight," i.e., the weight of the required heat shield after the ablation mass loss, and  $\Delta T_M$  is the mean temperature rise of this weight at the end of ablation.

It is assumed that an exponential temperature distribution corresponding to average steady-state ablation rate exists in  $W_{ins}$  at time  $t_{fa}$ . This temperature distribution is given mathematically as

$$\Delta T(x, t_{fa}) = \Delta T_A e^{-\dot{s}x/a} \quad (27)$$

where  $\dot{s}$  is the ablation rate.

For this distribution, the following expression can be obtained for  $Q_K$ ,

$$Q_K = \rho C_P \int_0^{\infty} \Delta T dx = \frac{K \Delta T_s}{\dot{s}} \quad (28)$$

In this expression,  $\dot{s}$  is taken to be the average value in the ablation period:

$$\dot{s} = \frac{W_A}{\rho (t_{fa} - t_{ia})} \quad (29)$$

The mean temperature corresponding to a semi-infinite bar is obtained from the constant wall temperature chart, figure I-40, for

$$\frac{K \rho t}{C_P W^2} = 0.05. \text{ Integration of this curve yields:} \quad (30)$$

$$\Delta T_M = \frac{1}{4} \Delta T_s$$

Combining equations (26) through (30), the required insulation weight is found to be the following:

$$W_{ins} = \frac{4(t_{fa} - t_{ia})}{W_a} \left( \frac{\rho K}{C_P} \right) \quad (31)$$

The insulation weight given by equation (31) is that corresponding to a barely noticeable backface temperature rise at the instant  $t_{fa}$ . The sum  $(W_A + W_{ins})$  is not the total weight of shield required, since the heating from the end of ablation to impact has not been accounted for. The problem is to find the amount of insulation required such that the backface temperature rise does not exceed a given design value. During the post-ablation period, the problem is simply that of a radiation shield which starts (at time  $t_{fa}$ ) with an initial temperature distribution. To use the procedure described for the radiation system, it is necessary to transform the time

scale such that the problem starts at some "adjusted" time,  $t_{adj}$ , and runs thenceforth with some constant surface temperature, such that a temperature distribution corresponding to  $\frac{K \rho t}{C_p W^2} = 0.05$  exists at  $t_{fa}$  and a backface temperature rise of  $\Delta T_R$  is achieved.

Using a value of  $\frac{K \rho t}{C_p W^2} = 0.05$  and solving for  $t$ , the time required to establish the distribution corresponding to this value is found to be:

$$t = \frac{0.05}{(\rho K / C_p)} W_{ins}^2 \quad (32)$$

Using equation (31) for  $W_{ins}$ , the following expression is obtained.

$$t = \frac{4}{5} \frac{\rho K}{C_p} \left( \frac{t_{fa} - t_{ia}}{W_a} \right)^2 \quad (33)$$

Relating this to the time scale used in the problem, the "adjusted" time,  $t_{adj}$  is found to be the following:

$$t_{adj} = t_{fa} - \frac{4}{5} \left( \frac{\rho K}{C_p} \right) \left( \frac{t_{fa} - t_{ia}}{W_a} \right)^2 \quad (34)$$

Note that a condition is placed on  $t_{adj}$ , namely that  $t_{adj} \geq t$ , where  $t_l$  is defined by equation (5). The total heat applied to the bar during the adjusted heating period is the following.

$$Q'_c = \int_{t_{adj}}^{t_f} q_c dt - \int_{t_{adj}}^{t_{fa}} \left\{ q_c \left[ 1 - \frac{h_w}{H_g} \right] - \epsilon \sigma (T_A + 460)^4 \right\} dt \quad (35)$$

$$Q'_R = \int_{t_{adj}}^{t_f} q_R dt \quad (36)$$

The first term on the right side of equation (35) is the integrated convective heating applied to the bar between  $t_f$  and  $t_{adj}$ , and the second term represents the heat absorbed during ablation between  $t_{fa}$  and  $t_{adj}$  had there been only convective heating. A similar term is neglected in equation (36).

The additional weight of material,  $W_N$ , required to achieve the design limit temperature rise,  $\Delta T_R$ , at the backface at impact is calculated by the same procedure described for radiation shields. However,  $Q_C'$  and  $Q_R'$ , as described in equations (35) and (36), are used in place of  $Q_C$  and  $Q_R$  respectively, and  $t_{adj}$  in place of  $t_1$  in equation (13) through (17). The total weight of shield required  $W_T$  is then the sum:  $W_T = W_a + W_N$ .

#### d. Inclusion of Heat Sink Effects of Structure

The analytical solution for the rear temperature response in a finite slab backed by a capacitive structure, whose surface is at a constant surface temperature and whose backface is insulated, is given by Carslaw and Jaeger. The solution is:

$$\frac{\Delta T(R, t)}{\Delta T_s} = 1 - \sum \frac{2(\beta_n^2 + \phi^2) e^{-\left(\frac{K_1 \rho_1 \beta_n t_o}{C_{p1} W_1^2 3600}\right)} \sin \beta_n}{\beta_n (\beta_n^2 + \phi^2 + \phi)} \quad (37)$$

where  $\beta_n$ 's are the eigenvalues of the transcendental equation

$$\beta_n \tan \beta_n = \phi = \frac{W_1 C_{p1}}{W_2 C_{p2}}$$

In the above equation, the subscript (1) refers to the heat shield and the subscript (2) to the structure.

If the surface temperature history is assumed unchanged by the structure, the temperature ratio,  $\Delta T_R / \Delta T_s$ , remains the same. Therefore, the temperature ratio found from figure I-40, satisfying equation (10), can be employed in equation (37) to find  $W_1$ , the required heat shield weight accounting for structure. Equation (37) is represented graphically in figure I-42.  $\Delta T_R / \Delta T_s$  is plotted versus the

dimensionless time parameter,  $\tau = \frac{K \rho (t_f - t_i)}{C_p W_1^2}$ , for various ratios of

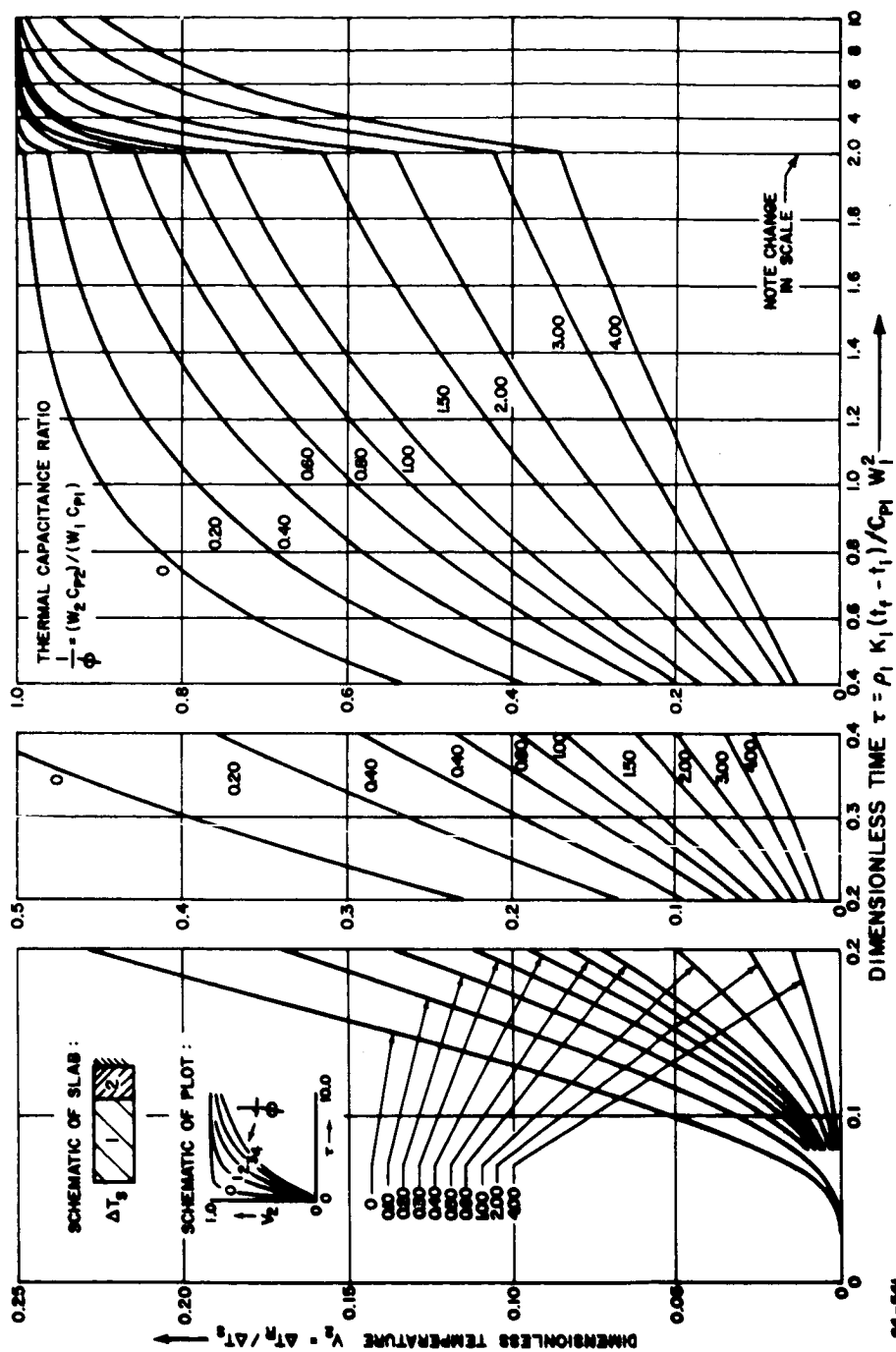


Figure 1-42 COMPOSITE SLAB WITH CONSTANT SURFACE TEMPERATURE WHERE SECOND LAYER ACTS AS A CAPACITANCE

$\phi = \frac{W_1 C_{p1}}{W_2 C_{p2}}$ . It is seen that the solution of equation (37) for  $W$ , is an iterative procedure, as  $W_1$  appears in both  $\phi$  and  $r$ .

An alternate method for determining the heat sink effects of the structure can also be employed. The system being considered is shown in figure I-37. The problem is to find the weight  $W_1$  of radiative shield required to guard a given structure whose weight  $W_2$  and properties are known, so that the structure will be limited to a specified temperature rise  $\Delta T_R$  at the instant of impact,

Three assumptions are made in order to perform this calculation.

- 1) The structure is a pure capacitance.
- 2) The total amount of thermal energy stored in the shield ( $Q_1$ ) and structure ( $Q_2$ ) is the same as that stored in a single radiative shield ( $Q^N$ ) designed for the same backface temperature limit.
- 3) The heat per unit mass stored in the radiation shield of the composite system is the same as the heat stored per unit mass in a single radiation shield designed to the same backface temperature limit.

As a consequence of the first assumption, the temperature of the structure is always uniform and the energy stored in the structure at impact is:

$$Q_2 = W_2 C_{p2} \Delta T_R \quad . \quad (38)$$

As a consequence of the second assumption, the total heat stored in the shield and structure of the composite system is equal to the heat stored in the pure radiation shield.

$$Q_1 + Q_2 = Q^N = W^N C_{p1} \Delta T_M^N \quad . \quad (39)$$

As a consequence of the third assumption, the required weight,  $W_1$ , of the radiation shield portion of the composite system is:

$$W_1 = W^N \frac{Q_1}{Q^N} \quad . \quad (40)$$



Solving equation (39) for  $Q_1/Q^N$  and substituting into (40) the required weight is found to be:

$$w_1 = w^N \left( 1 - \frac{w_2 C_{p2} \Delta T_R}{w^N C_{p1} \Delta T_M^N} \right) \quad (41)$$

Equation (37) represents a more accurate structure correction technique than equation (41). This will be demonstrated in the section entitled, Comparison with Finite Difference Solution for Surface Ablators. Because of space limitations, the solution to equation (37) was programmed in the form of curve fits of figure I-42. For cases where  $r$  was greater than 2.0, the heat shield weight,  $w_1$ , was calculated based on  $r = 2.0$  and based on equation (41); the smaller of the two was selected as the answer. If the uncorrected heat shield weight is calculated from equation (11) directly, because the slab has equilibrated, equation (41) is employed setting  $\Delta T_R = \Delta T_M$ . The total heat shield required is  $w_A + w_1$ .

#### e. Thermodynamic Analysis of a Thin Skin Heat Sink

From a thermodynamic viewpoint, any heat sink thickness will suffice if the combined convective and radiative heating is never greater than the energy reradiated from a surface at the design temperature,  $T_D$ . This criteria can be expressed as:

$$q_c \left[ 1 - \frac{h_D/RT_o}{H_g/RT_o} \right] + (1-r) q_R - \sigma \epsilon T_D^4 = q_k < 0 \quad (42)$$

If, however,  $q_k > 0$ , there is a minimum heat sink thickness associated with the design temperature. An estimate of this thickness can be obtained by noting that the maximum temperature for a "thin slab" will occur when  $q_k = 0$ . The energy absorbed to this time will then determine the thickness. A temperature history can be assumed, thus allowing the first and third terms in equation (42) to be evaluated. For the purposes of this analysis, a sinusoidal temperature history corresponding to an isosceles triangular heating pulse is assumed. Integrating equation (42) between the end of effective heating (time when  $\dot{q}_k = 0$ ) and the start of the triangular pulse, the following is obtained:

$$Q_c \left[ 1 - \frac{h_D/RT_o}{H_g/RT_o} \right] + (1-r) Q_R - \sigma \epsilon \int_{t_i}^{t_D} T_D^4 dt = w_1 C_p (T_D - T_1) \quad (43)$$

where

$$Q_c = \int_0^{t_D} q_c dt$$

$$H_g'/R T_o = \frac{\int_{t_i}^{t_D} H_g/R T_o}{(t_D - t_i)}$$

$$h_D'/R T_o = A \left( \frac{T_1 + T_D}{2} \right) + B \left( \frac{T_1 + T_D}{2} \right)^2 + \frac{B}{2} \left( \frac{T_D - T_1}{2} \right)^2$$

$$Q_R = \int_0^{t_D} q_R dt$$

$$\int_{t_i}^{t_D} T_D^4 dt = \left[ \left( \frac{T_1 + T_D}{2} \right)^4 + 3 \left( \frac{T_1 + T_D}{2} \right)^2 \left( \frac{T_D - T_1}{2} \right)^2 + \frac{3}{8} \left( \frac{T_D - T_1}{2} \right)^4 \right] (t_D - t_i)$$

A and B are constants

$T_1$  = initial temperature of slab

$W_1$  = weight of slab lb/ft<sup>2</sup>

$C_p$  = specific heat Btu/lb-°F

$t_D$  = time when  $q_K = 0$

$t_i$  = initial time of triangular pulse (ref. I-82)

$$t_i = t_{q_{\max}} - \frac{2 \int_0^{t_{q_{\max}}} q_c dt + 2(1-r) \int_0^{t_{q_{\max}}} q_R dt}{[q_c + (1-r) q_R]_{\text{peak}}}$$

$t_{q_{\max}}$  = time when  $[q_c + (1-r) q_R]$  is maximum

From equation (43)  $W_1$  the required heat sink weight can easily be obtained.

#### f. Wall Enthalpy

The enthalpy at the surface temperature of the slab is required to correct the cold wall convective heat transfer for the enthalpy difference across the boundary layer. The enthalpy will differ considerably with atmospheric model, temperature, and pressure. At lower temperatures ( $<2500^\circ\text{R}$ ) enthalpy is independent of pressure and can be calculated from its definition,  $H = \sum m_i c_{pi} T$ , where the subscript  $i$  stands for the constituents of the atmosphere. At higher temperatures and low pressures, dissociation occurs.

Static enthalpies for temperatures between 0 and  $5400^\circ\text{R}$  have been computed for the four Martian atmospheres. The results for a pressure of 10 atmospheres are shown in figure I-43. Approximate curve fits used in the heat shield computer program are also plotted. As can be seen, the enthalpies increase more rapidly with temperature for the atmospheres containing a greater amount of  $\text{CO}_2$ . This is the result of the dissociation of the  $\text{CO}_2$ .

Static enthalpies have also been computed for the Venus atmospheres for temperatures between 0 and  $7200^\circ\text{R}$  for a pressure of 1000 atmospheres. The computed data and the curve fit is shown in figure I-44.

Pressures of 10 atmospheres for Mars and 1000 atmospheres for Venus were chosen since these pressures represent conservative upper limits to the largest expected dynamic pressure at the stagnation point. The selection of this pressure results in a conservative heat shield weight. This results since the enthalpy increases with decreasing pressure and the heat transfer is a function of the enthalpy difference across the boundary layer.

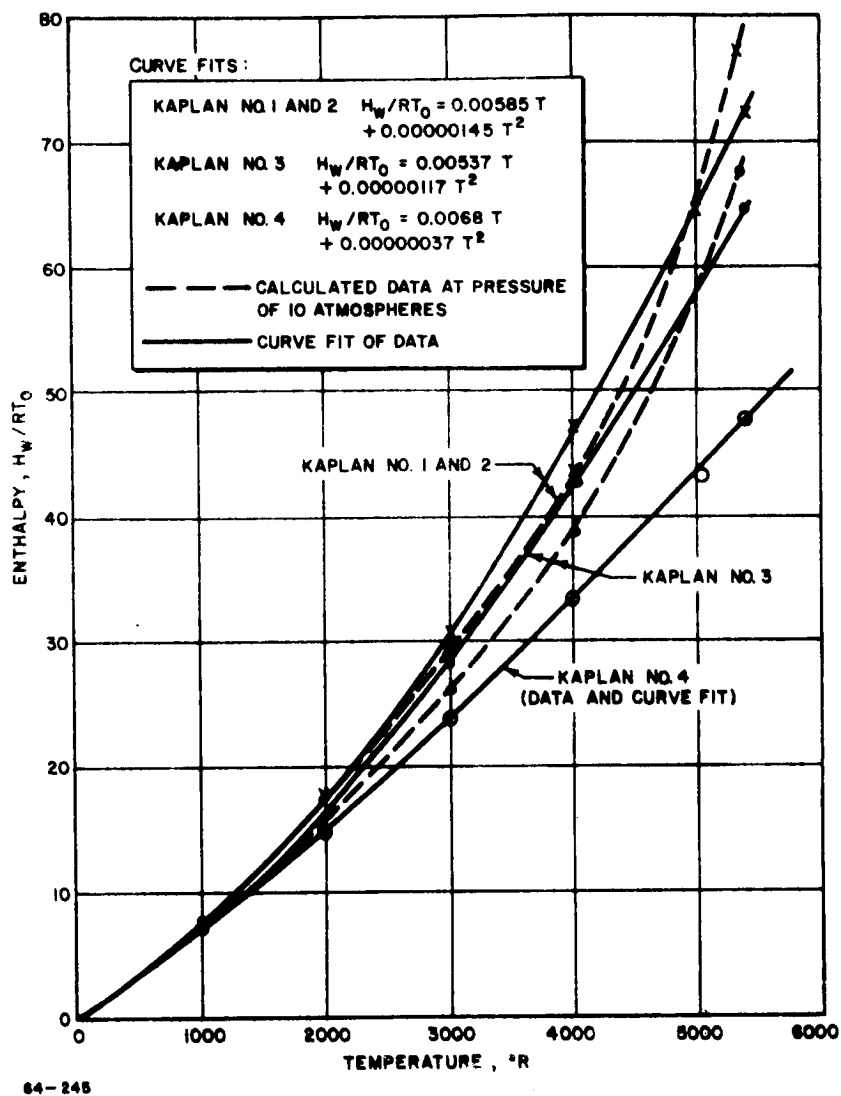


Figure 1-43 ENTHALPY VERSUS TEMPERATURE FOR MARS KAPLAN ATMOSPHERES

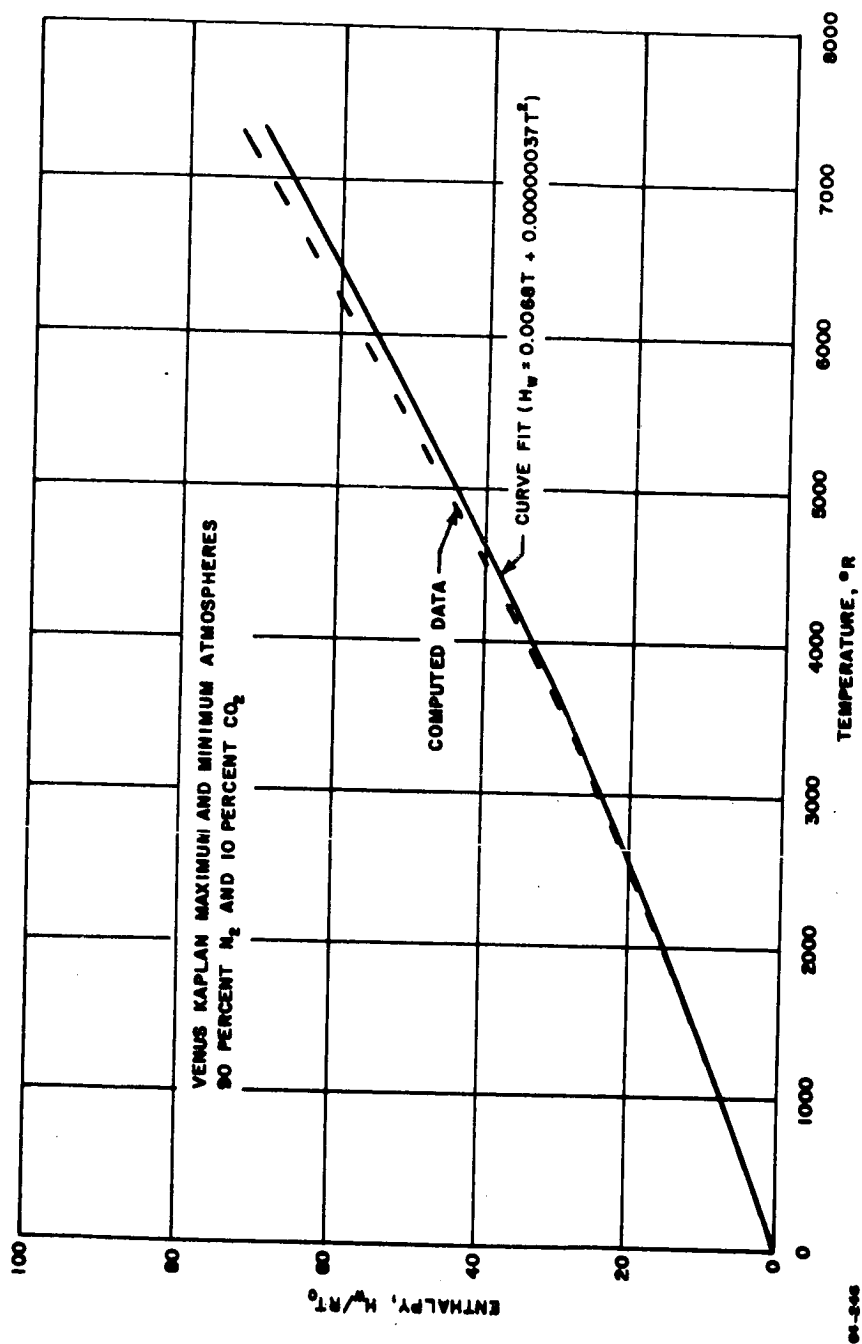


Figure 1-44 ENTHALPY VERSUS TEMPERATURE FOR VENUS KAPLAN ATMOSPHERE

### 3. Materials

#### a. Material Behavior

A low-density heat shield material was selected for the Mars vehicles. The material is a silica-epoxy-phenolic composite. Heat shield weights were obtained over the entire body using this material. A high temperature graphite-phenolic Avcoat heat shield material was employed on the high heating surfaces of the Venus-bound vehicles. The low density material used for Mars, was also used in low heat input areas of the Venus vehicles. The Mars material is a high temperature charring ablator with a low thermal conductivity. It is composed of organic resins and silica fibers and powder. The Venus material is a graphite epoxy material with good ablation characteristics and relatively poor insulation properties. These materials were selected on the basis of material tradeoff studies.

Charring materials have been studied extensively both experimentally (ref. I-84) and mathematically (ref. I-83) under a convective heating environment. Most of these studies were for an earth environment. Reference I-85 shows the results of an experimental study aimed at determining the effects of gas composition on material performance, i. e. the importance of different chemical reactions at the surface or in the boundary layer. Preliminary results of ablation tests at Avco indicate a similar effect as reference I-85 of gas composition on ablation performance, although there is substantial scatter in the data. The experimental evidence indicates that surface or boundary layer combustion is more significant in an earth environment than for most proposed Mars and Venus environments. It is also evident that the combustion effect is a strong function of the quantity of free oxygen in the boundary layer. However, the Martian atmospheres contain from 0 to 65 percent CO<sub>2</sub> and the Venus atmospheres 10 percent CO<sub>2</sub>, which can form free oxygen by dissociation at the high boundary layer temperatures encountered during planetary entry. Therefore, to perform an adequate analysis, the gas composition at the edge of the boundary layer must be determined, including dissociation of the CO<sub>2</sub>.

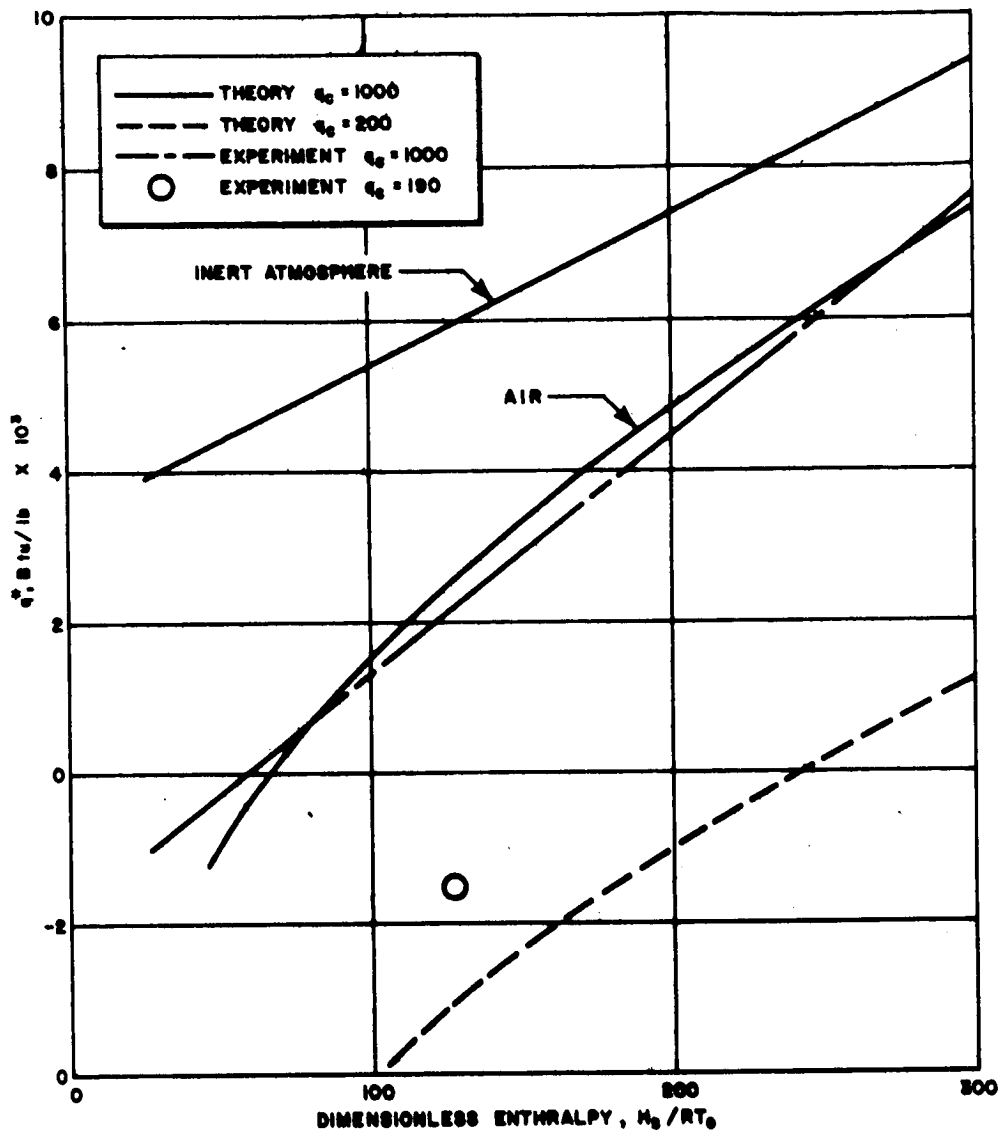
For the material selected for the Mars calculation, the resins decompose to form a char, which contains carbon. The latter will react to some extent with the silica within the char; at or near the surface the remaining silica will vaporize, liberating free oxygen, which in turn reacts with the carbon to form carbon monoxide. The net energy associated with these reactions is about 340 Btu/lb of char. Excess carbon is available for reaction with the boundary layer gases; these reactions will occur at the surface if they are diffusion controlled or

in the boundary layer if the surface temperature is high enough to cause sublimation of the carbon. Which of these processes will occur depends on the heating rate and enthalpy, as well as on the gas composition.

Calculations were made assuming the reaction to occur in the boundary layer. The results are shown in figure I-45 for two different heat fluxes. Also shown are data obtained from Avco tests. The agreement is seen to be excellent for air at the higher heat flux level. The data also show the same trend, but to a lesser extent, with heat flux as the theory. Tests were also performed in a nitrogen atmosphere; the results showed considerable scatter and are difficult to interpret. However, there was no evidence of a substantial improvement in ablation efficiency, such as predicted by the theory. This is possibly due to reactions between the graphite and nitrogen.

The ability to predict the temperature gradients within the material has been checked many times by comparisons of test and theory. Figure I-46 shows one such comparison where the data are compared with both charring and surface ablation theories. It can be seen that both theories do a moderately good job of predicting the internal temperature response of the material, although the charring ablation theory shows better correlation.

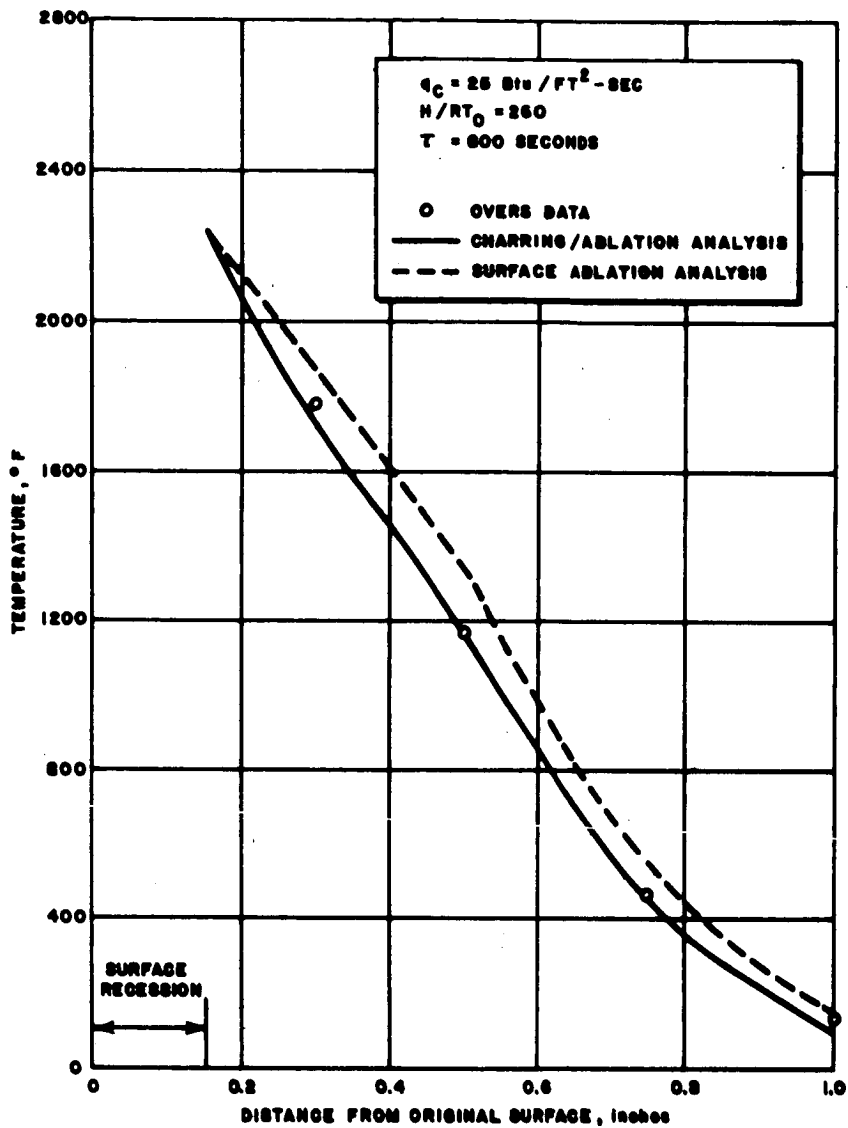
To date, there is a scarcity of information in the literature on the effect of combined radiative and convective heating. Several unreported test results indicate that materials perform better than what might at first be expected. Preliminary thinking suggests two possible reasons for this. First, absorption of the radiant heat input by the boundary layer gases, including the ablation products, undoubtedly exists and possibly to a fairly large extent. Secondly, absorption of the radiant heat at the surface increases the surface temperature, thus increasing the likelihood of carbon sublimation, and therefore material efficiency. Calculations have been made for a material such as the graphite-phenolic Venus material predicting the effect of a radiant input on material performance. The calculations assumed the graphite to vaporize at the surface and react with the oxygen in the boundary layer; also, the boundary layer was assumed transparent to the radiant input. The results are presented in figure I-47 in the form of  $q^*$  versus enthalpy for a constant convective heating of  $1000 \text{ Btu/ft}^2\text{-sec}$ . A large increase in material efficiency is observed when the radiation is of the same level as the convection. Further increases in radiant heating are not nearly as beneficial; in fact, the material efficiency is predicted to decrease when the heating is mostly radiative. Similar calculations were made and results obtained for the low density Avcoat material.



64-181

Figure 1-45 ABLATION PERFORMANCE OF MARS AVCOAT MATERIAL





64-120

Figure 1-46 TEMPERATURE GRADIENT COMPARISON

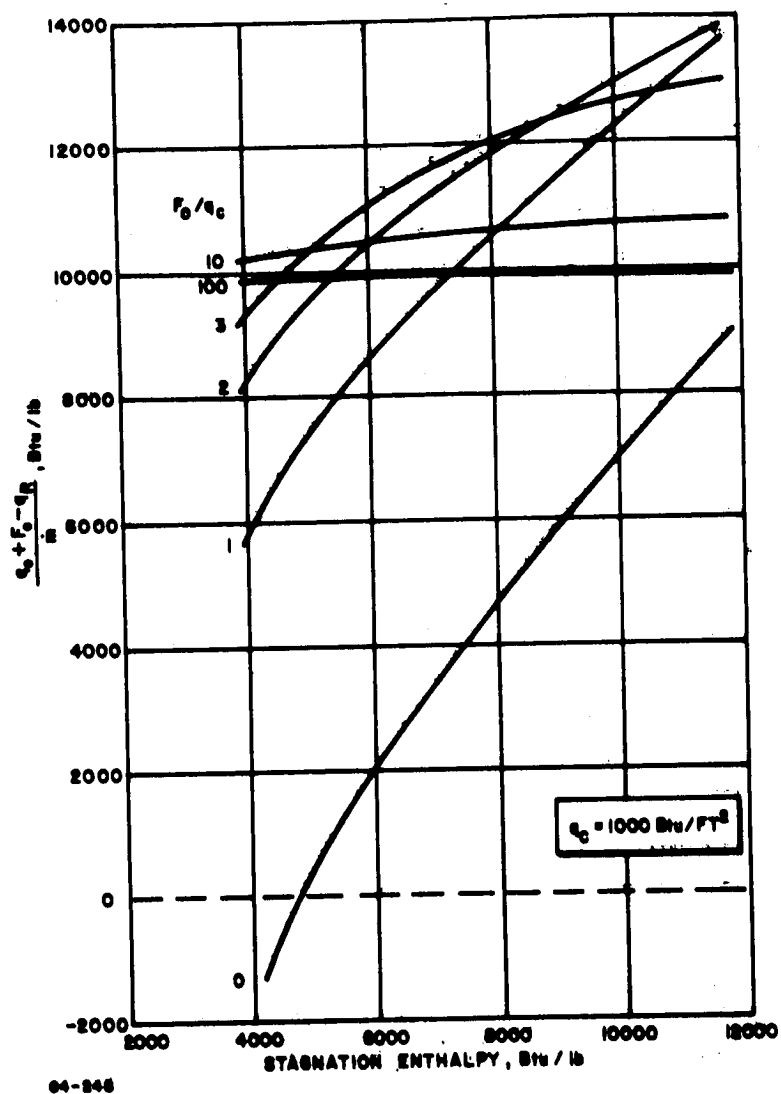


Figure 1-47 EFFECT OF RADIANT HEATING ON THE ABLATION PERFORMANCE OF A GRAPHITE-EPOXY COMPOSITE

The above analysis is based on several assumptions, and therefore open to question. The only data available are at low enthalpies ( $H_g/RT_0$  between 70 to 170) in an earth environment. The ratio of radiative heating to convective heating was between 0 and 2.0, but the total heating was not kept constant. Results of these tests (performed at NASA Ames) show that  $Q^*$  generally increased with an increased ratio of radiative to convective heating. Also determined during these tests was the fact that the surface temperature increased as the radiative heating increased. This is consistent with the predictions.

#### b. Material Properties

Successful design of heat shields for earth and planetary entry depend not only on having adequate analysis methods and a proper understanding of material behavior, but also on the availability of accurate thermodynamic properties. It is not an easy matter to perform all the tests required to determine the necessary properties; nor is it always clear how to interpret test results (e. g., surface emissivity of an ablating specimen). Therefore, there is a tendency, and sometimes a need, to assume values for purposes of preliminary design and tradeoff studies. Rather than to become the subject of arbitrary guessing in this study, consideration was given to materials for which extensive testing has been done.

Each of these materials, particularly the Mars material, has been fairly well characterized at Avco RAD through numerous ground tests. Each of these materials is considered to be outstanding for certain types of environment; the low density material for low to moderate heat flux and long soak time conditions and the graphite-phenolic material for high heat flux situations, when ablation is the principal mode of heat dissipation.

The thermal properties selected for this study based on the above two materials are given in table I-29.

The ablation properties for Avcoat materials for Mars and Venus atmospheres are based on the following assumptions:

- 1) Vaporization of silica and subsequent dissociation into  $\text{SiO}$  and  $\text{O}_2$  both occurring at or very near the surface
- 2) Combustion at the surface of the carbon in the char supported by the available oxygen from the silica reaction and by oxygen from the boundary layer

TABLE I-29

## MATERIAL PROPERTIES

Parameter	Mars	Venus	Aluminum	Beryllium
Thermal Conductivity (K) (Btu/ft/hr°F)	0.068	0.44	120.0	93.0
Specific heat ( $C_p$ ) (Btu/lb)	0.37	0.28	0.214	0.475
Density ( $\rho$ ) (lb/ft <sup>3</sup> )	37.0	80.0	168.0	115.0
Emissivity ( $\epsilon$ )	0.75	0.90	----	0.50
Surface Absorbtivity ( $\alpha$ )	0.90	0.90	----	0.90
Ablation Temperature (°F)	4950	6050	----	----
Solid fraction ( $f_1, f_2$ )	1.0, 0.0	0.8, 0.20	----	----
Vaporization fraction	1.0	0.6	----	----
Heat absorbed by phase change or reaction ( $H_{v1}, H_{v2}$ ) (Btu/lb)	85.0 0.0	11000.0, 750.0	----	----
Laminar transpiration, factor ( $\eta_L$ )	0.57	0.56	----	----
Turbulent Transpiration factor ( $\eta_T$ )	0.38	0.36	----	----

3) Charring of the material below the surface. The total energy absorbed by the reactions of the first two assumptions can be calculated if the quantity of char produced per pound of virgin material and the quantity of silica in the virgin material are known. The latter is determined by the material specifications and the former by thermogravimetric analysis. For the Mars material, the first two reactions produce a net exothermic reaction of 170 Btu/lb of virgin material. From the third assumption, charring characteristics can be transformed into a surface ablation model, i. e., the 255 Btu absorbed by the resin

decomposition must be added to the surface heat absorption terms. The net result is a heat of absorption,  $H_{V1}$ , of 85 Btu/lb.

The transpiration coefficients are based on arc test data and by a consideration of the probable gas composition. The ablation temperature and surface emissivity are also based on arc test data. An average constant ablation temperature was chosen because of the model used in the program.

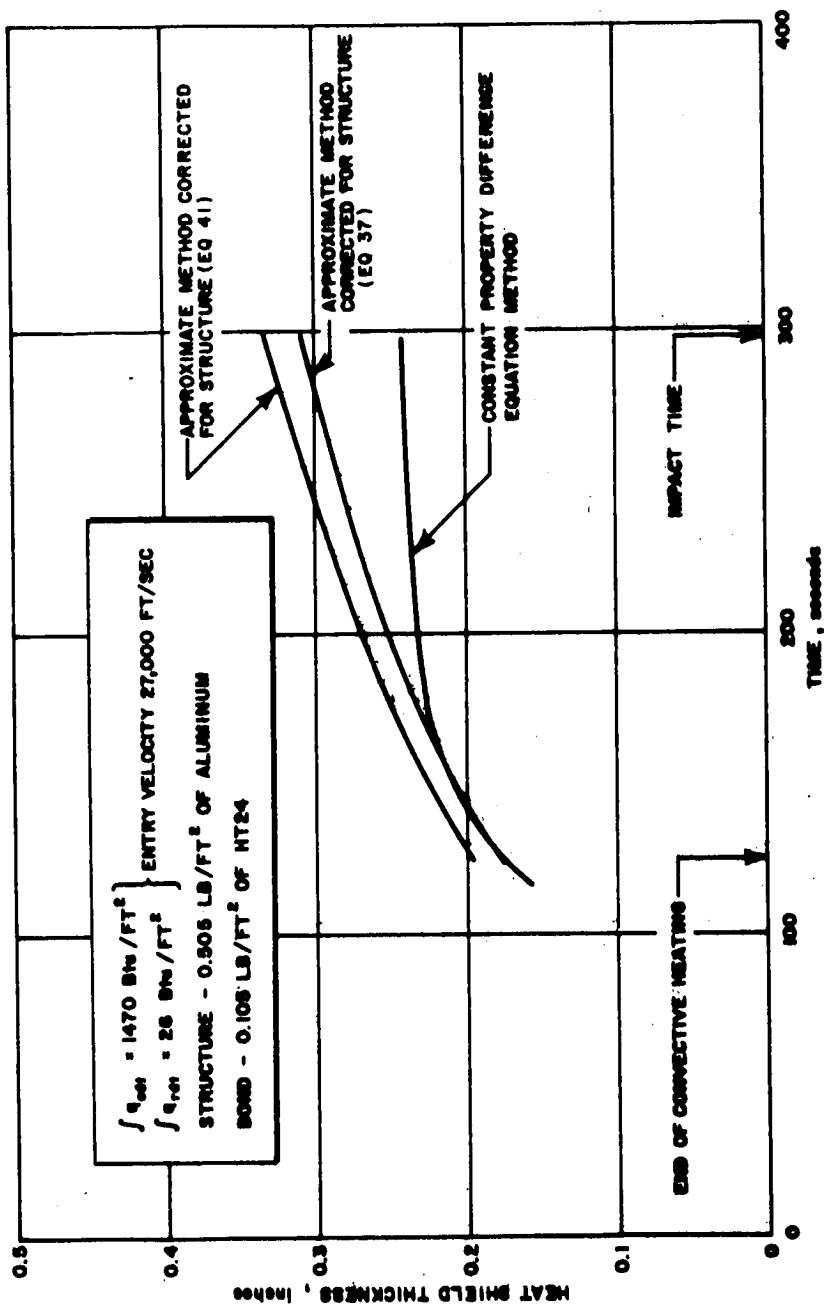
#### 4. Evaluation of Heat Shield Block

Various types of comparisons have been made between the approximate method described above and more exact solutions. They can be classified as follows:

- 1) Comparisons with more exact numerical difference equation techniques employing the identical mathematical model (non-charring model)
- 2) Comparison between more exact difference numerical techniques employing the identical mathematical model and simulated charring model
- 3) Comparisons with more exact numerical techniques employing a mathematical charring model.

##### a. Comparison with Finite Difference Solutions for Surface Ablators

Comparisons were made for Mars type heating (most Mars cases produced no ablation) using constant thermophysical properties. The system consisted of an Avcoat heat shield and aluminum structure. The numerical solutions used for making the comparisons were obtained by solving the actual transient problem (equations (1) to (4)) by means of difference equations, implicit in time and central in space. A description of this solution and an analysis of its accuracy is reported in references I-78 through 81. The comparisons also included both structure correction techniques. The results are shown in figure I-48 where heat shield weight is plotted versus soak time. They show that the heat shield weight, computed by the approximate method, continues to rise within the soak time range shown while the results, computed by the numerical solution of the Fourier Conduction equation, rise to a maximum and then, of course, stays constant. Furthermore, the approximate method yields results closer to the numerical solution when corrected for the structure by equation (37) than by equation (41). In both cases, however, the agreement is quite good, considering the savings in computer time.



04-200

Figure 1-48 HEAT SHIELD THICKNESS VERSUS TIME OF HEAT SHIELD JETTISON

The difference introduced by soak periods is caused by the nonlinearity of the problem. By necessity the equivalent pulse that results in a constant surface temperature and defined by equation (6), is taken from  $t$  to  $t_f$  where  $t_f$  is the end of the soak period.  $H_g'$  and the reradiation term, similarly, are taken over this period. Thus, there is no real soak period in the approximate method. The resulting effect is shown in figure I-49, where the energy content of the system, obtained from equation (10) and from the numerical solution is plotted versus soak time. Notice that the curves are close to each other until the system starts to lose heat. After this time the approximate technique continues to rise slowly. As expected, the heat shield weight comparisons tend to part when the energy content curves deviate also. In all cases considered, the maximum heat shield weight, as calculated by the numerical solution, occurred before the soak period equaled the heating period. The heat shield weights calculated for this time period by the approximate method were thought to be within acceptable accuracy. Therefore, an upper limit to  $t_f$  has been ascribed;  $t_f$  was allowed to be no greater than twice the length of the convective pulse.

The difference in the two structure correction techniques can be attributed to the assumption necessary to derive equation (41). This equation applies the additional constraint that the mean temperature history ( $\Delta T_M$ ) of the heat shield is unchanged when backed by a capacitive structure. A capacitive structure and no change in surface heating is assumed in both methods. The assumption of a capacitance will introduce no noticeable difference. However, the validity of the assumption that the surface temperature and mean temperature histories remain the same for appreciable structure weight is dependent upon the degree to which these temperatures in the composite and single system satisfy a semi-infinite slab analysis. This is a complex function of material properties, pulse magnitude and shape and structure weight. A low thermal conductivity, short pulse period, heavier heat shield, and lighter structure tend to increase the tendency of these temperatures to satisfy a semi-infinite slab analysis. The mean temperature history will deviate rapidly, however, and the surface temperature will follow a semi-infinite slab analysis reasonably well to impact when the dimensionless time

parameter  $\tau = \frac{K_1 \rho_1 t_D}{C_p W_I^2} < 0.09$  where  $t_D$  is the length of the actual

pulse defined by equation (3). For a linearized heating problem with an isosceles triangular pulse,  $t_D$  may double and only effect the surface temperature 20 percent at the end of a soak period equal to the pulse length. Thus, equation (37) should represent a more reliable structure correction technique than equation (41).

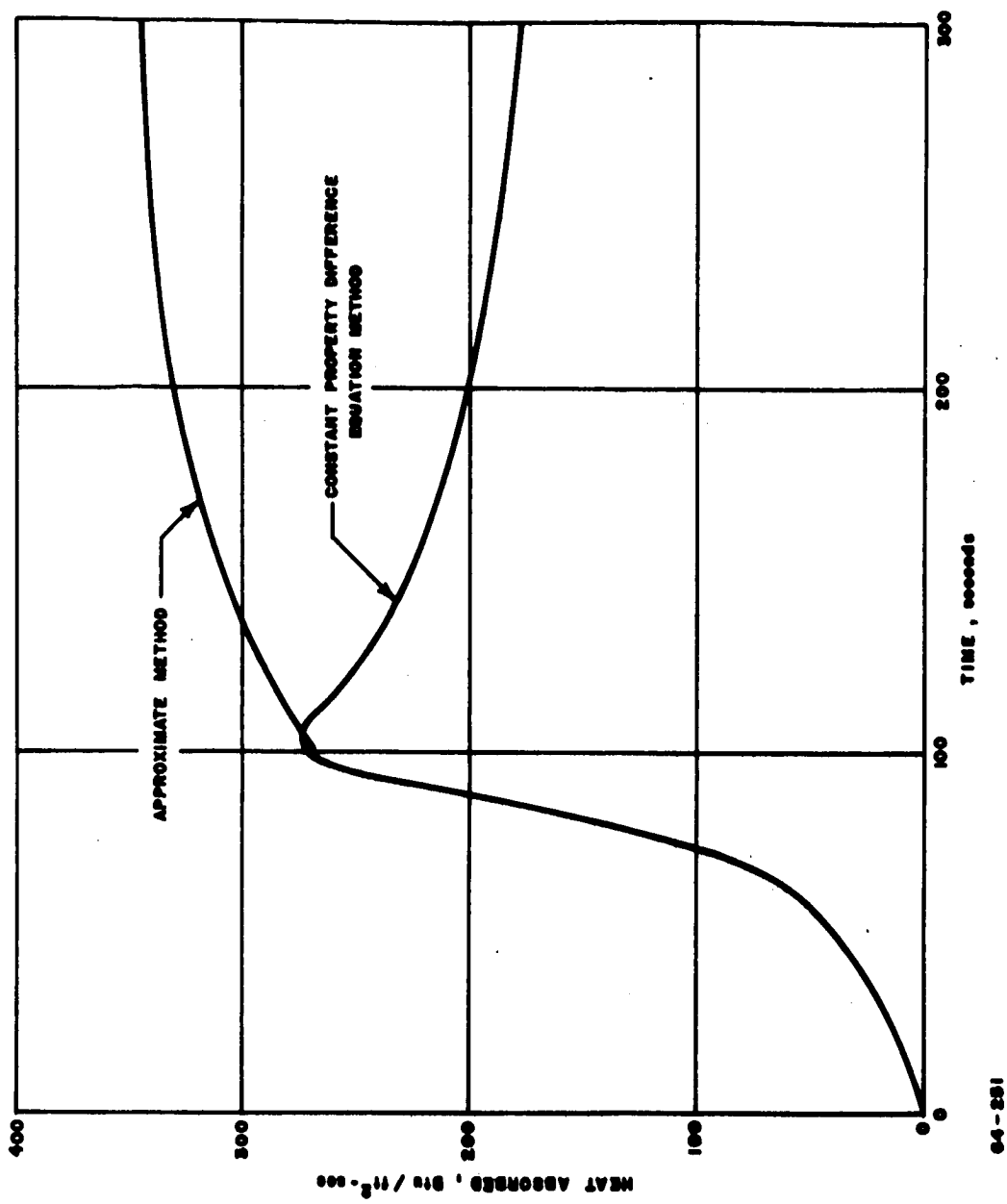


Figure 1-49 HEAT ABSORBED BY THERMAL PROTECTION SYSTEM VERSUS TIME OF HEAT SHIELD JETTISON



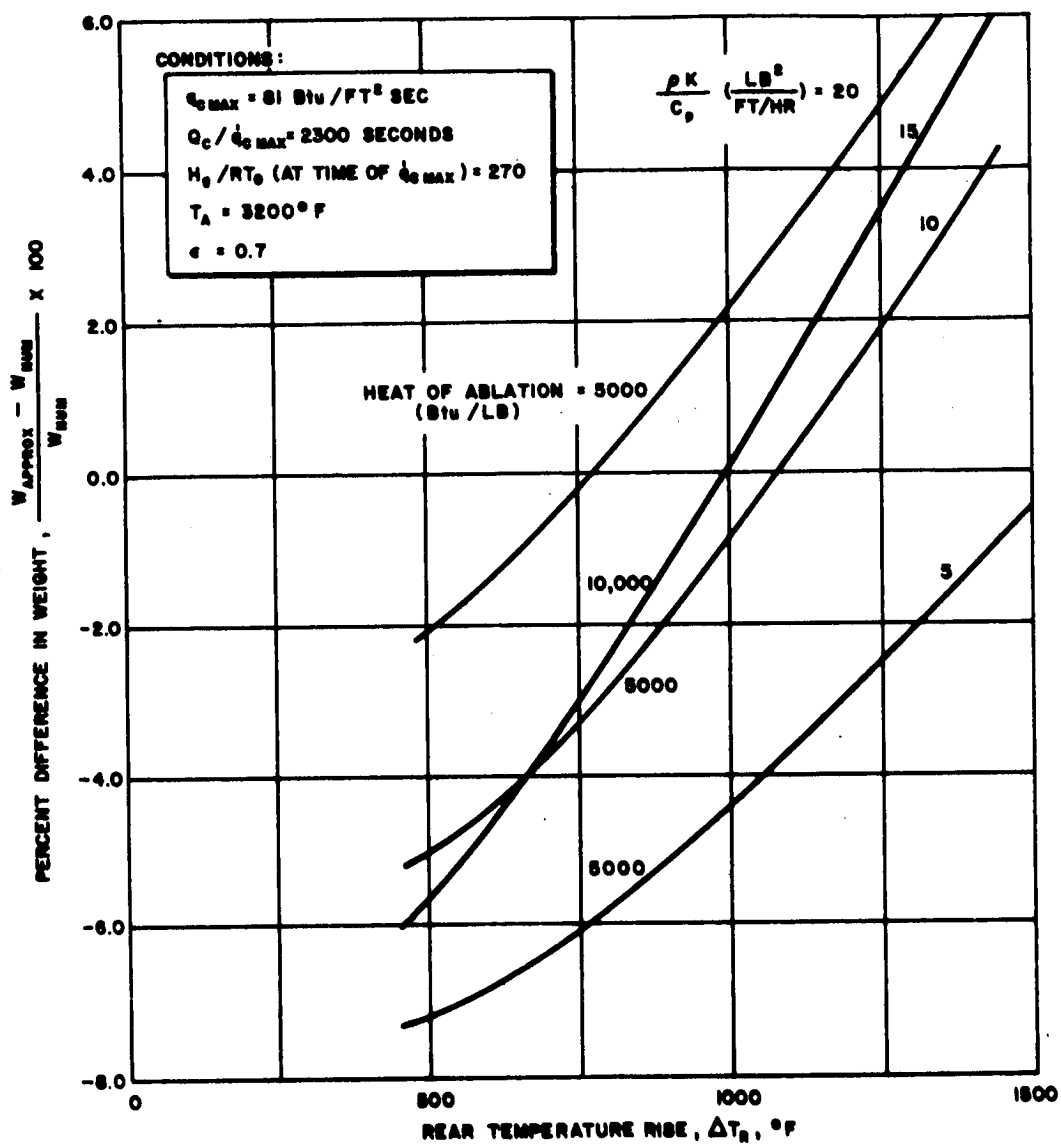
Comparisons for an ablating system in a convective heating environment have been reported in reference (I-82). They are repeated in figure (I-52). Again the approximate method is seen to be quite accurate.

b. Comparisons with a Charring Theory

Ground tests of the Mars Avcoat material in both convective and radiative environments, have clearly shown that a char layer is formed. Previous experience with charring materials have indicated that, under some conditions, the charring process can have a significant effect on the temperature response of the heat shield and structure. Reference I-83 presents an analysis applicable to charring materials, together with comparisons with experimental data; the comparisons show the charring theory to be a significant improvement over the noncharring model. Unfortunately, the computer program needed to solve the differential equations is quite complicated and therefore lengthy to run. Thus, it is not at all amenable to a parametric study such as is presented in this report, nor even to large numbers of comparisons with the approximate method. Calculations were made, however, for purposes of comparison for one trajectory and several thicknesses. The conditions were a Mars Kaplan No. 1 atmosphere,  $V = 24,000$  ft/sec,  $\gamma = -45$  degrees, and  $M/CDA = 0.2$ . The total heating was  $Q_C = 750$  and  $Q_R = 700$  Btu/ft<sup>2</sup>. The results are shown in figure I-51 for both the charring and non-charring theories. One other significant difference existed between the sets of calculations--the calculations labeled "charring theory" assumed the material to be somewhat transparent, i. e. the radiation was absorbed in depth. The surface ablation calculations on the other hand assumed the gas cap radiation was absorbed at the surface, a more optimistic assumption.

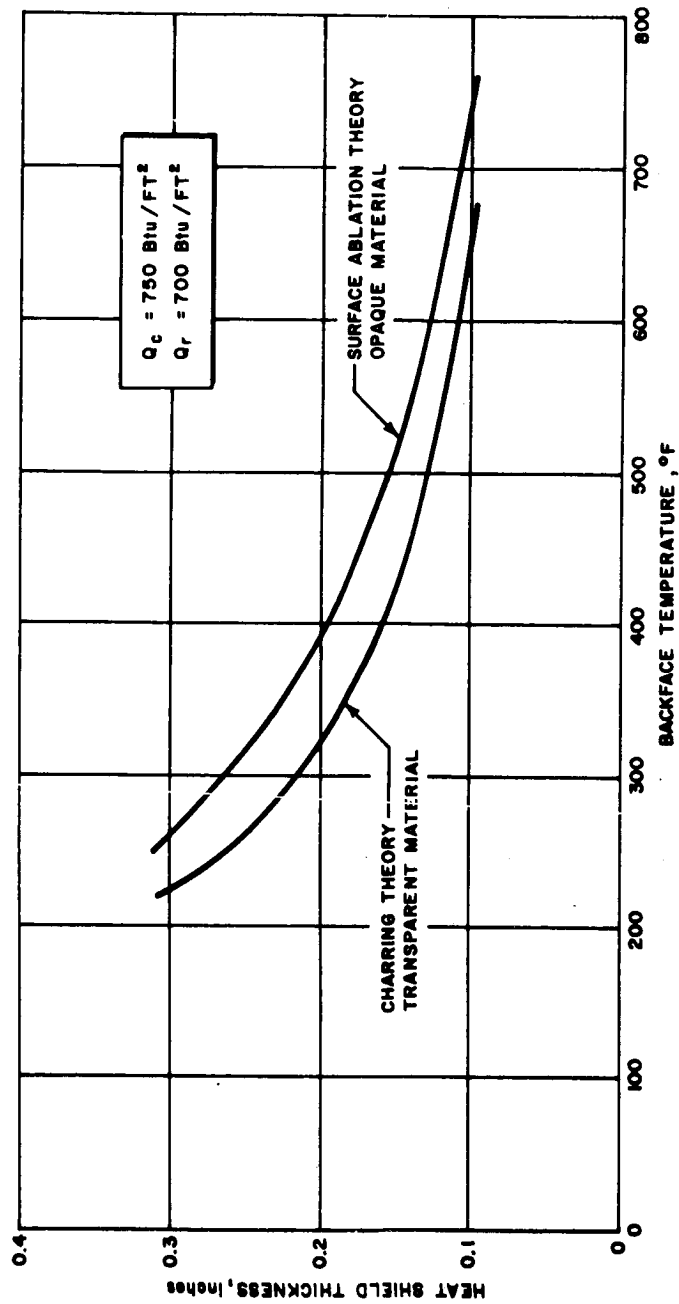
For this particular case, it can be concluded that the surface ablation theory is conservative for a backface temperature of 600°F. Other cases would also produce similar results, i. e. lower temperatures and heat shield requirements when charring is accounted for. The potential weight savings are felt to be about the same for other environments and to be more a function of the material.

Another way of viewing the differences indicated by figure I-51 is that the heat shield thicknesses determined by the surface ablation theory and/or approximate method contain a desirable conservatism, i. e. safety factor. While a more realistic approach in designing heat shields is to employ the best available theory and to use conservative values for the input parameters (properties and environment); the use of a conservative theory and best values of the properties is justified by the savings in computer time.



64-288

Figure 1-50 COMPARISON OF ABLATION WEIGHTS CALCULATED BY APPROXIMATE AND NUMERICAL SOLUTIONS



94-122

Figure 1-51 COMPARISON OF CHARRING AND NONCHARRING THEORIES

## REFERENCES

- I-1. Hochstim, A. R., Equilibrium Compositions, Thermodynamic and Normal Shock Properties of Air with Additives, ASTIA AD 274-930, 1(1 December 1961).
- I-2. Gilmore, F. R., Equilibrium Composition and Thermodynamic Properties of Air to 24,000°K, RAND TM-1543 (24 August 1955).
- I-3. Penner, S. S., Chemistry Problems in Jet Propulsion, Pergamon Press, 1957.
- I-4. Mayer, M. G. and J. E. Mayer, Statistical Mechanics, John Wiley and Sons, Inc. 1961.
- I-5. Hertzberg, G., Molecular Spectra and Molecular Structure I. Spectra of Diatomic Molecules, Van Nostrand Co., 1950.
- I-6. Rudin, M. and B. Regent, High Temperature Thermodynamic Properties of Selected Gases, Aeronautical Research Lab., VIDYA Report No. 69(10 March 1962).
- I-7. Moore, C. E., Atomic Energy Levels, National Bureau of Standards Circular 467 (1948).
- I-8. McBride, B.J. and S. Gordon, Thermodynamic Functions of Several Triatomic Molecules in the Ideal Gas State, J. of Chem. Phys. 35, 6 (December 1961).
- I-9. Schwartz, R. N., Z. I. Slawsky, K. F. Herzfeld, Calculation of Vibrational Relaxation in Gases, J. of Chem. Phys. 20, 10 (October 1952).
- I-10. Hansen, C.F., Approximateions for the Thermodynamic and Transport Propefties of High Temperature Air, NASA TR-R-50 (1959).
- I-11. Lunev, V. V., Motion of a Slender Blunted Body in the Atmosphere with High Supersonic Speed, Izves. Akad. Nauk, U.S.S.R. Otdelenie Tekhnicheskikh Nauk, Mekhanika i. Mashinostroenie, 4, 131-139 (1959). Translated in ARS J. 30, 4, 414-416 (1960).
- I-12. Sychev, V. V., In the Theory of Hypersonic Gas Flow with a Power-law Shock Wave, Prik. Mat. Mekh 24, 3, 518-523 (1960). Translated in J. Appl. Math. and Mech. 24, 3, 756-764 (1960).

- I-13. Cheng, H. K., J. G. Hall, T. C. Golian, and A. Hertzberg, Boundary-layer Displacement and Leading-edge Effects in High-Temperature Hypersonic Flow, J. Aerospace Sci. 28, 5, 353 (May 1961).
- I-14. Yakura, J. K., A Theory of Entropy Layers and Nose Bluntness in Hypersonic Flow, International Hypersonics Conference, Massachusetts Institute of Technology, Preprint 1983-61 (August 1961).
- I-15. Taylor, G. I., (The) Formation of a Blast Wave by a Very Intense Explosion, Proc. Roy. Soc. London Ser. A 201, 159-186 (1950).
- I-16. Sedov, L. I., Propagation of Strong Blast Waves, Prik. Mat. Mekh. 10, 241-250 (1946). See also, Sedov, L. I., Similarity and Dimensional Methods in Mechanics; English translation, M. Holt, ed., Academic Press, New York (1959).
- I-17. Lin, S. C. Cylindrical Shock Waves Produced by Instantaneous Energy Release, J. Appl. Phys. 25, 54-57 (1954).
- I-18. Cheng, H. K., and A. J. Pallone, Inviscid Leading-Edge Effect in Hypersonic flow, J. Aeronaut. Sci. 23, 8, 700 (July 1956).
- I-19. Lees, L., and T. Kubota, Inviscid Hypersonic Flow Over Blunt-Nosed Slender Bodies, J. Aeronaut. Sci. 25, 3, 195 (March 1957).
- I-20. Einbinder, H., (A) Note on Blast-Wave Theory, J. Aerospace Sci. 26, 3, 191 (March 1959).
- I-21. Freeman, N. C., (A) Note on the Explosion Solution of Sedov with Application to the Newtonian Theory of Unsteady Hypersonic Flow, J. Aerospace Sci. 27, 1, 77 (January 1960).
- I-22. Lees, L., and T. Kubota, Inviscid Hypersonic Flow Over Blunt Nosed Slender Bodies, JAS 24 (March 1957).
- I-23. Klugerman, J. and C. W. Shipman, A Numerical Method of Solving the Thermochemical Equilibrium Problem, Avco Doc. RAD-TM-62-11 (12 April 1962).
- I-24. Stern, R. G., A Thermochemical Equilibrium Machine Program, Avco Doc. RAD-TM-62-57 (28 July 1962).
- I-25. Yos, J. M., Transport Properties of Nitrogen, Hydrogen, Oxygen, and Air to 30,000°K, Avco Doc. RAD-TM-63-7 (22 March 1963).

- I-26. Van Tassell, W. and A. Pallone, Similar Solutions of the Compressible Laminar Boundary Layer Equations for Air in Equilibrium Dissociation and Ionization with and Without Air Injection in Stagnation Region, Avco Doc. RAD-TM-61-22 (28 June 1961).
- I-27. Vinokur, M., Inviscid Hypersonic Flow Near the Stagnation Point of Oblate Ellipsoidal Noses, JAS (October 1958).
- I-28. Thyson, N. A. and G. D. Waldman, Three Dimensional Stagnation Point Heating, Avco Doc. RAD-TM-62-92 (21 November 1962).
- I-29. Kemp, H. H., P. H. Rose, and R. W. Detra, Laminar Heat Transfer Around Blunt Bodies in Dissociated Air, J. Aeronaut. Sci. (July 1959).
- I-30. Schurmann, E. H., Engineering Methods for the Analysis of Aerodynamic Heating, Avco Doc. RAD-TM-63-68 (11 November 1963).
- I-31. Chandrasekhar, S., Radiative Transfer, Oxford University Press, London, 1950.
- I-32. Kivel, B. and K. Bailey, Tables of Radiation From High Temperature Air, AERL Research Report 21 (October, 1959).
- I-33. Rosseland, S., Handhler Astrophys, 3, Part I 443-457, (1930).
- I-34. Patch, R. W., W. L. Shockleford, and S. S. Penner, Approximate Spectral Absorption Coefficient Calculations for Electronic Band Systems Belonging to Diatomic Molecules, J. Quant. Spect. Rad. Trans. 2, 263-271 (1962).
- I-35. Unsold, A., Continuous Spectrum of High-Pressure Hg Lamp and Similar Gas Discharges, Ann. der Physic, 33, 607-616 (1938).
- I-36. Biberman, L. M. and G. E. Norman, Calculation of Photo-Ionization Absorption, Opt. Spektr., 8, 433-438 (1960).
- I-37. Biberman, L. M., G. E. Norman, and K. N. Ulyanoo, On the Calculation of Photo-Ionization Absorption in Atomic Gases, Opt. i., Spektr. 10, 565-569.
- I-38. Bergess, A., and M. J. Seaton, A General Formula for the Calculations of Atomic Photo-Ionization Cross-Sections, Monthly Notices of the Roy. Astron. Soc., 120, 121-151 (1960).
- I-39. Fairbairn, A., The Spectrum of Shock-Heated Gases Simulating the Venus Atmosphere, Avco Everett Research Note 371 (July 1963).

- I-40. James, C. S., Experimental Study of Radiative Transport from Hot Gases Simulating in Composition the Atmospheres of Mars and Venus, Paper 63-455 presented at AIAA Conference on Physics of Entry into Planetary Atmospheres (26 - 28 August, 1963).
- I-41. Morris, J. C., Research On Radiation from Arc Heated Plasmas - Avco RAD Quart. Progress Report No. 7, Contract No. AF33(616)-8390 (8 September 1963).
- I-42. Teare, J. D., S. Georgiev, and R. A. Allen, Radiation From the Non-Equilibrium Shock Front, Avco Everett RR 112 (October 1961).
- I-43. Page, W. A., Shock Layer Radiation of Blunt Bodies Travelling at Lunar Return Entry Velocities, IAS Paper No. 63-41, Presented at the IAS 31st Annual Meeting, N. Y. (21-23 January 1963).
- I-44. Lindenmeier, C. W., Kramers Radiation from Hot Air, Avco Everett Research Note 157 (September 1959).
- I-45. Biberman, L. M., and G. E. Norman, On the Calculation of Photoionization Absorption, Opt. i. Spektr., 8 433-438 (1960).
- I-46. Burgess, A. and M. J. Soaton, A General Formula for the Calculation of Atomic Photoionization Cross-Sections, Monthly Notices of the Astron. Soc., 120, 121-151 (1960).
- I-47. Olsen, H. N., Partition Function Cutoff and Lowering of the Ionization Potential in an Argon Plasma, Phys. 124, 6, 1703 (1961).
- I-48. Morris, J. C., and G. Bach, Private Communication.
- I-49. Allen, R. A., P. H. Rose, J. C. Camm, Non-equilibrium and Equilibrium Radiation at Super-Satellite Re-entry Conditions, IAS Paper 63-77, Presented at the IAS 31st Annual Meeting, N. Y. (21-23 January 1963).
- I-50. Venus-Mars Capsule Study, Volume II, General Electric Document, Work Performed Under JPL Contract 950626 (30 July 1962).
- I-51. Raymond, J. L., Thermodynamic Properties of Carbon Dioxide to 24,000°K - With Possible Application to the Atmosphere of Venus, RM-2292 (26 November 1958).
- I-52. Treanor, C. E. and J. G. Logan, Jr., Thermodynamic Properties of Nitrogen from 2000°K to 8000°K, Cornell Aero. Lab. Inc., Report No. BE-1007-A-5 (January 1957).

- I-53. Chushkin, P. I., and N. P. Shulishnina, Tables of Supersonic Flow About Blunted Cones, Computation Center Monograph, Academy of Sciences USSR, Moscow (1961). Translated in Avco RAD-TM-62-63 by J. F. Springfield (14 September 1962).
- I-54. Kopal, F., Tables of Supersonic Flow Around Cones, Technical Report 1, Department of Electrical Engineering, Massachusetts Institute of Technology, Cambridge, Massachusetts (1947).
- I-55. Cheng, H. K., Hypersonic Flow with Combined Leading-Edge Bluntness and Boundary-Layer Displacement Effect, Cornell Aeronautical Laboratory Report AF-1285-A-4 (1960).
- I-56. Bertram, M. H., Tip-bluntness Effects on Cone Pressure at  $M = 6.85$  J. Aerospace Sci. Reader's Forum 23, 9, 898 (September 1956).
- I-57. Gruszczynski, J. S. and W. R. Warren, Jr., Experimental Heat Transfer Studies of Hypervelocity Flight in Planetary Atmospheres, AIAA Paper 63-450 (1963).
- I-58. James C., and J. E. Terry, Shock Wave Profiles Over Ellipsoidal-Nosed Bodies in Hypersonic Flow, JAS (September 1962).
- I-59. Friedrich, H. R., and F. Dore, The Dynamic Motion of a Missile Descending Through the Atmosphere, J. Aero. Sci., 22, 9 628-632 (September 1955).
- I-60. Allen, H. J. Motion of a Ballistic Missile Angularly Misaligned with the Flight Path Upon Entering the Atmosphere and its Effect Upon Aerodynamic Heating, Aerodynamic Loads, and Miss Distance, NACA-TN-4048 (October 1957).
- I-61. Nicolaides, John D., On the Free Flight Motion of Missiles Having Slight Configurational Asymmetries, Ballistic Research Laboratories Report No. 858 (June 1953).
- I-62. Nelson, Robert L., The Motions of Rolling Symmetrical Missiles Referred to a Body-Axis System, NACA-TN-3737 (November 1956).
- I-63. Garber, T. B., On the Rotational Motion of a Body Re-entering the Atmosphere, J. Aero. Sci., 26, 7 443-449 (July 1963).
- I-64. Migotsky, E., On the Motion of Spinning Reentry Bodies, Avco Doc. RAD-TR-9-59-6 (1959).
- I-65. Sommer, C., and M. Tobak, Study of the Oscillatory Motion of Manned Vehicles Entering the Earth's Atmosphere, NASA-Memo-3-2-59A.



- I-66. Bodner, S. R., Correlation of Buckling Parameters for Sandwich and Solid Wall Spherical Caps, Avco RAD Technical Release, S220-T-355 (5 August 1963).
- I-67. Homewood, R. H., A. C. Brine, and A. E., Johnson, Buckling Instability of Monocoque Shells, The Society of Experimental Stress Analysis, Paper No. 457, Presented at Washington, D. C. (20-22 May 1959).
- I-68. Gjelsvik, A. and S. R. Bodner, Nonsymmetrical Snap Buckling of Spherical Caps, J. Eng. Mech. Div. Proc. of the ASCE p 135 (October 1962).
- I-69. Budiansky, B., Buckling of Clamped Shallow Shells, Proc., LVTAM Symposium on the Theory of Thin Elastic Shells, No. Holland Pub. Co. 64, (1960).
- I-70. Serpico, J. C., The Structural Strength of Sandwich Cylindrical and Conical Shells Subjected to Rotationally Symmetric Loading Avco Doc. RAD-TR-61-35 (1961).
- I-71. McFarland, R. K., Jr., Hexagonal Cell Structures under Post-Buckling Axial Load, AIAA Journal, p. 1380 (June 1963).
- I-72. Serpico, J., Elastic Stability of Orthotropic Conical and Cylindrical Shells Subjected to Axisymmetric Loading Conditions, Avco Doc. RAD-TR-61-7 (1961)
- I-73. Gerard, G. and H. Becker, Handbook of Structural Stability - Part III - Buckling of Curved Plates and Shells, NACA-TN-3783, p. 95 (August 1957).
- I-74. Kaplan, A. and Y. C. Fing, A Nonlinear Theory of Bending and Buckling of Thin Elastic Shallow Spherical Shells, NACA-TN-3212 (August 1954).
- I-75. Kloppel, K. von, and O. Jungbluth, Beitrag zum Durchschlag Problem dunnwandiger Kugelschalen, Der Stahlbau 22, 121-130 (errata p. 288) Berlin, Springer (1935).
- I-76. Carslaw, H. S. and J. C. Jaeger, Conduction of Heat in Solids, 2nd ed., Oxford Press, London (1959), p. 282.
- I-77. Mascola, R. E., Temperature Response in Slabs Subject to a Sinusoidal Heat Pulse, Avco Doc. RAD-9-(7)-TM-60-72 (15 December 1960).
- I-78. Brown, J. D. and R. E. Mascola, Numerical Solution of the Heat Conduction Equation for a Receding Surface, Avco Doc. RAD-2-TM-58-101 (September 1958).
- I-79. Landan, H. G., Heat Conduction in a Melting Solid, Quart. Appl. Math. 8, 81 (1950).

- I-80. Lotkin, M., The Calculation of Heat Flow in Melting Solids, Quart. Appl. Math., 18, 1 (1960).
- I-81. Brown, J. and R. E. Mascola, Digital Program 1327, Avco RAD Internal Memorandum S230 REM/JB-470 (29 March 1963).
- I-82. Brown, J. D. and F. A. Shukis, An Approximate Method for Design of Thermal Protection Systems, Presented at IAS 30th Annual Meeting, (January 1962).
- I-83. Munson, T. R. and R. J. Spindler, Transient Thermal Behavior of Decomposing Materials, Part I: General Theory and Application to Convective Heating, IAS Paper No. 62-60, Presented at IAS 30th Annual Meeting, New York, (January 1962).
- I-84. McAllister, L. E., J. C. Bolger, E. L. McCaffery, P. J. Roy, F. W. Ward, and A. C. Walker, Jr., Behavior of Pure and Reinforced Charring Polymer During Ablation Under Hypervelocity Reentry Conditions, from Application of Plastic Materials in Aerospace, Chemical Engineering Progress, Symposium Series 40, 59 (1963).
- I-85. Vojvodich, N. S. and R. B. Pope, An Investigation of the Effect of Gas Composition On the Ablation Behavior of a Charring Material, Presented at AIAA Conference on Physics of Entry into Planetary Atmospheres, M.I.T. Cambridge, Mass. (August 1963) Paper No. 63-465.
- I-86. Hartnett, J. P., and Eckert, E. R. G., Mass Transfer Cooling with Combustion in a Laminar Boundary Layer. Heat Transfer and Fluid Mechanics Institute, University of California, Stamford University Press, (1958).
- I-87. Brown, J., Program 1448, Avco Internal Memorandum S230-JB-532 (8 May 1963).
- I-88. Seiff, A., Ames Hypervelocity Free Flight Research, Astronautics and Aerospace Engineering (December 1963).
- I-89. Flinn, D. J., and T. R. Munson., Equilibrium Composition and Thermodynamic Properties of N, C, O, and A Mixtures to 4000°K (Avco internal Memorandum to be published).